Optical Property Studies and Metalorganic Chemical Vapor Deposition of Ferroelectric Thin Films

by

Chien–Hsiung Peng

Dissertation submitted to the Faculty of the

Virginia Polytechnic Institute and State University

in Partial fulfillment of the requirements for the degree of

Doctor of Philosophy

in

Materials Engineering Science

APPROVED:

S. B. Desu, Chairman

C. R. Houska

W. T. Reynolds, Jr.

R. Zallen

J. G. Dillard

August, 1992

Blacksburg, Virginia

Optical Property Studies and Metalorganic Chemical Vapor Deposition of Ferroelectric Thin Films

by

Chien–Hsiung Peng

Committee Chairman: Seshu B. Desu

Materials Engineering Science

(ABSTRACT)

Ferroelectric lead zirconate titanate thin films, $Pb(Zr_xTi_{1-x})O_3$ or PZT, have aroused considerable interest in recent years for the application in nonvolatile electronic memories because of their excellent ferroelectric properties. In this research, PZT thin films were studied from two aspects: the scientific aspect and the technical aspect.

The optical properties of PZT solid solutions and the structure development in PZT films were extensively investigatedIn the scientific aspect. The PZT films used in this part of study were prepared by metalorganic decomposition (MOD) process. The envelope method, with consideration of light intensity loss from the back surface of the substrate, was demonstrated to be a simple and convenient tool for obtaining the optical properties of the PZT films in the medium and weak absorption regions. In the near optical band gap region, both the transmission and reflection spectra were used to successfully calculate the optical constants of the films. The film thickness derived from the envelope method was cross checked by a computer simulation method and was found to have an accuracy better than 2%. An effective, versatile, and nondestructive optical method was developed for the study of the structure development in MOD PZT films. Also, the models for the structure development

were proposed and were verified by this optical method. Using this method, the characteristic temperatures (i.e., the initiation and completion temperatures) of each phase can be easily identified. In addition, the volume fraction of the perovskite phase in the pyrochlore–perovskite phase transformation region was obtained from this optical method.

From the technical point of view, ferroelectric PZT films were successfully and reproducibly deposited for the first time by hot–wall metalorganic chemical vapor deposition (MOCVD). One of the problems associated with the MOCVD technique is the availability of the precursors. After intensive studies searching for the most suitable precursors for MOCVD PZT thin films, the safe and stable precursors, namely lead tetramethylheptadione [$Pb(thd)_2$], zirconium tetramethylheptadione [$Zr(thd)_4$], and titanium ethoxide [$Ti(OEt)_4$] were chosen. The films were deposited at temperatures as low as 550^{0}C and had pure perovskite phase in the as–deposited state. Also, the films were smooth, specular, crack–free, uniform, and adhered well on the substrates. The stoichiometry of the films can be easily controlled either by varying the individual precursor temperature and/or the flow rate of the carrier gas. Auger electron spectroscopic (AES) depth profile showed good uniformity through the thickness of the films. The AES spectra also showed no carbon contamination in the bulk of the films. As–deposited films were dense and showed uniform and fine grains. The film (Pb/Zr/Ti = 50/41/9) annealed at 600^{0}C showed a spontaneous polarization of 23.3 $\mu C/cm^2$ and a coercive field of 64.5 kV/cm.

ACKNOWLEDGEMENTS

I wish to express my sincere appreciation to my advisor, Prof. Seshu B. Desu, for his advice, patience, and support throughout the course of this work. He has been an excellent advisor and also a friend, philosopher, and guide. I wish to thank him for all his help through which I have gained the confidence. In addition, I have learned how to present my work and how to communicate with people with his inspiration. His inspiration will continue serving well in my future career.

I am grateful to the members of my advisory committee for their invaluable conversations. To Prof. Richard Zallen, who has spent much time in discussing both the general and specific optical properties of materials. To Prof. William Reynolds for his invaluable discussion on the structure development of PZT films. To Prof. Charles Houska for his help in the analyses of the x–ray diffraction. To Prof. John Dillard for his expertise in the surface analyses.

It has been my pleasure and good fortune to have worked with many brilliant and humorous people in thin films laboratory of Materials Science Engineering Department. I have enjoyed the fun and fruitful period of time that I shared the office and the laboratory with them. Special thanks go to: Jhing–Fang Chang for her help in preparing MOD PZT samples and optical measurements; Warren Hendricks for his help in correcting the English errors of the manuscript; Jie Si for her help in preparing all the figures and tables of this work; Prof. Shi Tian, Kazuya Ishihara, and Yasuyuki Ito for their help in MOCVD PZT films; Gene Li for his help in depositing the electrodes for electric property measurements; Dr. In Yoo for his help in measuring the ferroelectric properties. I would also like to thank Prof. Z.

Chen, Prof. C. Qiu, Dr. E. Dayalan, S. W. Park, Chi Kong Kwok, Chien–Chia Chiu, Ching–Yi Tsai, May Nyman, Justin Gaynor, Wei Pan, Dilip Vijay, Ashraf Khan, Claire Chen, Zhiqi Xing, Gang Chen, Dr. Boaping He, and many others for many interesting discussions and being good friends.

I am indebted to Frank Cromer of surface analysis laboratory in Chemistry Department for his expert help in the composition analysis (AES and EDS) and in the microstructure analysis (SEM). I would also like to acknowledge the professional support of the staff members in Materials Science Engineering Department: Cindy Klein, Fran Lee, Laurie Dodge, Susette Sowers, and Jan Doran.

Finally, I wish to express my deepest love and appreciation to my wife, Yuchuan. Without her total support, sacrifices, and love I could not have finished this work.

This work is dedicated to my parents.

Table of Contents

List of Figures

List of Tables

Chapter 1 Introduction

1.1 Ferroelectric Materials

Ferroelectric materials are a subgroup of the pyroelectric materials, which are in turn a subgroup of the piezoelectric materials. In other words, pyroelectric materials present piezoelectric properties as well as pyroelectric properties, and ferroelectric materials possess both pyroelectric properties and piezoelectric properties, in addition to their unique ferroelectric properties.

Most of the ferroelectric materials have the ABO_3 perovskite structure as shown in Figure 1.1. As can be seen in Figure 1.1, the A element (which is Pb in the case of $Pb(Zr_xTi_{1-x})O_3$) is a large cation situated at the corners of the unit cell and the B element (which is Zr or Ti in $Pb(Zr_xTi_{1-x})O_3$) is a smaller cation located at the body center. The oxygen atoms are positioned at the face centers. These materials exhibit a characteristic temperature, the Curie temperature, at which the material makes a structural phase change from a polar phase (ferroelectric phase) to a non–polar phase, typically called the paraelectric phase.

Triglycine sulphate (TGS) [1] and KNO_3 [2] are some of earlier ferroelectric materials studied, but they are very unstable in the presence of moisture. The perovskite titanate [3] and niobate [4] families have been studied since 1950s. Among these ferroelectric materials, $BaTiO_3$ [5] and $Pb(Zr_xTi_{1-x})O_3$ [6] have been

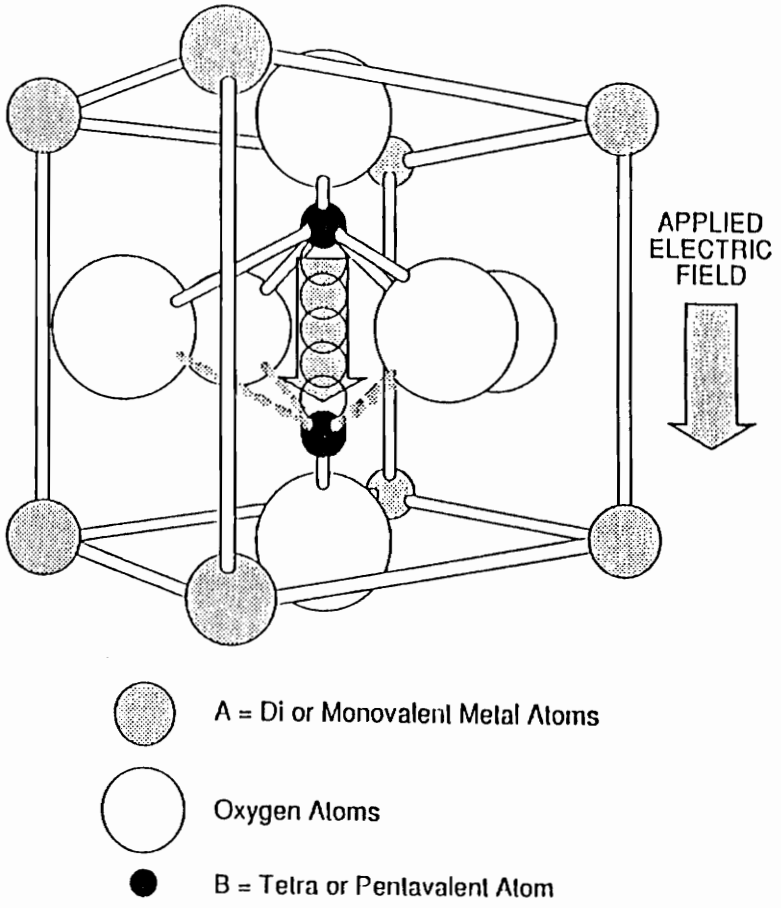

Figure 1.1 Unit cell of the perovskite structure.

extensively investigated because of their excellent ferroelectric and piezoelectric properties.

1.2 Properties and Applications of Ferroelectric Materials

1.2.1 Ferroelectric Properties and Applications

One of the well–known features of ferroelectric materials is the response of the polarization to the external electric field, which is often referred to as simply the hysteresis loop or hysteresis curve as shown in Figure 1.2. PZT is one of the best–known ferroelectric materials with the ABO_3 perovskite structure. In the ferroelectric phase, i.e., at the temperatures below the Curie temperature, the crystal structure of the PZT can be one of three structural formations: tetragonal, orthorhombic, or rhombohedral, depending on the Zr/Ti ratio. Figure 1.3 shows the phase diagram of the $PbZrO_3$ – $PbTiO_3$ solid solution [7]. As can be seen in Figure 1.3, when $x < 0.53$ (x is defined by the Zr fraction), PZT displays a tetragonal structure, in the range of 0.53 to 0.92 PZT has a rhombohedral structure, while when $x > 0.92$ it exhibits a orthorhombic structure. In the tetragonal structure, the spontaneous polarization aligns itself parallel to the c–axis. In a rhombohedral structure, a cube is stretched along a body diagonal and the spontaneous polarization aligns in the direction of the stretched body diagonal. The orthorhombic structure is formed by stretching a cube along a face diagonal along which the spontaneous polarization aligns itself.

The most attractive application of the ferroelectric materials is for nonvolatile memory devices because of their characteristic polarization response to an electric

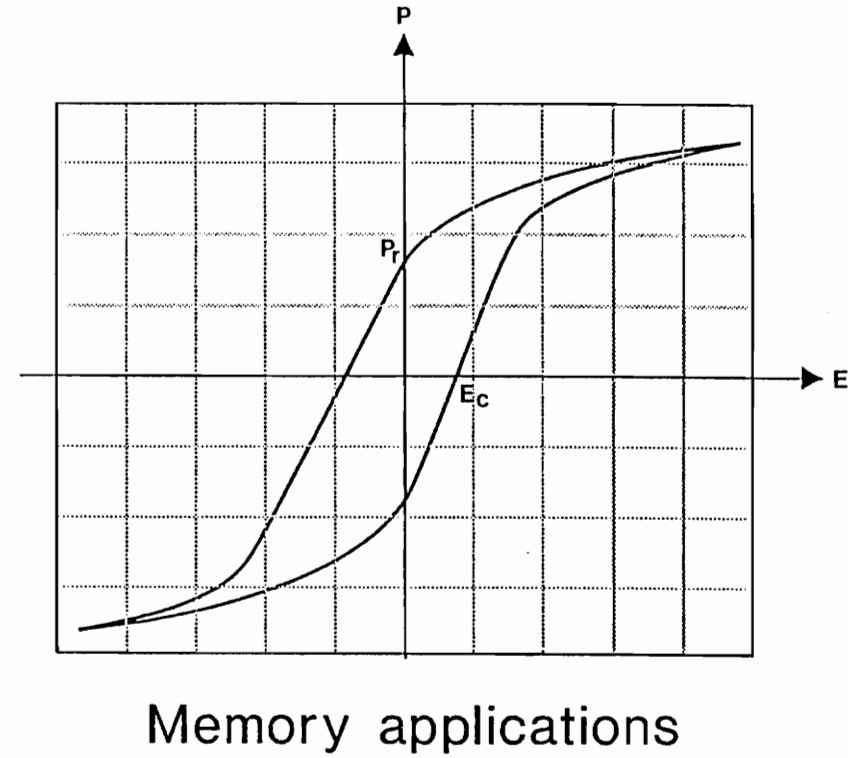

Figure 1.2 Hysteresis loop of a ferroelectric material.

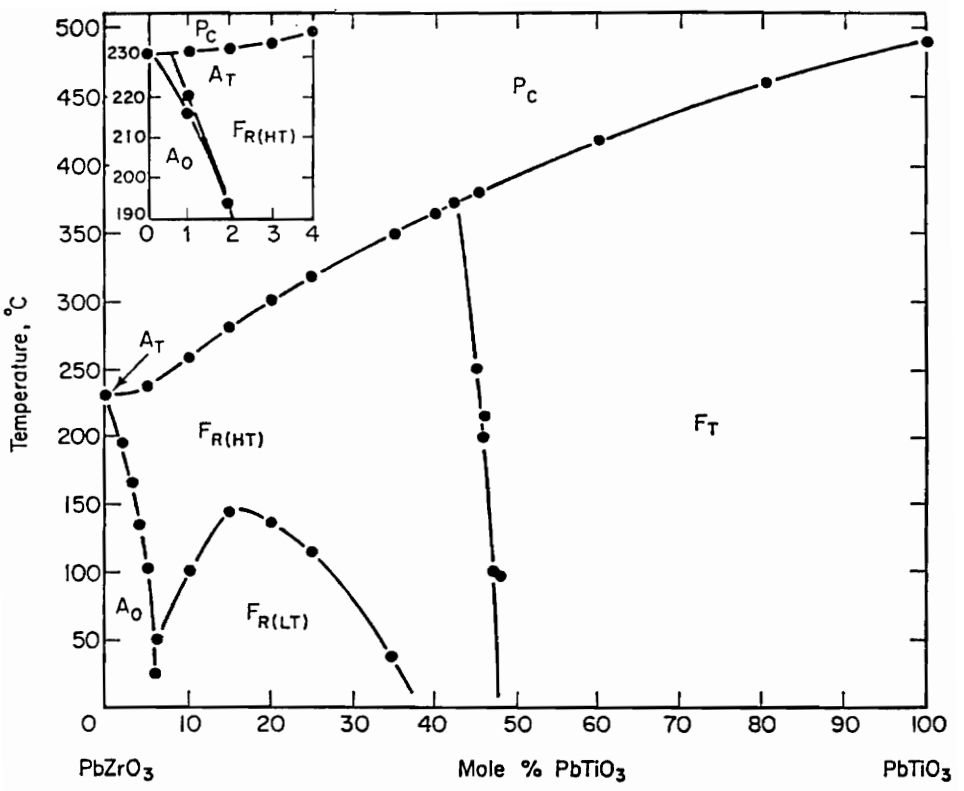

Figure 1.3 Phase diagram of $PbTiO_3$–$PbZrO_3$ solid solution [7].

field [8]. As can be seen in Figure 1.2, there is a threshold electric field, also called coercive field E_c, above which the polarization switches. When the external electric field is removed, the polarization decreases to a remaining value: the remanent polarization, P_r. In other words, no applied field is required to maintain the stored charge. Therefore, ferroelectric materials can be modeled as bistable capacitors with two distinct polarization values and thus can be used as a true nonvolatile memory.

The goal of the use of ferroelectric memories is to integrate them into the existing semiconductor devices. Figure 1.4 shows a ferroelectric random access memory (FRAM) cell developed by Ramtron corporation [9]. As can be seen in Figure 1.4, a layer of PZT film with the top and bottom electrodes is superimposed on a metal–oxide–semiconductor (MOS) transistor. The polarization of the PZT film switches to the opposite polarity when the transistor is turned on. In order to sense the polarization state of the PZT film, the film is pulsed and monitored for a given current/time wave form envelope which is indicative of its polarization state.

1.2.2 Pyroelectric Properties and Applications

Ferroelectric materials also present pyroelectric properties. Pyroelectricity results from the temperature dependence of the spontaneous polarization, P_s [10]. In other words, a change in temperature produces a change in polarization. A pyroelectric material is usually described by its pyroelectric coefficient which is defined by

$$\Delta P = p \, \Delta T \tag{1.1}$$

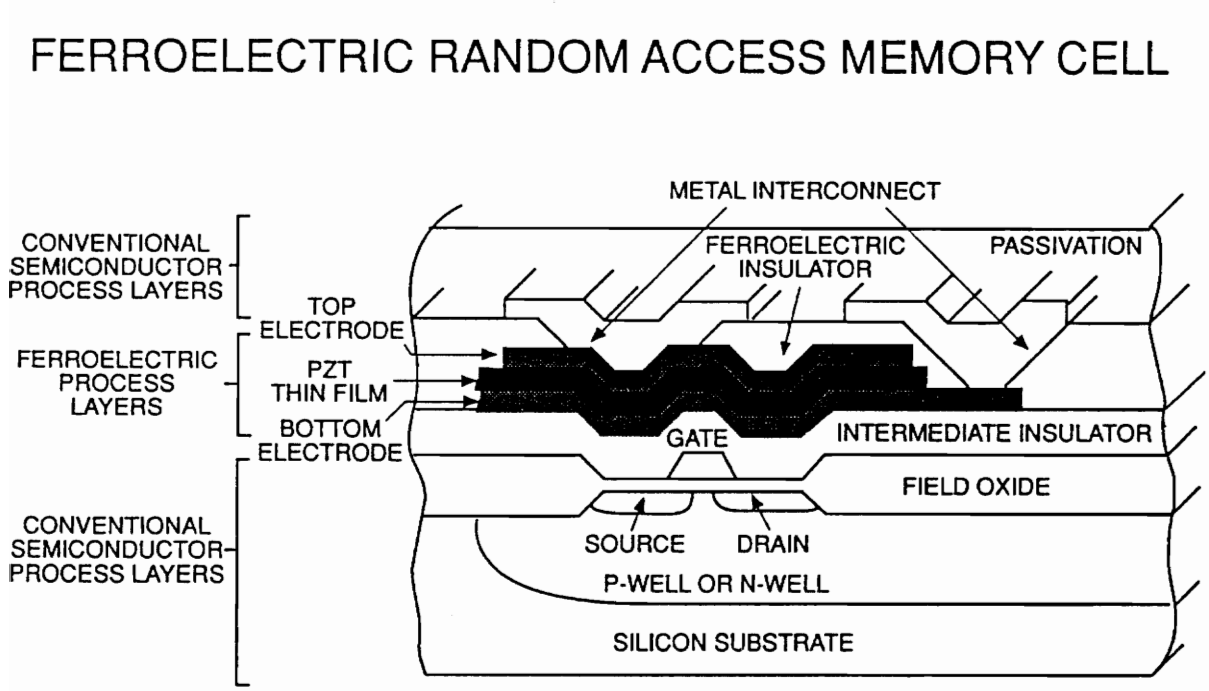

Figure 1.4 Ferroelectric random access memory (FRAM) cell [9].

where ΔP is the change in the polarization, ΔT is the change in the temperature, and p is the pyroelectric coefficient which has the unit of $nC/(cm^2\ ^0C)$. Because a change in polarization in a solid is accompanied by a change in surface charges, it can be detected by an induced current in an external circuit.

Pyroelectric materials respond to changes in the intensity of incident radiation and not to a temporally uniform intensity. Thus humans or animals moving across the field of view of a pyroelectric detector will produce a response as a result of the movement of their warm bodies which emit infrared radiation. On the other hand, to obtain a response from stationary objects requires the radiation from them to be periodically interrupted. This is usually achieved by a sector disc rotating in front of the detector and acting as a radiation chopper.

The pyroelectric properties have been used to design a wide range of devices. For example, a pyroelectric radiometer measures the surface temperature of an object. The radiation emitted from the object has to be chopped, and so the detector receives pulses of radiation from the source and the chopper alternately. Thus the temperature is measured relative to the temperature of the chopper surface. A particular commercial pyroelectric radiometer made from an $LiTaO_3$ single crystal can be used to measure the temperatures in a range of 0 to 600^0C [11]. Many other pyroelectric devices have been commercially available such as the pollutant detector, the intruder alarm, and the pyroelectric vidicon [11].

1.2.3 Piezoelectric Properties and Applications

The piezoelectric effect occurs when the materials are strained by an applied stress, a polarization is developed in the materials, and vice versa, i.e., when a

polarization is developed in the materials, they are strained [12]. The piezoelectric materials are often characterized by the effective electromechanical coupling coefficient κ_{eff}^2 which is defined as follows:

$$\kappa_{eff}^2 = \frac{\text{mechanical energy converted to electrical energy}}{\text{input mechanical energy}} \quad (1.2)$$

or

$$\kappa_{eff}^2 = \frac{\text{electrical energy converted to mechanical energy}}{\text{input electrical energy}} \quad (1.3)$$

One of the most important applications of the piezoelectric materials is the actuator. For example, in the fabrication of semiconductor chips, circuit components have to be precisely positioned for the various processing steps. In optical equipment, lenses and mirrors require micropositioning. In autofocusing cameras, there are actuators capable of producing precise rotational displacements. Actuators are also required for ink–jet printers, for positioning videotape–recording heads, and for micromachining metals.

1.2.4 Electro–optic Properties and Applications

The electro–optic effect is the dependence of the refractive index on an external electric field. In other words, the refractive index of an electro–optic material can be changed by an applied electric field [13].

Transparent single crystal ferroelectrics, such as lithium niobate [4], potassium dihydrogen phosphate (KDP) [14] and $BaTiO_3$ [5] have been recognized as useful electro–optic materials. However, the use of single crystal is limited by the available size, cost, and, in case of KDP, susceptibility to moisture attack. The development of

highly transparent lanthanum doped PZT (PLZT) ceramics in the 1960s led to a variety of successful electro–optic devices [15]. Recently, PLZT have been successfully prepared into a thin film form by several deposition techniques [16,17], which further enlarged the applications of electro–optic devices.

One of the very successful devices may be the integrated optic total internal reflection switch (TIR) in which the laser light confined in a PLZT thin film can be redirected by an applied field [18].

1.3 Fabrication Techniques of Ferroelectric Thin Films

A variety of techniques have been used for the deposition of ferroelectric thin films. In general, the thin film deposition techniques can be divided into two major categories; i.e., (1) physical vapor deposition (PVD) and (2) chemical processes. Among the PVD techniques, the most common methods used for the deposition of ferroelectric thin films are electron beam evaporation [19], rf diode sputtering [20], rf magnetron sputtering [21–23], dc magnetron sputtering [24], ion beam sputtering [25], molecular beam epitaxy (MBE), and laser ablation [26–29]. The chemical processes can be further divided into two subgroups; i.e., the chemical vapor deposition (CVD) and the wet chemical process including sol–gel process and metalorganic decomposition (MOD).

A chronological history of the developments of ferroelectric thin films is given in Table 1.1 [18] with the bold letters for PZT thin films. As can be seen, focusing on the PZT film development, the first successful PZT films were produced by PVD techniques (e–beam evaporation [19] and rf diode sputtering [20]) in 1976, then followed by MOD process [30] and sol–gel technique [31–32] in mid 1980s. The laser

Table 1.1 History of ferroelectric thin films [18]

Year	Developments
1969	e–beam evaporated $BaTiO_3$
1971	radio–frequency (rf) sputtered $BaTiO_3$
1972	rf sputtered $Bi_4Ti_3O_{12}$
1974	rf sputtered $LiNbO_3$
1975	liquid phase epitaxial (LPE) grown PLZT and $LiNbO_3$
1976	**e–beam evaporated PZT, rf diode sputtered PZT**
1977	rf sputtered epitaxial PLZT, rf sputtered $(Ba,Sr)Nb_2O_6$
1980	**ion beam sputtered PZT**
1982	**chemical vapor deposited (CVD) PT**
1983	rf planar magnetron sputtered epitaxial PLZT, direct–current (dc) sputtered $Pb_5Ge_3O_{11}$
1984	Metalorganic decomposition (MOD) process for PLZT, LPE grown $KNbO_3$
1985	dc reactive sputtered PLZT with metal targets, **sol–gel PT, PZ, PZT, and PLZT**
1987	sol–gel and sputtered PZT and PLZT for random access memory (RAM), sol–gel $LiNbO_3$
1990	**Laser ablation PZT** **metalorganic CVD (MOCVD) PZT**

ablation [26–29] and metalorganic chemical vapor deposition (MOCVD) [33–38] PZT films did not appear until the beginning of the 1990s.

The PVD techniques require a high vacuum, usually better than 10^{-5} torr, in order to obtain a sufficient flux of atoms or ions capable of depositing onto a substrate. The advantages of the PVD techniques are (1) dry processing, (2) high purity and cleanliness, and (3) compatibility with semiconductor integrated circuit processing. However, these are offset by disadvantages such as (1) low throughput, (2) low deposition rate, (3) difficult stoichiometry control, (4) high temperature post deposition annealing, and (5) high equipment cost.

Sputtering and e–beam evaporation are examples of well established and successful PVD techniques. Although they have the above mentioned advantages and disadvantages, there are still some significant issues for these techniques. For the complex oxide films, different sputtering yields from different metal targets and the oxidation of the metal targets are some of the problems associated with reactive sputtering. Sputtering of an oxide target may avoid these problems. However, in order to incorporate sputtering into the large scale applications, some of the technical issues still need to be solved, such as the inflexibility to modify or change the stoichiometry of the deposition film. In addition, since the sputtering and the e–beam evaporation are line–of–sight deposition processes, the step coverage is a significant issue for these deposition technique.

Laser ablation is a newly developed thin film deposition technique and the understanding of this process is in its infant period. Laser ablation has found some success in depositing high temperature superconducting films [29]. There are only a few reported works on laser deposition of PZT films [26–29]. The major problems of this technique are the composition and thickness nonuniformity of the deposited films

over a large scale. The wet chemical processes including MOD and sol–gel process consist of the following steps: (1) preparation of metalorganic precursor solution, (2) hydrolysis (for sol–gel process), (3) deposition onto a substrate by spin or dip–coating technique, (4) removal of solvent and pyrolysis, and (5) crystallization of the films. The advantages of the wet chemical process are

(1) molecular homogeneity

(2) high deposition rate and high throughput

(3) excellent composition control

(4) easy introduction of dopants

(5) low capital cost; deposition can be done in ambient condition, no vacuum processing is needed.

The major problems due to this wet process are (1) film cracking during the post–annealing process and (2) possible contamination which results in a difficulty to incorporate this technique into the semiconductor processing. However, because it provides a fast and easy way to produce the complex oxide thin films, this wet chemical process acts a very important role in the investigation of the interrelationship among the processing, the microstructure, and the property of the films.

Of all the above mentioned techniques, the MOCVD technique appears to be the most promising because it offers advantages of simplified apparatus, excellent film uniformity, composition control, high film densities, high deposition rates, excellent step coverage, and amenability to the large scale processing. The excellent film step coverage that can be obtained by MOCVD cannot be equaled by any other technique. Purity, controllability, and precision that have been demonstrated by MOCVD are competitive with the MBE technique. More importantly, novel

structures can be grown easily and precisely. MOCVD is capable of producing materials for an entire class of devices which utilize either ultra–thin layers or atomically sharp interfaces. In addition, different compositions, for example $Pb(Zr_xTi_{1-x})O_3$, can be fabricated using the same sources.

1.4 Objectives of Research

The objectives of this research were as follows:

1. To obtain good quality ferroelectric PZT thin films by chemical methods, namely, the MOD process and the MOCVD technique.

2. To study the optical properties of PZT thin films.

3. To develop an optical method for studying the structure development in MOD PZT films.

4. To understand the structure development in MOD PZT films.

5. To interrelate process parameters, composition, structure, and properties of MOCVD ferroelectric PZT films.

Chapter 2 Experimental Procedure

This chapter describes the preparation of PZT thin films by the metalorganic decomposition (MOD) process and the film characterization methods. The metalorganic chemical vapor deposition (MOCVD) process for PZT thin films will be discussed in Chapter 5 separately.

Sections 2.1 and 2.2 describe the preparations of the PZT solutions and films, respectively. The transmission and reflection spectra measurements are given in Section 2.3. The phase identification and the microstructure of the films were carried out by an x–ray diffractometer and a scanning electron microscope, respectively, which are described in Section 2.4. Section 2.5 describes the composition analysis using energy dispersive spectroscopy (EDS). The method for obtaining the Auger electron spectroscopic depth profile is given in Section 2.6. Finally, a detailed description of the ferroelectric property measurements is given in Section 2.7.

2.1 Preparation of Precursor Solutions

Reagent grade chemicals were used in preparing the precursor solutions. The starting precursors, lead acetate [$Pb(O_2C_2H_3)_2 \cdot 3H_2O$], titanium isopropoxide [$Ti(OC_3H_7)_4$], and zirconium n–propoxide [$Zr(OC_3H_7)_4$] were purchased from

Johnson Matthey. The solvent, methoxyethanol ($C_3H_8O_2$), was obtained from Fisher Scientific.

The preparation process of the PZT precursor solutions was a modification of the process developed by Budd et al. [30]. The properties and the decomposition behavior of these precursors were discussed in Chang's M.S. Thesis [39]. Figure 2.1 shows the flow chart for the preparation of PZT precursor solutions. To prepare the PZT precursor solutions, lead titanate (PT) and lead zirconate (PZ) precursor solutions were first prepared separately. The PT solution was prepared by dissolving lead acetate and titanium isopropoxide in methoxyethanol; the PZ solution was prepared by dissolving lead acetate and zirconium n–propoxide in methoxyethanol. Lead acetate was first dissolved in methoxyethanol and distilled at around 120°C to boil off the water contained in the lead acetate before the appropriate metalorganic compound of either titanium or zirconium was added. A 10% excess of lead acetate was added in both PT and PZ solutions to compensate for the PbO loss expected to take place during later high temperature post–annealings. After the solutions were cooled to room temperature, a proper amount of methoxyethanol was added to adjust their molar concentration. PZT solutions of different Zr/Ti ratio were prepared by mixing the desired volume fractions of PT and PZ solutions. The final concentration of the solutions was fixed at 0.5 molarity. A detailed step–by–step procedure for preparing the PZT precursor solutions can be found in Appendix A.

2.2 PZT Film Preparation

PZT thin films were made by placing a few drops of the precursor solution on a

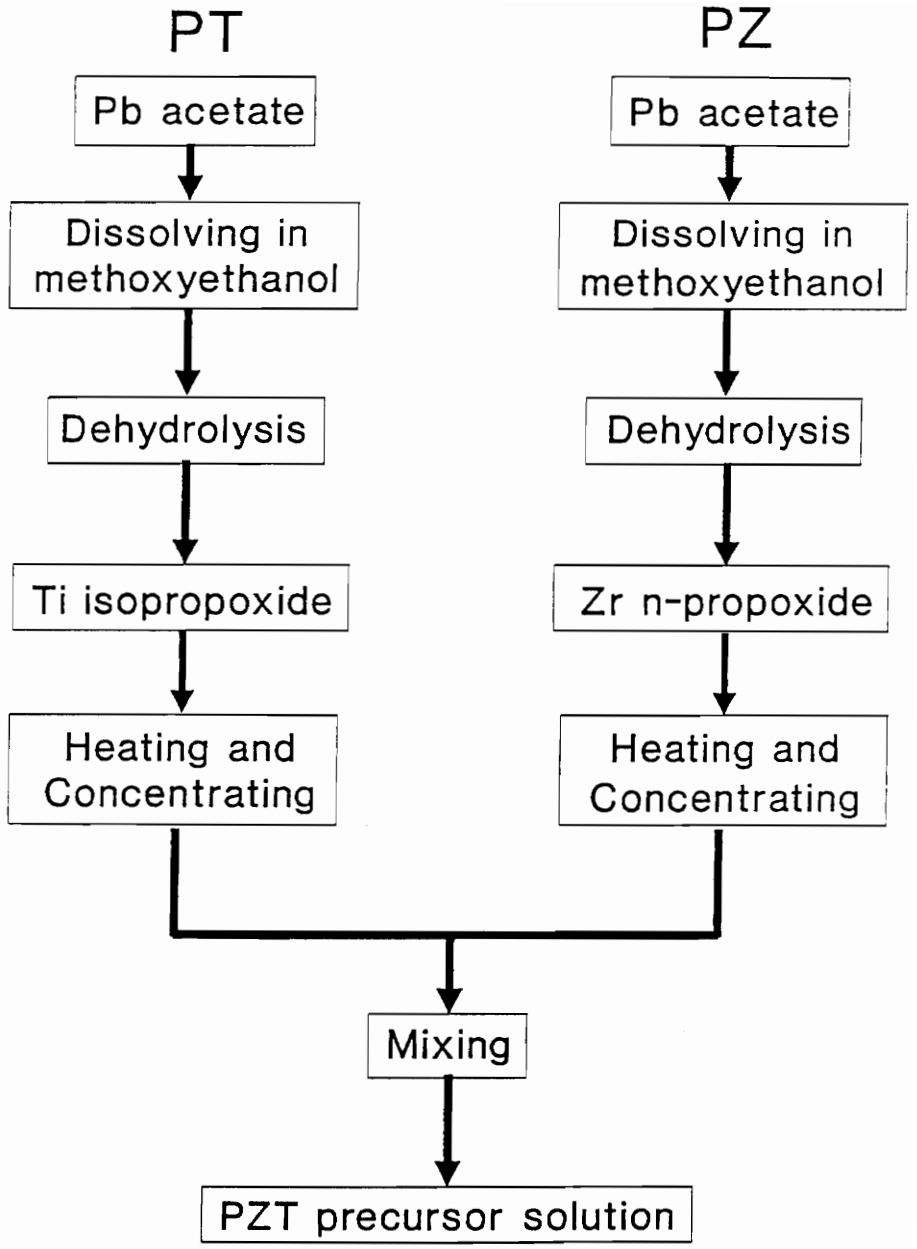

Figure 2.1 A flow chart for the preparation of PZT precursor solutions.

1 inch diameter sapphire disk mounted on a Headway Research Photo–Resist Spinner and spinning at 2000 rpm for 30 seconds. The sapphire substrates were obtained from Swiss Jewel Company and had a surface orientation within a 30^0 cone of the [100] direction. After spin coating, the specimens were dried on a hot plate at 150^0C for 5 minutes. The drying process removed the solvents in the films. In order to obtain a thick enough film for optical measurements, the above coating–drying cycle was repeated three times. Each coating resulted in a film approximately 100 nm thick. The desired film thickness can be achieved by adjusting the concentration of the precursor, the spin speed, or the number of the coating–drying cycles. Seven different $Pb(Zr_xTi_{1-x})O_3$ compositions, i.e., x = 0.0, 0.2, 0.4, 0.5, 0.6, 0.8, and 1.0 were prepared.

Two different post–annealing treatment routes were used. For the specimens used in the optical property study (Chapter 3), after three coating–drying cycles, they were directly annealed at 650^0C for 1 hour. For the specimens used in the structure development study (Chapter 4), they were heat treated at 150^0C, 250^0C, and 300^0C and at successively higher temperatures with 20^0C increments, i.e., 150^0C, 250^0C, 300^0C, 320^0C, 340^0C, etc., up to 700^0C for 30 min for each heat treatment. The heating rate was 10^0C/min for both heat treatment routes. All the heat treatments were performed in air. Note that the same specimen was used through the entire heat treatment sequence for the structure development study. The specimens were characterized using both UV–VIS–NIR spectrophotometry and x–ray diffraction after every heat treatment. A flow chart for the preparation of PZT films by the MOD process is shown in Figure 2.2.

2.3 Optical Transmission and Reflection Spectra Measurements

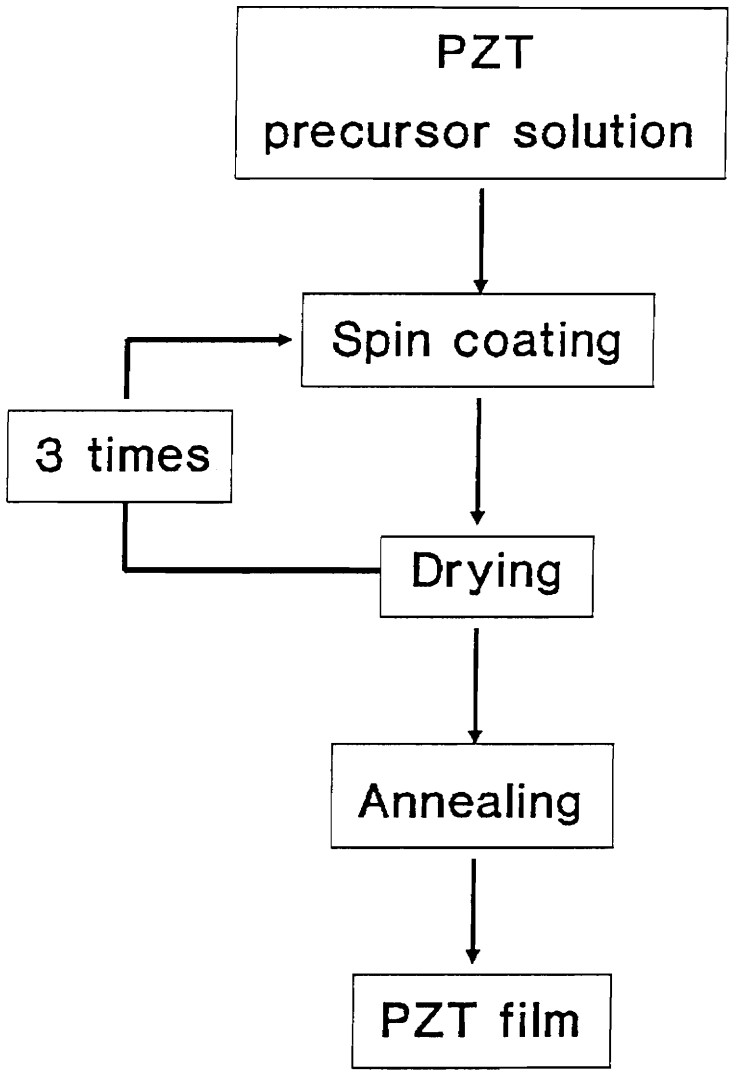

Figure 2.2 A flow chart for the preparation of PZT films by MOD process.

The transmission and reflection spectra measurements were performed using a Shimadzu UV–3101PC double–beam UV–VIS–NIR scanning spectrophotometer. The transmission spectra of the samples were measured using air as a reference at a wavelength ranging from 200 nm to 2000 nm, a slit width of 3 nm, a scan speed of 200 nm/min, and a sampling interval of 1 nm. Because of its hexagonal crystalline structure, the sapphire substrate exhibits anisotropy in many optical and physical properties. The optical properties of sapphire depend on the orientation of the optic axis, or c–axis, relative to its surface. Sapphire exhibits birefringence, which is a difference in index of refraction in orthogonal directions.

The reflection spectra were measured using an aluminum mirror as a reference at a wavelength ranging from 300 nm to 2000 nm. The reflection spectrum of the aluminum mirror was pre–measured at Shimadzu by using an absolute reflectance measurement attachment. Therefore, the "real" reflection spectra of the samples were obtained by multiplying the measured spectra by the spectrum of the aluminum mirror, i.e.,

$$R_S = R_m \, (I_S/I_m) \qquad (2.1)$$

where R_S and R_m are reflectances of the sample and the mirror, respectively, and I_S and I_m are the intensities measured from the sample and the mirror, respectively.

Two reflection spectra were measured for each sample; one was from the sample without the black paint on the back surface of the substrate, the other was from the sample with the black paint on the back of the substrate. The incident light is not expected to be reflected from the back surface of the sample with the black paint. The purpose of doing these two measurements is to determine the wavelength at

which the light is completely absorbed by the sample.

2.4 X–ray Diffraction and Scanning Electron Microscopy

The phase identification of the PZT films was carried out by x–ray diffraction (XRD) using a Philips PW–1792 diffractometer with Cu–$K\alpha$ radiation. The specimens (deposited films on substrates) were directly characterized by the XRD. No further specimen preparation was required. The typical measurement conditions were as follows: 2θ ranged from 20^0 to 60^0, speed was 0.1^0/sec, time constant was 1 sec, slit was 0.2 mm, and intensity ranged from 1000 counts to 5000 counts. In addition, the diffractometer was operated at 30 mA and 40 kV.

The surface morphologies of the films were investigated by an ISI–SX–40 scanning electron microscope (SEM). Prior to loading the specimens into the SEM chamber, they were coated with a thin layer of gold (approximately 100 A thick) for the purpose of electric conduction. The SEM was operated at 20kV.

2.5 Composition Determination

The composition of the films was investigated using energy dispersive spectroscopy (EDS). In the EDS measurements, the specimen was tilted 30^0 to the direction of the electron beam. The acceleration voltage was 20 kV. The $K\alpha$ line at 4.51 eV was used for titanium, the $L\alpha$ line at 2.042 eV was used for zirconium, and the $M\alpha$ line at 2.34 eV was used for lead. The composition of the films observed by EDS were compared to those obtained by the electron probe microanalysis (EPMA) and were found to be in good agreement. Quantitative analysis of Pb, Zr, and Ti

ions was performed using a 8 kV, 50 mA source. Ten measurements were made at different areas of each specimen and averaged to obtain the final data point.

2.6 Auger Electron Spectroscopy

A Perkin–Elmer PHI 610 scanning Auger microprobe was used to examine the carbon contamination and to study the composition depth profile of the films. For the carbon contamination examination, the carbon KLL peak at 271 eV was used. The detection limit was better than 1 atomic percent. For the composition depth profile study, the detection windows and peaks for the elements studied were chosen as follow:

Pb: 79 – 104 eV, MNN (94 eV)

Zr: 132 – 157 eV, MNN (147 eV)

Ti: 372 – 397 eV, LMM (387 eV)

O: 495 – 515 eV, KLL (503 eV)

Ru: 258 – 283 eV, MNN (273 eV)

The operation voltage and beam current for the electron beam were 3 kV and 0.05 μA, respectively. The operation voltage and beam current for the Ar beam were 4 kV and 5 μA, respectively. The sputtering rate was approximately 10 nm/min.

2.7 Ferroelectric Property Measurements

For the ferroelectric property measurements, the PZT films were deposited either on $Pt/Ti/SiO_2/Si$ wafers or on $RuO_x/SiO_2/Si$ wafers. A simple parallel–plate capacitor configuration was used for the ferroelectric property measurements.

Either a 400 nm thick sputtered Pt layer or a 500 nm thick sputtered RuO_x layer was used as a bottom electrode, depending on the substrate used. Room temperature electron beam evaporation was used for the deposition of the palladium (Pd) top electrode. Circular Pd top electrodes (300 – 400 nm thick, 0.016 cm in diameter, and 2.2×10^{-4} cm^2 in area) were pattern–deposited on top of the PZT films using a mask. No post–annealing was made after the Pd top electrode deposition. The ferroelectric properties of the PZT films were determined by hysteresis loop measurements using a modified Sawyer–Tower circuit [8] at 60 Hz. In this study, a commercially available ferroelectric test system (Radiant Technology RT66A) controlled by a personal computer was used to determine ferroelectric properties. The applied voltage used was 5 volts.

Chapter 3 Optical Properties of PZT Thin Films

3.1 Introduction

Nature of phases (i.e., composition and structure), thickness, packing density, and surface roughness are important structural parameters for thin films, because these parameters control the properties, for example, electrical, optical, and mechanical properties. X–ray diffraction is a convenient method for the phase identifaction of crystalline materials, although in some cases diffraction peaks from the film interfere with those of the substrate. The thickness and surface roughness of the film can be easily obtained using a profilometer [40]. However, this requires forming a sharp step between the film and the substrate. Scanning electron microscopy is a powerful tool for examining the surface morphology of the film, but it requires a metal coating on the top of electrically insulating specimens. Furthermore, none of the above mentioned techniques can be used to determine the packing density of the film.

Film packing density can be quite easily estimated from the optical properties (i.e., the refractive index) of the film [41]. In addition to providing packing density, optical property chracterization of PZT films is quite valuable for the fabrication of both optical and electro–optic devices.

In this chapter, the thin film optics is first discussed in detail. Based on the

thin film optics, the envelope method with the consideration of the light intensity loss from the back surface of the substrate is then derived. The original envelope method was proposed without the consideration of the light intensity loss from the back surface of the substrate by Manifacier in 1976 [42]. Although Swanepoel [43] took the back surface of the substrate into consideration in 1983 and improved the accuracy of the extinction coefficient, he still derived the same equation for the calculation of the refractive index as Manifacier had. The mistake they made will be pointed out in this study.

In this study, the thickness measurement from the interference fringes of the transmission spectrum is cross checked by a computer simulation procedure. The accuracy in the thickness measurement is found to be better than 2%. The optical properties were measured not only in the medium and weak absorption regions by the envelope method but also in the strong absorption region by both the transmission and the reflection spectra.

Optical properties of perovskite PZT films, fabricated by the MOD process, were investigated using both transmission and reflection spectra in the wavelength range from 200 nm to 2000 nm. The refractive index, extinction coefficient, and the thickness of the film were calculated from the transmission spectra. The packing density of each film was derived from its refractive index. The refractive indices were fit to a Sellmeier type dispersion equation [44]. The surface roughness of each film was qualitatively estimated from the extinction coefficient. Also, the absorption coefficient and the near band gap energy of each film was calculated from its extinction coefficient.

3.2 Theoretical Background

3.2.1 Thin Film Optics

A starting point from which to derive the equations for thin film optics is Maxwell's equations. For an isotropic medium, Maxwell's equations are

$$\text{div } \mathbf{D} = \epsilon \text{ div } \mathbf{E} = 4\pi\rho \tag{3.1}$$

$$\text{div } \mathbf{D} = \mu \text{ div } \mathbf{H} = 0 \tag{3.2}$$

$$\text{curl } \mathbf{E} = -\frac{\mu}{c}\frac{\partial \mathbf{H}}{\partial t} \tag{3.3}$$

$$\text{curl } \mathbf{H} = \frac{4\pi\sigma\mathbf{E}}{c} + \frac{\epsilon}{c}\frac{\partial \mathbf{E}}{\partial t} \tag{3.4}$$

where the symbols have their usual meanings. For a non–conducting medium ($\sigma = 0$) in which there is no space–charge, these relations reduce to the well–known simple form of wave equations, which show that the wave propagates with velocity $c/\sqrt{\epsilon\mu}$.

$$\frac{\epsilon\mu}{c^2}\frac{\partial^2 \mathbf{E}}{\partial t^2} = \nabla^2\mathbf{E} \tag{3.5}$$

$$\frac{\epsilon\mu}{c^2}\frac{\partial^2 \mathbf{H}}{\partial t^2} = \nabla^2\mathbf{H} \tag{3.6}$$

Because the value of μ for all materials is insensibly different from unity at optical frequencies, the velocity of propagation is $c/\sqrt{\epsilon}$ where ϵ is the dielectric constant at the frequency of the light wave. From the definition of refractive index, the

well–known result, $n = \sqrt{\epsilon}$ is obtained. The problem of determining the fraction of light reflected and transmitted at a boundary separating two media is dealt with by applying boundary conditions to the solutions of wave equations, i.e. equations 3.5 and 3.6 in the present case.

For the convenience and to avoid any confusion, the notations of thin film optics used hereafter are described in Table 3.1.

3.2.1.1 Multi–layer Thin Film System

Figure 3.1 schematically illustrates the transmittance and reflectance of a multi–layer thin film system. The system consists of an m–layer thin film with the complex refractive index of each layer given by N_i and the corresponding film thickness by d_i and a semi–infinite substrate with the complex refractive index ,N_{m+1}. The angle between the incident light and the surface normal is given by φ_0. The intensity of the incident light is denoted by I_0, that of the reflected light by I_r, and that of the transmitted light by I_t. The transmittance (T) and reflectance (R) are then defined by:

$$T = I_t/I_0 \tag{3.7}$$

and

$$R = I_r/I_0 \tag{3.8}$$

T and R are experimentally measurable quantities and may also be defined in terms of a function of N_i and d_i for a given λ and φ_0. Thus if N_i and d_i are known, T and R can be mathmetically calculated for a given λ and φ_0. The equations for

Table 3.1 Notation descriptions of thin film optics

Notation	Description
T_m	Transmittance of m–layer thin films on a finite substrate
R_m	Reflectance of m–layer thin films on a finite substrate
T_m'	Transmittance of m–layer thin films on a semi–infinite substrate
R_m'	Reflectance of m–layer thin films on a semi–infinite substrate
r_i	Reflectance at the i^{th} interface
d_i	Thickness of the i^{th} layer thin film
N_i	Complex index of refraction of the i^{th} layer thin film
n_i	Refractive index of the i^{th} layer thin film
k_i	Extinction coefficient of the i^{th} layer thin film
α_i	Absorption coefficient of the i^{th} layer thin film

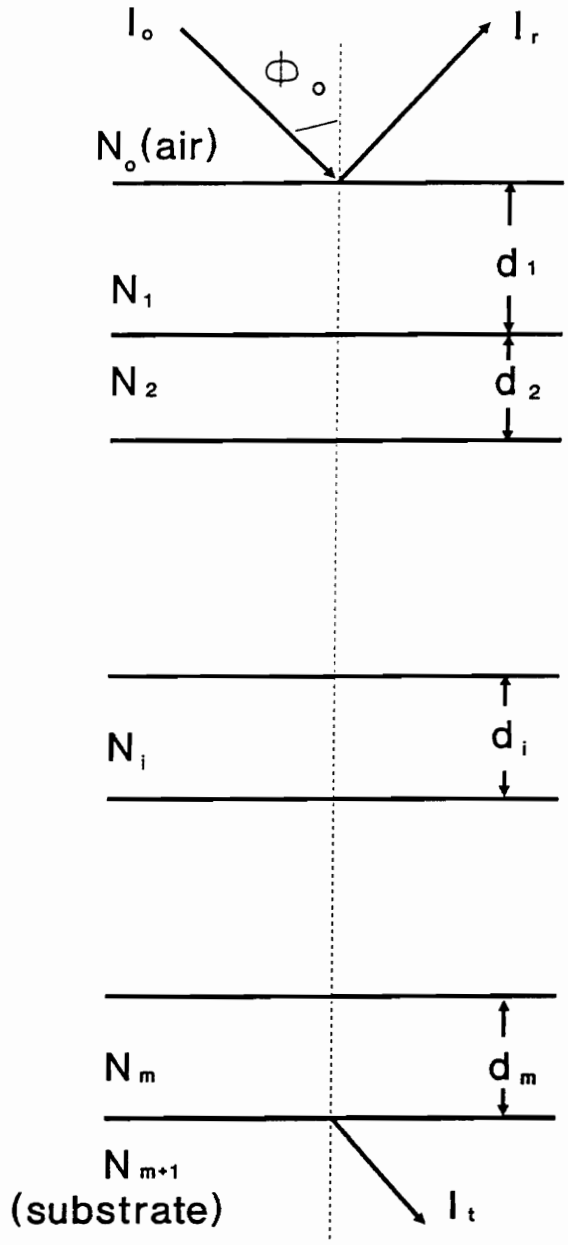

Figure 3.1 A schematic diagram of the transmitted and reflected light in a m–layer thin film system.

calculating T and R from N_i and t_i can be found in two excellent books, Heavens [45] and Azzam and Bashara [46].

If the direction of the incident light is normal to the surface of the system, i.e. $\varphi_0 = 0$, the calculation of T and R can be dramatically simplified. A comprehensive recurrence relation method provided by Heavens [45] is adopted in this study for the purpose of easy computer programming. In Heavens method, T_m' and R_m', below, taking note that the notations are different from his (see Table 3.1), are expressed as:

$$T_m' = (n_{m+1}/n_0) \left(\prod_{i=1}^{m+1} [(1+g_i)^2+h_i^2]\right)/(p_{1,m+1}^2 + q_{1,m+1}^2) \qquad (3.9)$$

$$R_m' = (t_{1,m+1}^2 + u_{1,m+1}^2)/(p_{1,m+1}^2 + q_{1,m+1}^2) \qquad (3.10)$$

where

$$p_{1,i+1} = p_{1,i}\, p_{i+1} - q_{1,i}\, q_{i+1} + r_{1,i}\, t_{i+1} - s_{1,i}\, u_{i+1} \qquad (3.11a)$$

$$q_{1,i+1} = q_{1,i}\, p_{i+1} + p_{1,i}\, q_{i+1} + s_{1,i}\, t_{i+1} + r_{1,i}\, u_{i+1} \qquad (3.11b)$$

$$t_{1,i+1} = t_{1,i}\, p_{i+1} - u_{1,i}\, q_{i+1} + v_{1,i}\, t_{i+1} - w_{1,i}\, u_{i+1} \qquad (3.11c)$$

$$u_{1,i+1} = u_{1,i}\, p_{i+1} + t_{1,i}\, q_{i+1} + w_{1,i}\, t_{i+1} + v_{1,i}\, u_{i+1} \qquad (3.11d)$$

$$r_{1,i+1} = p_{1,i}\, r_{i+1} - q_{1,i}\, s_{i+1} + r_{1,i}\, v_{i+1} - s_{1,i}\, w_{i+1} \qquad (3.11e)$$

$$s_{1,i+1} = q_{1,i}\, r_{i+1} + p_{1,i}\, s_{i+1} + s_{1,i}\, v_{i+1} + r_{1,i}\, w_{i+1} \qquad (3.11f)$$

$$v_{1,i+1} = t_{1,i}\, r_{i+1} - u_{1,i}\, s_{i+1} + v_{1,i}\, v_{i+1} - w_{1,i}\, w_{i+1} \qquad (3.11g)$$

$$w_{1,i+1} = u_{1,i}\, r_{i+1} + t_{1,i}\, s_{i+1} + w_{1,i}\, v_{i+1} + v_{1,i}\, w_{i+1} \qquad (3.11h)$$

$$p_i = \exp(\alpha_{i-1} d_{i-1}/2) \cos(\gamma_{i-1} d_{i-1}/2) \qquad (3.12a)$$

$$q_i = \exp(\alpha_{i-1}d_{i-1}/2)\sin(\gamma_{i-1}d_{i-1}/2) \tag{3.12b}$$

$$t_i = \exp(-\alpha_{i-1}d_{i-1}/2)\,[g_i\cos(\gamma_{i-1}d_{i-1}/2) + h_i\sin(\gamma_{i-1}d_{i-1}/2)] \tag{3.12c}$$

$$u_i = \exp(-\alpha_{i-1}d_{i-1}/2)\,[h_i\cos(\gamma_{i-1}d_{i-1}/2) - g_i\sin(\gamma_{i-1}d_{i-1}/2)] \tag{3.12d}$$

$$r_i = \exp(\alpha_{i-1}d_{i-1}/2)\,[g_i\cos(\gamma_{i-1}d_{i-1}/2) - h_i\sin(\gamma_{i-1}d_{i-1}/2)] \tag{3.12e}$$

$$s_i = \exp(\alpha_{i-1}d_{i-1}/2)\,[h_i\cos(\gamma_{i-1}d_{i-1}/2) + g_i\sin(\gamma_{i-1}d_{i-1}/2)] \tag{3.12f}$$

$$v_i = \exp(-\alpha_{i-1}d_{i-1}/2)\cos(\gamma_{i-1}d_{i-1}/2) \tag{3.12g}$$

$$w_i = -\exp(-\alpha_{i-1}d_{i-1}/2)\sin(\gamma_{i-1}d_{i-1}/2) \tag{3.12h}$$

$$\alpha_i = \frac{4\pi k_i}{\lambda} \tag{3.13a}$$

$$\gamma_i = \frac{4\pi n_i}{\lambda} \tag{3.13b}$$

$$g_i = \frac{n_{i-1}^2 + k_{i-1}^2 - n_i^2 - k_i^2}{(n_{i-1} + n_i)^2 + (k_{i-1} + k_i)^2} \tag{3.14a}$$

$$h_i = \frac{2\,(n_{i-1}\,k_i - n_i\,k_{i-1})}{(n_{i-1} + n_i)^2 + (k_{i-1} + k_i)^2} \tag{3.14b}$$

with the initial values of $p_{1,1} = 1$, $q_{1,1} = 0$, $t_{1,1} = g_1$, $u_{1,1} = h_1$, $r_{1,1} = g_1$, $s_{1,1} = h_1$, $v_{1,1} = 1$, and $w_{1,1} = 0$. In addition, the range of the subscript i is different for the above equations, and is listed in Table 3.2. Equations 3.9 and 3.10 are valid only if the film is homogeneous and the thickness of the film is uniform.

3.2.1.2 Single Layer Film on a Transparent Substrate

For a system of a single layer absorbing film on a transparent substrate, equation 3.9 becomes:

Table 3.2 The range of subscript i in equations 3.11–3.14

Equations	running range of i
3.11a – 3.11d	$1 \leq i \leq m$
3.11e – 3.11h	$1 \leq i \leq m-1$
3.12a – 3.12d	$2 \leq i \leq m+1$
3.12e – 3.12h	$2 \leq i \leq m$
3.13a – 3.13b	$1 \leq i \leq m$
3.14a – 3.14b	$1 \leq i \leq m+1$

$$T_1' = \frac{n_2}{n_0} \frac{[(1+g_1)^2 + h_1^2]\ [(1+g_2)^2 + h_2^2]}{p_{1,2}^2 + q_{1,2}^2} \qquad (3.15)$$

Recall that T_1' represents the transmittance of a single film on a semi–infinite substrate and n_2 is the refractive index of the substrate. By using equations 3.11–3.14, T_1' can be explicitly expressed in terms of the optical constants of the film and the substrate, the film thickness, and the wavelength λ:

$$T_1' = \frac{Ax}{B - Cx - Dx^2} \qquad (3.16)$$

where

$$x = \exp(-\alpha_1 d_1)$$

$$A = 16\, n_0\, n_2\, (n_1^2+k_1^2)$$

$$B = [(n_0+n_1)^2 + k_1^2]\ [(n_1+n_2)^2 + k_1^2]$$

$$C = 2\,[(n_1^2-n_0^2+k_1^2)(n_1^2-n_2^2+k_1^2)-4k_1^2n_2]\cos(\gamma) - 2[2k_1n_2(n_1^2-n_0^2+k_1^2)+2k_1(n_1^2-n_2^2+k_1^2)]\sin(\gamma)$$

$$D = [(n_1-n_0)^2+k_1^2]\ [(n_1-n_2)^2+k_1^2]$$

and α_1 is the absorption coefficient which is equal to $4\pi k_1/\lambda$, γ is equal to $4\pi n_1 d_1/\lambda$, d_1 is the film thickness, k_1 is the extinction coefficient, and n_0, n_1, and n_2 are the refractive indices of the ambient (air), film, and substrate, respectively. In addition to the assumptions made in section 3.2.1.1, equation 3.16 assumes that the substrate is completely transparent, i.e. $k_2 = 0$.

3.2.2 Envelope Method

In a multi–layer thin film system, if the complex refractive index and the thickness of each thin film layer are known, the reflectance and transmittance can be calculated exactly no matter how many layers are in the system or what the incident angle of the light is. All these quantities except the film thickness are wavelength dependent. However, in practice, a reverse calculation is needed, i.e., the optical constants and thickness of the film need to be calculated from the measured reflection and transmission spectra. There are only two measurable quantities T and R, but 3m+2 unknowns (three unknowns n, k, and d for each layer and two unknowns n and k for the substrate) at a given wavelength and incident angle. For a simple thin film system consisting of a single film on substrate, there are still three unknowns for the film but two measured T and R for a given wavelength and incident angle, assuming the optical constants of the substrate are known. The difficulty of calculating the optical constants and the thickness of the film from T and R is not only that the number of unknowns is larger than the number of quantities one can measure, but also that the optical constants cannot be explicitly expressed in terms of T and R.

Fortunately, for a single layer weakly absorbing film on a transparent substrate, the refractive index and extinction coefficient as a function of wavelength, and film thickness can be obtained from the transmission spectra alone. This method, which is referred to as the "envelope method" hereafter, was first presented by Manifacier [42]. This is a very useful approach to study the optical properties of insulating films since most of them are weakly absorbing materials.

Before starting to derive the equations for describing the envelope method,

some subscripts used in section 3.2.1.2 are droped for the sake of simplicity. Figure 3.2 shows the schematic diagram of a weakly absorbing thin film on a completely transparent substrate. The refractive index of the ambient is n_0; n_s is the refractive index of the substrate; n, k, and d denote the refractive index, extinction coefficient, and the thickness of the film, respectively.

The transmittance of a single film on a transparent substrate has been described in equation 3.16 of section 3.2.1.2. The equations describing the envelope method can be derived from equation 3.16 with the further assumptions that:

(1) The substrate is completely transparent, i.e. $k_s = 0$;

(2) the square of the refractive index of the film is much greater than that of the extinction of the film, i.e. $n^2 >> k^2$;

(3) the square of the refractive index difference between the film and air and the film and substrate is much greater than that of the extinction coefficient of the film, i.e. $(n-1)^2 >> k^2$ and $(n-n_s)^2 >> k^2$.

The first assumption will be verified in section 3.3. The second assumption leads to $A = 16\ n_0\ n^2\ n_s$ and $B = (n_0+n)^2\ (n+n_s)^2$ (equation 3.16). The third assumption leads to $C = 2\ [(n^2-n_0^2)(n^2-n_s^2)]\ \cos(\gamma)$ and $D = (n-n_0)^2(n-n_s)^2$ in equation 3.16. The most critical assumption of these is $(n-n_s)^2 >> k^2$. For the present study, the films are PZT solid solutions having a refractive index greater than 2.1 and the substrate is sapphire having the refractive index around 1.76. Therefore, if $k^2/(n-n_s)^2 \leq 0.01$ and if $n = 2.1$ and $n_s = 1.76$, k must be smaller than 0.034.

With the above assumptions, equation 3.16 becomes

$$T_1' = \frac{16\ n_s\ n^2\ x}{(1+n)^2(n+n_s)^2 - 2x[(n^2-1)(n^2-n_s^2)]\cos(\gamma) + (n-1)^2(n-n_s)^2x^2} \qquad (3.17)$$

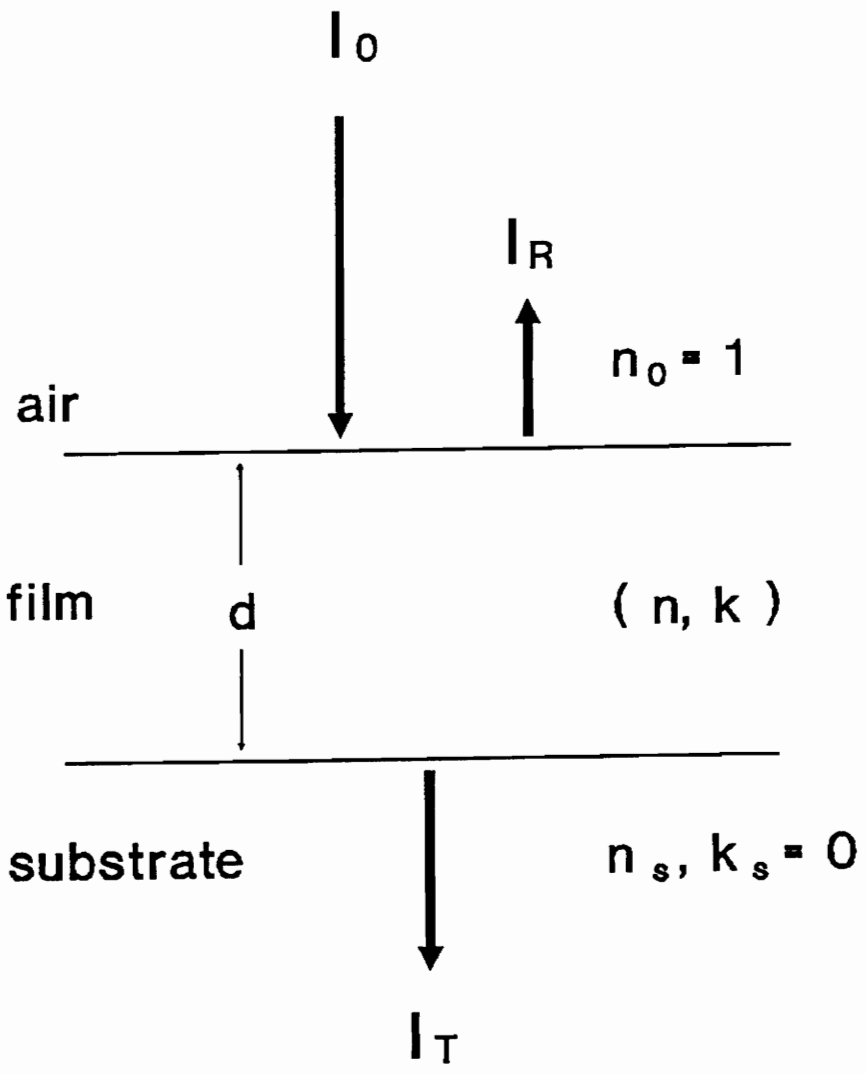

Figure 3.2 A schematic diagram of a weakly absorbing thin film on a completely transparent semi–infinite substrate.

here 1 is used to replace n_0 which is the refractive index of air and $\gamma = 4\pi nd/\lambda$. It is identical to the formula derived by Manifacier [42]. The cosine function in the denominator oscillates between +1 and –1, which results in the well–known equation for the interference fringes in the transmission spectrum:

$$2\pi d = m\lambda \tag{3.18}$$

where the order number m is an integer for maxima and a half integer for minima. Equation 3.17 gives the top envelope equation for $\cos(\gamma) = 1$ as

$$T_{max}' = \frac{16\, n_s\, n^2\, x}{[(1+n)(n+n_s) - (n-1)(n-n_s)x]^2} \tag{3.19}$$

whereas, for $\cos(\gamma) = -1$, the bottom envelope equation becomes

$$T_{min}' = \frac{16\, n_s\, n^2\, x}{[(1+n)(n+n_s) + (n-1)(n-n_s)x]^2} \tag{3.20}$$

Equations 3.19 and 3.20 can be solved for n and x giving

$$x = \frac{(n+1)(n+n_s)[(T_{max}'/T_{min}')^{0.5}-1]}{(n-1)(n-n_s)[(T_{max}'/T_{min}')^{0.5}+1]} \tag{3.21}$$

$$n = [N' + (N'^2 - n_s^2)^{0.5}]^{0.5} \tag{3.22}$$

where $N' = \frac{1}{2}(1+n_s^2) + 2n_s \frac{T_{max}'-T_{min}'}{T_{max}'T_{min}'}$. Once T_{max}' and T_{min}' are obtained from the measured transmission spectrum and the refractive index of the substrate is known, the refractive index of the film can be calculated as a function of

wavelength using equation 3.22. If $n(\lambda_1)$ and $n(\lambda_2)$ are the refractive indices at two adjacent maxima (or minima), at λ_1 and λ_2, it follows that the film thickness is given by the expression

$$d = \frac{\lambda_1 \lambda_2}{2[n(\lambda_1)\lambda_2 - n(\lambda_2)\lambda_1]} \tag{3.23}$$

Also, the extinction coefficient (k) and absorption coefficient (α) of the film can be calculated by equation 3.21 and the relation $\alpha = 4\pi k/\lambda$.

3.2.3 Consideration of Light Intensity Loss from the Back Surface of the Substrate

In all of the equations derived in sections 3.2.1 and 3.2.2 for calculating transmittance and reflectance it was assumed that the substrate is semi–infinite. In other words, for the transmittance measurement, the specimen could have to be a free standing film or else the detector could have to be installed "inside" the substrate in order for these equations to be valid. Therefore, if the specimen consists of a film on a thick substrate and if the detector has to be installed "outside" the substrate, the light intensity loss from the back surface of the substrate must be taken into account.

To take the back surface of the substrate into account, we start from the basic equations for Fresnel reflection coefficients. Consider the reflection and transmission of light at the planar interface between two semi–infinite homogeneous and optically isotropic media denoted by 0 and 1 with complex indices of refraction N_0 and N_1, respectively. The Fresnel reflection coefficients for the parallel polarization (r_p) and perpendicular polarization (r_s) can be expressed as

$$r_p = \frac{N_0\cos\varphi_1 - N_1\cos\varphi_0}{N_1\cos\varphi_0 + N_0\cos\varphi_1} \tag{3.24}$$

$$r_s = \frac{N_0\cos\varphi_0 - N_1\cos\varphi_1}{N_0\cos\varphi_0 + N_1\cos\varphi_1} \tag{3.25}$$

where φ_0 is the angle of incidence and φ_1 is the angle of refraction. The reflectances r_p and r_s, defined by the fraction of the total intensity that appears in the reflected wave for the p and s polarizations, are the amplitudes of the Fresnel reflection coefficients, i.e. $r_p = r_p r_p^*$ and $r_s = r_s r_s^*$. For the case of normal incidence, $\varphi_0 = \varphi_1 = 0$, if the complex refractive index is written in terms of the refractive index and the extinction coefficient, i.e. $N = n - i\,k$, the reflectance may be written:

$$r = r_p = r_s = \frac{(n_1-n_0)^2 + (k_1-k_0)^2}{(n_1+n_0)^2 + (k_1+k_0)^2} \tag{3.26}$$

To modify the equations in sections 3.2.1.1 and 3.2.1.2 by adding the back surface of the substrate, the simplest example of a "thick" substrate is used. The term "thick" is emphasized because the interference fringes disappear if the sampling interval $\Delta\lambda$ is several times larger than $\lambda^2/4nd$ [47]. Also, for the purpose of this study, the extinction coefficient of this "thick" substrate is assumed to be zero and the case of the normal incidence is considered. Figure 3.3 schematically shows how the transmittance and reflectance of an uncoated substrate are calculated. Summation of the intensities from the multi–reflection and –transmission at each interface gives the total transmittance and reflectance as

$$T_0 = \frac{1-r}{1+r} \tag{3.27}$$

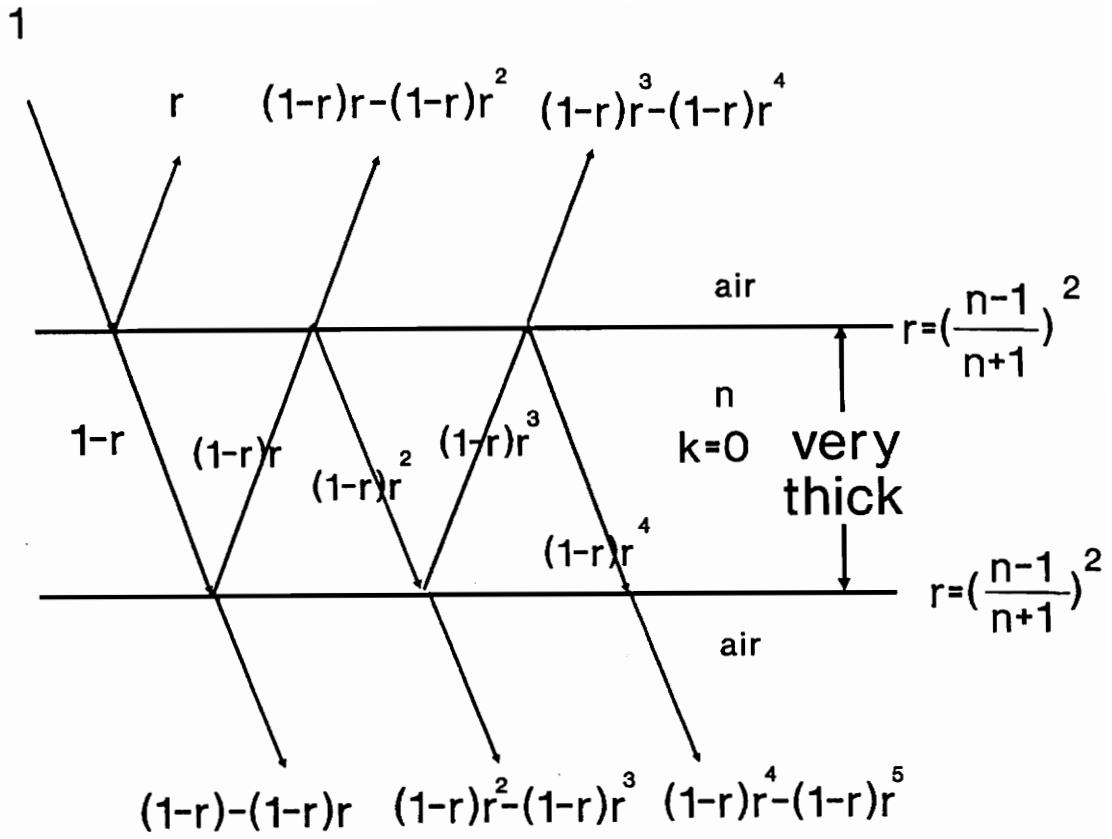

Figure 3.3 A schematic diagram for the calculation of the transmittance and the reflectance of an uncoated substrate.

$$R_0 = \frac{2r}{1+r} \tag{3.28}$$

where r is the reflectance at each interface; it may be expressed as given in equation 3.26. Recall that T_0 and R_0 are the transmittance and reflectance of 0 layer film on a finite substrate, i.e., an uncoated finite substrate. Following the same procedure, for a sample consisting of m layers "thick" transparent films on a transparent substrate, the transmittance becomes

$$T_m = \frac{\prod_{i=1}^{m+2}(1-r_i)}{\prod_{i=1}^{m+1}(1-r_i r_{i+1})} \tag{3.29}$$

where r_1, r_2, ..., r_{m+2} are the reflectances at the first interface, which is the air/first film interface to the last interface, which is the substrate/air interface; r_i is given by equation 3.26. Therefore, the transmittance of a thin film consisting of m layers on a substrate, with the consideration of the back surface of the substrate, can be approximately treated as

$$T_m = T_m' \frac{1-r_{m+2}}{1-r_{m+1}r_{m+2}} \tag{3.30}$$

where T_m' is the transmittance of a thin film consisting of m layers on a semi–infinite substrate (see equation 3.9). The reflectance can be approximated as

$$R_m = R_m' + (T_m'-T_m)(R_m'+T_m') \tag{3.31}$$

where R_m' is the reflectance of a thin film consisting of m layers on a semi–infinite

substrate (see equation 3.10).

Since $r_{m+1}r_{m+2} << 1$, which can be easily verified, equation 3.30 can be further approximated by neglecting $r_{m+1}r_{m+2}$. Applying this approximation to equation 3.30 and combining it with equation 3.17, it follows that

$$T_1 = \frac{16\ n_s\ n^2\ x\ (1-r_3)}{(1+n)^2(n+n_s)^2\ -\ 2x[(n^2-1)(n^2-n_s^2)]\cos(\gamma)\ +\ (n-1)^2(n-n_s)^2x^2} \qquad (3.32)$$

where r_3 is the reflectance at the interface of air–back substrate surface, which is equal to $(n_s-1)^2/(n_s+1)^2$. Equation 3.32 differs from equation 3.17 by a factor of $1-r_3$. Starting from equation 3.32 and following the same procedure in section 3.2.2, the solutions for x and n are found to have the exact same forms as equations 3.21 and 3.22, respectively. The only difference appears in N' (see equation 3.22), due to the extra factor of $(1-r_3)$, which becomes

$$N = \frac{1}{2}(1+n_s^2) + \frac{8n_s^2}{(n_s+1)^2}\frac{T_{max}-T_{min}}{T_{max}T_{min}} \qquad (3.33)$$

To demostrate the significant difference between the calculations with and without regard to the back surface of the substrate, an example is used. We take $T_{max} = 0.85$, $T_{min} = 0.70$, d = 300 nm, $n_s = 1.76$, and $\lambda = 600$ nm; a comparison of these two cases is listed in Table 3.3. Although the difference in the refractive index n is only 1.5%, a surprising difference in the extinction coefficient k, of as large as 17 times was observed. This huge difference in k can be easily understood by checking the reflection loss on a bare substrate. Taking the above example, for a semi–infinite substrate with $n_s = 1.76$, $R_0' = 0.076$ at the interface (equation 3.26);

Table 3.3 A comparison of the envelope method with and without the back surface of the substrate by using the following values: T_{max} = 0.85, T_{min} = 0.70, d = 300nm, n_s = 1.76, and λ = 600nm.

	N	n	x	$a(cm^{-1})$	k
Manifacier[1]	2.9362	2.2992	0.9272	2521	0.0120
Swanepoel[2]	2.9362	2.2992	0.9907	313	0.0015
This study	2.8689	2.2659	0.9956	146	0.0007

[1]Reference 42

[2]Reference 43

hence, $T_0' = 0.924$. For a real substrate (finite thickness), $R_0 = 0.141$ and $T_0 = 0.859$ (see equations 3.27 and 3.28). Consequently, it becomes clear that the small k (0.0007) is expected from the difference between T_{max} and T_0, while the huge k (0.0120) results from the big difference between T_{max} and T_0'. This means that if the formulae in section 3.2.2 are used to calculate n and k of the film, the reflection loss from the back surface of the substrate is counted into the extinction coefficient of the film.

To the best of my knowledge, equations 3.32 and 3.33 are being reported for the first time to calculate n and k of a weakly absorbing film on a transparent substrate. This is surprising because since the time Manifacier first derived the envelope method in 1976, many authors have used his equations without mentioning the importance of the back surface of the substrate.

3.2.4 Effective Medium Approximation

The dielectric response of a heterogeneous medium can be described in terms of the dielectric properties of its components [48]. The effective dielectric response of a heterogeneous medium can be described by the Bruggeman effective medium approximation (EMA) [49,50]. According to the effective medium approximation, the relationship of the effective dielectric function (ϵ) of a heterogeneous medium, the dielectric function (ϵ_i) of each component, and the volume fraction (f_i) of each component is given by

$$\sum_{i=1}^{n} f_i \frac{\epsilon_i - \epsilon}{\epsilon_i + 2\epsilon} = 0 \qquad (3.34)$$

where n is the number of components in the heterogeneous medium.

In general, most methods produce films with packing densities less than one. Therefore, the porosity needs to be considered as a separate phase in the so–called "single phase" film. The EMA can consequently be applied to calculate the packing density of a single phase film. For most oxides, the extinction coefficient is much smaller than the refractive index at a given wavelength. Thus the dielectric function at optical frequencies can be related to the refractive index (n) by $\epsilon = n^2$. For a single phase porous film, the EMA becomes

$$f\frac{n_b^2 - n^2}{n_b^2 + 2n^2} + (1-f)\frac{1 - n^2}{1 + 2n^2} = 0 \qquad (3.35)$$

where f is the volume fraction or the packing density of the film, n_b is the refractive index of the bulk material, and n is the effective (or measured) refractive index.

3.2.5 Optical Constants at Near Band Gap

At near optical band gap region, for a single film on a transparent substrate, the transmittance of the specimen can be written as [51]

$$T = \frac{(1-r_1)(1-r_2)(1-r_3)\exp(-\alpha d)}{(1-r_1r_2)\{1 - [r_1r_2 + r_1r_3(1-r_2)^2]\exp(-2\alpha d)\}} \qquad (3.36)$$

where α is the absorption coefficient of the film, d is the film thickness, and r_1, r_2, and r_3 are the reflectance of air–film, film–substrate, and substrate–air interfaces, respectively. Since $r_1r_2 << 1$ and $\exp(-2\alpha d) << 1$, equation 3.36 can be reduced to

$$T \cong (1-r_1)(1-r_2)(1-r_3)\exp(-\alpha d) \tag{3.37}$$

On the other hand, because of the strong absorption of the film, light cannot reach the second (film–substrate) and the third (substrate–air) interfaces. Therefore, the reflectance of the specimen is approximately equal to the reflectance of the air–film interface, i.e.,

$$R = r_1 \tag{3.38}$$

Although the extinction coefficient (k) is large at wavelengths near the optical band gap, it is still negligible compared to the refractive index (n). Thus, the refractive index of the film can be related to the reflectance of the specimen by equations 3.26 and 3.38

$$n = (1 + \sqrt{R})/(1 - \sqrt{R}) \tag{3.39}$$

Therefore, the absorption coefficient of the film can be obtained by rewriting equation 3.37

$$\alpha = \frac{1}{d} \ln \frac{(1-R)\ [1-(n-n_s)^2/(n+n_s)^2]\ [1-(n_s-1)^2/(n_s+1)^2]}{T} \tag{3.40}$$

All the computer programs used in this study are collected in Appendix C.

3.3 Optical Properties of Sapphire Substrate

The substrate used in this study is sapphire (single crystal Al_2O_3). Optical grade sapphire disks 1 inch in diameter and 1 mm thick were obtained from Swiss Jewel Company and had a surface orientation within a 30^0 cone of the [100] direction. Sapphire is in many ways an excellent window material. Because of its extreme surface hardness, sapphire can be scratched by only a few substances (such as diamond or boron nitride) other than itself. Chemically inert and insoluble in almost everything at room temperature, sapphire can be cleaned with impunity; even hydrogen fluoride fails to attack sapphire at temperatures below 300^0C. Because of its excellent hardness and inertness to chemicals, sapphire can be reused many times. A solution of hydrogen fluoride, nitric acid, and water (1:1:1 in volume) can be utilized to remove the film at room temperature without damaging the sapphire.

A dispersion relation for the ordinary ray in sapphire has been determined by Malitson [52]:

$$n^2 = 1 + \frac{A\lambda^2}{\lambda^2-\lambda_1^2} + \frac{B\lambda^2}{\lambda^2-\lambda_2^2} + \frac{C\lambda^2}{\lambda^2-\lambda_3^2} \qquad (3.41)$$

where

$$A = 1.023798$$

$$B = 1.058264$$

$$C = 5.280792$$

$$\lambda_1 = 0.00377588$$

$$\lambda_2 = 0.0122544$$

$$\lambda_3 = 321.3616$$

The unit of λ is in μm.

By using the above dispersion relation for the refractive index and assuming the extinction coefficient to be zero, the transmittance of sapphire substrate can be calculated. Figure 2.4 shows the experimental transmission spectrum and the calculated spectrum of sapphire. As can be seen from Figure 2.4, these two spectra agree with each other very well. Therefore, equation 3.41 and the assumption of k = 0 can be applied for all the optical property calculations in this study.

3.4 X–ray Diffraction Study

Before the optical measurements, the films were insured of having the perovskite structure by X–ray diffraction (XRD). The XRD patterns of the specimens are shown in Figure 2.5. Figure 2.5 shows that the formation of the perovskite phase was completed for all compositions at an annealing temperature of 650^{0}C for 1 hour. As can be seen from the splitting of the {100}, {110}, {200}, and {211} peaks, the films with compositions between x = 0.0 and 0.4 showed a tetrogonal structure while those with composition x = 0.5 were on the porphotropic phase boundary. On the other hand, films with compositions x = 0.6 and 0.8 were rhombohedral, while those with composition x = 1.0 showed orthorhombic structure. From the position of the x–ray diffraction peaks it can be seen that the lattice parameters also showed the expected systematic variation with the Zr/Ti ratio [32].

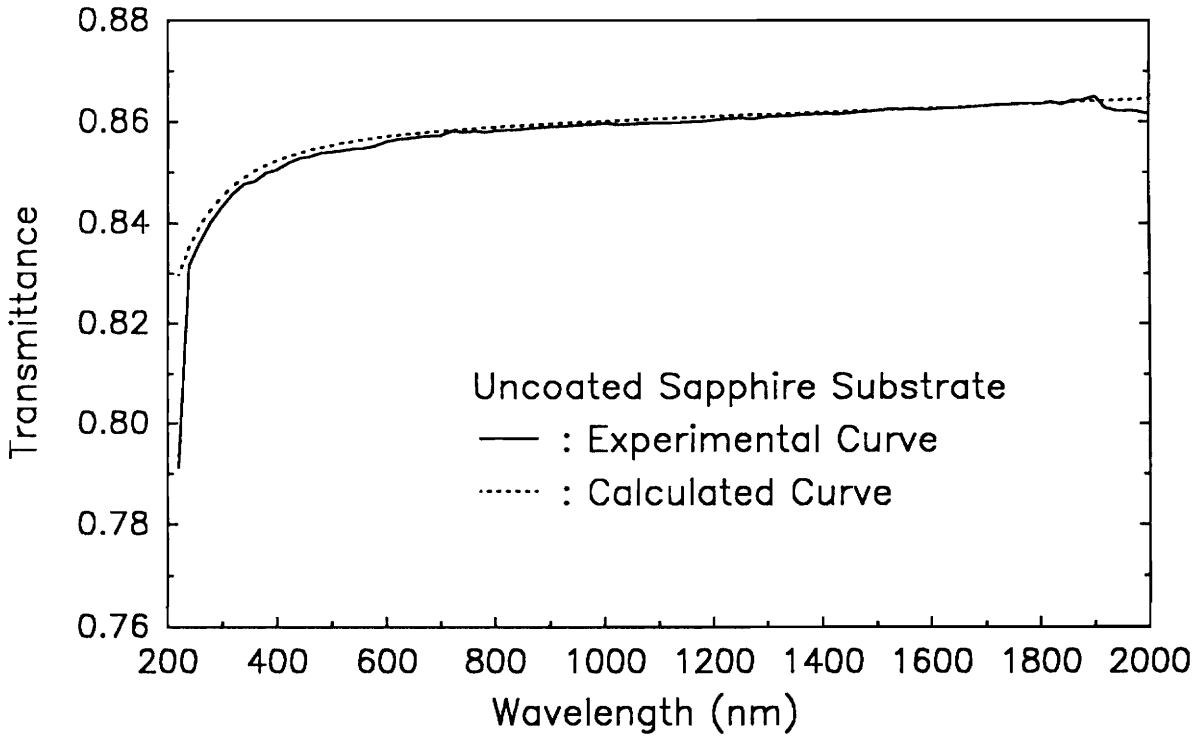

Figure 3.4 Comparison of the experimental and the calculated transmission spectra of sapphire.

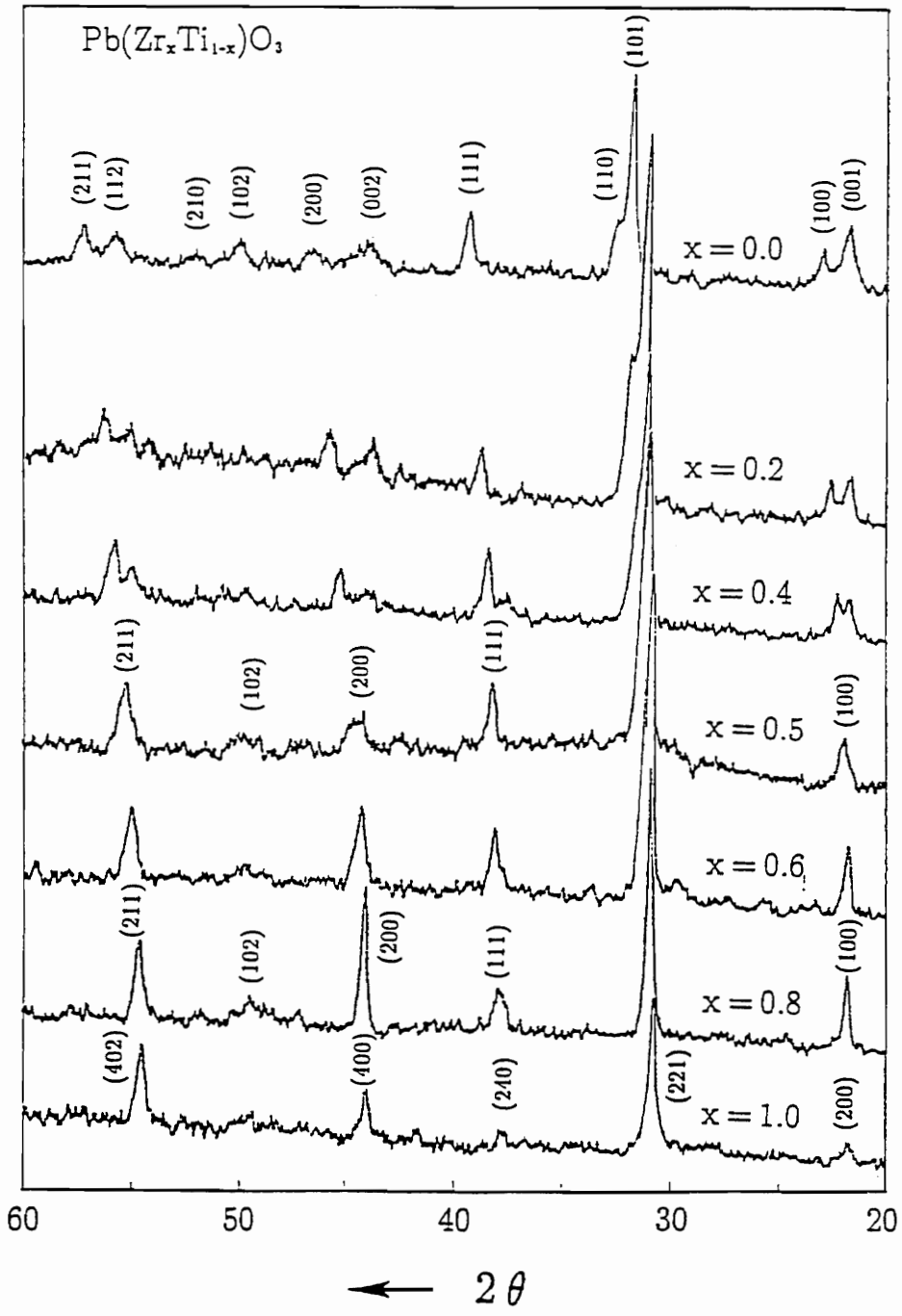

Figure 3.5 XRD patterns of MOD $Pb(Zr_xTi_{1-x})O_3$ films on sapphire substrates. The samples were annealed at 650°C for 1 hour.

3.5 Optical Constants and Film Thickness of PZT Solid Solutions

Figure 3.6 shows an example of the transmission spectrum of a weakly absorbing $Pb(Zr_{0.6}Ti_{0.4})O_3$ film on a completely transparent substrate (sapphire). The top solid curve is the transmittance of the uncoated sapphire. The fringes are a result of the interference between two interfaces: the air–film and the film–substrate. The transmittance [$T(\lambda)$] of the sample is enveloped by two dashed curves, T_{max} and T_{min}, which are the curves drawn through the maxima and minima of $T(\lambda)$. The "gap" between the transmission spectrum of the substrate and T_{max} is indicative of the light loss due to the scattering and/or absorption. Based on the strength of the absorption, the transmission spectrum can be roughly divided into three regions: weak, medium, and strong absorption regions. In this study, the region at the transmittance values higher than 0.6 will be considered as the weak absorption region, the values between 0.3 and 0.6 will be considered as the medium absorption region, and the values lower than 0.3 will be considered as the strong absorption region. For the given example (Figure 3.6), the region at the wavelength longer than 450 nm is assigned to be the weak absorption region, from 350 nm to 450 nm is the medium absorption region, and at wavelengths shorter than 350 nm is the strong absorption region.

Once T_{max} and T_{min} are obtained, the refractive index of the film can be easily calculated by using equations 3.22 and 3.33 as a function of wavelength. It seems to be quite straightforward to calculate the optical constants using the envelope method. The questions are how to determine the envelope curves and where the wavelength limit of the envelope method is.

For the first question, although a computer program called ENVELOPE was

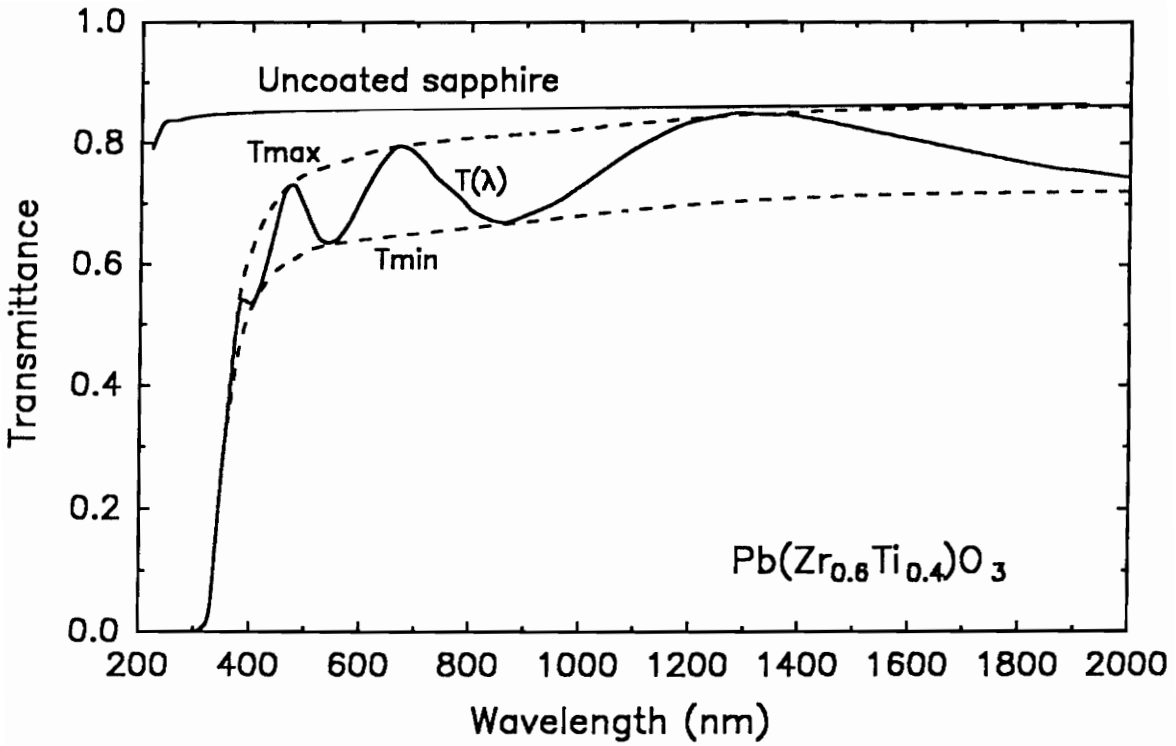

Figure 3.6 Optical transmission spectrum of $Pb(Zr_{0.6}Ti_{0.4})O_3$ film on sapphire with that of the uncoated substrate. The envelope curves are shown as the dashed curves.

obtained from National Institute of Standards and Technology [53] to help the determination of the envelope curves (T_{max} and T_{min}), it does not work in our case. The reason may be that the films are too thin for this computer program. For a film having a thickness of about 300 nm, the number of the maxima or minima of the interference fringes is three or four, as can be seen in Figure 3.6. Therefore, in many cases, an unsatisfactory curve generated by a computer program from only three points is understandable. In addition, we tried to write a computer program to solve this problem by using B–spline interpolation. It also does not work well. Therefore, the envelope curves were manually determined. A quite accurate curve can be obtained by hand in the weak absorption region as can be seen in Figure 3.6.

For the second question, in theory, the envelope method is valid as long as the sample meets the assumptions discussed in section 3.2.2. However, even though these assumptions may be met at the medium absorption region, the envelope curves are not easy to be accurately determined. This can be understood by the very steep drop in the transmittance occurring in a small wavelength range. Thus a small error in the determination of the envelope curves can result in a significant error in the refractive index. In short, the envelope method is good in the weak absorption region ($\lambda > 450$ nm for the given example), is questionable in the medium absorption region (450 nm $> \lambda >$ 350 nm), and is invalid in the strong absorption region ($\lambda < 350$ nm).

In the strong absorption region, both the refractive index and extinction coefficient of the film region can be calculated from the transmission and reflection spectra. The reflection spectrum of $Pb(Zr_{0.6}Ti_{0.4})O_3$ film on sapphire is shown in Figure 3.7. The solid curve is the reflectance of the sample without black paint on the back surface of the substrate, while the dashed curve is that with black paint on

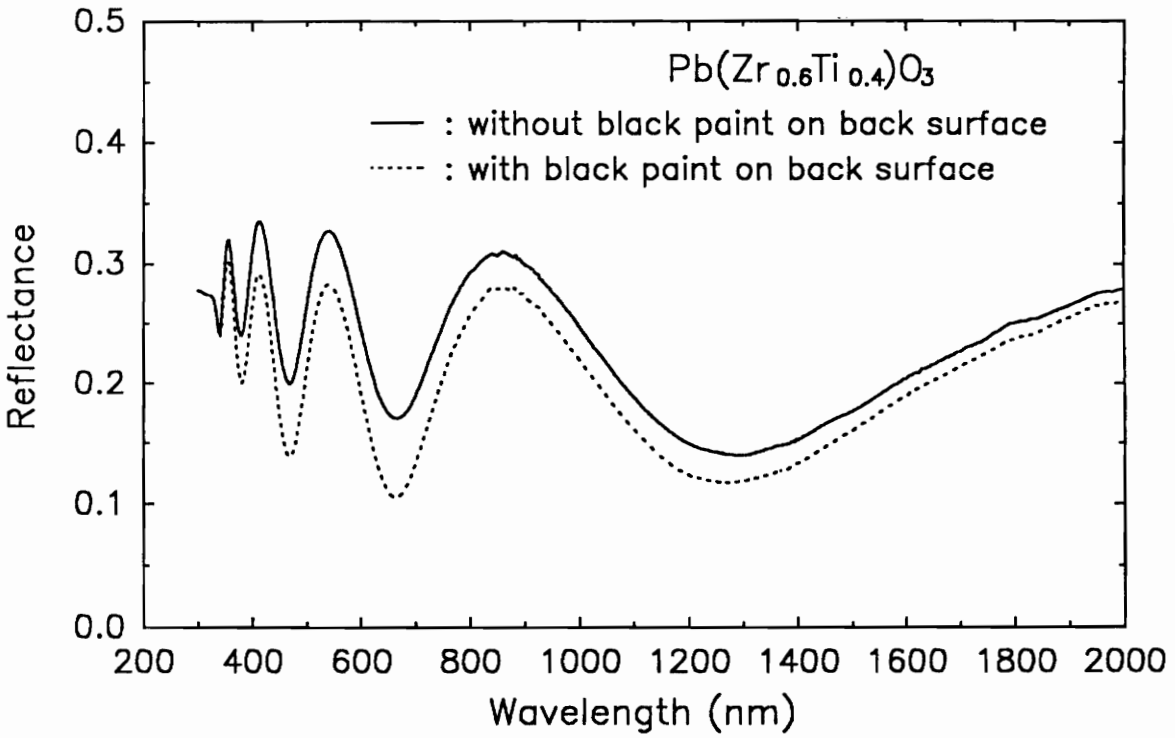

Figure 3.7 The reflection spectra of $Pb(Zr_{0.6}Ti_{0.4})O_3$ film on sapphire in the wavelength range of 300 nm to 2000 nm. The dashed curve is the spectrum with the black paint on the back surface of the substrate.

the back surface of the substrate. The reflectance of the sample with black paint shows lower values than that without black paint because the black paint eliminates most of the reflection from the back surface of the substrate. One very interesting observation is that these two reflection spectra merge together at the strong absorption region, as shown in Figure 3.8. This means that almost no light can reach the back surface to be eliminated by the black paint. In other words, the incident light is either reflected or absorbed by the film. In addition, it can be clearly seen that the interference effect starts at the point where the two reflection spectra merge together. The interference fringes of the reflection spectrum show the opposite behavior as those in the transmission spectrum. That is, the maxima of the interference fringes in the reflection spectrum are the minima in the transmission spectrum, as shown in Figure 3.9 for the case of $Pb(Zr_{0.6}Ti_{0.4})O_3$ film. The reflection spectrum in Figure 3.9 was measured without the black paint on the back surface of the substrate. The top curve in Figure 3.9 is the sum of the transmittance and the reflectance which indicates how much light intensity was absorbed and/or scattered by the sample. The reflection and the transmission spectra for the rest of the compositions are shown in Figures B.1 – B.6 in Appendix B.

Figure 3.10 shows the refractive index of $Pb(Zr_{0.6}Ti_{0.4})O_3$ film as a function of wavelength. For the rest of the compositions, the refractive indices as a function of wavelength are shown in Figures B.7 – B.12. The open circles are data calculated from the envelope method and the filled circles are data calculated from equation 3.39.

As can be seen in Figure 3.10, the refractive index has a value of 2.16 in the near infrared region, and gradually increases to a value of 2.42 at a wavelength

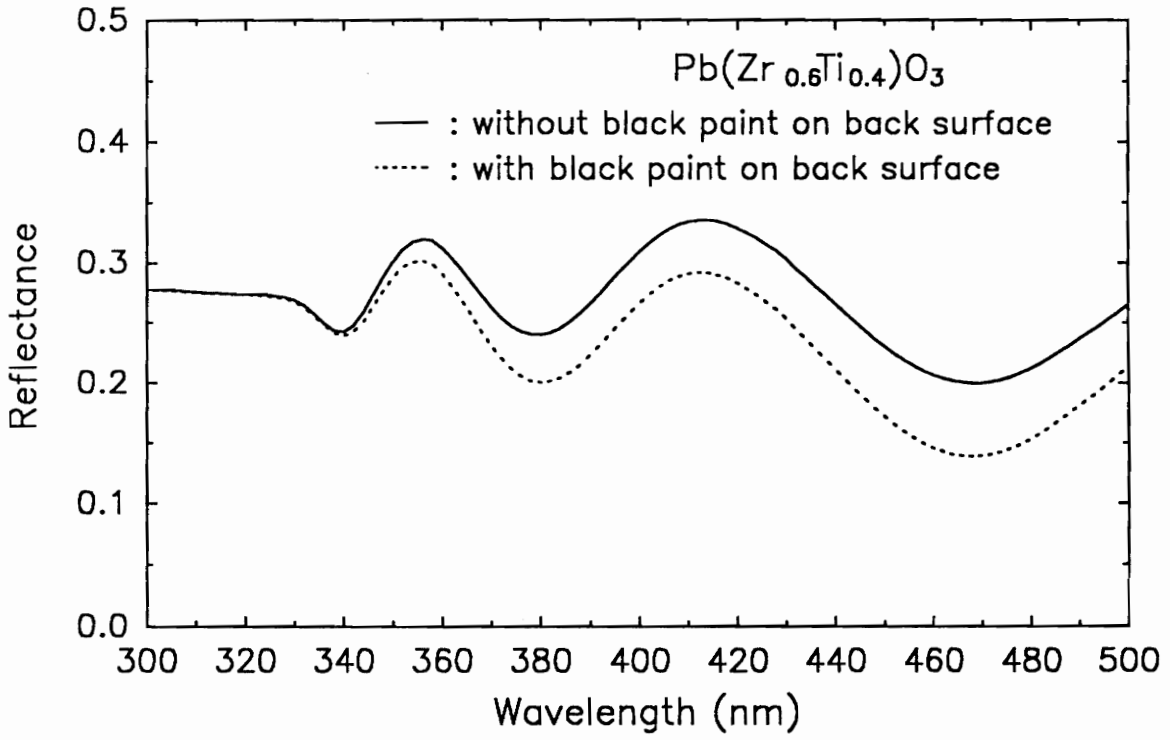

Figure 3.8 The reflection spectra of $Pb(Zr_{0.6}Ti_{0.4})O_3$ film on sapphire in the wavelength range of 300 nm to 2000 nm. The dashed curve is the spectrum with the black paint on the back surface of the substrate.

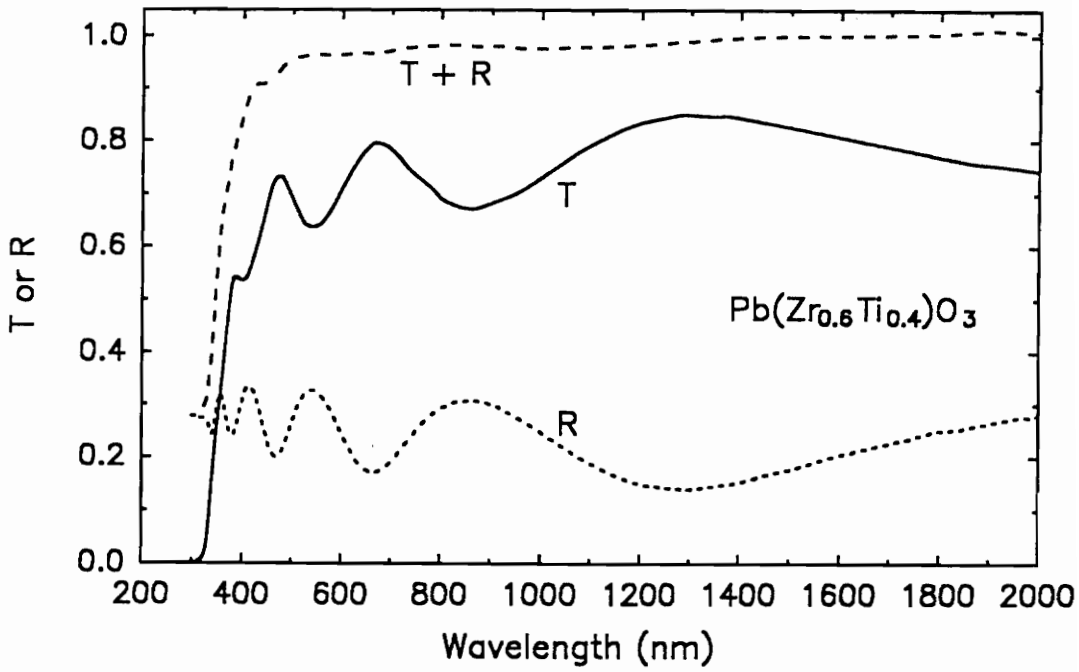

Figure 3.9 The reflectance, transmittance, and their sum of the $Pb(Zr_{0.6}Ti_{0.4})O_3$ film on sapphire in the wavelength range of 300 nm to 2000 nm. The reflection spectrum was measured without the back paint on the back surface of the substrate.

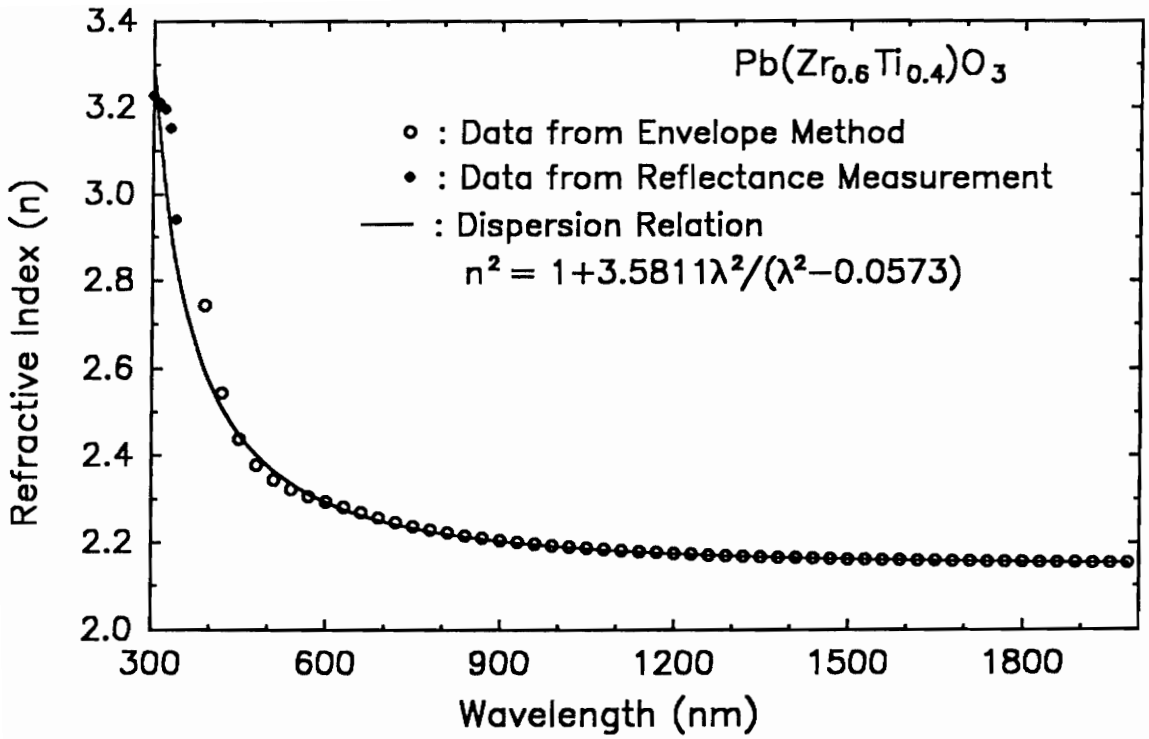

Figure 3.10 The refractive index as a function of wavelength and the dispersion curve of $Pb(Zr_{0.6}Ti_{0.4})O_3$ film.

around 450 nm; it then rises abruptly in the ultraviolet region to a value of 3.15 at 340 nm and finally flattens out at a wavelength of 300 nm with a value of 3.2. In addition, the data obtained from the envelope method at a wavelength range from 400 nm to 2000 nm "relate" very well with those from the reflectance measurement at a wavelength range from 300 nm to 340 nm. The "gap" between 340 nm and 400 nm can be interpolated by a dispersion relation which will be discussed later.

Since most refractive index data were presented at $\lambda = 632.8$ nm which is the wavelength of a He–Ne laser, a summary of the refractive index at this wavelength for the entire PZT solid solutions is given in Figure 3.11. The refractive index of the film decreases linearly for an increase in x, i.e. with increasing zirconium content. For example, $PbTiO_3$ ($x = 0.0$) has an n value of 2.481, whereas $PbZrO_3$ ($x = 1.0$) shows an n value of 2.125. Compared to the refractive indices of the bulk materials [54], which are 2.668 for $PbTiO_3$ and 2.420 for $PbZrO_3$, the films showing lower indices were possibly due to the porosity and/or the stress in the films [55].

If the lower indices are only due to the porosity in the films, the packing densities of the films can be calculated by using the effective medium approximation as discussed in section 3.2.4. Table 3.4 summaries the packing densities of $Pb(Zr_xTi_{1-x})O_3$ films made by MOD in this study. The packing densities display a higher value for the titanium–rich side, while a lower value for the $PbZrO_3$ film. This may be due to the fact that the compeletion temperature of the perovskite phase for the titanium–rich side is much lower than that for the zirconium–rich side. The structure development of MOD PZT films will be discussed in detail in Chapter 4.

Coming back to Figure 3.10, the refractive index data as a function of wavelength can be fitted to a Sellmeier type dispersion relation [44]. For pure

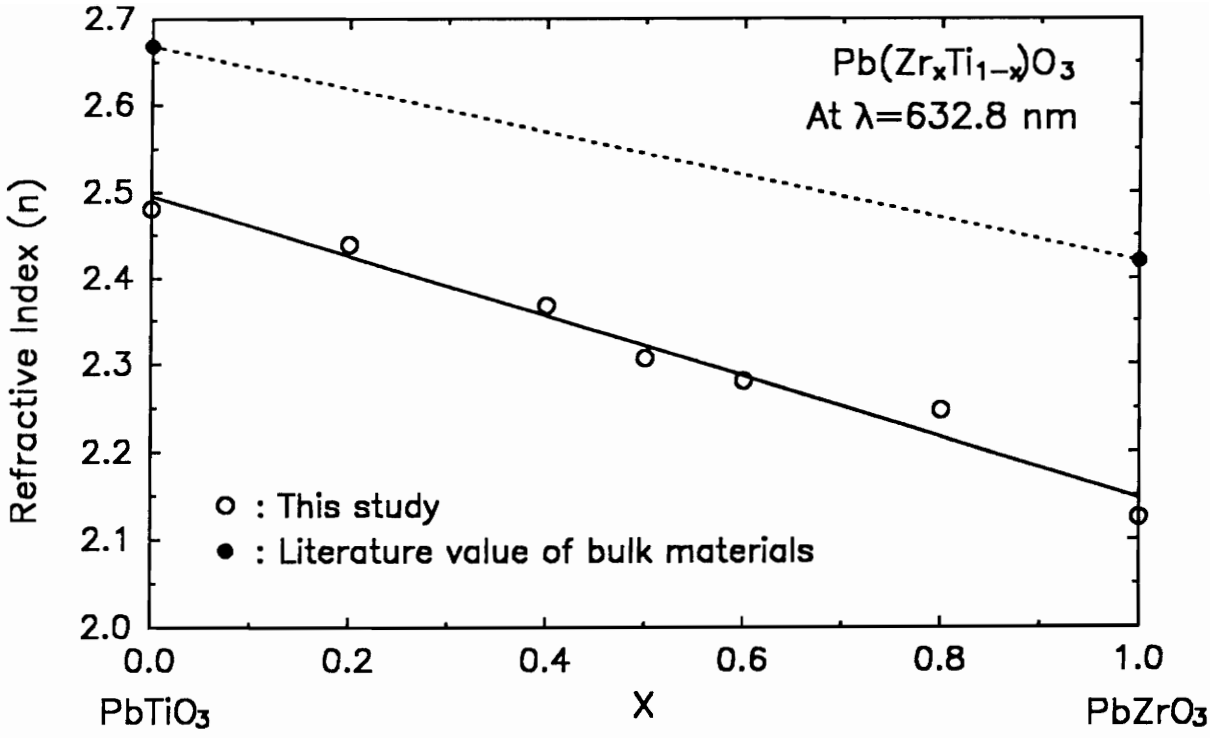

Figure 3.11 Variation of the refractive index at λ = 632.8 nm with x value in $Pb(Zr_xTi_{1-x})O_3$ films. Filled circles and the dashed line are data from reference 54.

Table 3.4 Packing density of MOD $Pb(Zr_xTi_{1-x})O_3$ thin films

Composition, x	0.0	0.2	0.4	0.5	0.6	0.8	1.0
Packing Density	.887	.888	.871	.847	.844	.849	.796

substances, the wavelength dependence of the optical constants may be described by the classical treatment of Lorentz. This theory assumes that the solid is composed of a series of independent oscillators, which are set into forced vibrations by the incident radiation. For both insulating and semiconducting materials, the well–known Sellmeier type equation, neglecting absorption, follows [44]

$$n^2 = 1 + \frac{A\lambda^2}{(\lambda^2 - B)} \tag{3.42}$$

where A and B are constants to be determined and λ is the wavelength in μm.

By fitting the refractive index data (Figure 3.10) to equation 3.42, the dispersion relation constants were found to be 3.5811 for A and 0.0573 for B. As can be seen in Figure 3.10, the dispersion curve fits very well to the experimental data for wavelengths longer than 450 nm. The first two data points (at a wavelength around 400 nm) obtained from the envelope method deviate considerably from the dispersion curve because of the large error of the envelope method in this region. On the other hand, the dispersion curve also has its wavelength limit. This can be understood from the fact that the experimental data "flattens" out at 300 nm, while the dispersion curve continuously increases. It is also clear that if $\lambda^2 = 0.0573$ or $\lambda = 0.240$ μm $= 240$ nm, the n value is infinite. Combining these two sets of experimental data and the curve fitting result, it is concluded that the dispersion curve is valid from 350 nm to 2000 nm.

As discussed earlier, if the reduction in the index of the film from its bulk value is only due to porosity in the film and if the effective medium approximation is valid in the wavelength range of this study, the indices of the films can be "adjusted" to those of the bulk materials for the study of the dispersion relations of

the bulk materials. For example, for $PbTiO_3$, the n value at $\lambda = 632.8$ nm is 2.668 for the bulk material and 2.481 for the film. Therefore, 0.187 is added to the indices of the film in the wavelength range studied to find the indices of the corresponding bulk materials. By applying equation 3.42 to the adjusted data, the fitting constants were 5.3617 for the A and 0.0527 for the B, as shown in Figure 3.12. Singh et al [56] also studied the dispersion relation of the single crystal $PbTiO_3$ by using the same Sellmeier–type equation. They reported a value of 5.3636 for the A and 0.05027 for the B. The fitting results of the original refractive indices and the adjusted refractive indices are listed in Table 3.5. As can be seen in Table 3.5, the A values decreased linearly from 4.4556 for $PbTiO_3$ to 2.9500 for $PbZrO_3$ for the MOD films of this study and from 5.3617 for $PbTiO_3$ to 4.2033 for $PbZrO_3$ for the "bulk" materials. For the B values, they were in the range from 0.05011 to 0.06070, which correspond to the wavelengths 0.224 and 0.246 μm, respectively, and were independent of the composition. The figures for the rest of compositions which are not presented in this chapter are collected in Appendex B (Figures B.13 – B.18).

One of the most direct applications of the interference fringes of the transmission spectrum is the estimation of the film thickness. If the refractive indices at two adjacent maxima (or minima) are known, the film thickness can be determined using equation 3.23. The wavelength at each peak and valley of the interference fringes, corresponding n values which were calculated from the envelope method, and the thickness calculated from each pair of peaks or valleys are listed in Table 3.6 for all PZT compositions in this study. The average thickness $\overline{d'}$ can now be used, along with n, to calculate the order number m' for the different extremes using equation 3.18. As can be seen in Table 3.6, the values of m' are not exact integers or half integers. The accuracy in thickness can now be significantly

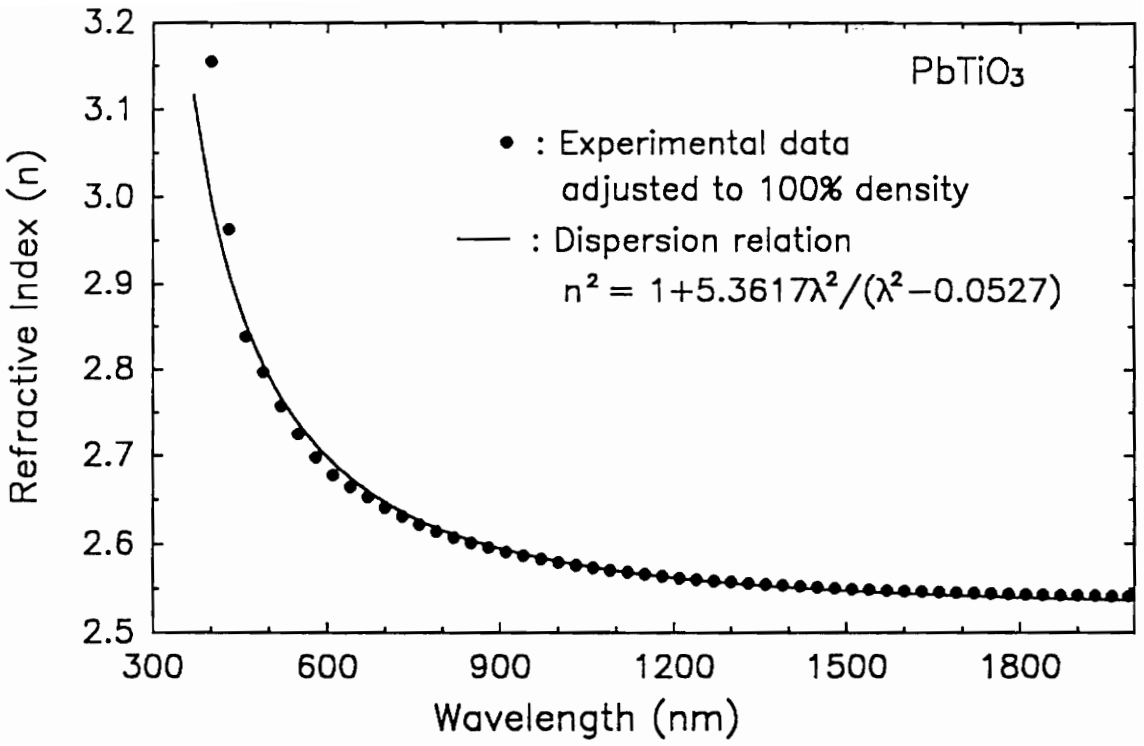

Figure 3.12 Adjusted refractive index as a function of wavelength and the dispersion curve of $PbTiO_3$ film.

Table 3.5 Constants of the dispersion relations for $Pb(Zr_xTi_{1-x})O_3$ thin films. The dispersion relation is written as $n^2 = 1 + A\lambda^2/(\lambda^2-B)$, where λ is in μm.

For the original data							
x	0.0	0.2	0.4	0.5	0.6	0.8	1.0
A	4.4556	4.2533	3.9330	3.6778	3.5811	3.4333	2.9501
B	0.05778	0.05589	0.05944	0.06071	0.05733	0.05967	0.05922
For the adjusted data†							
x	0.0	0.2	0.4	0.5	0.6	0.8	1.0
A	5.3617	5.1056	4.8656	4.7567	4.6533	4.4183	4.2033
B	0.05267	0.05130	0.05362	0.05367	0.05089	0.05310	0.05011

†The original refractive indices were adjusted to those of the bulk materials according to the effective medium approximation.

Table 3.6 Film thickness calculation of $Pb(Zr_xTi_{1-x})O_3$ thin films by envelope method and equation $2nd = m\lambda$. Both of λ and d are in nm.

Composition	λ	n	d′	$\overline{d'}$	m′	m	d	$\overline{d}$
	460 (p)	2.652	245		3.09	3	260	
	663 (p)	2.469	276		2.00	2	269	
x = 0.0	1240 (p)	2.373		268	1.03	1	261	267
	432 (v)	2.768	296		3.43	3.5	273	
	540 (v)	2.549	254		2.53	2.5	265	
	875 (v)	2.410			1.48	1.5	272	
	467 (p)	2.572	273		2.92	3	272	
	661 (p)	2.428	278		1.95	2	272	
x = 0.2	1241 (p)	2.328		265	1.00	1	267	271
	415 (v)	2.761	240		3.53	3.5	263	
	544 (v)	2.486	271		2.43	2.5	274	
	870 (v)	2.368			1.44	1.5	276	
	458 (p)	2.526	259		2.94	3	272	
	658 (p)	2.357	279		1.91	2	279	
x = 0.4	1259 (p)	2.257		266	0.95	1	279	277
	418 (v)	2.697	254		3.43	3.5	271	
	540 (v)	2.420	273		2.39	2.5	279	
	867 (v)	2.297			1.41	1.5	283	
	395 (p)	2.803	252		4.06	4	282	
	477 (p)	2.437	278		2.93	3	294	
	690 (p)	2.284	310		1.90	2	302	
x = 0.5	1292 (p)	2.196		286	0.97	1	294	296
	436 (v)	2.556	300		3.36	3.5	299	
	560 (v)	2.349	292		2.40	2.5	298	
	899 (v)	2.232			1.42	1.5	302	

Table 3.6 (*Continued*)

Composition	λ	n	d′	$\overline{d'}$	m′	m	d	$\overline{d}$
	465 (p)	2.409	284		2.88	3	290	
	663 (p)	2.269	289		1.91	2	292	
x = 0.6	1281 (p)	2.171		278	0.94	1	295	290
	411 (v)	2.604	236		3.53	3.5	276	
	550 (v)	2.318	304		2.35	2.5	297	
	861 (v)	2.213			1.43	1.5	292	
	467 (p)	2.372	287		2.88	3	295	
	669 (p)	2.232	300		1.89	2	300	
x = 0.8	1280 (p)	2.136		284	0.95	1	300	296
	417 (v)	2.579	247		3.51	3.5	283	
	550 (v)	2.289	302		2.36	2.5	300	
	869 (v)	2.177			1.42	1.5	299	
	476 (p)	2.207	302		2.90	3	324	
	704 (p)	2.097	333		1.86	2	336	
x = 1.0	1362 (p)	2.009		313	0.92	1	339	331
	426 (v)	2.332	293		3.42	3.5	320	
	571 (v)	2.152	323		2.36	2.5	332	
	922 (v)	2.047			1.39	1.5	338	

p = wavelength at peak position of interference fringes

v = wavelength at valley position of interference fringes

increased by rounding the value of m to the nearest exact integer or half integer value of m associated with each extreme point and deriving a new thickness d from equation 3.18. For example, the standard deviation for d′ was found to be 17 nm which corresponds to an error of 6.5%, whereas that of d was 4.8 nm which corresponds to an error of 1.8% for the film with composition x = 0.2.

The thicknesses of the films derived from the above method are 267, 271, 277, 296, 290, 296, and 331 nm corresponding to the compositions of x = 0.0, 0.2, 0.4, 0.5, 0.6, 0.8, and 1.0, respectively. These thickness values were used to calculate the extinction coefficients of PZT films as a function of wavelength using equations 3.16 and 3.21, as shown in Figure 3.13 for $Pb(Zr_{0.6}Ti_{0.4})O_3$ and Figures B.19 – B.24 for the rest of the compositions. In order to reveal these values in the visible and the near infrared region, the ordinate was broken into two different scales. The extinction coefficients of MOD PZT films were in the range of 10^{-2} to 10^{-3}, in the visible and the infrared region, which are one order of magnitude higher than that of MOCVD PZT films (the optical properties of MOCVD PZT films will be discussed in Chapter 5). These higher values may be due to the scattering of the incident light from the sample surface.

An alternative but more tedious method, in which the film thickness is simulated from the the optical constants obtained from the envelope method, was used to cross check the validity of the above thickness calculation method. This thickness simulation method is considered to be more accurate than the envelope method because the only assumptions for this method are that the film is homogeneous and the thickness of the film is uniform. In addition, this simulation process has only one unknown, namely, film thickness, that needs to be determined. The simulation process is as follows:

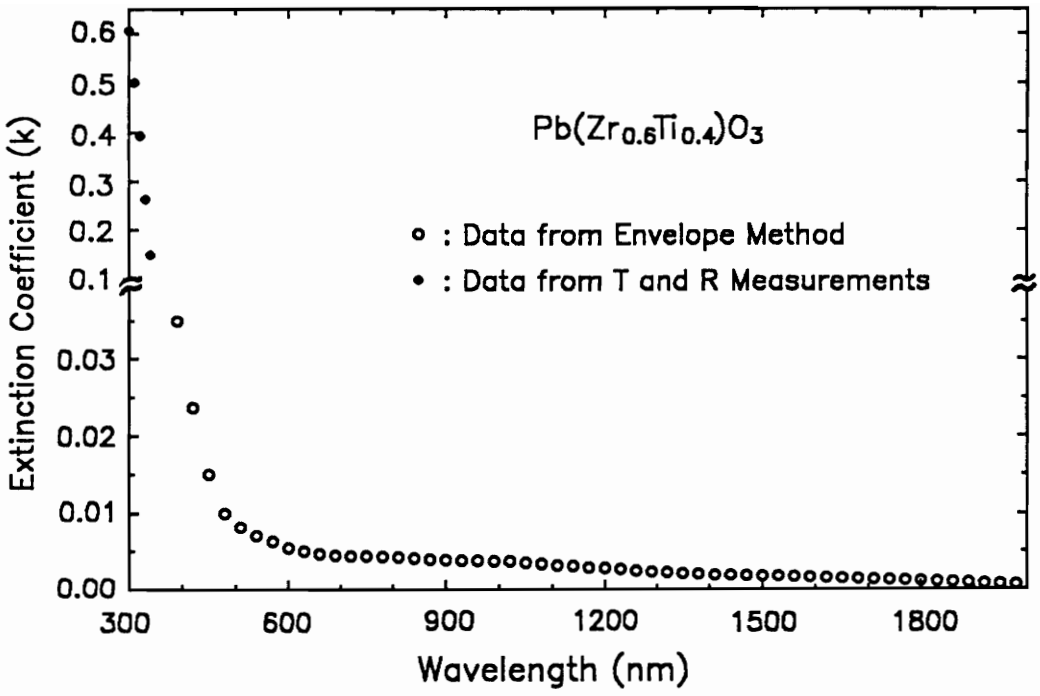

Figure 3.13 The extinction coefficient as a function of wavelength of $Pb(Zr_{0.6}Ti_{0.4})O_3$ film in the wavelength range of 300 nm to 2000 nm.

(1) use the known optical constants (n and k) of the film

(2) give an initial guess of the film thickness

(3) use equations 3.9 and 3.30 to calculate the transmission spectrum and compare to the experimental transmission spectrum which will generate a fitting error, χ^2, defined as

$$\chi^2 = \frac{1}{n} \sum_{i=1}^{n} (T_i^c - T_i^e)^2 \qquad (3.43)$$

where n is the number of data points, T_i^c is the calculated transmittance, and T_i^e is the experimental transmittance

(4) add a small increment of thickness (0.1 nm in the present study) and continue step (3) until the smallest χ^2 is met.

Figure 3.14 shows the fitting result of the $Pb(Zr_{0.6}Ti_{0.4})O_3$ film whose n and k values were shown in Figures 3.10 and 3.13, respectively. The fitted thickness is 295 nm which is in reasonable agreement with the result of 290 nm obtained from the envelope method. As can be seen in Figure 3.14, the simulated curve fits well to the experimental data in the visible, near infrared, and near the absorption edge range. However, a considerable deviation was found in the neighborhood of wavelength around 400 nm. As discussed earlier, the refractive indices at around wavelength 400 nm also deviate from the dispersion curve. The fitting results along with the results obtained from the envelope method are listed in Table 3.7 for the entire PZT solid solutions. The figures for the rest of compositions are presented in Appendex B as Figures B.25 – B.30.

3.6 Absorption Coefficients at Near Band Gap

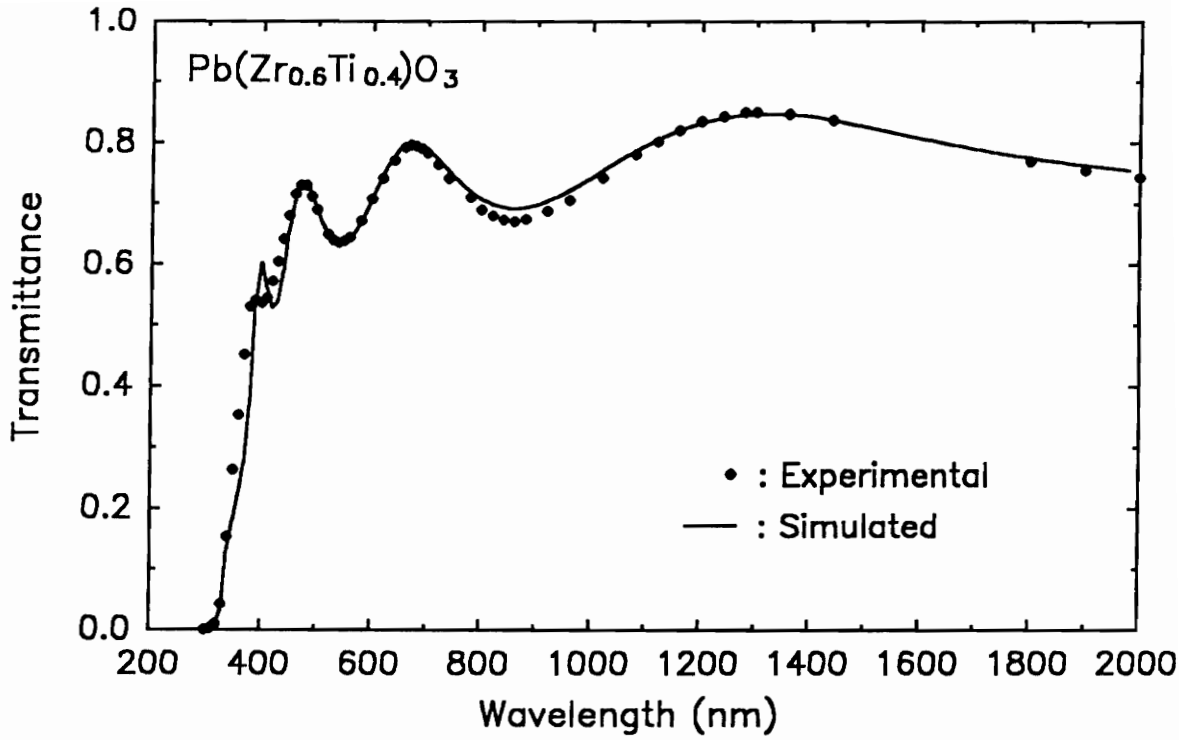

Figure 3.14 The experimental and simulated transmission spectra of $Pb(Zr_{0.6}Ti_{0.4})O_3$ film.

Table 3.7 Comparison of the film thickness of $Pb(Zr_xTi_{1-x})O_3$ thin films obtained from the envelope method with that from the simulation. The optical constants obtained from envelope method were used for film thickness simulation. The wavelength range of simulation is from 450 nm to 2000 nm. The least square fit error χ^2 is defined in equation 3.43.

Composition, x	0.0	0.2	0.4	0.5	0.6	0.8	1.0
Thickness, t (nm) (Envelope Method)	267	271	277	296	290	296	331
Thickness, t (nm) (Simulated)	268	272	280	300	295	301	331
χ^2 (10^{-5}) (Least square error)	7.96	3.22	2.71	2.62	6.21	11.8	24.6

Since the envelope method is invalid in the strong absorption region, the calculation of the absorption coefficients of the film needs both the transmission and reflection spectra. Figure 3.15 shows the absorption coefficients, calculated using equation 3.40, as a function of incident photon energy for the entire PZT solid solution range. As can be seen in Figure 3.15, at a given photon energy of the incident light, the absorption coefficient decreased with increasing zirconium content of the PZT film. The photon energy of the incident light as a function of composition is shown in Figure 3.16 at three different absorption coefficients, namely, α = 1.5 x 10^5, 1 x 10^5, and 5 x 10^4 cm^{-1}. For a given α, the photon energy increased with increasing zirconium content of the PZT film. For example, for α = 1.5 x 10^5 cm^{-1}, the value of the photo energy for $PbTiO_3$ was 3.7 eV, whereas $PbZrO_3$ had a value of 4.3 eV. In addition, these three curves were approximately parallel. Zametin [57] reported the band gap energies (E_g) for bulk $PbTiO_3$ and $PbZrO_3$ ceramics as 3.6 eV and 3.93 eV, respectively. The reported values (E_g) are very close to the present values which were 3.59 eV and 3.88 eV for α = 1 x 10^5 cm^{-1} for $PbTiO_3$ and $PbZrO_3$, respectively. The E_g values for PZT ceramics have not been reported to the best of my knowledge.

3.7 Surface Morphology

The SEM micrographs of the surface morphology of MOD PZT films are shown in Figure 3.17. The surface morphologies of the films at the zirconium–rich side are very different from those of the films at the titanium–rich side. Very large (diameters ranging from 5 μm to 35 μm) spheroidal grains with very fine grains occupying the space between the large grains were seen for the films at the

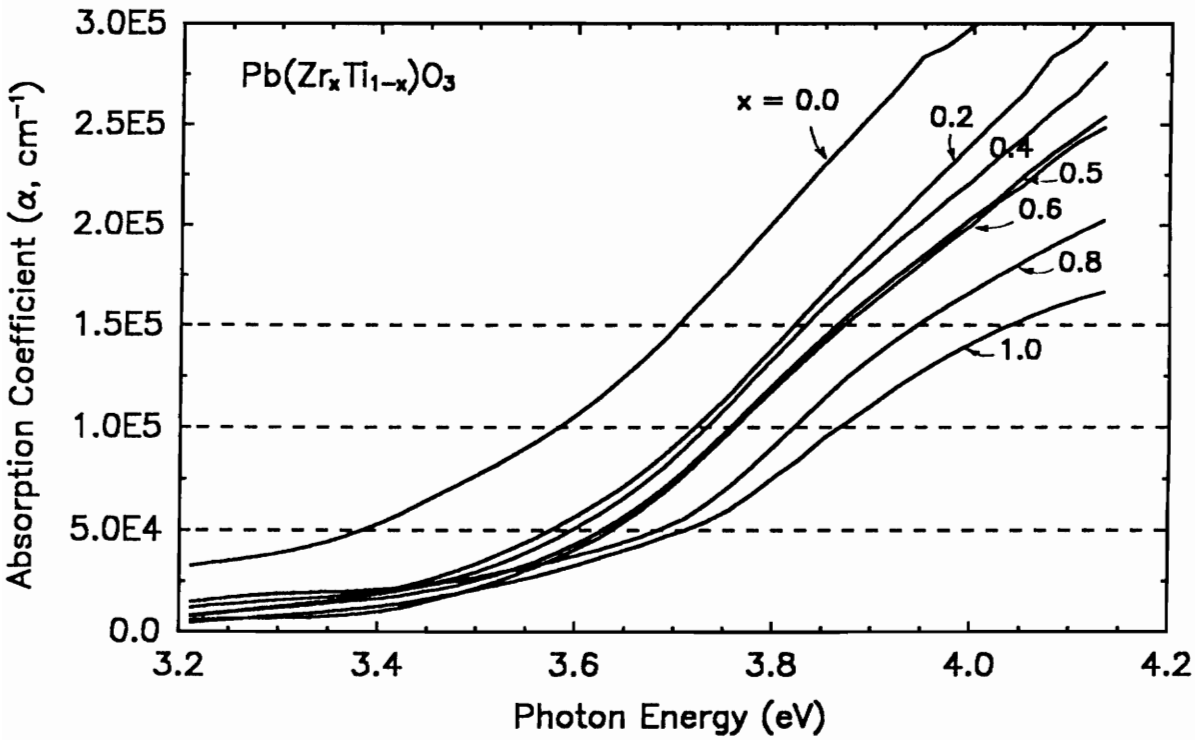

Figure 3.15 The absorption coefficients as a function of incident photon energy in the near band gap region for $Pb(Zr_xTi_{1-x})O_3$.

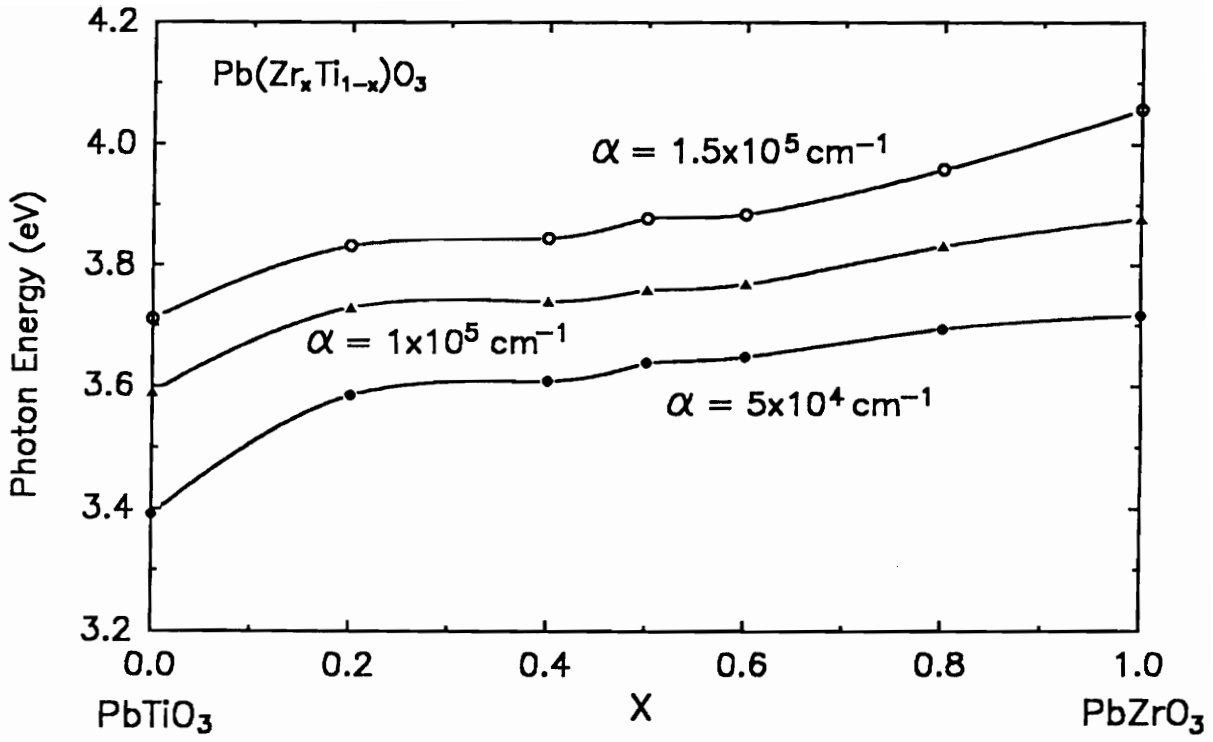

Figure 3.16 The incident photon energy as a function of composition at three different absorption coefficients.

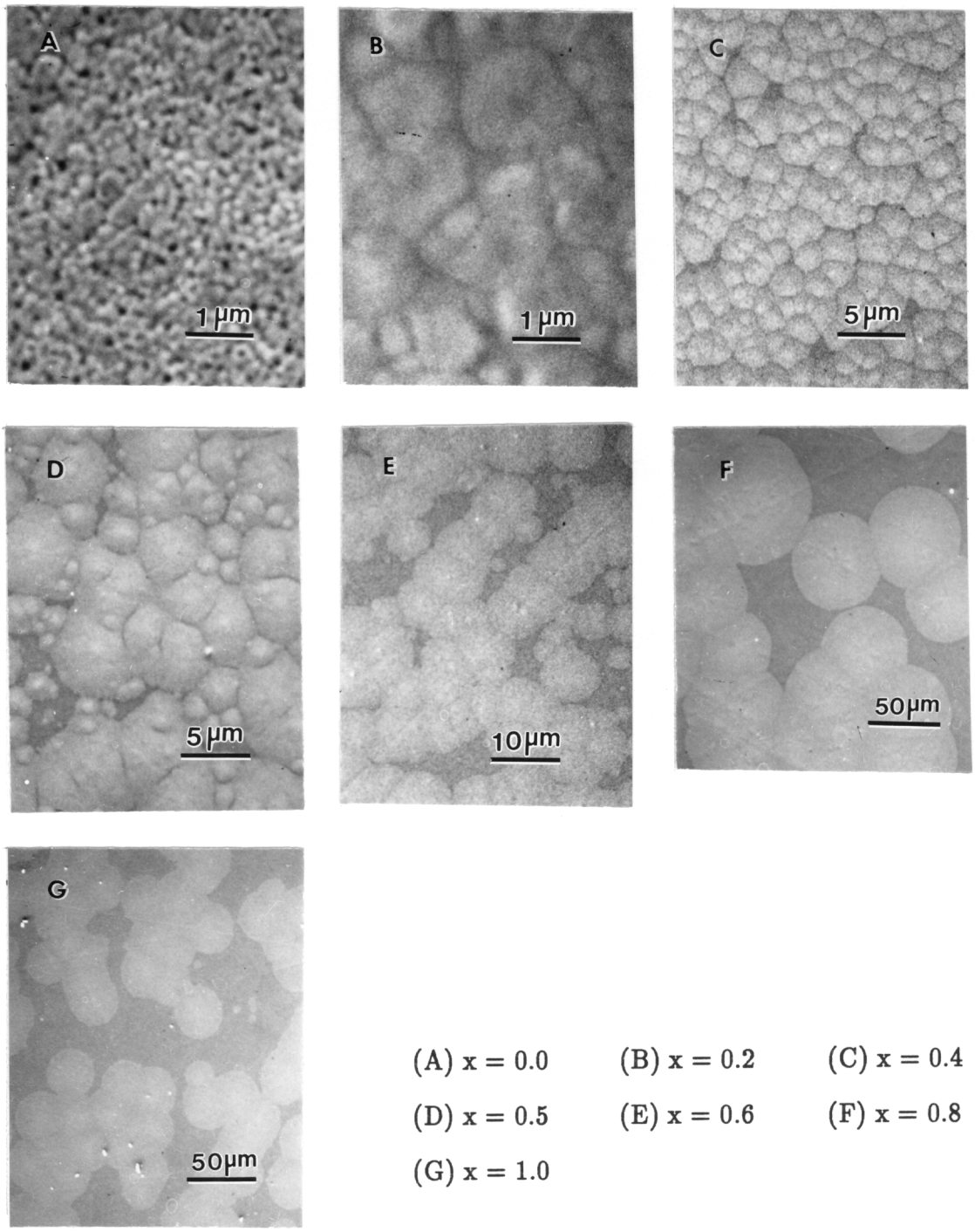

(A) x = 0.0 (B) x = 0.2 (C) x = 0.4

(D) x = 0.5 (E) x = 0.6 (F) x = 0.8

(G) x = 1.0

Figure 3.17 SEM micrographs of the surface morphology of MOD $Pb(Zr_xTi_{1-x})O_3$ films. The samples were annealed at 650^{0}C for 1 hour.

zirconium–rich side. These very large grains are believed to be the pure perovskite phase, while the the fine grains may be the residual pyrochlore phase [39,58]. On the other hand, the grains of the films at the titanium–rich side were well developed with the sizes ranging from 0.1 to 2 μm. The surface morphology and the average grain size of the films with x = 0.0 and 0.2 are very similar to those from the sputtering [59] and MOCVD [38] PZT films. The average grain size increased with increasing zirconium content in the film, as can be seen in Figure 3.18.

This observation of the microstructure dependence on the composition of the PZT film may indicate that the nucleation barrier for the film at the titanium–rich side is lower than that at the zirconium–rich side.

3.8 Summary

The optical properties (the refractive index, the extinction coefficient, and the absorption coefficient near the band gap) and the thickness of the PZT thin films were studied. The envelope method, accompanied with the consideration of the light intensity loss from the back surface of the substrate, was shown to be a simple and convenient tool for obtaining the optical properties and the film thickness of the PZT films by using the transmission spectra alone in the medium and weak absorption regions. In the near optical band gap region, both the transmission and the reflection spectra were used to successfully calculate the optical constants of the films. The film thickness derived from the envelope method was cross checked by a computer simulation method. In addition, the refractive indices were fitted to a simple Sellmeier type equation for determining the dispersion constants for both porous PZT films and bulk PZT materials. The valid wavelength range of these

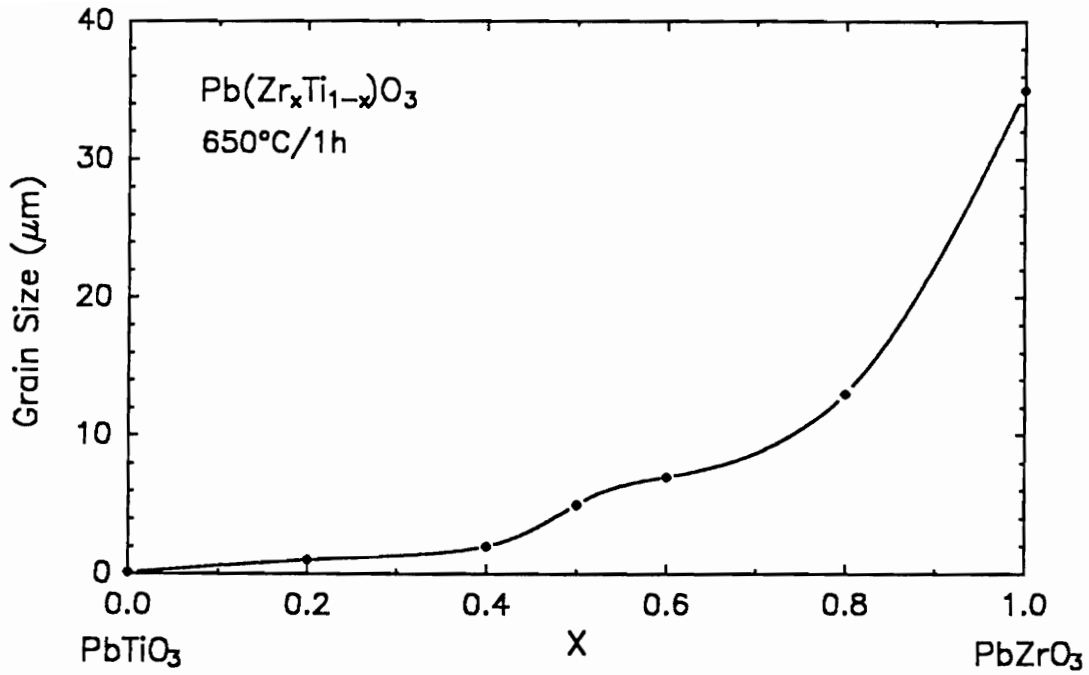

Figure 3.18 Average grain size of $Pb(Zr_xTi_{1-x})O_3$ films as a function of composition. The samples were annealed at 650°C for 1 hour.

dispersion relations was from 350 nm to 2000 nm. A flow chart for the entire calculation procedure for this study is illustrated in Figure 3.19.

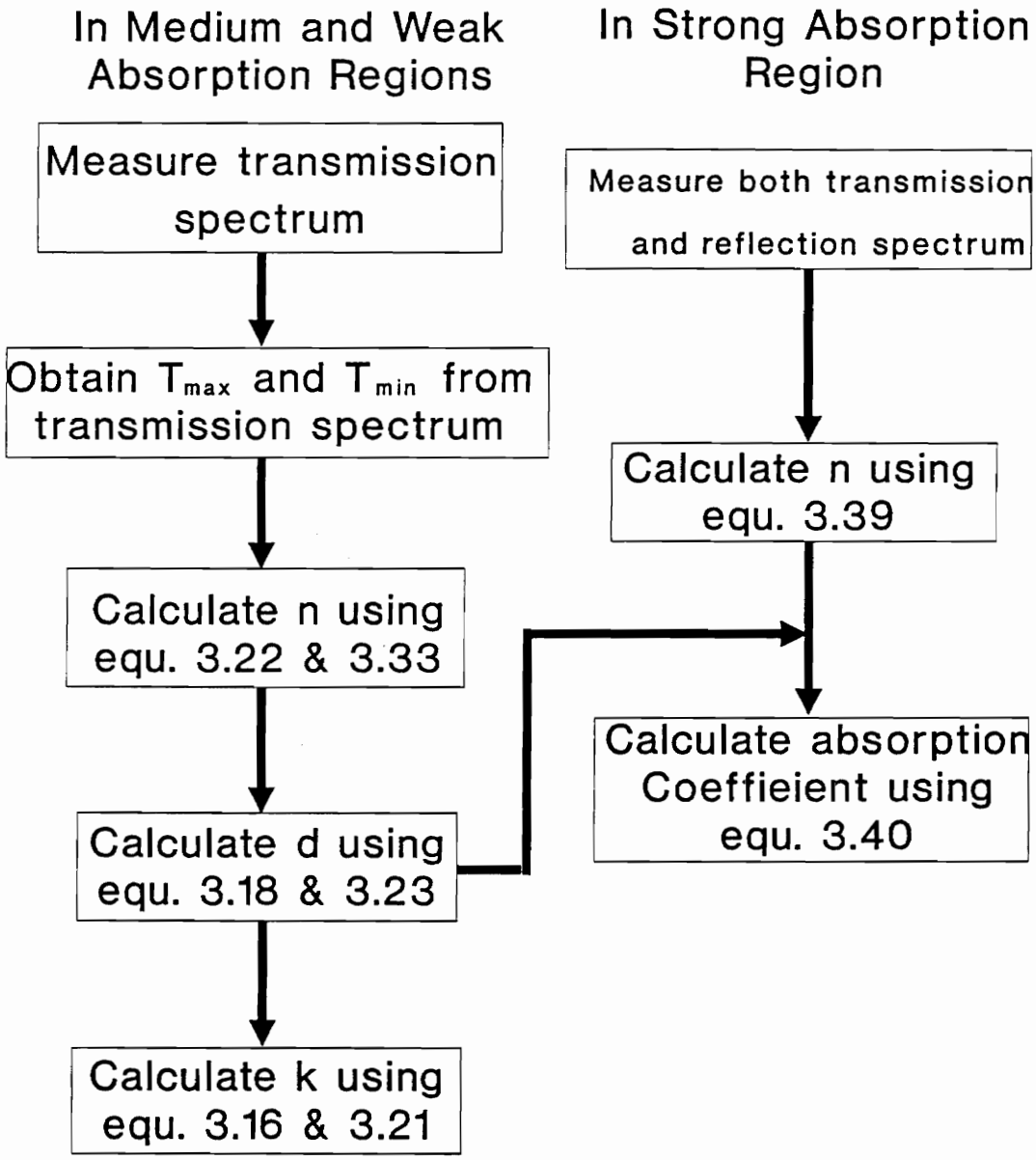

Figure 3.19 A flow chart for calculation the optical constants and the film thickness of a single layer film on a transparent substrate.

Chapter 4 Structure Development Study of PZT Thin Films by an Optical Method

4.1 Introduction

Reaction mechanisms of PZT bulk materials, prepared by sintering the mixed oxide powders, have been extensively studied [60–63]. $PbTiO_3$ forms first from the PbO–ZrO_2–TiO_2 system in the temperature range of 450°C to 600°C [63]. Single phase PZT was observed at temperatures around 785°C but no $PbZrO_3$ phase was observed [62]. Therefore, Chandratreya et al [62] concluded that $PbTiO_3$ was formed at lower temperatures which subsquently reacted with ZrO_2 to form PZT bulk material. However, in the case of sputtered PZT thin films, amorphous PZT phase was reported to transform to a metastable pyrochlore phase at temperatures as low as 350°C and finally formed the perovskite phase at temperatures higher than 500°C [64]. It was anticipated that the results of the phase transformation study for PZT bulk materials would be very different from those for the PZT thin films. The difference may be due mainly to the short diffusion distance in the thin films compared to that of the bulk materials.

For a typical MOD process, an amorphous PZT phase is observed at temperatures around 300°C. As the annealing temperature is increased, the films transform from the amorphous phase to the pyrochlore phase and then finally to the

perovskite phase [65]. The pyrochlore phase has the chemical formula $A_2B_2O_6$ and has a cubic structure. However, the perovskite phase has the chemical formula ABO_3 and can exhibit tetragonal, rhombohedral, or orthorhombic structure depending on the Zr/Ti ratio. Both the amorphous phase and the pyrochlore phase do not display ferroelectric properties. In order to obtain the useful perovskite phase, most often, annealing temperatures above 550^0C are required, again, depending on the Zr/Ti ratio.

Several device applications require processes which form the perovskite phase at low temperatures. Understanding the various aspects of structure development in MOD PZT films is the key for developing such low temperature processes. A nondestructive optical method for characterizing the various phase transformations in MOD PZT films is proposed. The effectiveness of this technique (1) in identifying various characteristic temperatures will be shown and (2) the kinetics of phase transformations in PZT films will be studied.

Even though the composition of the amorphous, pyrochlore and perovskite phase may be similar [58], they are expected to have different refractive indices since they have different structures. Therefore, by following the refractive index of the film as a function of annealing temperature one can obtain information on structure development. By noting the changes in the refractive index, the initiation and completion temperatures of a new phase from the existing one can be identified. In addition, by using the effective medium approximation (section 3.2.4), the concentration of each phase as a function of time or temperature (i.e., phase transformation kinetics) can also be obtained.

The sample preparations and the transmission spectrum measurements have been described in Chapter 2.

4.2 Models of Structure Development of PZT Thin Films

The structure development of MOD PZT films from the initial as–deposited state to the final perovskite phase involves phase transformations of four different phases, namely, metalorganic compounds (MO), the amorphous phase (A), the pyrochlore PZT phase (Py), and the perovskite PZT phase (Pe). There are many possible ways for the initial metalorganic compounds to transform into the final perovskite phase through the amorphous and the pyrochlore phases. Two extreme cases are presented in Figures 4.1 and 4.2 to illustrate the complexity of the structure development in MOD PZT films involving these four different phases. The simplest case which will be referred to as model A hereafter is shown in Figure 4.1, while the most complicated case which will be referred to as model B hereafter is presented in Figure 4.2. Also, one example of the possible cases which are in between the model A and model B is given in Figure 4.3 and this case will be referred to as model C.

In model A, the film is assumed to have four single phase regions at four certain annealing temperature intervals and three two phases mixtures in between. In other words, no more than two phases can exist at any temperature. After the solvent removal, the film can be represented by one or a mixture of metalorganic compounds. As the temperature is increased at T_i^A the amorphous PZT phase is formed. At the temperature T_c^A the MO is completely converted into amorphous phase. In other words, the formation of amorphous phase is completed at T_c^A. Similarly, T_i^{Py} and T_i^{Pe} represent, respectively, the temperatures at which the pyrochlore and the perovskite formation is initiated. Likewise, T_c^{Py} and T_c^{Pe} are the temperature at which the formation of pyrochlore and perovskite is completed,

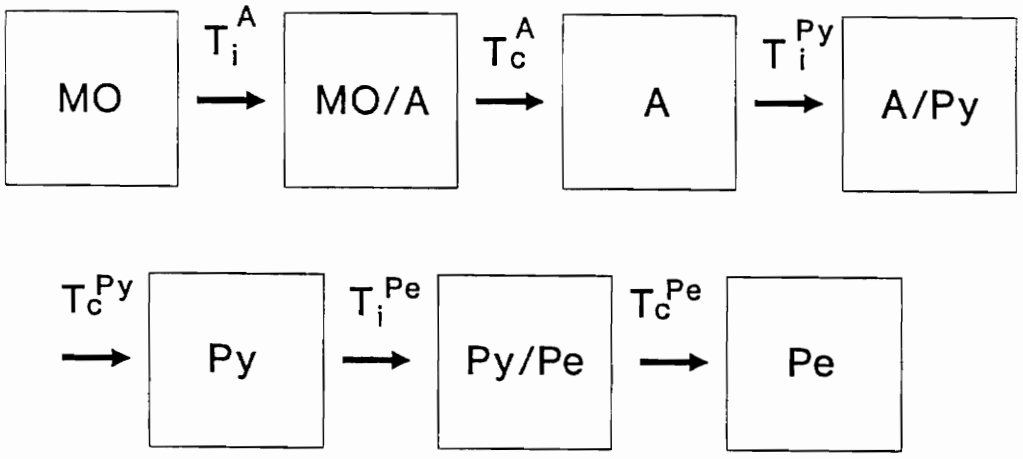

Figure 4.1 Model A: the simplest hypothetical model for the structure development in MOD PZT thin films.

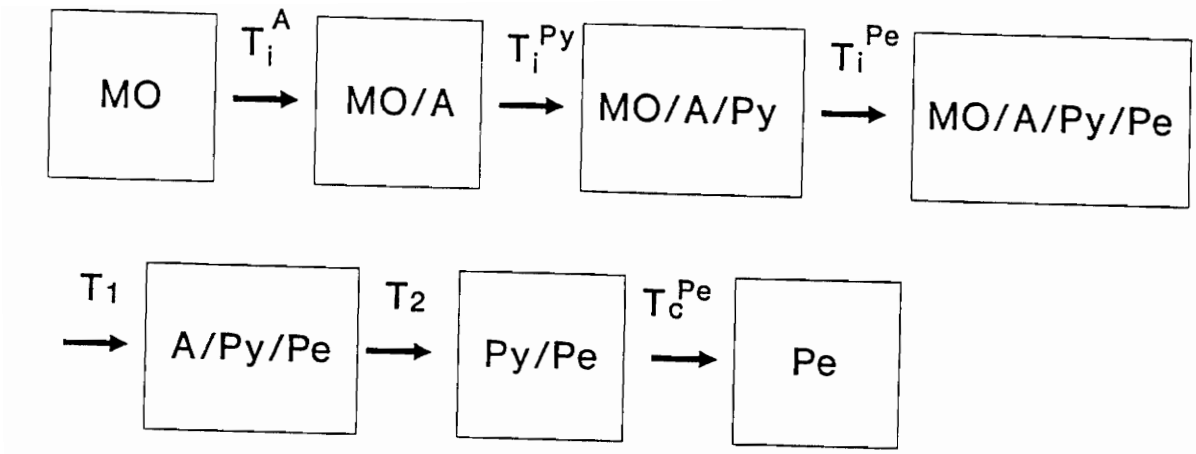

Figure 4.2 Model B: the most complicated hypothetical model for the structure development in MOD PZT thin films.

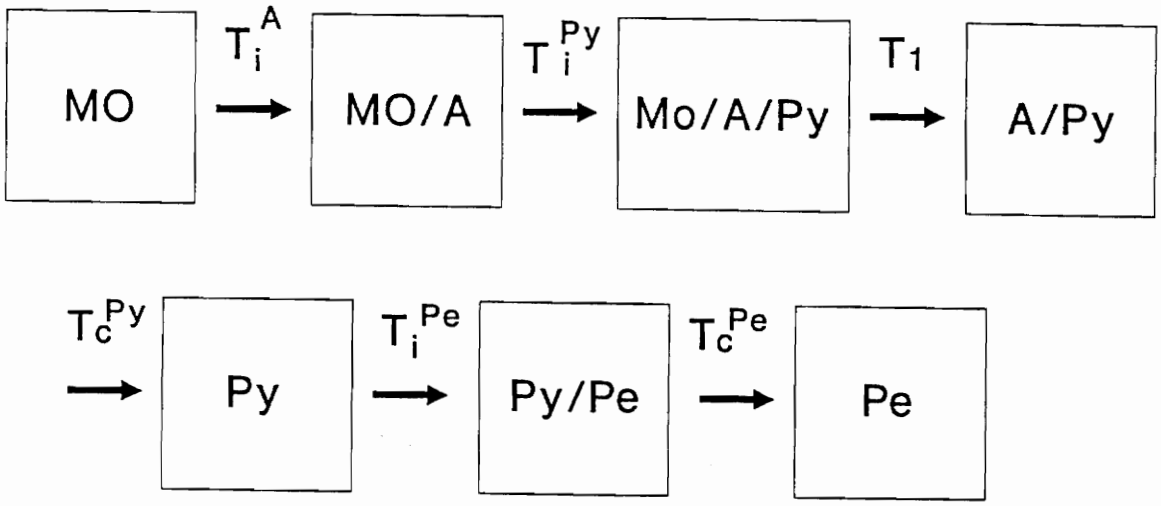

Figure 4.3 Model C: an example of the hypothetical models between model A and model B for the structure development in MOD PZT thin film.

respectively.

According to this simple model, two phase mixtures of MO/A, A/Py, and Py/Pe are presented in the temperature intervals T_i^A to T_c^A, T_i^{Py} to T_c^{Py}, and T_i^{Pe} to T_c^{Pe}, respectively. In other words, it should be possible to identify these six characteristic temperatures. In this simple model, not only can the characteristic temperatures be identified, but also information on the phase transformation kinetics of each two phase mixture can be obtained.

For model B, a maximum of four phases can exist in a certain temperature range. Similar to the early development stage of model A, the film is represented by a mixture of metalorganic compounds after the solvent removal and the amorphous phase is formed as the temperature is increased at T_i^A. However, unlike model A, before the metalorganic compounds are completely converted into the amorphous phase, the pyrochlore phase has started forming at temperature T_i^{Py}. In other words, it is not possible to define the T_c^A. Similarly, the perovskite phase is initiated at the temperature T_i^{Pe} before the metalorganic compounds are completely decomposed. As the temperature is increased, the metalorganic compounds and the amorphous phase completely disappear at temperatures T_1 and T_2, respectively. The temperatures T_1 and T_2 are used only for the purpose of convenience and have no meaningful definitions. Finally, the perovskite phase is completely formed at the temperature T_c^{Pe}.

Based on model B, only two single phases, i.e. metalorganic compounds and perovskite phase, can exist in a certain temperature interval during the whole structure developments. Two phase mixtures of MO/A and Py/Pe are present in the temperature intervals T_i^A to T_i^{Py} and T_2 to T_c^{Pe}, respectively. Three phase mixtures of MO/A/Py and A/Py/Pe are present in the temperature intervals T_i^{Py}

to T_i^{Pe} and T_1 to T_2, respectively, and a four phase mixture of MO/A/Py/Pe is present in the temperature interval T_i^{Pe} to T_1.

For model C, as shown in Figure 4.3, the pyrochlore phase can exist in a certain temperature range, while the amorphous phase cannot. In this example, the pyrochlore phase has started forming before the metalorganic compounds are completely transformed to the amorphous phase. In other words, as can be seen in Figure 4.3, the entire phase transformation route is a combination of the first three steps of the model B and the last four steps of the model A.

4.3 Structure Development in MOD PZT Thin Films

4.3.1 X–ray Diffraction Study

As mentioned in the previous section, the structure development of MOD PZT thin films involves four different phases. Among these four phases, the pyrochlore phase and the perovskite phase are the crystalline phases. Therefore, the temperatures at which the perovskite phase is initiated (T_i^{Pe}) and completed (T_c^{Pe}) can be determined by an x–ray diffraction study.

Figure 4.4 shows the selected XRD patterns of the $Pb(Zr_{0.5}Ti_{0.5})O_3$ thin film in the temperature range from 460°C to 620°C. The major XRD peaks of pyrochlore (222) and perovskite (111) are at $2\theta = 29.5^0$ and 31^0, respectively. As can be seen in Figure 4.4, the T_i^{Pe} can be determined in the temperature range from 520°C to 540°C, whereas the T_c^{Pe} is in the temperature range from 600°C to 620°C. The T_i^{Pe}s and T_c^{Pe}s of the entire PZT solid solution are summarized in Figure 4.5. Both T_i^{Pe} and T_c^{Pe} increase with increasing Zr concentration in the film. For

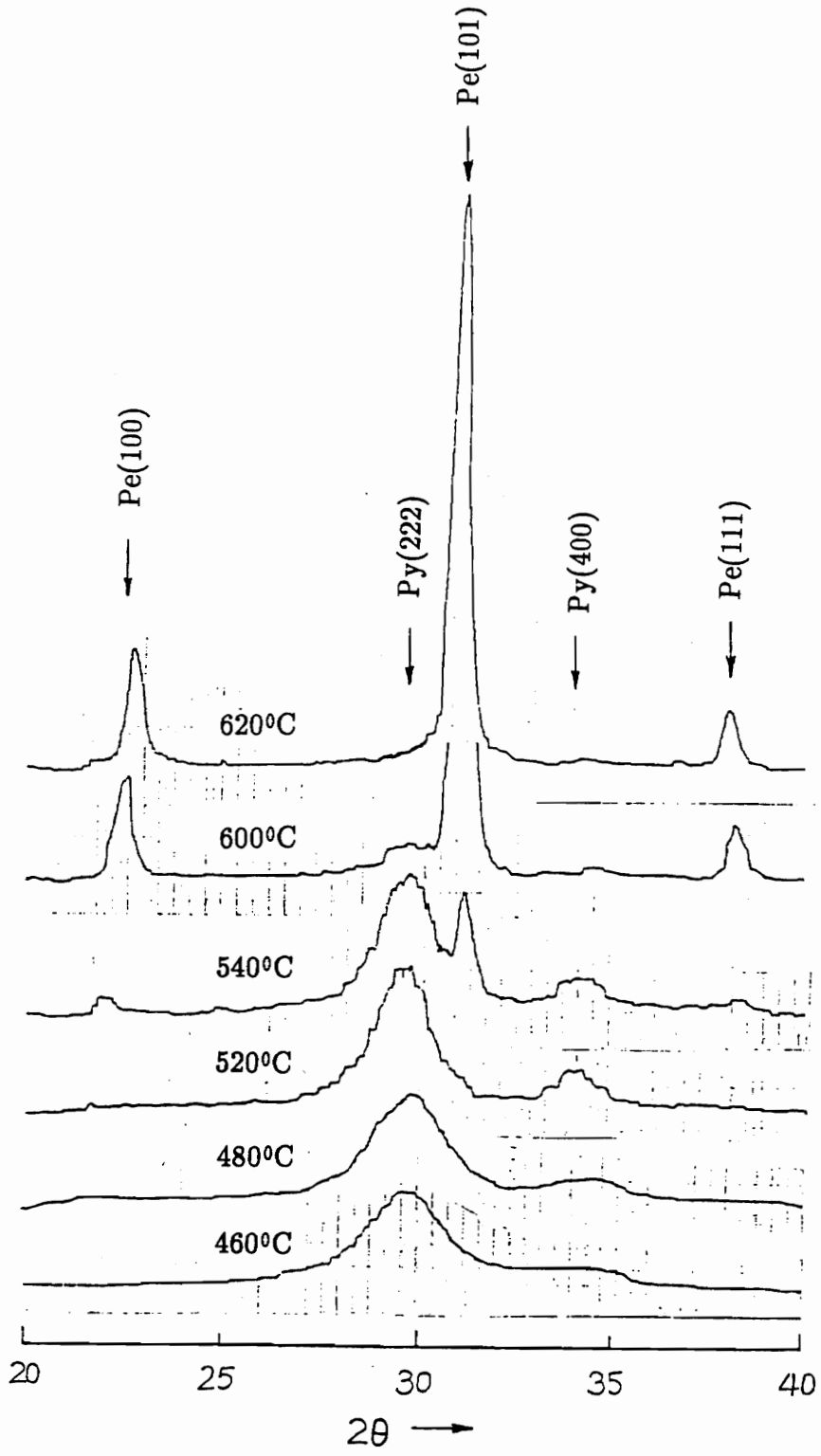

Figure 4.4 XRD patterns of the MOD $Pb(Zr_{0.5}Ti_{0.5})O_3$ film for the annealing temperatures ranging from 460°C to 620°C for 30 min at each temperature.

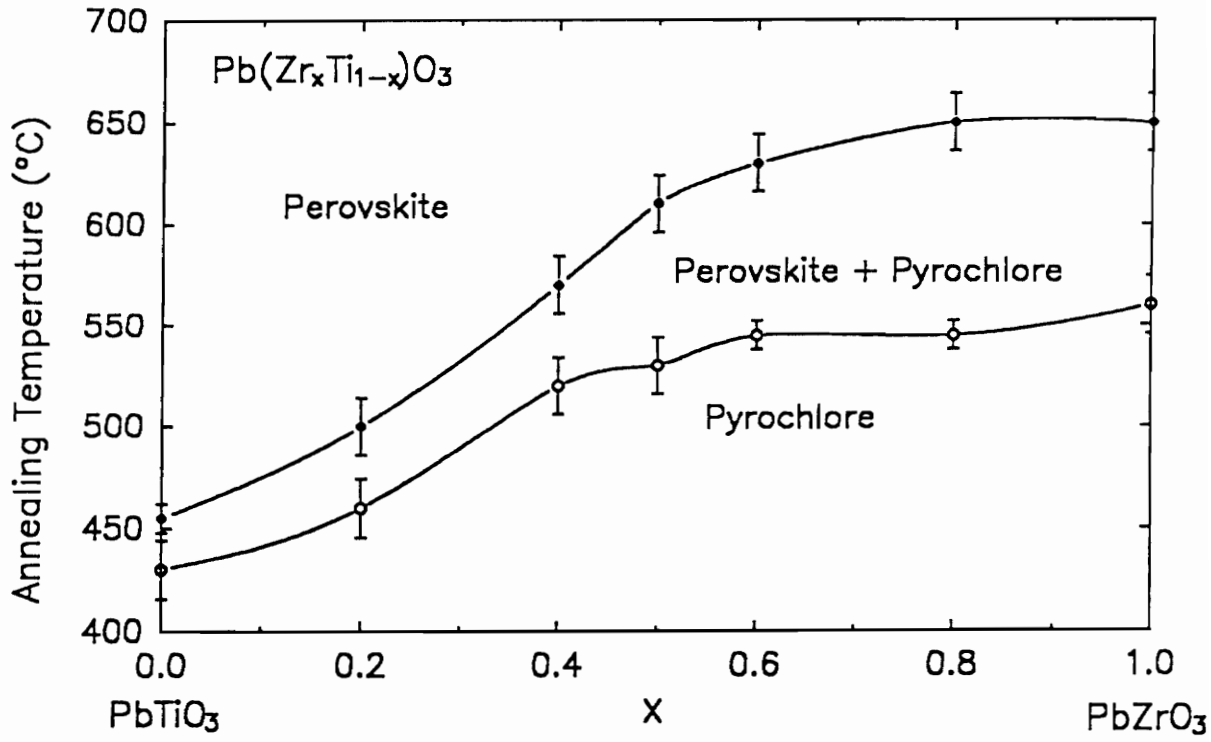

Figure 4.5 Initiation and completion temperature of the perovskite phase as a function of composition in the $Pb(Zr_xTi_{1-x})O_3$ films.

example, the temperatures where the formation of the perovskite phase is completed are around 460°C and 650°C for $PbTiO_3$ and $PbZrO_3$, respectively. In addition, the higher the Zr concentration, the wider the phase transformation temperature range, as can be seen in Figure 4.5. In other words, the pyrochlore–perovskite transformation is initiated at lower temperature and completed faster for the films on the titanium rich side than those on the zirconium rich side.

4.3.2 Optical Method

The optical properties and thickness of the films were derived by using the envelope method as described in Chapter 3 from the transmission spectra only. For the structure development study, only the envelope values (T_{max} and T_{min}) at extremes and $\lambda = 632.8$ nm were used.

The refractive index (at $\lambda = 632.8$ nm) and film thickness as a function of annealing temperature for MOD $Pb(Zr_xTi_{1-x})O_3$ films across the entire solid solution, i.e., from x = 0.0 to x =1.0, are shown in Figures 4.6 – 4.12. The refractive indices are represented as open circles, while the thickness values are the filled circles. Based on the shape of the refractive index curve, these PZT films are classified into two groups: (1) x = 0.0 and 0.2 and (2) x = 0.4 – 1.0.

At a first glance (Figures 4.6 and 4.7), the refractive indices of the first group have the lowest value of 2.04 for $PbTiO_3$ and 2.08 for $Pb(Zr_{0.2}Ti_{0.8})O_3$ in the temperature range from 150°C to 250°C, the highest value of 2.29 for $PbTiO_3$ and 2.47 for $Pb(Zr_{0.2}Ti_{0.8})O_3$ in the temperature range from around 520°C to 700°C, and intermediate values at temperatures between these two ranges. For the second group, the refractive index curves behave much different than those in the first

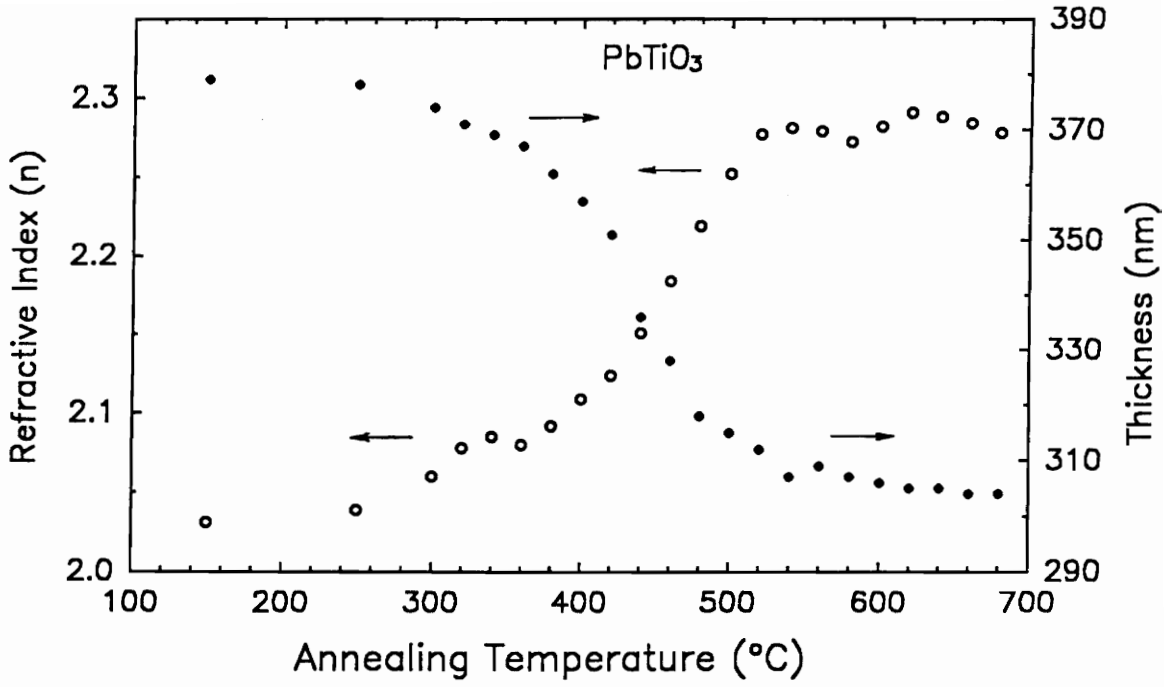

Figure 4.6 Refractive index (at λ = 632.8 nm) and film thickness as a function of annealing temperature for MOD $PbTiO_3$ film.

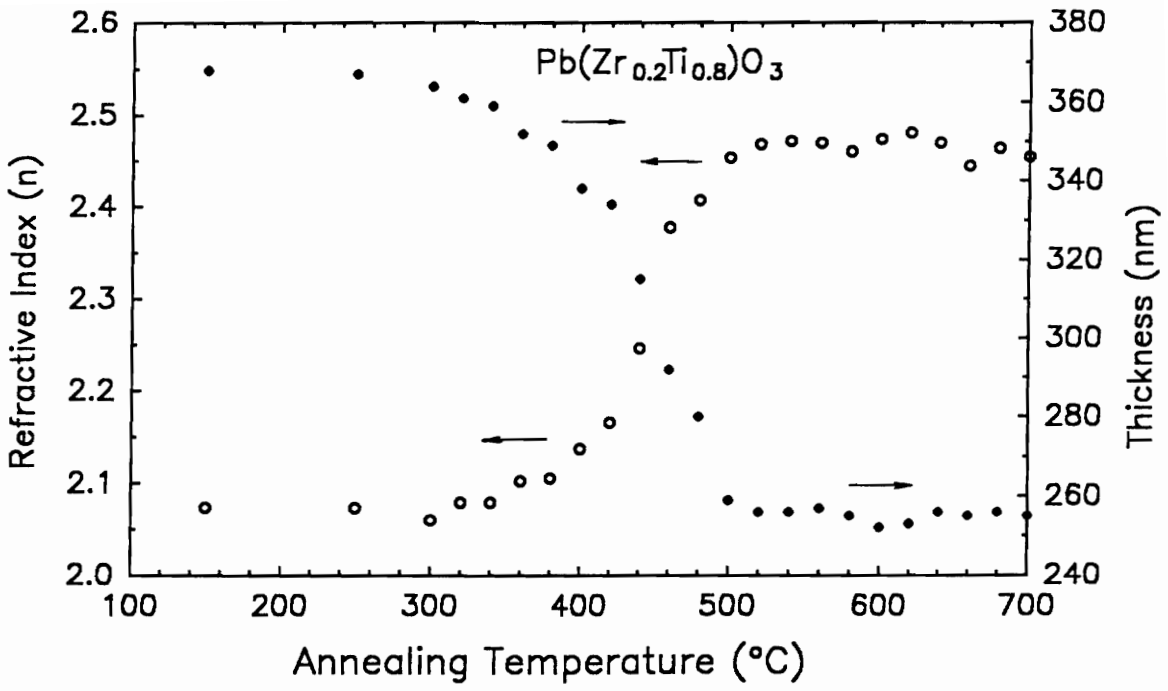

Figure 4.7 Refractive index (at λ = 632.8 nm) and film thickness as a function of annealing temperature for MOD $Pb(Zr_{0.2}Ti_{0.8})O_3$ film.

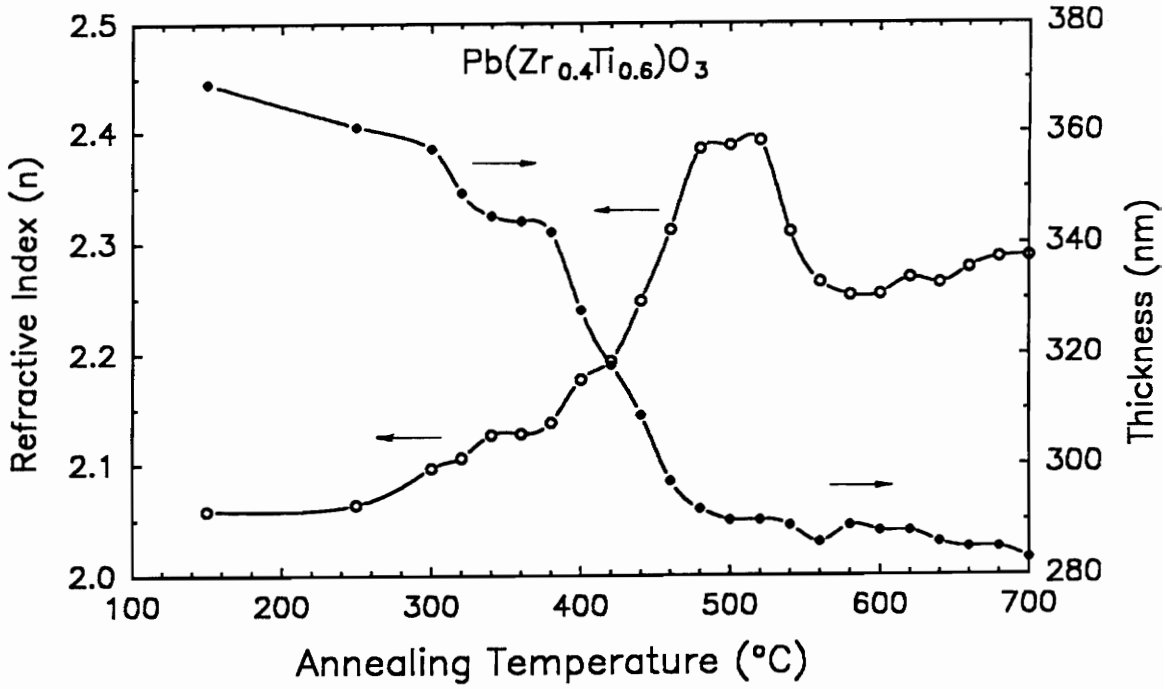

Figure 4.8 Refractive index (at λ = 632.8 nm) and film thickness as a function of annealing temperature for MOD $Pb(Zr_{0.4}Ti_{0.6})O_3$ film.

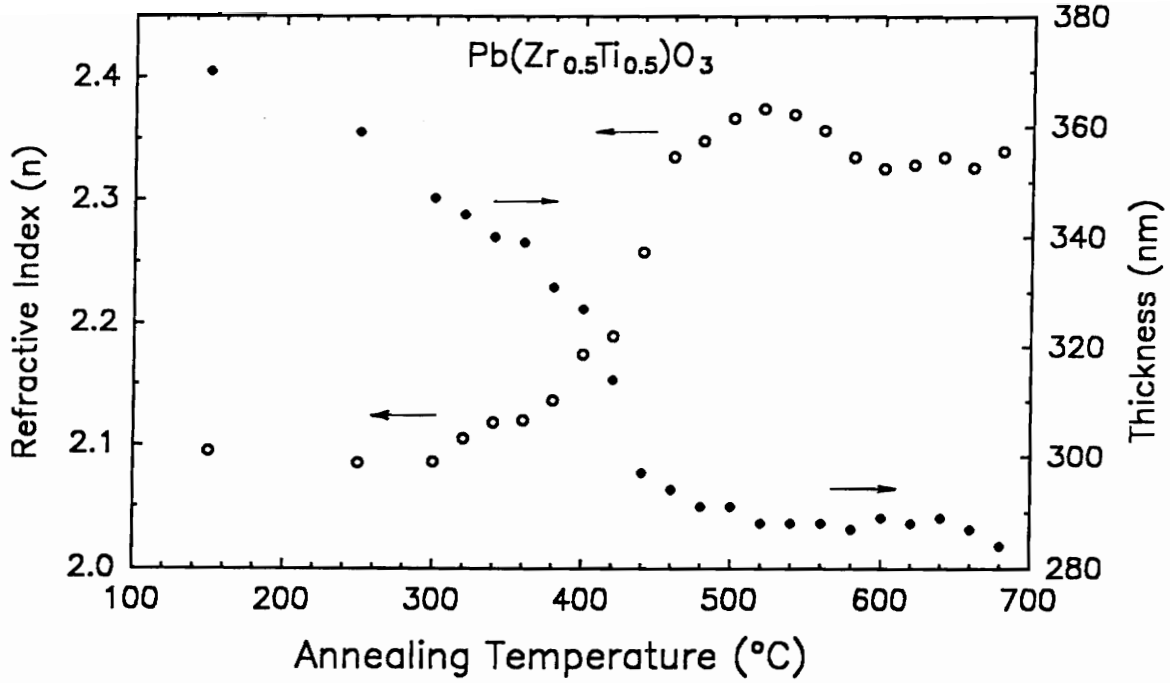

Figure 4.9 Refractive index (at λ = 632.8 nm) and film thickness as a function of annealing temperature for MOD $Pb(Zr_{0.5}Ti_{0.5})O_3$ film.

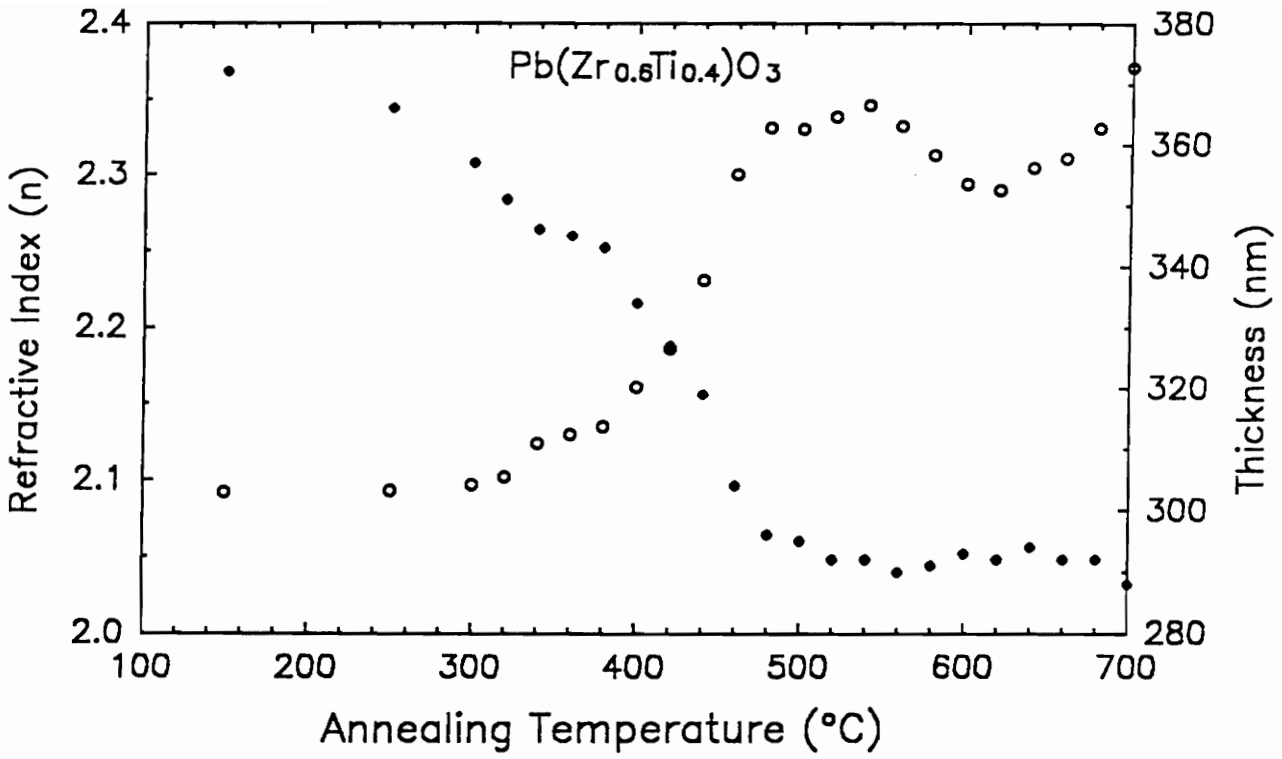

Figure 4.10 Refractive index (at $\lambda = 632.8$ nm) and film thickness as a function of annealing temperature for MOD $Pb(Zr_{0.6}Ti_{0.4})O_3$ film.

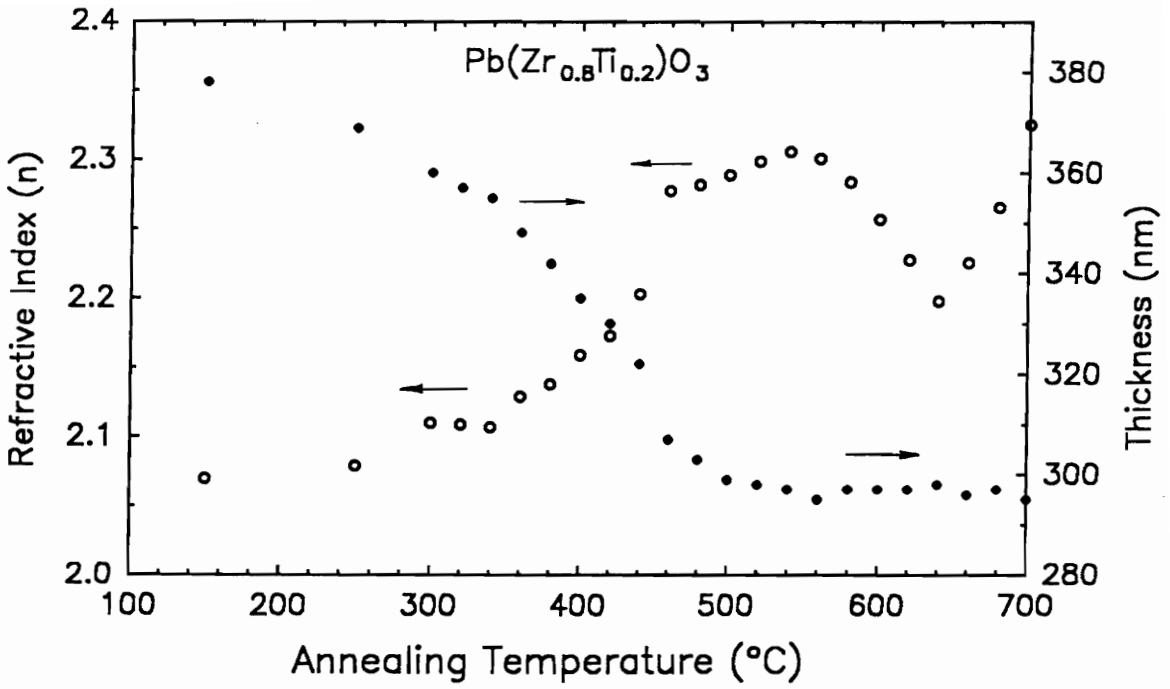

Figure 4.11 Refractive index (at $\lambda = 632.8$ nm) and film thickness as a function of annealing temperature for MOD $Pb(Zr_{0.8}Ti_{0.2})O_3$ film.

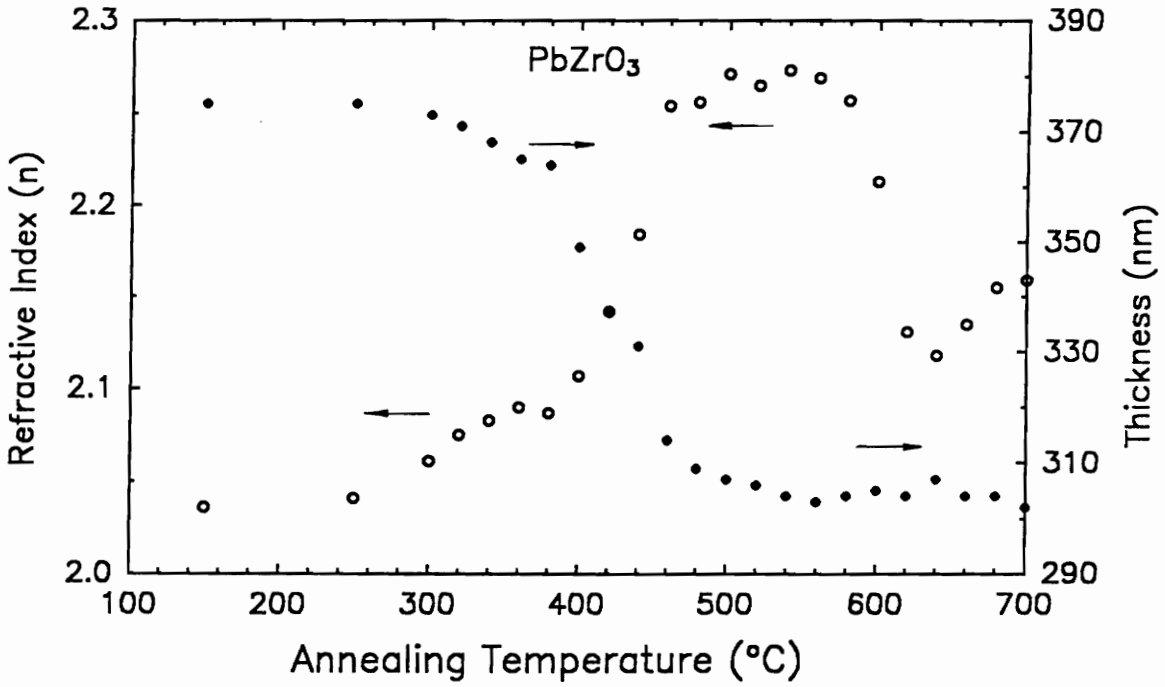

Figure 4.12 Refractive index (at $\lambda = 632.8$ nm) and film thickness as a function of annealing temperature for MOD $PbZrO_3$ film.

group. As can be seen in Figures 4.8 – 4.12, the refractive index curves display a "flat top", which is not shown in the first group, at temperatures around 500°C. The "flat tops" are not quite flat. This may be due to an increase in the packing density of the film as the temperature is increased which causes an increase in the refractive index according to the effective medium approximation (EMA).

For the convenience of discussion, start from the group 2 and take the case of $Pb(Zr_{0.4}Ti_{0.6})O_3$ as an example. As can be seen from Figure 4.8, the refractive index curve can be divided into five regions in terms of temperature range, i.e.,

(1) from 150°C to 250°C: the indices have a minimum and constant value of 2.06

(2) from 250°C to 480°C: the indices increase to a maximum value of 2.39 at 480°C

(3) from 480°C to 520°C: the indices show a "flat top"

(4) from 520°C to 580°C: the indices drop steeply to a value of 2.25 at 580°C

(5) from 580°C to 700°C: the indices increase slightly to a value of 2.29 at 700°C

From the results of the XRD study as discussed in section 4.3.1, it is known the perovskite phase is initiated at around 520°C and completed at the temperature range from 560°C to 580°C for the $Pb(Zr_{0.4}Ti_{0.6})O_3$ thin film. In addition, Kwok [58] has observed a pure pyrochlore phase at a temperature around 500°C by XRD study. From the above observation, along with the XRD results, four characteristic temperatures can be easily picked, i.e., 250°C, 480°C, 520°C, 580°C; They are assigned to be T_i^A, T_c^{Py},T_i^{Pe}, and T_c^{Pe}, respectively. It should noted that the characteristic temperatures: T_i^A and T_c^{Py} cannot be easily identified from x–ray

diffraction studies because of the involvement of amorphous phase and due to the fine grain size of the pyrochlore phase. Among these four temperatures, T_c^{Py},T_i^{Pe}, and T_c^{Pe} are most important. They are tabulated in Table 4.1. It is clear that the structure development in this example is not the case of either model A or model B.

Some fine structure in the refractive index curve in Figure 4.8 may be observed in the temperature range of 250°C to 480°C. In this temperature region, it is believed that the structure development involves the phase transformations of three different phases, namely, the metalorganic compounds, the amorphous phase, and the pyrochlore phase. The n values increase as the temperature is increased with two break points at 340°C and 400°C. This may be interpreted as the decomposition of the metalorganic compounds occurring in the temperature range of 250°C to 400°C. An independent study [39] of the same precursor solution, by using thermal gravimetric analysis (TGA), showed that the PZT solution decomposed slowly in the temperature range from 200°C to 400°C which agrees well with the present observation. Therefore, the structure developments which occur in the group 2 PZT films are best represented by the proposed model C.

The variation of the film thickness with the annealing temperature for $Pb(Zr_{0.4}Ti_{0.6})O_3$ is also shown in Figure 4.8. The thickness variation curve shows a less complicated feature than the refractive index curve. As expected, the thickness of the as–deposited film has the thickest value of 370 nm. The most noticeable change in thickness occurs in the temperature range from 380°C to 480°C. This indicates that a significant density change takes place in this temperature range. This large thickness change is believed to be due to the phase transformation of the amorphous material to the pyrochlore phase. As the temperature was increased up to 700°C, the thickness decreased slightly from a value of 290 nm at 480°C to a

Table 4.1 The values of T_c^{Py}, T_i^{Pe}, and T_c^{Pe} determined by the optical method for MOD $Pb(Zr_xTi_{1-x})O_3$ thin films.

x	0.0	0.2	0.4	0.5	0.6	0.8	1.0
T_c^{Py}	—	—	480	460	480	460	460
T_i^{Pe}	—	—	520	520	540	540	540
T_c^{Pe}	—	—	580	600	620	640	640

value of 284 nm at 700^{0}C.

Now, coming back to the MOD PZT films in group 1, recall the refractive index and film thickness as a function of annealing temperature shown in Figures 4.6 and 4.7. From the XRD results, notice that the formation of the perovskite phase is completed at a temperature around 460^{0}C for the $PbTiO_3$ film as can be seen in Figure 4.5. In addition, it was found that the pyrochlore phase has a higher refractive index than the perovskite phase for the PZT materials. However, for both $PbTiO_3$ and $Pb(Zr_{0.2}Ti_{0.8})O_3$ films, the refractive indices keep increasing as the temperature is increased up to a temperature around 520^{0}C. This increase in refractive index above the perovskite completion temperatures may be interpreted as an effect of the densification of the film. On the other hand, no "flat top" was observed which characterizes the pyrochlore phase in the intermediate temperature range. With the help of the XRD results, the lack of a visible flat top may be due to the very narrow temperature range between T_i^{Pe} and T_c^{Pe} which are 430^{0}C and 460^{0}C, respectively, for the $PbTiO_3$ film. By comparing the above observation with the proposed models as described in section 4.2, it is believed that the structure development in the MOD PZT films of group 1 may be described by model B. In other words, a very complicated phase transformation involving a mixture of all four different phases takes place between the temperatures T_i^{Pe} and T_c^{Pe}.

4.3.3 Pyrochlore–Perovskite Phase Transformation

Although the above proposed optical method is an indirect method for studying the structure development in MOD PZT films, one of the advantages of this method is that the refractive index values in the temperature range from T_i^{Pe} to T_c^{Pe} can

be used to calculate the volume fraction of the perovskite phase by using the effective medium approximation. However, to take this advantage, one has to be able to identify T_i^{Pe} and T_c^{Pe} from the refractive index curve. Therefore, only the films in group 2 can be used and their T_i^{Pe} and T_c^{Pe} have been listed in Table 4.1.

As mentioned in Chapter 3, the porosity also needs to be considered as a separate phase in the effective medium approximation. For a single phase region, porosity can be easily obtained by comparing the experimental value of the refractive index with that of the literature value of the bulk material. Porosity values of the single phases can be included in the analysis of the two–phase region. Due to the lack of literature data for the refractive index of the pyrochlore phase, we have assumed that the porosity in these films (1) remains unchanged in the temperature range from T_i^{Pe} to T_c^{Pe} and (2) is the same as that of the perovskite phase with the same composition.

The volume fraction of the perovskite phase was plotted as a function of temperature in Figure 4.13 for the PZT films with $x = 0.4 - 1.0$. If the sample were studied as a function of time at several temperatures, the phase transformation kinetics could have been obtained.

4.3.4 Surface Morphology

The SEM micrographs of the surface morphology are shown in Figure 4.14 for the films with $x = 0.0 - 1.0$. These SEM pictures were taken from the samples which had suffered through 23 heat treatments at an annealing temperature in the range from 150^{0}C to 700^{0}C for 30 min at each annealing temperature. The surface morphologies of these films were similar to those shown in Figure 3.17. That is,

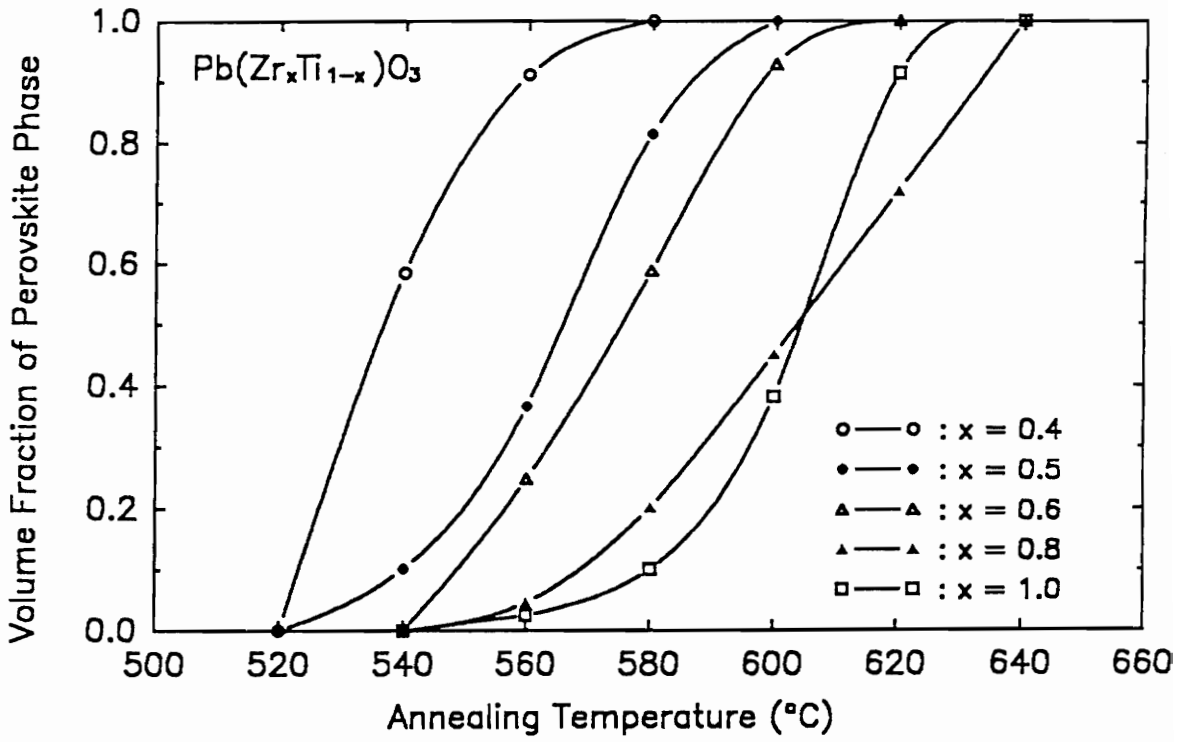

Figure 4.13 The volume fraction of the perovskite phase as a function of annealing temperature in MOD $Pb(Zr_xTi_{1-x})O_3$ films, which was derived from the refractive index by using the effective medium approximation.

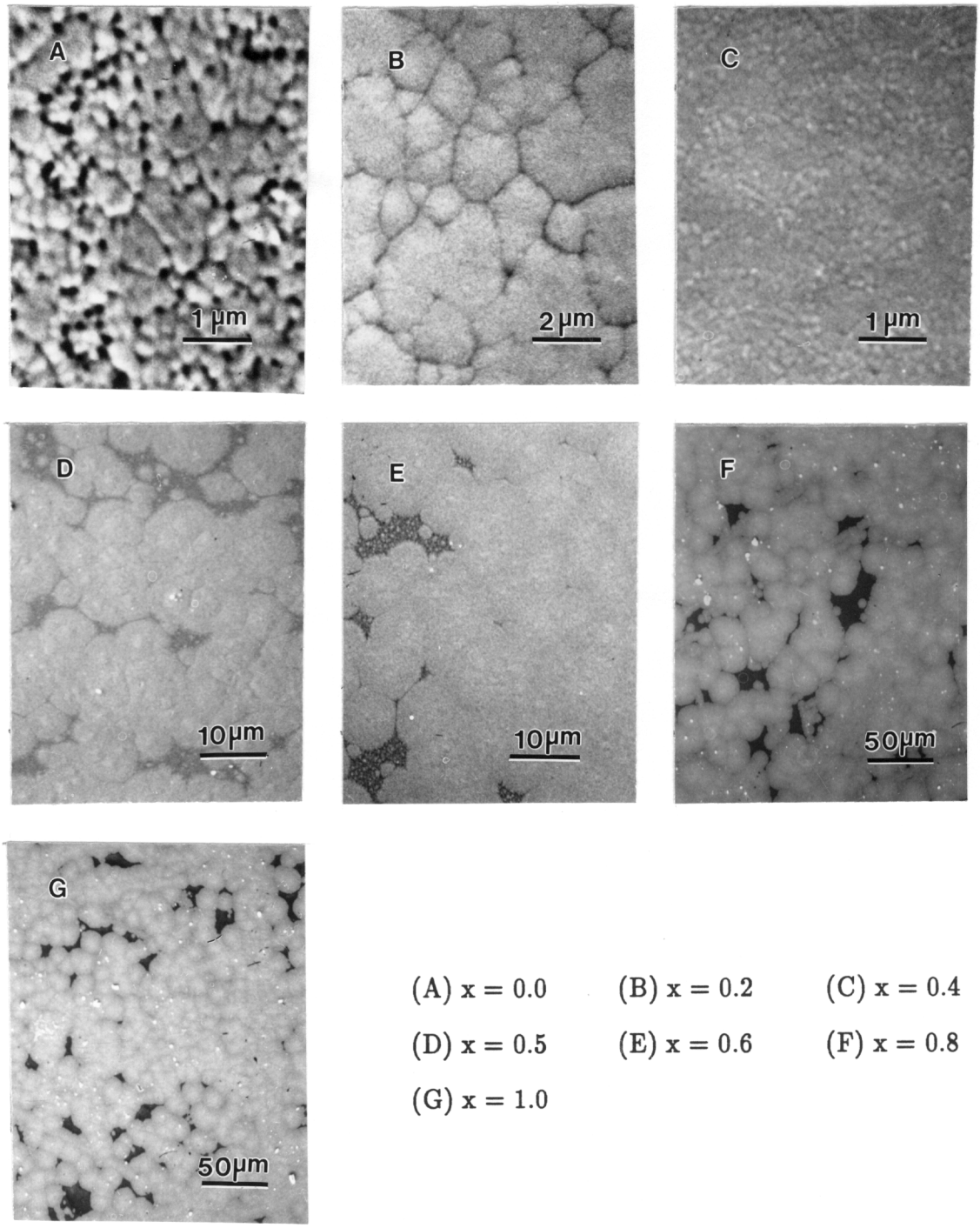

(A) x = 0.0 (B) x = 0.2 (C) x = 0.4

(D) x = 0.5 (E) x = 0.6 (F) x = 0.8

(G) x = 1.0

Figure 4.14 SEM micrographs of the surface morphology of MOD $Pb(Zr_xTi_{1-x})O_3$ films which had suffered through 23 heat treatments in the temperature range from 150°C to 700°C for 30 min at each annealing temperature.

large spheroidal grains with average sizes ranging from 7 to 15 μm were found for the samples at the zirconium–rich side, while fine grains with average sizes ranging from 0.3 to 2 μm were noted for those at the titanium–rich side. The average grain size is plotted as a function of the x value in Figure 4.15. As can be seen, the grains were larger than those shown in Figure 3.17 with the exception of the sample with x = 1.0.

4.4 Summary

Models for the structure development in MOD PZT films have been proposed and have been successfully used to interpret the experimental observations. Also, an effective, versatile, nondestructive optical method was developed for the study of the structure development in MOD PZT films. Using this method, the characteristic temperatures at which perovskite phase formation is initiated and completed were identified for the composition from x = 0.4 to 1.0. In addition, the volume fraction of each phase in a two–phase mixture can be obtained. This optical method is more effective than conventional nondestructive techniques such as x–ray diffraction in studying the pyrochlore to perovskite phase transformation in PZT films. The proposed models and this optical method could be applied to other thin film systems prepared by MOD or sol–gel techniques.

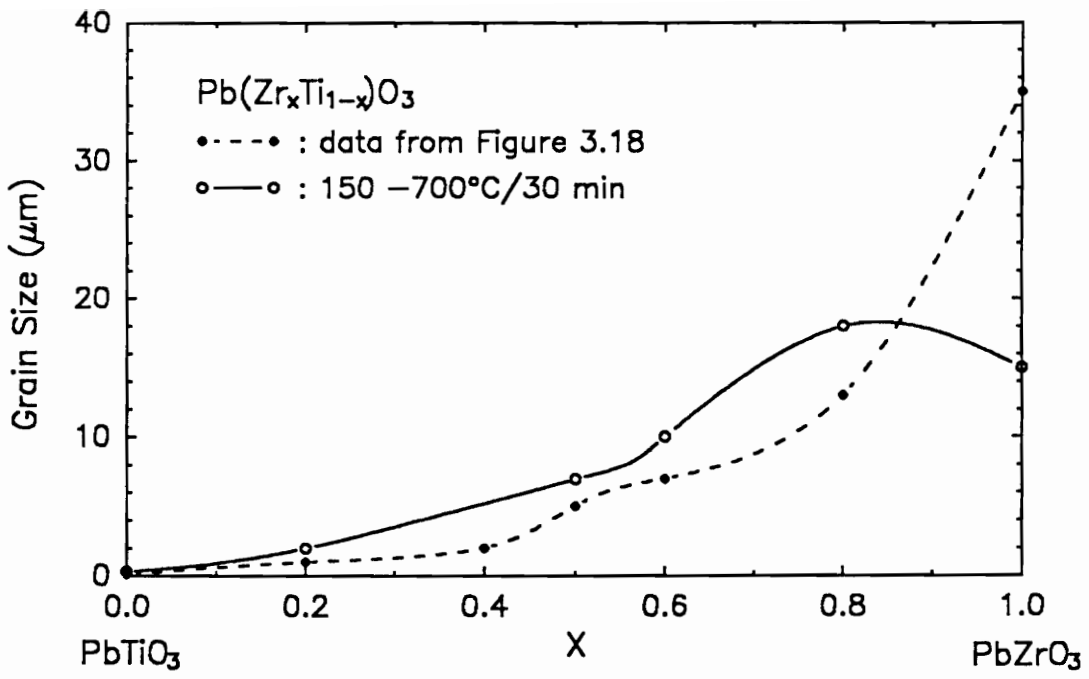

Figure 4.15 Average grain size of the $Pb(Zr_xTi_{1-x})O_3$ films as a function of composition. The samples had suffered through 23 heat treatments in the temperature range from 150°C to 700°C for 30 min at each annealing temperature.

Chapter 5 Metalorganic Chemical Vapor Deposition of PZT Thin Films

5.1 Introduction

Chemical vapor deposition (CVD) is a material synthesis method in which the constituents of a gaseous phase chemically react to form a condensed coating on a substrate. Thus the CVD process for depositing thin films contains four basic sequential steps:

(1) generation of precursor vapors

(2) transportion of precursor vapors from precursor container to reaction chamber

(3) reaction of precursor vapors and producing a solid film on a substrate

(4) exhausting of by–products and unused precursor

In the first step, the precursor is sealed in a container, conventionally called a bubbler, and is usually thermally evaporated to generate enough vapors. If the precursors are metalorganic compounds, the CVD process is called metalorganic CVD (MOCVD).

In the second step, the precursor vapors are transported into the reaction chamber which contains the specimens to be coated, vapors are transported by the flow of a foreign gas (carrier gas) or by a vacuum or both. If a vacuum pump is

used, the CVD process is called low pressure CVD (LPCVD). On the other hand, if the entire process is performed under atmospheric pressure, the CVD process is called atmosphere pressure CVD (APCVD). During the transporting process, a pre–mixing chamber may be needed for multiple precursors, and the transporting paths need to be kept at a temperature higher than the precursor evaporation temperature but lower than the precursor decomposition temperature.

The third step is the most complicated process which involves many fundamental aspects including thermodynamics, chemical reaction processes and kinetics, nucleation and growth modes, and transport phenomena [66]. Many methods have been used to decompose and activate the precursor vapors including thermal energy, photon energy (ultraviolet light or laser), and electric or magnetic energy. If the thermal energy is used and only the substrate is heated, it is called cold–wall CVD. On the other hand, if the substrate is placed in a hot chamber, it is called hot–wall CVD. For the case of using photon energy, it is called photo–CVD or laser assisted CVD (LACVD). In the plasma assisted CVD (PACVD) process, electric or magnetic energy is used to generate the plasma of the precursor.

Finally, the by–products and unused precursor need to be exhausted and disposed of safely.

It is clear from the above brief discussion, that the complexity of the CVD process cannot be overaddressed. From the technical point of view, it requires the precise control and feedback equipment for mass flow, temperature, and pressure. From the scientific point of view, it involves the understandings of precursor chemistry, reactor modeling and design, thermodynamics, chemical reaction processes and kinetics, nucleation and growth, and transport phenomena.

At the time when this study began three years ago, there was no reported PZT

thin films deposited by MOCVD. During the past three years, five other research groups sequentially published the results of MOCVD PZT films [33–37]. However, the reported MOCVD PZT films were fabricated at relatively high temperatures (> 600^{0}C) using cold wall type reactors. Cold–wall reactors are good for epitaxial films because of less particle contamination. However, cold–wall reactors suffer from their low throughput. In contrast, hot–wall reactors are conceptually simpler because of the isothermal environment. In addition, they offer much higher throughput than do cold–wall reactors. But hot–wall reactors suffer from particle contaminations from the walls of the chamber. This may not be a severe problem for polycrystalline films. Furthermore, low temperature deposition processes are needed to integrate ferroelectrics into semiconductor processing.

A summary of the properties of the reported MOCVD PZT thin films is given in Table 5.1. The results of this study are briefly included in Table 5.1 also for the purpose of comparison. As can be seen in Table 5.1, [001] oriented PZT films were obtained on (100) MgO and (100) Pt substrates by different investigators. The average grain sizes of PZT films in this study were much smaller than others. Electrical properties comparable to those of others were obtained. In addition, no other group reported the optical properties of MOCVD PZT films. The detailed discussion is in the sub–sections of section 5.4.

In this chapter, at first, because of the complexity of the CVD multi–component oxides, the selection of precursors is very carefully discussed in details in section 5.2. The hot–wall MOCVD apparatus and the deposition process are described in section 5.3. Section 5.4 discusses the effect of the deposition parameters on the film composition, the crystal structure and orientation study, the surface morphology, the reproducibility, the optical properties, and the

Table 5.1 Comparison of MOCVD PZT films from different investigators

Group	Substrates	Crystal Orientation	Microstructure	Ave. G.S. (μm)	Electric Properties	Optical Properties
a	Sapphire	Non–oriented*	Fine Grains	0.1**	ϵ_r=1000	n=2.413
	Pt/Ti/SiO_2		Fine Grains	0.15	P_r=12.3μC/cm^2	k=0.0008
	RuO_x/SiO_2		Fine Grains	0.15	E_c=64.5kV/cm	
b	(100)Si,(100)MgO	Completed [001]*	Tile structure	0.6(x=0) 2.0(x=.48)	ϵ_r=100–500	—
c	(100)Pt/(100)MgO	Completed [001]	Tile structure	1.0	ϵ_r=200–350 P_r=30–40 μC/cm^2 E_c=40–65 kV/cm	—
d	(100)MgO	Completed [001]	Fine Grains	0.8	—	—
e	(100)Si,(111)Pt	Non–oriented	Fine Grains	0.5	ϵ_r=1300–1700 P_r=18μC/cm^2 E_c=55kV/cm	—
f	Pt/Ti/SiO_2	Highly [001] Oriented	Fine Grains	0.5(x=0) 0.2(x=.57)	ϵ_r=240–870 P_r=50–60 μC/cm^2 E_c=75–170 kV/cm	—

a Virginia Tech, this study.

b Chubu University, Japan, Reference 33.

c Nippon Mining Co., Japan, Reference 34.

d Tokyo Institute of Technology, Japan, Reference 35.

e Mitsubishi Electric Co., Japan, Reference 36.

f Philips Research Laboratories, The Netherlands, Reference 37.

* Highly oriented [001] PZT films were occasionally obtained.

** The average grain size seemed to be independent of film thickness, composition, and substrate.

* Non–oriented PZT films were obtained when using TEL–ZIP–TIP system (see Table 5.7).

interrelationship of the composition uniformity and ferroelectric properties. PZT films were deposited using a cold–wall and a hot–wall reactor. The results of cold–wall MOCVD PZT films are demonstrated in section 5.5. Finally the conclusions are drawn in section 5.6.

5.2 Selection of Precursors

The selection of the precursors is the most critical step in CVD for successful depositions of complex oxide thin films. The first successful deposition of oxide–based ferroelectric thin films by CVD was reported by Nakagawa et al. in 1982 [67]. They deposited $PbTiO_3$ films on Pt–coated silicon wafers by using $TiCl_4$, $PbCl_2$, O_2, and H_2O as source materials. Several problems arose from their studies: (1) very high evaporation temperature (700^{0}C) was required of $PbCl_2$, (2) poor ferroelectric properties (P_r = 0.16 $\mu C/cm^2$ and E_c = 14.5 kV/cm), (3) poor composition uniformity in the bulk of $PbTiO_3$ films, and (4) crystallographic imperfections due to water and/or chloride contamination. Obviously, chlorides are not ideal precursors for the CVD process. In general, metalorganic precursors have relatively high vapor pressures at lower temperatures. By carefully selecting the organic compounds, the undesirable contaminations in the films can be completely excluded. Metalorganic compounds are now used almost exclusively for the deposition of oxide thin films.

5.2.1 General Consideration

The ideal precursors for MOCVD have to meet the following requirements:

(1) High vapor pressure at low vaporization temperature.

(2) Low decomposition temperature.

(3) Large enough temperature "window" between vaporization and decomposition temperatures.

(4) No contaminations from the organic constituents of the precursors

(5) Stable under ambient conditions.

(6) Nontoxic.

It is one of the goals in this study to identify the ideal precursors for MOCVD PZT films.

Several types of metalorganic compounds have been commonly used as precursors to grow metal oxide thin films including metal alkyls, metal alkoxides, and metal β–diketonates. Metal alkyls have the general formula $M^{n+}R_n$ where $R=C_mH_{2m+1}$, metal alkoxides have the general formula $M^{n+}(OR)_n$, and metal β–diketonates have the general formula

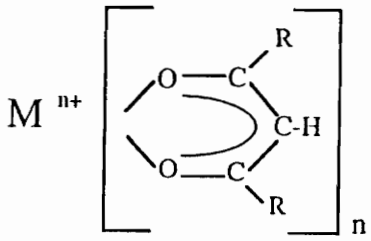

Metal β-diketonate

R = alkyl or fluoroalkyl group

Most of the metalorganic precursors have reasonable vapor pressures at relative low temperatures. Although metal alkoxides and metal β–diketonates tend to be less volatile than their alkyl equivalents, they are easier to handle and are much less toxic. One of the assets of metalorganic precursors is that their physical and chemical properties can be tailored by making small changes in their chemical

structure. For example, the volatility of a metal β–diketonate can be increased by varying the R–group on the chelating ring. In general, increased bulkiness of the R–group or increased fluorine substitution on the R–group increases volatility. This trend is demonstrated for lead β–diketonates in Table 5.2 [68]. The increased volatility is apparent with chelates of increased fluorination: $Pb(acac)_2 < Pb(tfa)_2 < Pb(hfa)_2$ and increased bulkiness: $Pb(acac)_2 < Pb(dhd)_2 < Pb(thd)_2$. Increasing the size of the ligand increases the metal chelate volatility by shielding the metal center from molecular interactions. Fluorination has the same effect because fluorine atoms are somewhat larger than the hydrogen atoms for which they substitute. The thermal and ambient stabilities of the metal β–diketonate are also sensitive to variation in the R–substituent and metal ion size. Effective shielding of the metal ion due to either small ion size or bulkiness of the ligand results in increased thermal and ambient stability. This effect can be explained in the same manner in which the increased volatility of the β–diketonate is explained. Increased shielding of the metal center renders the compound less prone to intermolecular reactions which form oligomers, and also less prone to reactions with water or oxygen to increase the coordination number.

In the case of metal alkoxides, their vapor pressures strongly depend on the nature of the organic group, R. In general, the vapor pressure increases as the molecular mass of R decreases. However, if R is too small, the alkoxide groups no longer shield the incompletely coordinated central metal ion and the molecule tends to oligomerise. This leads to an increased molecular weight and thus to a reduction of the vapor pressure. For the alkoxides, the vapor pressure also depends on the branching of R. The higher the branching, the more effective the shielding of the metal ion. In the case of the butoxides of Ti and Zr, this leads to a substantial

Table 5.2 Examples of lead β–diketonates [68]

Name	R_1, R_2	Abbr.	T(^{0}C) for 1 torr vapor pressure
Lead bis–acetylacetonate	CH_3,CH_3	$Pb(acac)_2$	95
Lead bis–trifluoroacetylacetonate	CF_3,CH_3	$Pb(tfa)_2$	72
Lead bis–hexafluoroacetylacetonate	CF_3,CF_3	$Pb(hfa)_2$	67
Lead bis–dimethylheptadione	CH_3,$C(CH_3)_3$	$Pb(dhd)_2$	76
Lead bis–tetramethylheptadione	$C(CH_3)_3$,$C(CH_3)_3$	$Pb(thd)_2$	60
Lead bis–heptafluoroheptadione	CH_3,C_3F_7	$Pb(fhd)_2$	95
Lead bis–heptaflurodimethyloctadione	$C(CH_3)_3$,C_3F_7	$Pb(fod)_2$	68

increase of the vapor pressure going from the n–butoxide, to iso–butoxide to tertiary–butoxide. The volatility of metal alkoxides is described by Bradley, Mehrotra, and Gauer [69].

5.2.2 Properties of Precursors

This section discusses the metalorganic precursors reported in the literature for $Pb(Zr_xTi_{1-x})O_3$ thin film deposition. The precursors for the Pb–component and their selected properties are listed in Table 5.3 [33–38,70–74]. Use of $Pb(hfa)_2$ and $Pb(fod)_2$ resulted in fluorine contamination in the films [75]. In addition, PbO formation from thermal decomposition of $Pb(fod)_2$ is initiated at 300°C, but PbF_2 becomes the dominant phase above 300°C [70]. On the other hand, although good quality PbO films were obtained from tetraethyl lead (TEL), the extremely toxic nature of this precursor may prevent its use in large scale applications. Additionally, lead alkyls are photosensitive, and decompose by free radical decay. Lead alkoxides, for example $Pb(OBu^t)_2$, are also liquids at room temperature, and possess significant vapor pressures which creates toxicity problems. In addition, the large Pb(II) ion suffers the hydrolysis problem which is typical of metal alkoxides. In summary, $Pb(thd)_2$ was found to be the most suitable precursor for lead–based ferroelectric thin film deposition.

The possible selection of metalorganic precursors for the Zr–component and their selected properties in PZT thin film deposition are listed in Table 5.4 [33–38,70,76,77]. Several difficulties were encountered in using $Zr(acac)_4$ and $Zr(tfa)_4$ precursors. For example, $Zr(acac)_4$ resulted in cubic ZrO_2 films with carbon contamination up to 15 atom% [76]. Changes in the gas composition when

Table 5.3 Possible selection of metalorganic precursors and their selected properties for PbO films

Name	Formula	Abbreviation
Tetraethyl lead	$Pb(C_2H_5)_4$	TEL
Lead t–butoxide	$Pb(O^tC_4H_9)_2$	$Pb(OBu^t)_2$
Lead bis–hexafluoroacetylacetonate	$Pb(C_5HF_6O_2)_2$	$Pb(hfa)_2$
Lead bis–heptaflurodimethyloctadione	$Pb(C_{10}F_7H_{10}O_2)_2$	$Pb(fod)_2$
Lead tetramethylheptadione	$Pb(C_{11}H_{19}O_2)_2$	$Pb(dpm)_2$ or $Pb(thd)_2$

Selected properties

Precursor	Appearance at RT	Air Stability	Melting Point	Boiling Point	Vaporization Temperature	Decomposition Temperature
TEL	Lq.	Sensitive	—	—	–20°C – 50°C	—
$Pb(OBu^t)_2$	Lq.	Sensitive	—	—	120°C	—
$Pb(hfa)_2$	White Powder	Stable	158°C	210°C	130°C	—
$Pb(fod)_2$	White Powder	Stable	76°C	—	100°C – 130°C	300°C
$Pb(thd)_2$	White Powder	Stable	128°C	320°C	135°C – 165°C	300°C

Table 5.4 Possible selection of metalorganic precursors and their selected properties for ZrO_2 films

Name	Formula	Abbreviation
Zirconium isopropoxide	$Zr(O^iC_3H_7)_4$	$Zr(OPr^i)_4$ or ZIP
Zirconium t–butoxide	$Zr(O^tC_4H_9)_4$	$Zr(OBu^t)_4$ or ZTB
Zirconium acetylacetonate	$Zr(C_5H_7O_2)_4$	$Zr(acac)_4$
Zirconium trifluoroacetylacetonate	$Zr(C_5H_4F_3O_2)_4$	$Zr(tfa)_4$
Zirconium tetramethylheptadione	$Zr(C_{11}H_{19}O_2)_4$	$Zr(dpm)_4$ or $Zr(thd)_4$

Selected properties

Precursor	Appearance at RT	Air Stability	Melting Point	Boiling Point	Vaporization Temperature	Decomposition Temperature
ZIP	Lq.	Sensitive	—	—	175°C	—
ZTB	Yellow Lq.	Sensitive	—	95°C	25°C – 50°C	—
$Zr(acac)_4$	White Powder	Sensitive	173°C	—	160°C	300°C
$Zr(tfa)_4$	White Powder	Sensitive	128°C	235°C	160°C	300°C
$Zr(thd)_4$	White Powder	Stable	345°C	—	180°C – 230°C	500 – 550°C

using $Zr(tfa)_4$ resulted in fluorine contamination in the films. The fluorine contamination problem can be solved by controlling the partial pressure of water vapor in the reactor during deposition. One of the problems in the use of the zirconium alkoxides, e.g. $Zr(OPr^i)_4$ and $Zr(OBu^t)_4$, is that they are very sensitive to air. $Zr(thd)_4$ is thermally stable over its vaporization temperature range, and is very easy to handle under ambient conditions [70]. It has been proven to be a suitable precursor for the CVD process despite its relatively high vaporization temperature ($180^0C - 230^0C$) and decomposition temperature ($500^0C - 550^0C$) [77]. Since the formation temperature of the perovskite phase of the PZT film is around 550^0C, the high decomposition temperature of $Zr(thd)_4$ is not a severe problem.

The possible selection of metalorganic precursors for the Ti–component and their selected properties in PZT thin film deposition are listed in Table 5.5 [33–38,70–74]. Titanium alkoxides have been used as precursors for TiO_2 thin film deposition without significant disadvantages. They are reasonably stable under ambient conditions, and do not present any extreme health hazards. The difference in degree of moisture sensitivity of the titanium alkoxides and zirconium alkoxides is a function of the metal atom size. Both are d^0 metals in the (IV) oxidation state, and are very electronegative. The smaller Ti^{4+} ion is somewhat shielded from atmospheric moisture by its organic ligands, but the larger Zr^{4+} ion is not completely shielded by its ligands, and reacts with atmospheric moisture.

Thus it is clear from the above discussion, that there is no ideal precursor combination for MOCVD PZT thin films. As mentioned before, when this study was initiated, there was no reported information available on MOCVD PZT films. After intensive studies searching for the most suitable compromise of precursors for MOCVD PZT thin films, the suggested combination is as follows:

Table 5.5 Possible selection of metalorganic precursors and their selected properties for TiO_2 films

Name	Formula	Abbreviation
Titanium ethoxide	$Ti(OC_2H_5)_4$	$Ti(OEt)_4$
Titanium isopropoxide	$Ti(O^iC_3H_7)_4$	$Ti(OPr^i)_4$ or TIP
Titanium (di–isopropoxide)–bis(acetylacetonate)	$Ti(C_5H_7O_2)_2(O^iC_3H_7)_2$	$Ti(acac)_2(OPr^i)_2$

Selected Properties

Precursor	Appearance at RT	Air Stability	Melting Point	Boiling Point	Vaporization Temperature	Decomposition Temperature
$Ti(OEt)_4$	Colorless Lq	Stable	—	122^0C	110^0C	300^0C
TIP	Colorless Lq		20^0C	58^0C	$25^0C - 106^0C$	—
$Ti(acac)_2$ $(OPr^i)_2$	Orange Lq.		—	—	87^0C	—

(1) For PbO: $Pb(thd)_2$.

(2) For ZrO_2: $Zr(thd)_4$.

(3) For TiO_2: $Ti(OEt)_4$ or $Ti(OPr^i)_4$.

In our study, the precursor combination of $Pb(thd)_2$, $Zr(thd)_4$, and $Ti(OEt)_4$ is chosen based on their high vapor pressures, no contamination (the AES detection level for the impurities is less than 1%) in the resulting films, and, most importantly, easy handling (stable and nontoxic).

5.3 Experimental Procedure

A schematic diagram of the home–made hot–wall CVD apparatus is shown in Figure 5.1. The reaction chamber is a stainless steel tube having 80 mm inside diameter. The temperature is maintained by a resistively heated three–zone furnace. The temperature profile of the reaction chamber is shown in Figure 5.2 at the set points of 550^{0}C for center zone (zone 2) and 555^{0}C for side zones (zone 1 and 3). As can be seen in Figure 5.2, a 300 mm uniform temperature zone is defined as 550 ± 5^{0}C. Low pressures are achieved by a mechanical pump. The pressure is monitored by an MKS BARATRON pressure sensor with a range of 12 to 10^{-3} torr. A cold trap filled with liquid nitrogen is installed between the reaction chamber and the mechanical pump to condense the products and/or the unreacted reagents. The precursor material is packaged in a stainless steel bubbler which has two connectors; one is connected to the reactor by a stainless steel line with a manual valve and the other is connected to a N_2 gas cylinder with a mass flow controller. Aluminum housed mantle heaters with temperature controllers are used to control the temperatures of the precursors. The precursors were kept at the desired

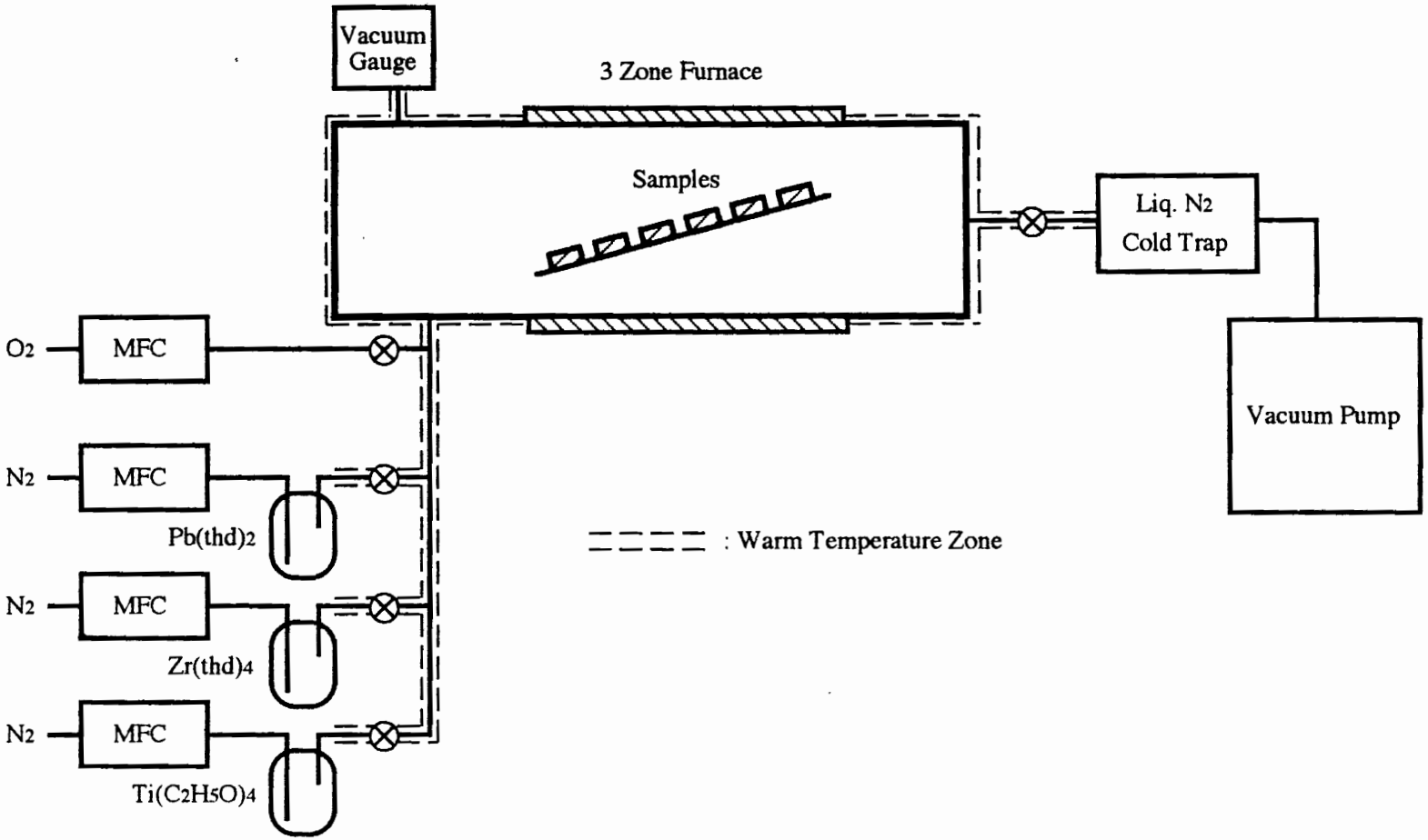

Figure 5.1 Schematic diagram of hot-wall MOCVD apparatus for PZT films.

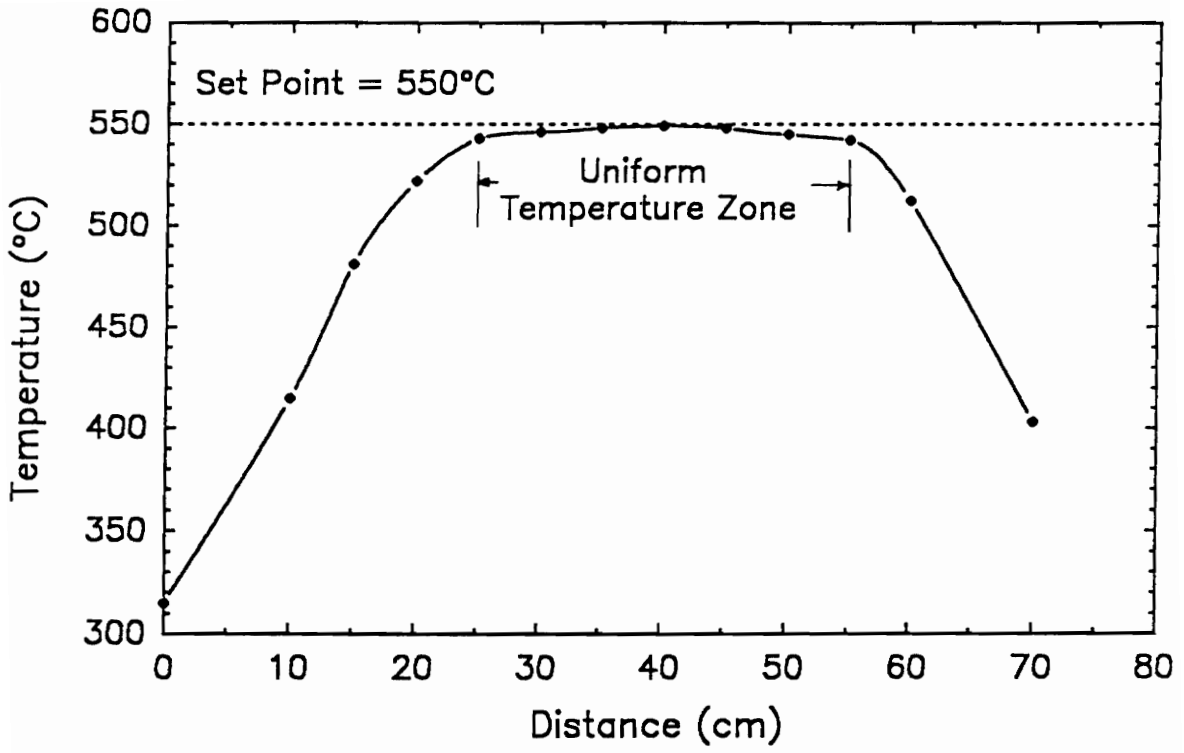

Figure 5.2 Temperature profile of the deposition zone of MOCVD apparatus.

temperatures within ± 0.5°C during deposition. The paths between the furnace and the precursor bubblers were heated by heating tapes to a temperature ranging from 200°C to 250°C; this prevents the precursors from either condensing or decomposing. Typical deposition conditions are listed in Table 5.6.

The bubblers used in this study were home–designed having a cylindrical shape 1.5 inches in diameter and 6 inches high. A volume of 40 cm^3 $Ti(OEt)_4$ packaged in the bubbler can be used for more than 20 depositions. After each deposition this liquid source was kept in vacuum. In this manner, $Ti(OEt)_4$ can last for at least one month without apparent degradation. On the other hand, 0.8 g each of fresh $Pb(thd)_2$ and $Zr(thd)_4$ were used for each deposition. All of these precursors are stable and safe in air at room temperature. The partial pressures of each of the precursors were in the ranges of 5 – 20 mtorr for $Ti(OEt)_4$, 10 – 20 mtorr for $Pb(thd)_2$, and 10 – 30 mtorr for $Zr(thd)_4$ under the conditions listed in Table 5.6.

The measurement of the bubbler temperature was done by inserting a thermocouple in between the inner wall of the bubbler heater and the outer wall of the bubbler. Therefore, the bubbler temperature may not be the "real" precursor temperature. A summary of the deposition parameters from different investigators is given in Table 5.7. Although the same precursor was used by different investigators, the bubbler temperatures that were used had a large divergence. For example, the bubbler temperature of TEL varied within a 40°C range among all authors. This may be due to the difference in the bubbler designs and/or the difference in the temperature measruing configurations.

The substrates were of three types: 1 inch diameter sapphire disks, $Pt/Ti/SiO_2/Si$ wafers, and $RuO_x/SiO_2/Si$ wafers. The sapphire disks were obtained from Swiss Jewel Company and had a surface orientation within a 30° cone of the

Table 5.6 Typical deposition conditions for MOCVD PZT thin films

Precursors	$Pb(thd)_2$	$Zr(thd)_4$	$Ti(OEt)_4$
Precursor Temperature	145–165°C	210–230°C	90–115°C
Carrier Gas (sccm,N_2)	20–30	15–30	5
Substrate	sapphire, $Pt/Ti/SiO_2/Si$, and $RuO_x/SiO_2/Si$		
Substrate Temperature	550°C		
Dilute Gas (sccm, O_2)	500–1000		
Total Pressure	6 torr		
Deposition Rate (nm/min)	3.0–20.0		

Table 5.7 Summary of deposition parameters from different investigators

Group	Source materials Carrier Gas (sccm) Bubbler Temperature (°C)			Dilute Gas(sccm)	Deposition Temperature (°C)	Total Press. (Torr)	Depos. Rate (nm/min)
a	$Pb(thd)_2$	$Zr(thd)_4$	$Ti(OEt)_4$	O_2	550	6	3.0–20
	N_2,20–30	N_2,15–30	N_2,5	500–1000			
	145–160	205–230	90–110				
b	TEL	ZIP	TIP	O_2	550	6	10–20
	Ar,40–100	Ar,40–100	Ar,40–100	120			
	–15	175	30				
	TEL	$Zr(thd)_4$	TIP	O_2	600	6	10–20
	Ar,40–100	Ar,40–100	Ar,40–100	120			
	–15	165	30				
c	TEL	$Zr(thd)_4$	TIP	O_2	600–650	5	8.5–12
	Ar,30–100	Ar,30–100	Ar,30–100	200			
	–10	180	25				
d	$Pb(thd)_2$	ZTB	TIP	O_2	700	20	20–30
	N_2,180	N_2,40	N_2,40	40			
	165	50	20				
e	$Pb(thd)_2$	ZTB	TIP	O_2	600–700	1–2	5–20
	N_2,100–200	N_2,0–100	N_2,0–100	700			
	135	30	30				
f	TEL	ZTB	TIP	O_2	700	3.75	—
	N_2,—	N_2,—	N_2,—	200			
	25	25	25				

*The designation of the research group can be found in Table 5.1.

Note: All the PZT films were deposited by using cold–wall type reactors, except this study.

[100] direction. The Pt layer on the Pt–coated substrate obtained from SHARP Co, Japan was a sputtered polycrystalline film. The RuO_x layer on RuO_x–coated substrate bought from Massachusetts Thin Films was also a sputtered polycrystalline film. Samples were loaded, the reactor tube was sealed, and the system was evacuated to 0.01 torr. The pressure was maintained until the samples reached thermal equilibrium. Deposition was initiated by sending each of the three precursors and the oxygen diluent gas at the same time and subsequently adjusting the vacuum to the desired pressure using the pump valve. At the end of the run the evaporators and diluent gas were shut off, and the reactor was evacuated to base pressure before backfilling with air to atmospheric pressure. The samples were furnace–cooled below 100°C before they were removed from the reactor.

As–deposited MOCVD PZT films were specular, crack–free, uniform, and adhered well on all substrates used and were highly transparent on sapphire substrates. These films also showed very smooth surfaces as viewed using both optical microscopy and scanning electron microscopy. The deposition rates were estimated from the weight changes of each specimen before and after deposition. The film thicknesses estimated in this manner agreed very well with that calculated from the optical interference fringes. For the deposition conditions described in Table 5.6, film growth rates were in the range of 3.0 to 20.0 nm/min. A very interesting result on the film growth rate was that the rates observed on the Pt–coated substrates were about 2 – 3 times larger than on the sapphire and RuO_x–coated substrates. A similar substrate effect was also reported by Swartz et al [74].

5.4 Results and Discussion of MOCVD PZT Thin Films

The characterization techniques of MOCVD PZT thin films have been described in detail in Chapter 2.

5.4.1 The Effect of the Deposition Parameters on the Composition of the Film

The stoichiometry of the films can be controlled mainly by varying the individual precursor temperatures and/or the diluent gas flow rates. The variation of the Zr/Ti ratio under different deposition conditions is illustrated in Figure 5.3. As can be seen from Figure 5.3, the desired Zr/Ti ratio can be easily obtained across the entire PZT solid solution range.

One of the advantages of the hot–wall MOCVD is its high throughput. In a production line, it is common to have more than 100 wafers in one run. Therefore, it is important to examine the composition uniformity from sample to sample. The composition uniformity across the entire uniform temperature zone (550 ± 5^{0}C) is shown in Figure 5.4. Figure 5.4 shows that the higher the diluent gas flow rate, the better the sample–to–sample composition uniformity. For example, the composition is relatively uniform in a region of up to two thirds of the size of the entire uniform temperature zone at a diluent gas flow rate of 1000 sccm, while it is less than one third of the uniform temperature zone at diluent gas flow rate of 500 sccm. Figure 5.4 also shows that zirconium content increased while the titanium content decreased when approaching the end of the uniform temperature zone. The increasing zirconium content at the end of the uniform temperature zone indicates that the $Zr(thd)_4$ is more difficult to decompose than $Ti(OEt)_4$ is. The decreasing titanium content is a consequence of the depletion of titanium precursors at the end of the uniform temperature zone.

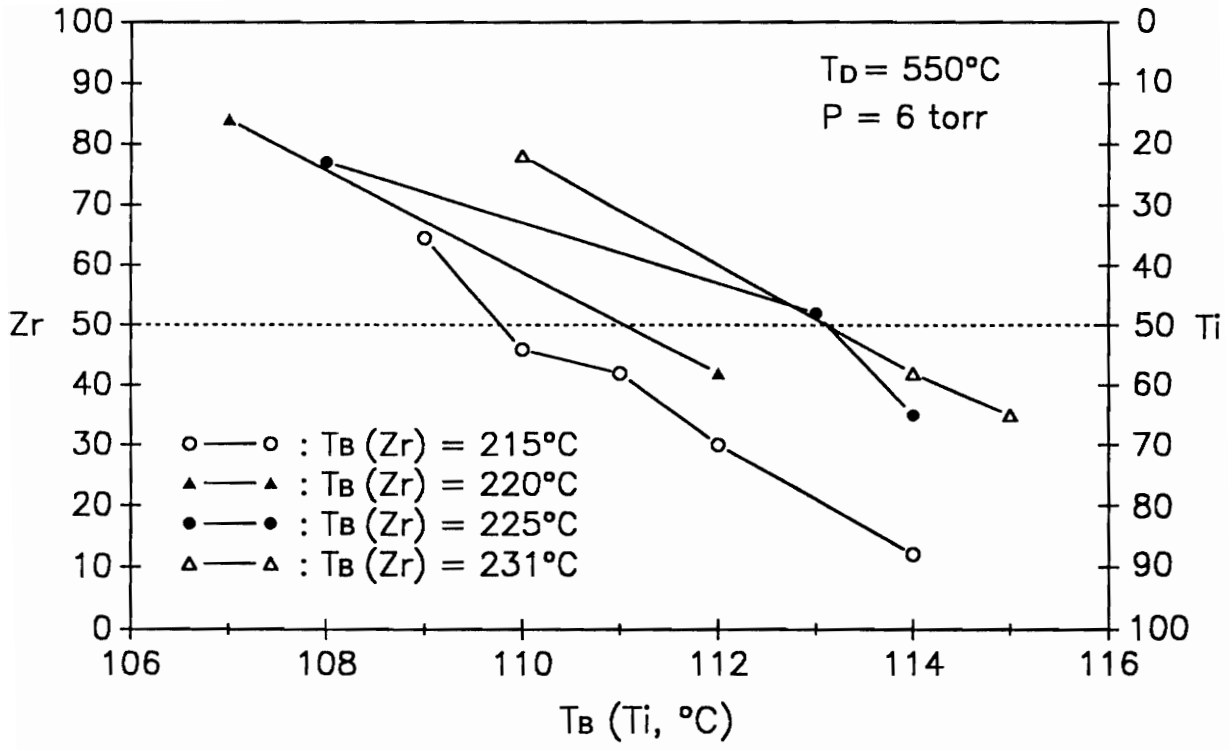

Figure 5.3 Variation of (Zr,Ti) composition with the bubbler temperature of Zr and Ti precursors.

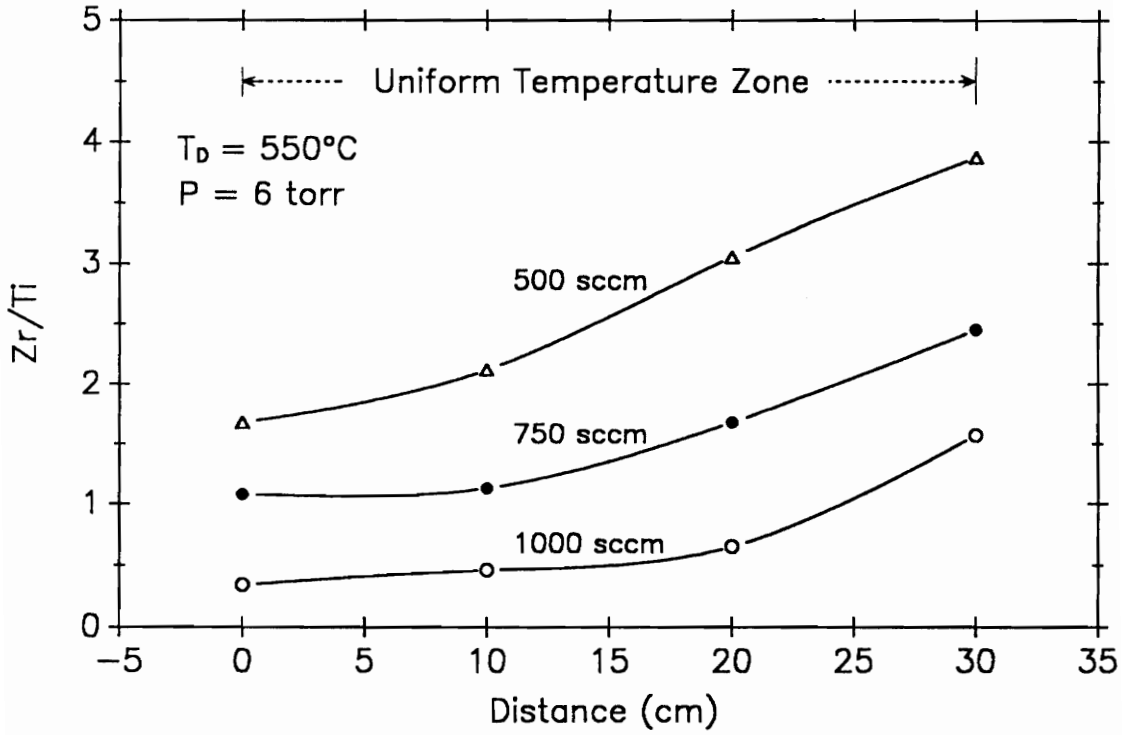

Figure 5.4 Sample–to–sample composition uniformity.

5.4.2 X–ray Diffraction Study

The specimens (deposited films on substrates) were directly characterized by x–ray diffraction. No further specimen preparation is required. All the as–deposited PZT films were single phase with perovskite structure, regardless of the substrate and the composition. The XRD patterns of the as–deposited PZT films on sapphire disks, $Pt/Ti/SiO_2/Si$ wafers, and $RuO_x/SiO_2/Si$ wafers are shown in Figures 5.5–5.7, respectively. One very interesting observation is that both non–oriented and highly [100] oriented films were obtained on each of these three different types of substrates. Figure 5.5 shows PZT films on sapphire disks with five different Zr/Ti ratios ranging from x = 0.07 to x = 0.70 where x = Zr/(Zr+Ti). As expected, the films with x values larger than 0.5 have rhombohedral structure, and the films with x values smaller than 0.5 have tetragonal structure. As can be seen from Figure 5.5, the films with x = 0.07 and x = 0.70 were highly [001] oriented, while the films with x = 0.33, 0.51, and 0.62 are non–oriented. Figure 5.6 shows PZT films on $Pt/Ti/SiO_2/Si$ substrates. Similar to the films on sapphire disks, both highly [001] oriented films [Figures 5.6(a) and 5.6(b)] and non–oriented films [Figure 5.6(c)] were observed. There are very strong XRD peaks at 2θ around 40 degree. By carefully examining these peaks, they were found to consist of two peaks, one at $2\theta = 38.4^0$ corresponding to (111) $PbPt_{5\text{-}7}$ [78] and the other at $2\theta = 40^0$ corresponding to (111) Pt (see the insert of Figure 5.6). This is direct evidence of the interaction of PZT films and Pt substrates. The XRD patterns for four different compositions on the $RuO_x/SiO_2/Si$ substrates are shown in Figure 5.7. The one with x = 0.55 is highly [001] oriented, while the others are non–oriented.

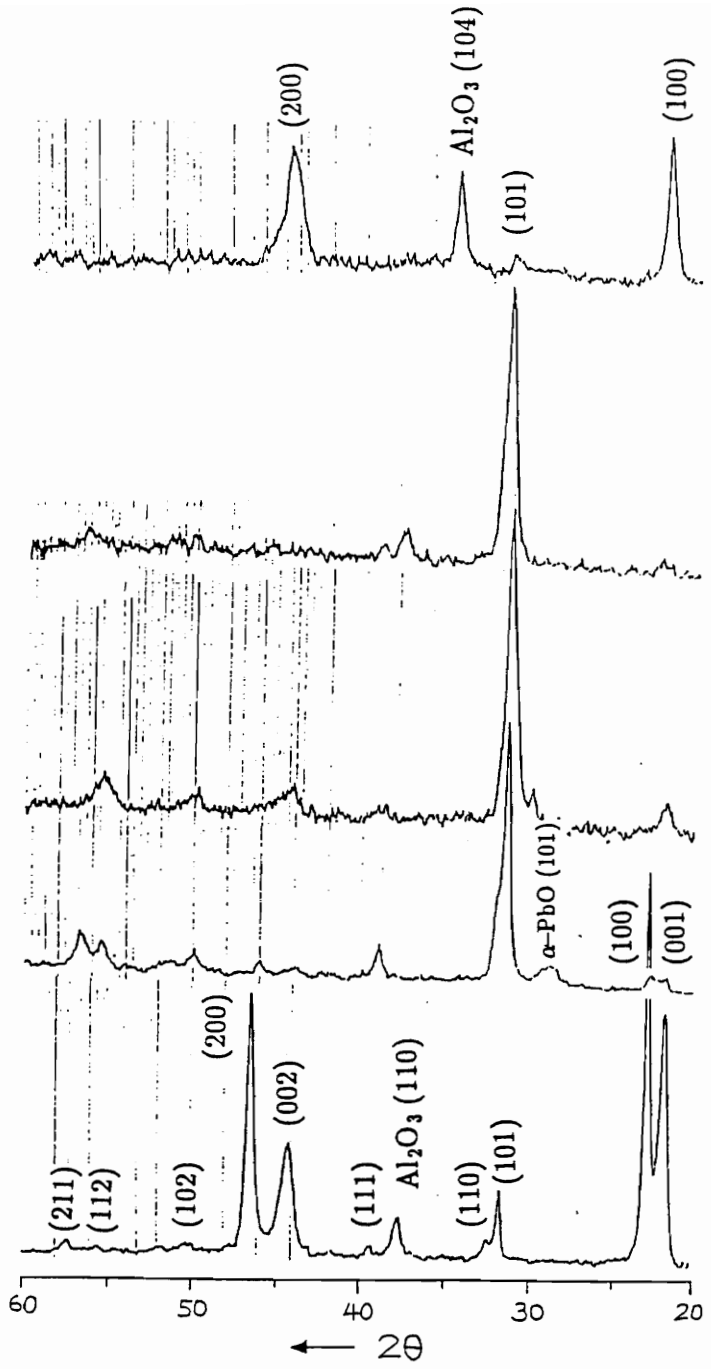

Figure 5.5 XRD patterns of as–deposited MOCVD PZT films on sapphire substrates.

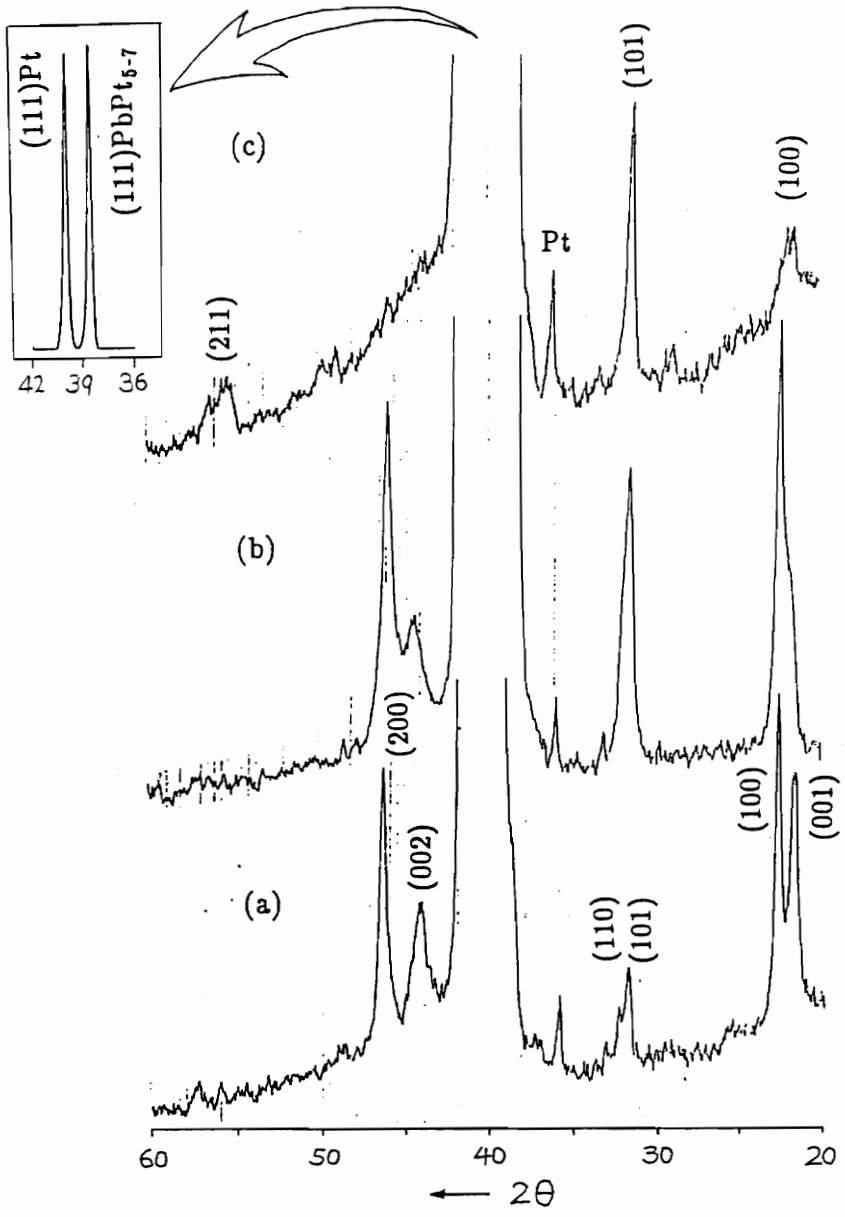

Figure 5.6 XRD patterns of as–deposited MOCVD PZT films on $Pt/Ti/SiO_2/Si$ substrates

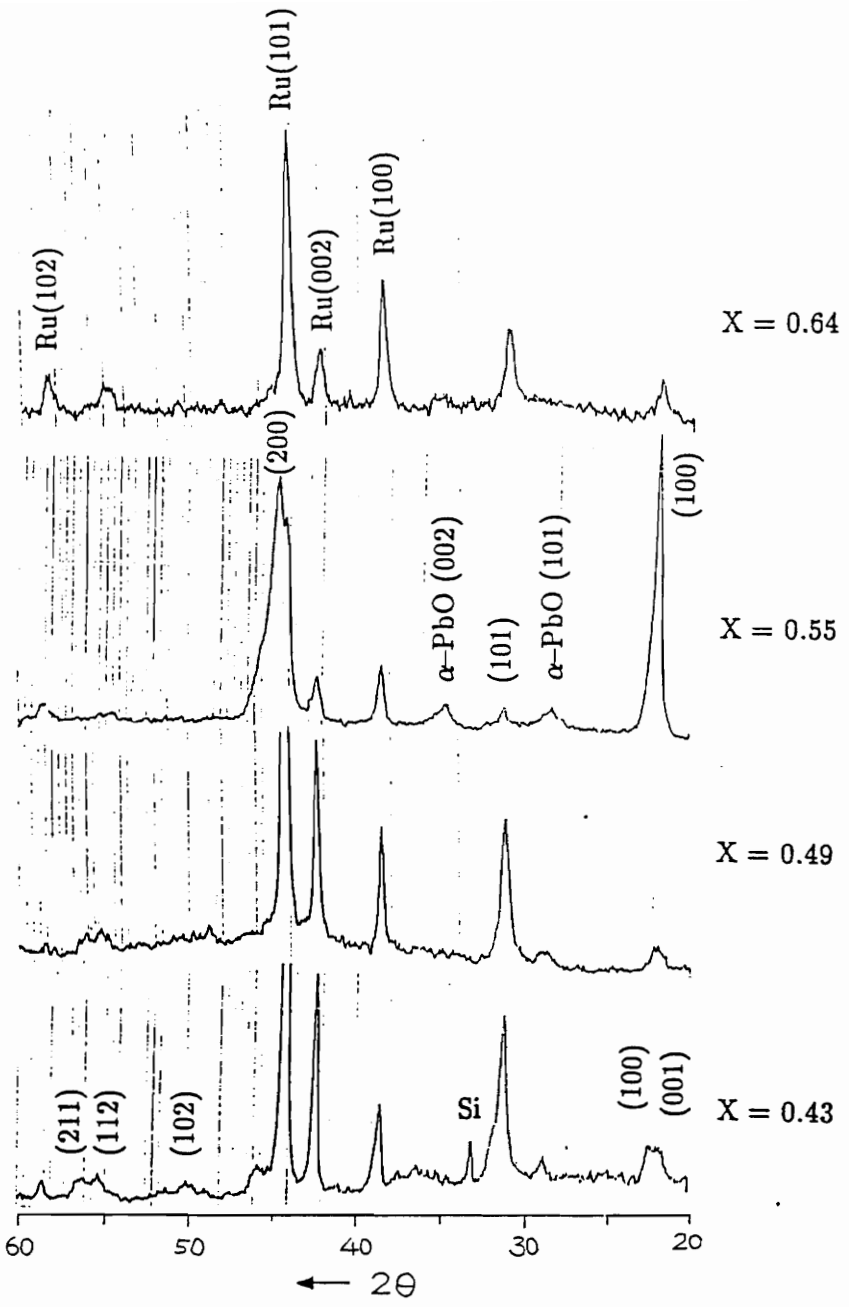

Figure 5.7 XRD patterns of as–deposited MOCVD PZT films on $RuO_x/SiO_2/Si$ substrates.

5.4.3 Surface Morphology

The surface morphology of the typical MOCVD PZT films was investigated by SEM and is shown in Figure 5.8. Figures 5.8(a) – (c) are the as–deposited films on sapphire disk with x = 0.4, on Pt–coated substrate with x = 0.6, and on RuO_x–coated substrate with x = 0.8, respectively. Figure 5.8(d) is the same sample as in Figure 5.8(c) after annealing in air at 650^{0}C for 30 min. The SEM micrographs show that the films were dense and smooth on all three different substrates used. The grains were very fine and uniformly distributed. The average grain size was estimated to be 0.15 μm for the film on $Pt/Ti/SiO_2/Si$ and $RuO_x/SiO_2/Si$ substrates and less than 0.1 μm for the film on the sapphire substrate.

Recall that the microstructures of MOD films presented in Chapters 3 and 4 are composition and heat treatment dependent, and the average grain size for the zirconium rich films was on the order of 10 μm which is about 100 times larger than that of MOCVD films. As can be seen in Figure 5.8, the microstructure of the MOCVD PZT films seems to be independent of the substrate used, the film composition, and the annealing temperature. In addition, the average grain sizes of MOCVD PZT films from other research groups were about 10 times larger than ours (see Table 5.1). From the view of large scale applications, it is very important to have a fine grain structure. For example, a submicro device can sit either on a single grain or on the grain boundary if the average grain size is about 1 μm. The resulting electrical properties of these two devices would be expected to be very different. On the other hand, for a film having an average grain size of 0.1 μm, all the devices will cover several tens of grains. Therefore, the performance of every

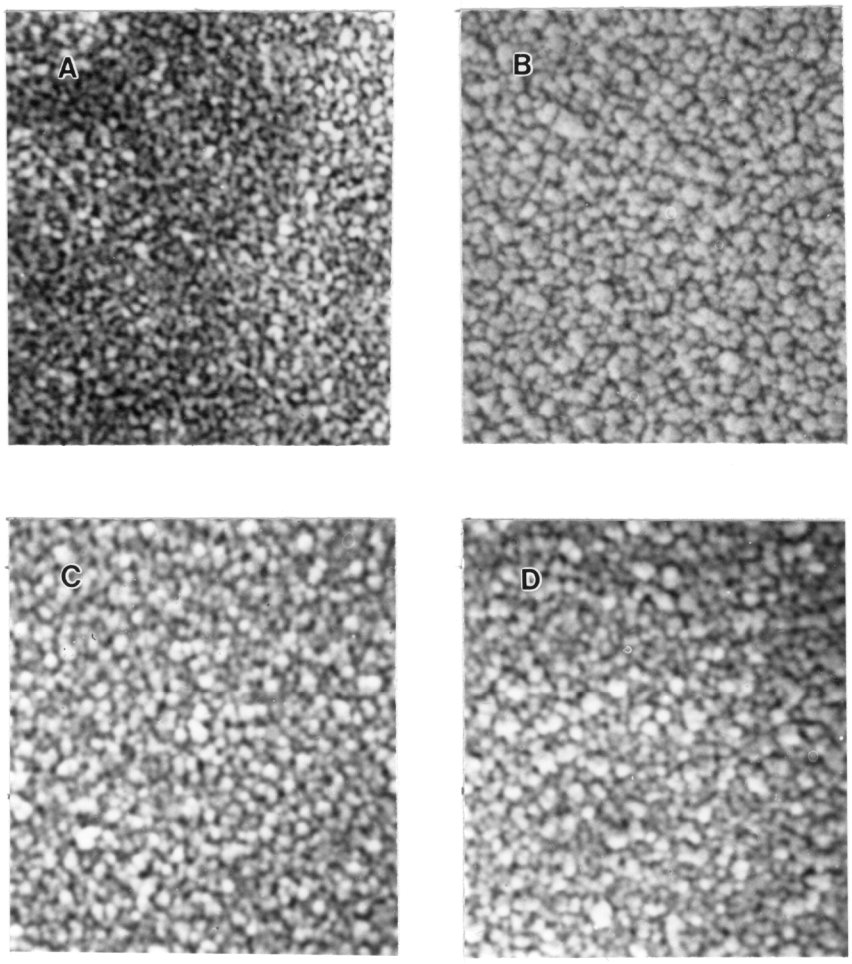

Figure 5.8 SEM micrographs of MOCVD $Pb(Zr_xTi_{1-x})O_3$ films: (a) as–deposited film on sapphire substrate with x = 0.4, (b) as–deposited film on $Pt/Ti/SiO_2/Si$ substrate with x = 0.6, (c) as–deposited film on $RuO_x/SiO_2/Si$ substrate with x = 0.8, and (d) 650^{0}C/30min annealed film on $RuO_x/SiO_2/Si$ substrate with x = 0.8.

device is expected to be uniform.

As mentioned earlier in section 5.4.2, highly [100] oriented films were occasionally obtained on all three different types of substrates used. A surprising result is that a different microstructure was observed only for the film on sapphire disk. Figure 5.9 shows the SEM micrograph of the highly [100] oriented film on sapphire disk whose XRD pattern is shown in Figure 5.5(a). The film has faceted grains, which indicates that they are well crystallized, with an estimated average grain size of 0.5 μm. This surface morphology is similar to those reported by Sakashita et al [34].

5.4.4 Reproducibility

The reproducibility is always the most important issue from the view of mass production. Figure 5.10 shows the reproducibility of the compositions and deposition rates of MOCVD PZT films on sapphire substrates for four consecutive runs with the same deposition parameters. The samples were picked from the same position in the reactor for each run. As can be seen in Figure 5.10, the composition concentrations of Pb, Zr, and Ti were almost constant: 54 ± 2, 32 ± 1, and 14 ± 1 atomic %, respectively, for all four runs. In addition, the variation in the deposition rate was also small, 3.8 ± 0.5 nm/min.

An excellent reproducibility in surface morphology is also shown in Figure 5.11. Each of these four samples was a film on $RuO_x/SiO_2/Si$ substrate which was also picked from the same position in the reactor for each run. As can be seen in Figure 5.11, the films were dense and smooth and had an average grain size around 0.15 μm.

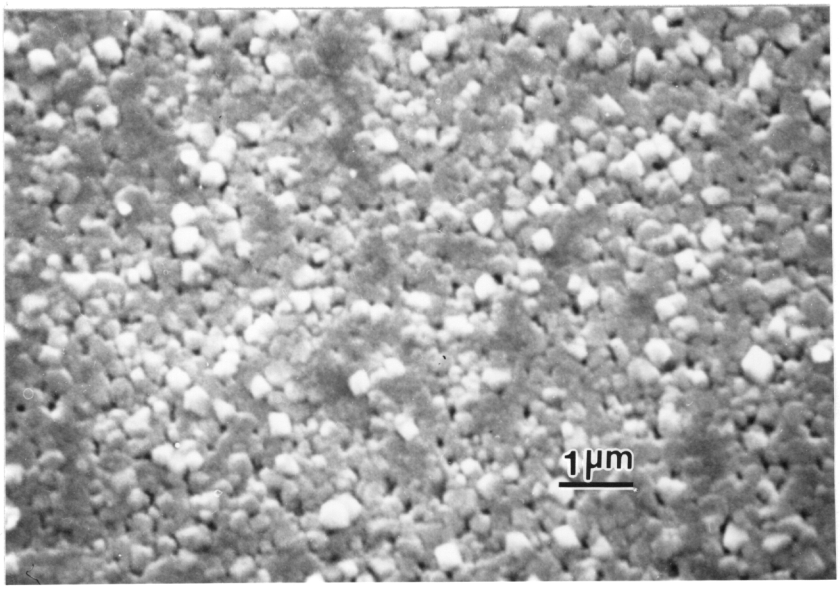

Figure 5.9 SEM micrograph of highly [100] oriented MOCVD PZT film on sapphire substrate.

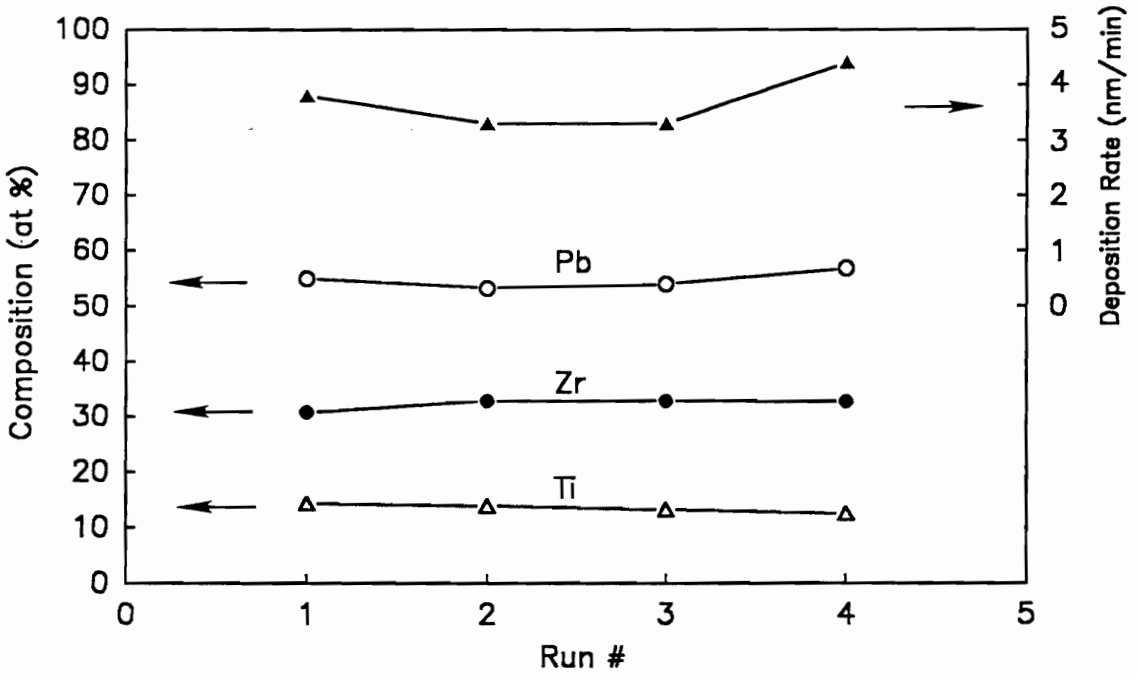

Figure 5.10 Reproducibility of composition and deposition rate gor four consecutive runs with the same deposition condition. The films were on sapphire substrates.

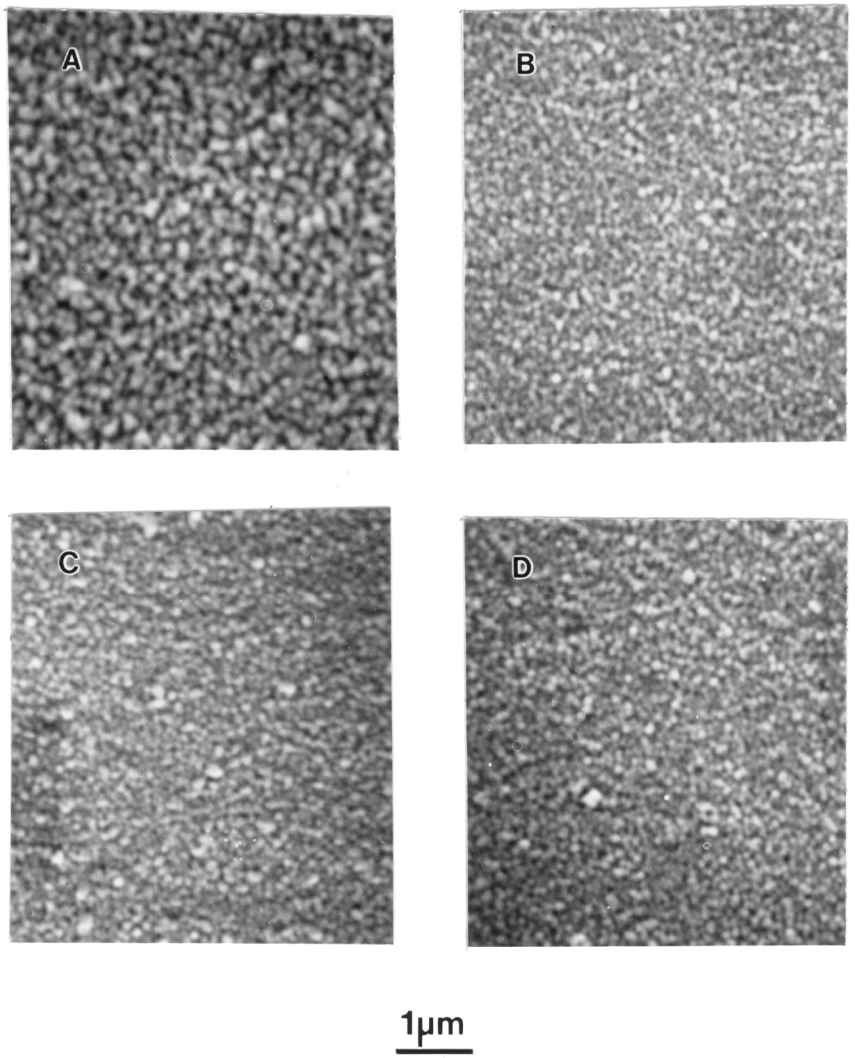

Figure 5.11 Reproducibility of surface morphology for four consecutive runs with the same deposition condition. The films were on $RuO_x/SiO_2/Si$ substrates.

5.4.5 Optical Properties

The UV–VIS–NIR transmission spectrum of the as–deposited PZT (x = 0.6) film on the sapphire substrate is shown in Figure 5.12. This spectrum illustrates that the transmittance drops down to 0% (the absorption edge) at a wavelength around 302 nm and has a value of 85% at a wavelength of 2000 nm. The envelope method (see Chapter 3) was used to calculate the film thickness as well as the refractive index and extinction coefficient of the film as a function of wavelength. This calculation procedure is mentioned in detail in Chapter 3. The film thickness calculated by this method is 510 nm. The n and k as a function of wavelength are shown in Figure 5.13. The n and k values are 2.413 and 0.0008, respectively at λ = 633 nm for the film with Zr/Ti = 60/40. The high refractive index value, compared to the value of 2.281 from MOD PZT films (Figure 3.11), indicates that the MOCVD PZT film is denser than the MOD film. The very low extinction coefficient illustrates the nature of the specular and highly transparent films.

5.4.6 Interrelationship of Composition Uniformity and Ferroelectric Properties

Although the phase, the microstructure, the "average" composition, and the electrodes of a particular MOCVD PZT film may all be good, the ferroelectric properties may not be as expected. One of the possible problems is that the composition uniformity through the bulk of the film may not be acceptable. Two typical samples were presented to demonstrate the effect of the composition uniformity across the film thickness on ferroelectric properties. Figure 5.14 shows the AES depth profile and selected AES spectra of the film with the "average"

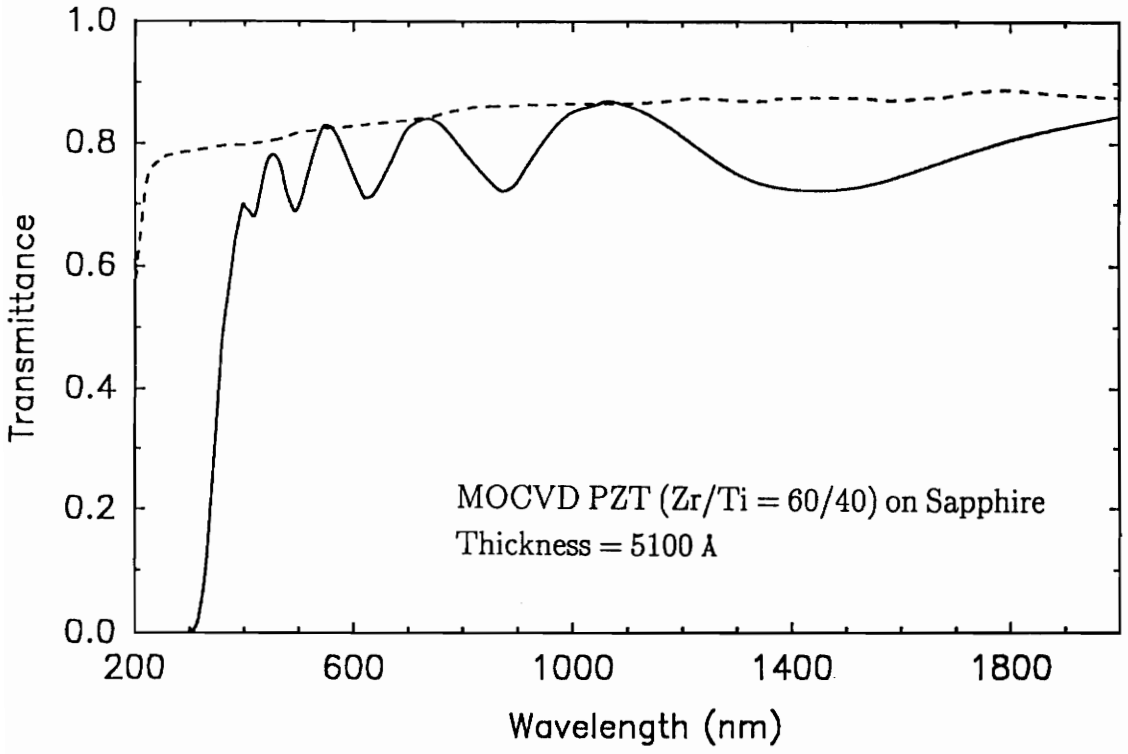

Figure 5.12 Optical transmission spectrum of as–deposited MOCVD $Pb(Zr_{0.6}Ti_{0.4})O_3$ film on sapphire on sapphire substrate. Dashed line shows the transmittance of the uncoated sapphire substrate.

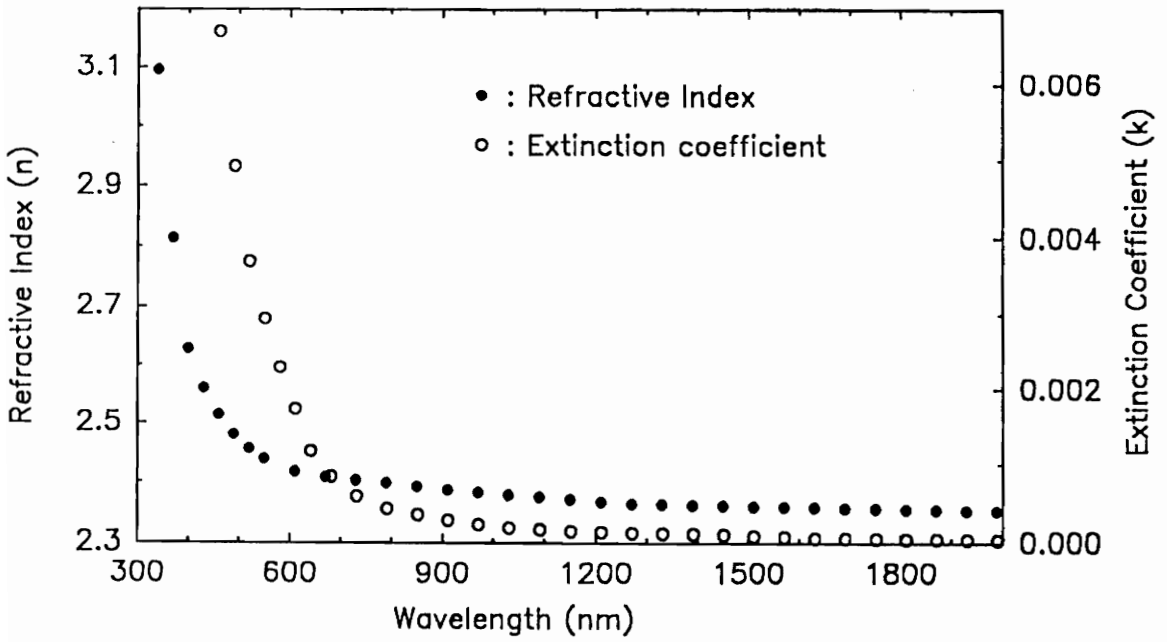

Figure 5.13 Variation of optical constants with wavelength for as–deposited MOCVD $Pb(Zr_{0.6}Ti_{0.4})O_3$ film.

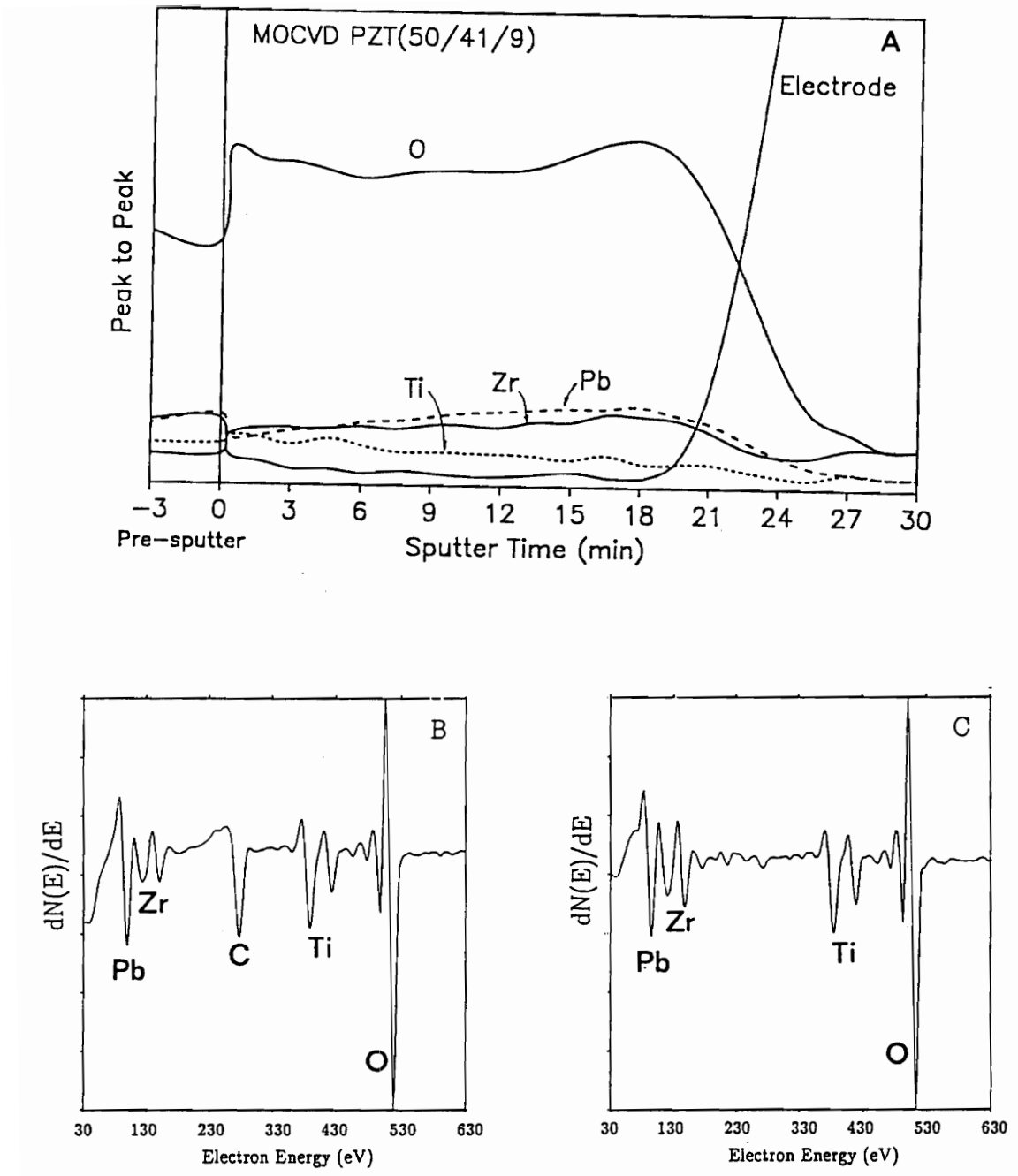

Figure 5.14 AES study of MOCVD PZT film with the composition of Pb/Zr/Ti = 50/41/9: (a) depth profile, (b) AES spectrum on the sample surface, and (c) AES spectrum after 3 min Ar sputtering.

composition of Pb/Zr/Ti = 50/41/9 which was measured by the EDS. For convenience, this sample will be referred to as sample A hereafter. Figure 5.15 shows the AES depth profile and selected AES spectra of the film with the "average" composition of Pb/Zr/Ti = 52/26/22 which was also measured by the EDS, and this sample will be referred to as sample B hereafter. The D–E hysteresis loops of sample A and B are shown in Figures 5.16 and 5.17, respectively.

As can be seen in Figure 5.14(a), the composition of sample A was quite uniform through the bulk of the film for all four elements i.e., Pb, Zr, Ti, and O. Figures 5.14(b) and 5.14(c) show the AES spectra both at the sample surface and after 3 minutes of Ar sputtering, respectively. The carbon peak shown in Figure 5.14(b) was due to the carbon adsorption on the sample surface. After 3 minutes of Ar sputtering, the carbon peak was not detected as can be seen in Figure 5.14(c). This indicates that no carbon contamination was found in the bulk of the film. On the other hand, the composition of sample B was less uniform through the thickness of the film than that of sample A. As can be seen in Figure 5.15(a), the Pb content appears to be uniform through the thickness of the film. In contrast to Pb content, the Zr content decreased, while the Ti and O contents increased with an increase in the sputtering time. This poor composition uniformity through the thickness of the film may be a result of the fairly high partial pressures of precursors during the initial stage of the deposition. The AES spectra of sample B at the sample surface and after 3 minutes Ar sputtering, which are shown in Figures 5.15(b) and 5.15(c), respectively, have similar behavior as those of sample A.

Although sample B has a preferable "average" composition than sample A (52/26/22 vs. 50/41/9), the composition profile through the thickness of each of the films resulted in sample A having superior ferroelectric properties: for sample A, the

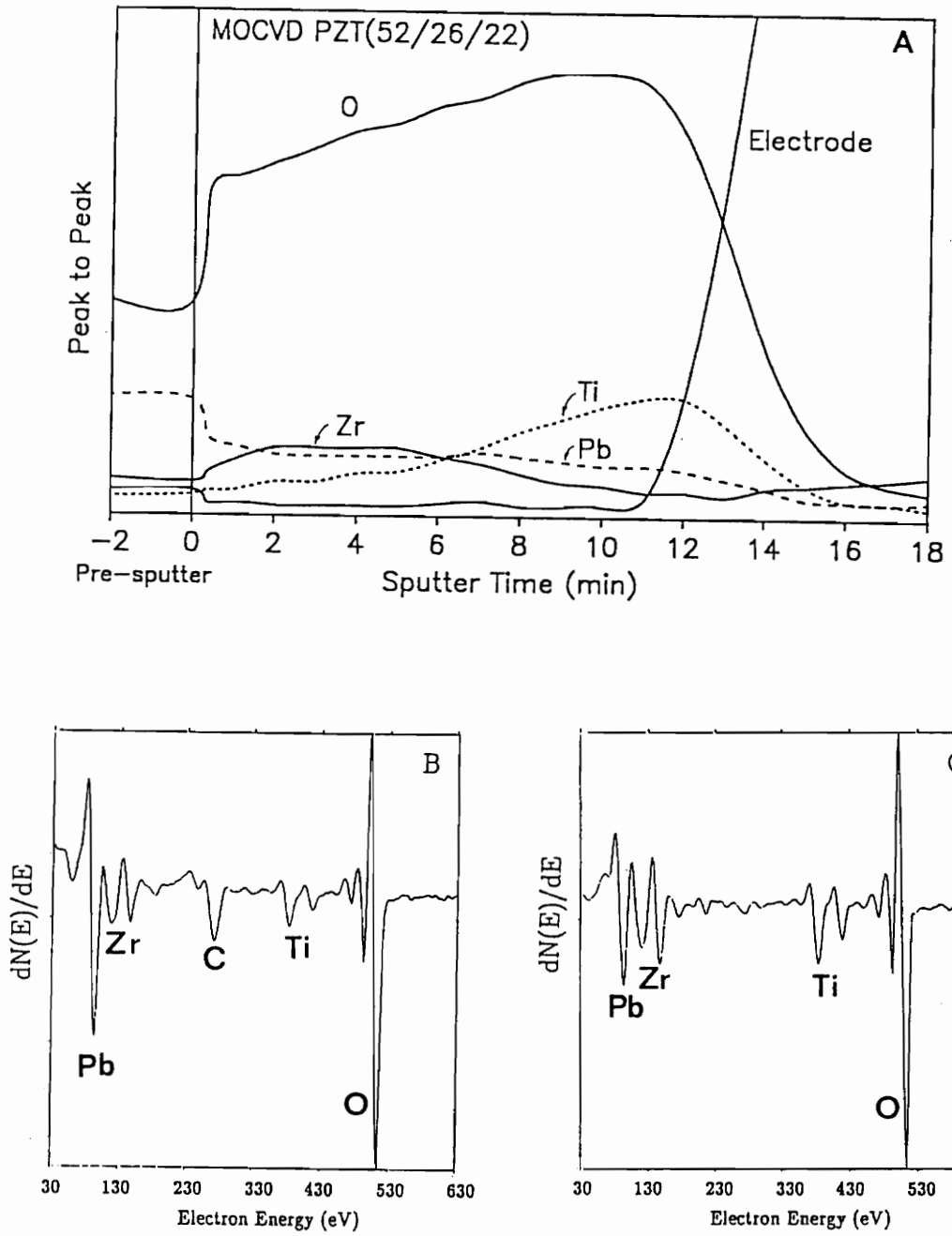

Figure 5.15 AES study of MOCVD PZT film with the composition of Pb/Zr/Ti = 52/26/22: (a) depth profile, (b) AES spectrum on the sample surface, and (c) AES spectrum after 3 min Ar sputtering.

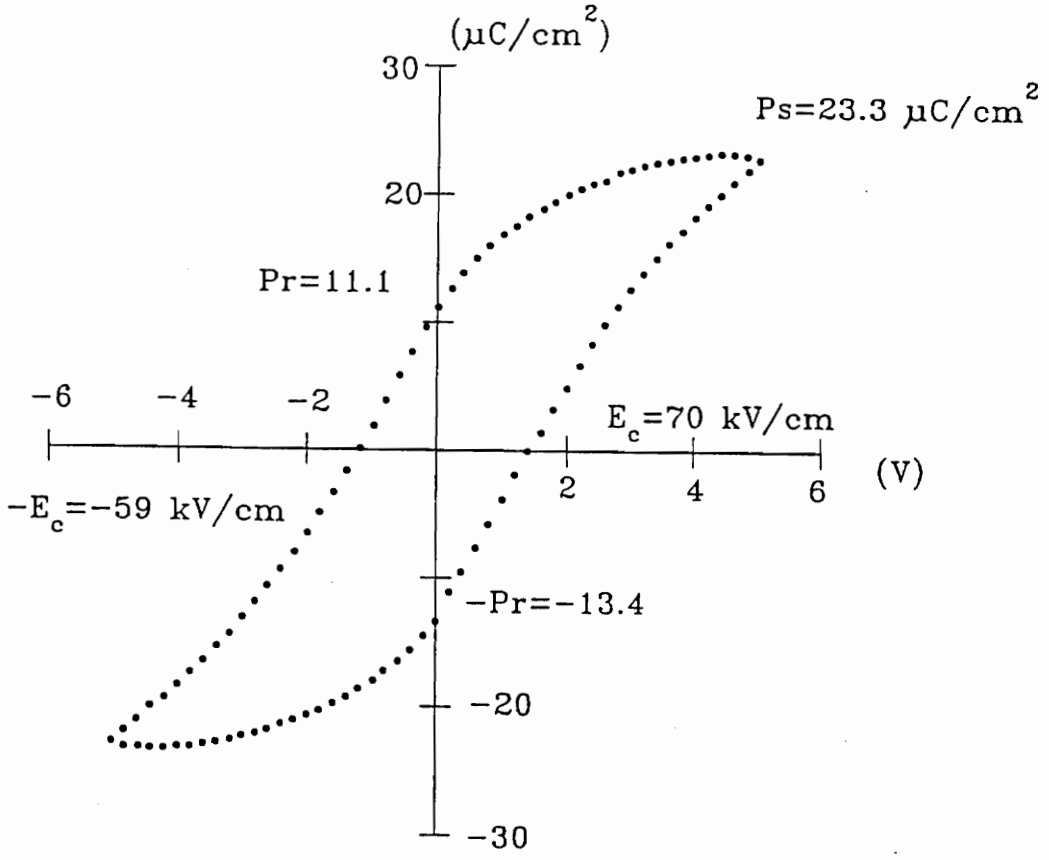

Figure 5.16 D–E hysteresis loop of 600°C/30min annealed MOCVD film whose composition profile is shown in Figure 5.14.

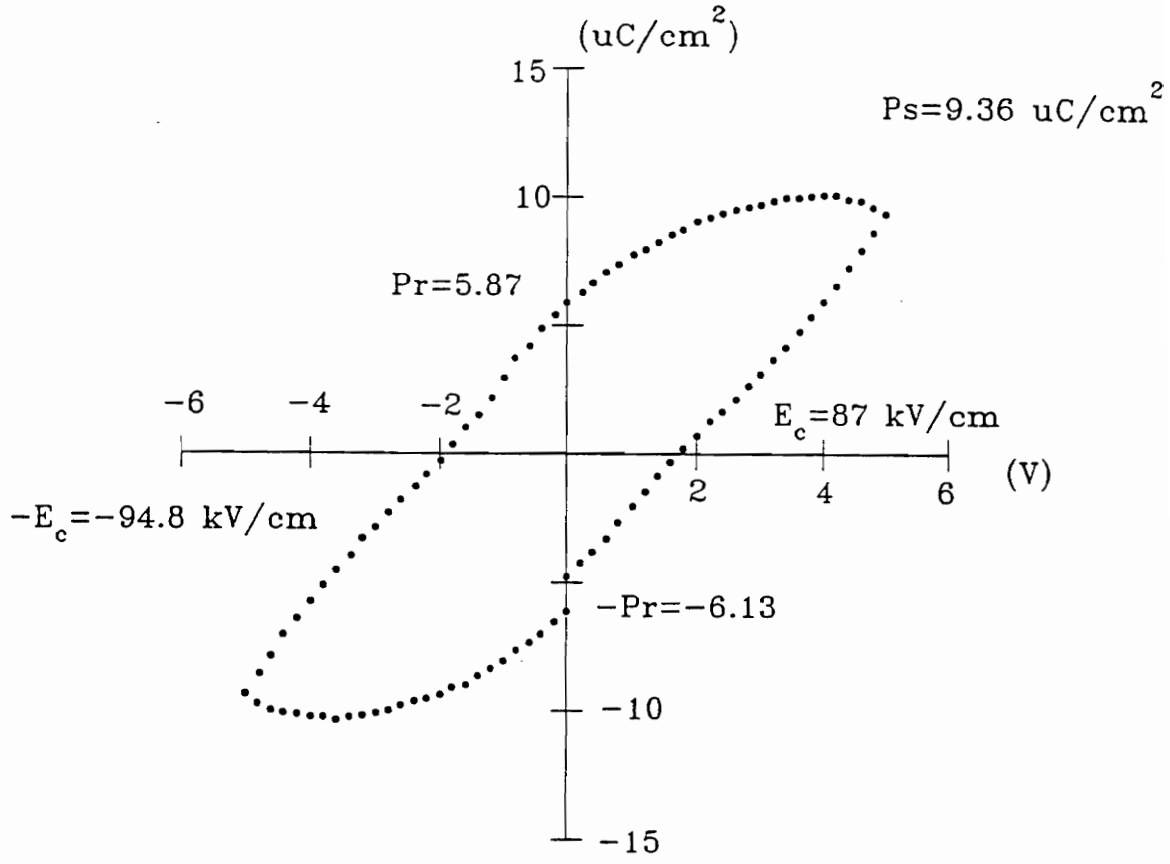

Figure 5.17 D–E hysteresis loop of 600°C/30min annealed MOCVD film whose composition profile is shown in Figure 5.15.

spontaneous polarization, P_s = 23.3 $\mu C/cm^2$, the remanent polarization, P_r = 12.3 $\mu C/cm^2$, and the coercive field, E_c = 64.5 kV/cm, see Figure 5.16. On the contrary, sample B had poor ferroelectric properties: P_s = 9.36 $\mu C/cm^2$, P_r = 6.0 $\mu C/cm^2$, and E_c = 90.9 kV/cm, as shown in Figure 5.17.

The composition non–uniformity at the interface of the film and the bottom electrode is due to the unstable source partial pressure during the initial deposition stage. To improve this problem, the CVD reactor was modified by adding a bypass line as shown in Figure 5.18. At the beginning of the deposition, the source vapors were flowed through the bypass line; oxygen was flowed through the deposition chamber to minimize the back diffusion of source vapors into the chamber. This bypass process was continued for about 3 minutes before beginning the deposition process. The effect of the bypass line can be seen in Figure 5.19. Figure 5.19(a) shows the AES depth profile of PZT film on $RuO_x/SiO_2/Si$ substrate without the bypass, and Figure 5.19(b) shows the AES depth profile of that with the bypass.

5.5 Cold–Wall MOCVD PZT Thin Films

A schematic diagram of the home–made cold–wall MOCVD apparatus with the bypass line is shown in Figure 5.20. The cold–wall reactor differs from the hot–wall reactor in that (1) only the substrates are heated, (2) the source vapors are vertically injected onto the substrates, and (3) the wall of the deposition chamber is kept around 250^{0}C. A three inch diameter substrate heater was employed, which can be operated at a maximum temperature of 900^{0}C. The temperature of the substrate heater is position insensitive within an 8^{0}C range, and the variation in temperature with time is within 1^{0}C. A substrate holder, which was made of

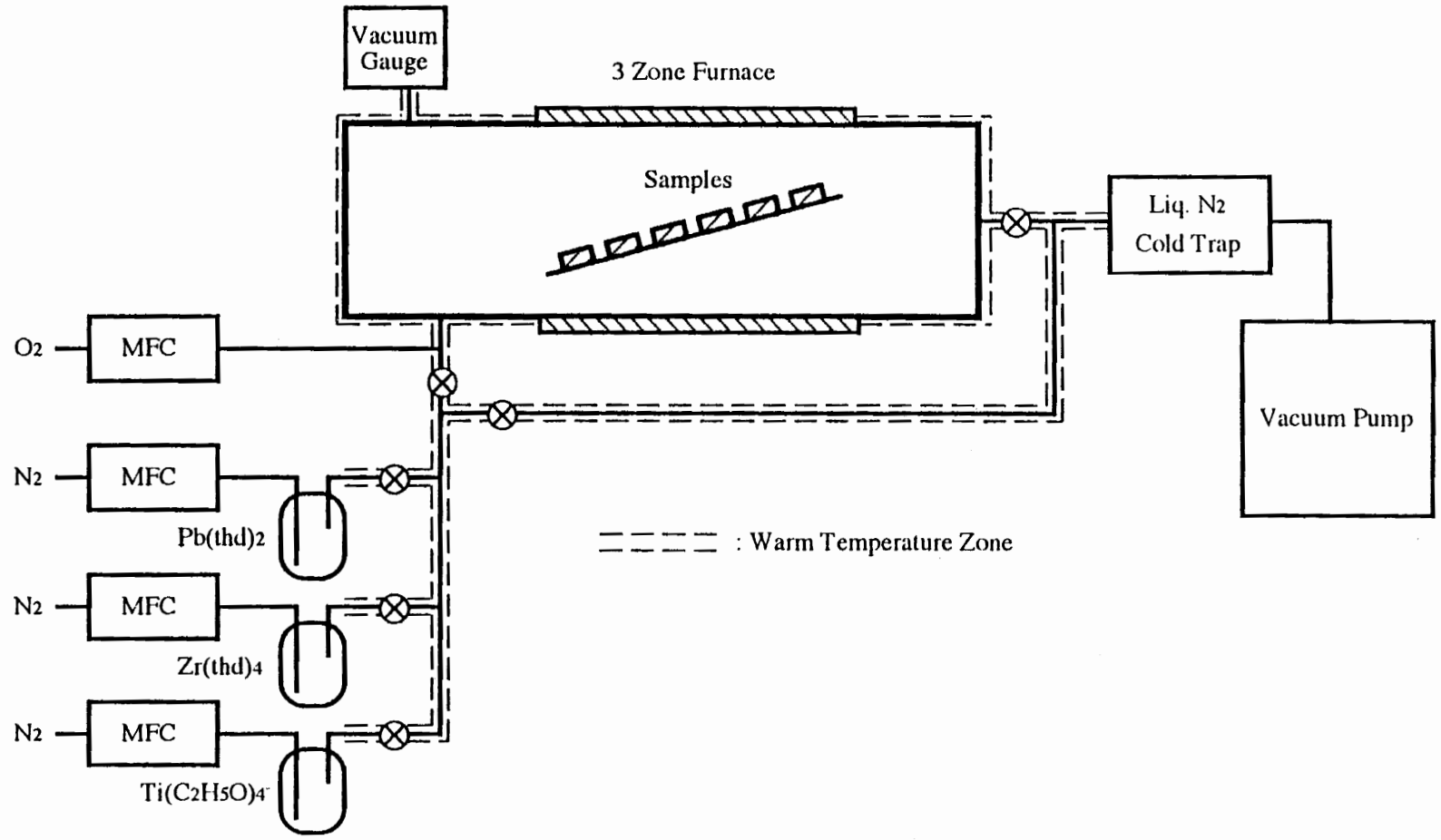

Figure 5.18 Schematic diagram of hot–wall MOCVD apparatus with bypass line.

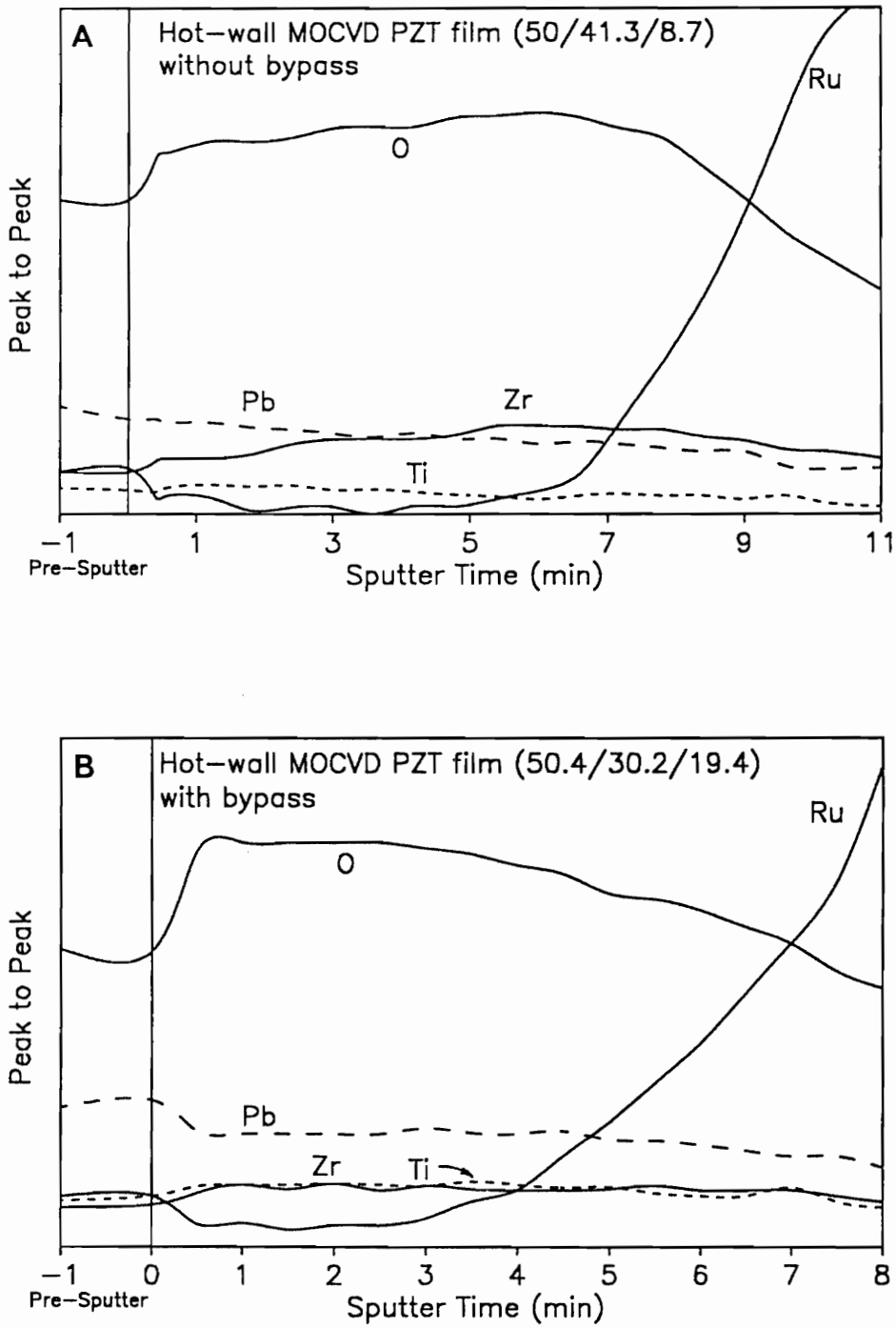

Figure 5.19 AES depth profiles of MOCVD PZT films on $RuO_x/SiO_2/Si$: (a) without bypass line and (b) with bypass line.

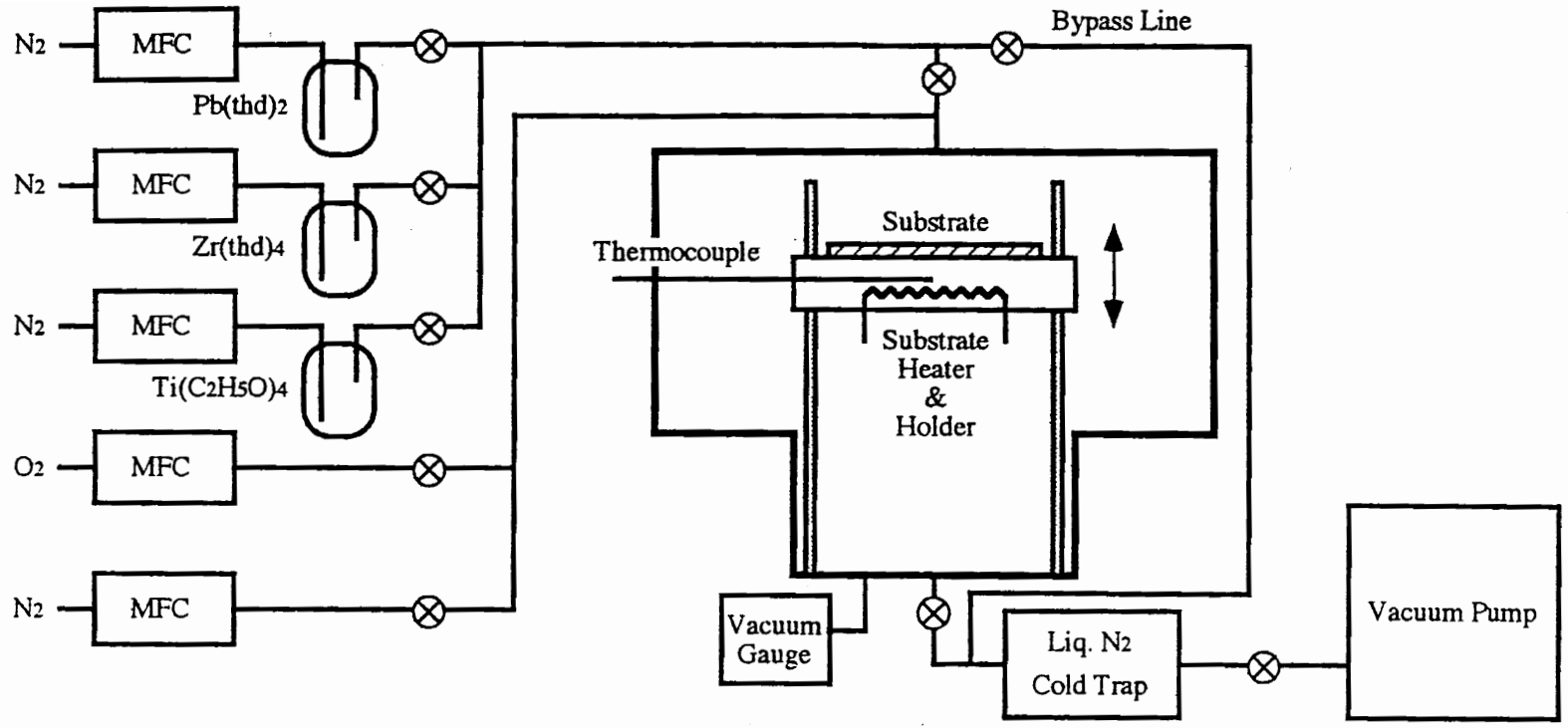

Figure 5.20 Schematic diagram of cold–wall MOCVD apparatus with bypass line.

INCONEL and was placed in direct contact with the substrate heater, was used to hold the substrates. The substrate temperature was monitored by a thermocouple which was directly placed inside the center of the substrate holder. The specimens were adhered on the substrate holder by silver paste. The silver paste was used to improve the heat conduction and the temperature uniformity of the specimens. The distance between the inlet of the source mixture and the substrates can be varied from 1.5 to 10 cm. The setup and the control of the bypass line and the bubbler heaters are similar to those of the hot–wall apparatus.

The deposition conditions of the cold–wall MOCVD PZT films were similar to those used in hot–wall apparatus except the deposition temperature was 600^{0}C. The PZT films obtained from cold–wall MOCVD were also uniform and specular on all three different substrates, i.e. sapphire disks, Pt/Ti/SiO_2/Si, and RuO_x/SiO_2/Si substrates. Typical XRD patterns of the as–deposited PZT films by cold–wall MOCVD are shown in Figure 5.21. The XRD patterns show that the films were single phase with perovskite structure. The film on the RuO_x–coated substrate was highly [111] oriented, while the films on the sapphire and Pt–coated substrates were non–oriented.

A very uniform and fine grain microstructure was also obtained from the cold–wall MOCVD PZT films. Figure 5.22 shows the SEM micrograph of the surface morphology of the cold–wall MOCVD PZT film on Pt–coated substrate whose XRD pattern is shown in Figure 5.21(b). The average grain size was estimated to be about 0.1 μm.

5.6 Summary

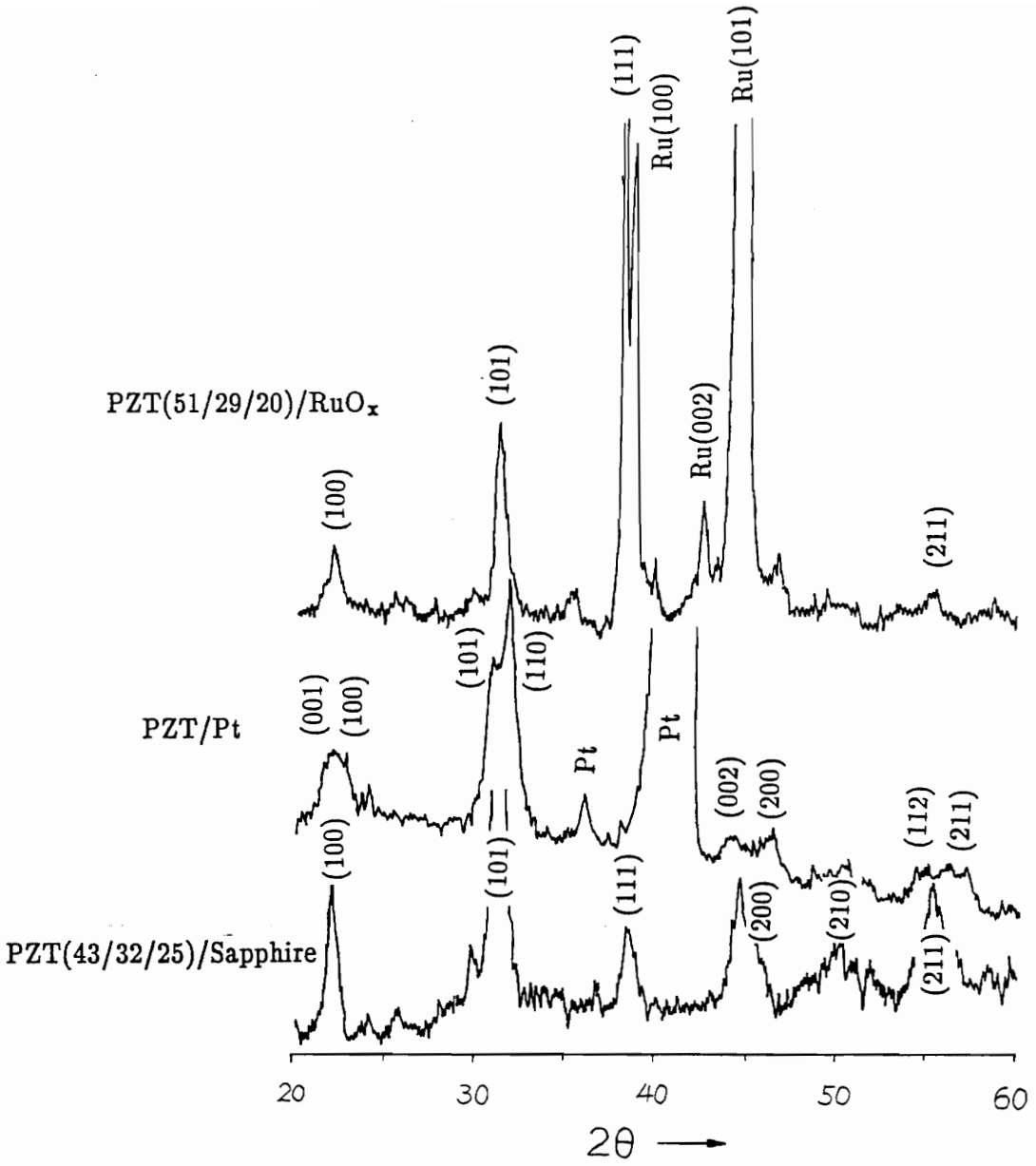

Figure 5.21 XRD patterns of MOCVD PZT films deposited by cold–wall reactor at 600°C: (a) on $RuO_x/SiO_2/Si$, (b) on $Pt/Ti/SiO_2/Si$, and (c) on sapphire.

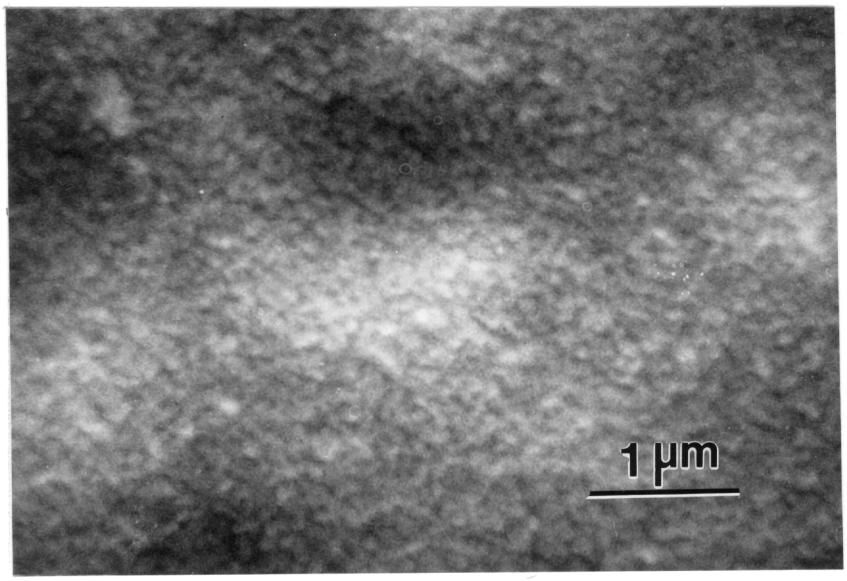

Figure 5.22 SEM micrograph of cold–wall MOCVD PZT film on $Pt/Ti/SiO_2/Si$.

(1) Smooth and specular PZT thin films with pure perovskite phase were successfully fabricated at temperatures as low as 550^{0}C on sapphire disks and Si wafers coated with either Pt or RuO_x by hot–wall MOCVD using $Pb(thd)_2$, $Zr(thd)_4$, $Ti(OEt)_4$, and O_2 as source materials.

(2) Highly [001] oriented films were occasionally obtained on all three different substrates.

(3) The reproducibility has been confirmed by four consecutive depositions.

(4) The stoichiometry of the films can be easily controlled either by varying the individual precursor temperature and/or the flow rate of the carrier gas.

(5) The compositions of films were uniform from sample to sample for up to two thirds of the length of the uniform temperature zone (i.e., 20 cm in this study) when 1000 sccm oxygen was used as the diluent gas.

(6) High refractive index (n = 2.413) and low extinction coefficient (k = 0.0008) were obtained for the films on the sapphire disks.

(7) The average grain sizes of the films on all three different substrates used were found to be $\approx$ 0.1 μm.

(8) The surface morphology of the films seems to be independent of the substrate, the film composition, and the annealing temperature.

(9) The AES spectrum showed no carbon contamination in the bulk of the film, and the AES depth profile showed an uniform composition distribution for the films deposited using the bypass.

(10) A well defined D–E hysteresis loop was observed with the ferroelectric properties of P_s=23.3 μC/cm^2, P_r=12.3 μC/cm^2, and E_c=64.5 kV/cm for the film with Zr/Ti = 82/18.

(11) Smooth and specular PZT films with pure perovskite phase were also

obtained by cold–wall MOCVD.

Chapter 6 Summary

The results of this research are now summarized as follows:

1. Ferroelectric thin films of lead zirconate titanate were successfully fabricated by the metalorganic decomposition process for the entire lead–titanate and lead–zirconate solid solution range. The average grain size of the MOD PZT films was found to increase with increasing zirconium content.

2. The optical properties (the refractive index, the extinction coefficient, and the absorption coefficient near the band gap) and the thickness of the PZT thin films were studied. The envelope method, with consideration of light intensity loss from the back surface of the substrate, was shown to be a simple and convenient tool for obtaining the optical properties and the film thickness of the PZT films by using the transmission spectra alone in the medium and weak absorption regions. In the near optical band gap region, both the transmission and the reflection spectra were used to successfully calculate the optical constants of the films. The film thickness derived from the envelope method was cross checked by a computer simulation method and was found to have an accuracy better than 2%. In addition, the refractive indices were fitted to a simple Sellmeier type equation for determining the dispersion constants for both porous PZT films and bulk PZT materials. The

valid wavelength range of these dispersion relations was found to be from 350 nm to 2000 nm.

3. The refractive index of the PZT films decreased linearly with increasing zirconium content. On the other hand, the near optical band gap energy of the PZT materials increased with increasing the zirconium content.

4. An effective, versatile, and nondestructive optical method was developed for the study of the structure development in MOD PZT films. Also, the models for the structure development were proposed and were verified by this optical method. Using this method, the characteristic temperatures (i.e., the initiation and the completion temperatures) of each phase can be easily identified. The structure developments in MOD PZT films were found to involve at least three phases in a certain temperature range. In addition, the volume fraction of each phase in a two–phase mixture can be obtained.

5. For the PZT films prepared by the MOD process, the perovskite phase formed at much lower temperatures in titanium rich PZT films compared to those of zirconium rich PZT films; for example, 460^{0}C for $PbTiO_3$ and 650^{0}C for $PbZrO_3$.

6. The ferroelectric PZT thin films were successfully deposited at temperatures as low as 550^{0}C on sapphire disks, $Pt/Ti/SiO_2/Si$ wafers, and $RuO_x/SiO_2/Si$ wafers by hot–wall MOCVD using safe and stable precursors, namely, lead tetramethylheptadione [$Pb(thd)_2$], zirconium tetramethylheptadione [$Zr(thd)_4$], titanium ethoxide [$Ti(OEt)_4$], and oxygen (O_2). The films had the pure perovskite

phase in the as–deposited state. Also, the films were smooth, specular, crack–free, uniform, and adhered well on all substrates used. The reproducibility has been confirmed by four consecutive depositions.

7. The stoichiometry of the films can be easily controlled either by varying the individual precursor temperature and/or the flow rate of the carrier gas. The sample–to–sample composition uniformity was found to be very good for up to two thirds of the length of the uniform temperature zone (i.e., 20 cm in this study) when 1000 sccm oxygen was used as the dilute gas.

8. The surface morphology of the MOCVD PZT films seems to be independent of the substrate, the film composition, and the annealing temperature. The average grain size of the films on all three different substrates used was found to be around 0.1μm.

9. Two significant differences on the structure properties between the MOD and the MOCVD films were observed: (1) the perovskite phase of the MOCVD film was completely formed at the deposition temperature (550^0C) regardless of the Zr/Ti ratio, while for the MOD film, the temperature at which the formation of the perovskite phase was completed was strongly dependent on the Zr/Ti ratio, (2) the microstructure of the MOCVD PZT film was found to be an insensitive function of the substrate, the composition, and the annealing temperature, while that of the MOD film was a strong function of the substrate, the composition, and the annealing temperature.

10. High refractive index (n = 2.413 at λ = 632.8 nm) and low extinction coefficient (k = 0.0008 at λ = 632.8 nm) were obtained for the $Pb(Zr_{0.6}Ti_{0.4})O_3$ film on the sapphire disk. The refractive index value of 2.413 at λ = 632.8 nm corresponds to a packing density of 0.93. The very low extinction coefficient illustrates the nature of the specular and highly transparent films.

11. The AES spectrum showed no carbon contamination (the detection level is less than 1 at%) in the bulk of the film, and the AES depth profile showed uniform composition distribution for the films deposited using the bypass. The composition uniformity through the thickness of the film was found to have a significant effect on the ferroelectric properties. For a film with a uniformly distributed composition with Zr/Ti = 82/18, a well defined D–E hysteresis loop was observed with the superior ferroelectric properties of P_s = 23.3 $\mu C/cm^2$, P_r = 12.3 $\mu C/cm^2$, and E_c = 64.5 kV/cm.

12. Highly [100] oriented films were occasionally obtained on all three different substrates by both the hot–wall MOCVD and the cold–wall MOCVD.

Chapter 7 Suggestions for Future Research

The results of this study are far from final, and in fact only touch the surface of the ferroelectric materials, especially in the MOCVD aspect. In this chapter several directions which follow from the present research will be suggested.

The film thickness measurements are very important in a thin film processing technique because they give information on the film growth rate. As mentioned in Chapter 2, the film thickness can also be measured by either an optical profilometer or a stylus profilometer, both of which require a sharp step between the film and the substrate. This sharp step may be created by either covering a small portion of the substrate during the deposition or etching away a small portion of the film after the deposition. However, either one of these methods may not work in many cases. For example, it is not easy to generate a sharp step during the chemical vapor deposition because of the high temperature process and the high penetration nature of the chemical vapors. Also, it is very difficult to find an etching solution which can isotropically etch the film away without damaging the substrate.

The film thickness measurement using the optical transmission or reflection spectrum is very attractive because it is nondestructive. Although an accurate measurement technique for the film thickness using the transmission interference fringes along with the envelope method has been demonstrated in Chapter 2, it is only good for films on a transparent substrate. For a film on an opaque substrate such as

silicon wafer or metal–coated silicon wafer, the following procedures are suggested for the film thickness calculation:

(1) measure the reflection spectrum of the sample

(2) use a simple Sellmeier type dispersion relation, for example equation 2.43, for refractive index

(3) use equation 2.10 with three unknowns, i.e., the film thickness and two dispersion constants, to fit the experimental reflection spectrum

For the case of the PZT thin films, the dispersion constants obtained in this study could be used for the initial guess in the above procedures.

The phase transformation kinetics can be easily obtained using the method developed in Chapter 3, if the refractive index of the sample is studied as a function of time at several temperatures in the pyrochlore–perovskite phase transformation region. In addition, the proposed models for the structure development in the PZT films may be confirmed by using Ramam scattering which is more direct and may be more sensitive than the method described in Chapter 3.

One of the goals of this research is to develop a reliable MOCVD process for PZT thin films. Although successful and reproducible depositions and good properties of PZT films have been achieved, many problems still need to be solved, such as

(1) Understanding of the deposition process

(2) Understanding how the deposition rate and the substrate affect the nucleation and the growth of the film

(3) Understanding the difference between the hot–wall and the cold–wall

MOCVD PZT films

Additionally, a dopant such as lanthanum can be incorporated into the PZT film by the established MOCVD PZT reactor and process.

Appendix A Preparation of PZT Precursor Solutions

To prepare an M molar fraction solution, it follows

$$M = \frac{w}{W_M V} \tag{A.1}$$

where W_M is molecular weight of solute, w is is the weight of solute, and V is the volume of the solution in liter. The molecular weight and purity of the starting precursors are listed in Table A.1. If, for example, we want to prepare a 0.5 mole 30 ml lead titanate (PT) precursor solution with 10% lead acetate excess, the detailed procedures are as follows:

1. Weigh 6.2589 g of lead acetate (0.5 x 379.33 x 0.03 = 5.6899 g with 10% excess).

2. Add about 50 ml methoxyethanol into lead acetate (referred to as solution A).

3. Distill solution A at 120^{0}C until the volume is reduced to about 30 ml (the purpose of this step is to boil off the water in lead acetate, solution B).

4. Add 4.2637 g titanium isopropoxide into solution B (0.5 x 284.25 x 0.03 = 4.2637 g) and stir it (solution C).

5. Distill solution C at 120^{0}C until the volume is reduced to less than 30 ml.

6. Add proper amounts of methoxyethanol to make the final solution volume of 30 ml.

The same procedure can be applied to prepare a 0.5 mole 30 ml lead zirconate (PZ) precursor solution except that at step 4, a 7.0191 g zirconium n–propoxide should be used (the purity of the precursor must be taken into acount). The final PZT precursor solutions are prepared by mixing PT and PZ solutions in volume fraction according to the desired Zr/Ti composition ratio.

Table A.1 The molecular weight and purity of PZT precursors

Precursor	Formula	Molecular Weight	Purity
Lead Acetate	$Pb(OOCCH_3)_2 \cdot 3H_2O$	379.33	100%
Titanium Isopropoxide	$Ti(OC_3H_7)_4$	284.25	100%
Zirconium n–Propoxide	$Zr(OC_3H_7)_4$	327.56	70%

Appendix B

This Appendix collects figures not presented in Chapter 2 for the optical properties study of PZT thin films. They are

Figures B.1 – B.6	The reflection and the transmission spectra and their sum of $Pb(Zr_xTi_{1-x})O_3$
Figures B.7 – B.12	The refractive index as a function of wavelength and the dispersion curve of $Pb(Zr_xTi_{1-x})O_3$
Figures B.13 – B.18	Adjusted refractive index as a function of wavelength and the dispersion curve of $Pb(Zr_xTi_{1-x})O_3$
Figures B.19 – B.23	The extinction coefficient as a function of wavelength of $Pb(Zr_xTi_{1-x})O_3$
Figures B.24 – B.30	The experimental and simulated transmission spectra of $Pb(Zr_xTi_{1-x})O_3$

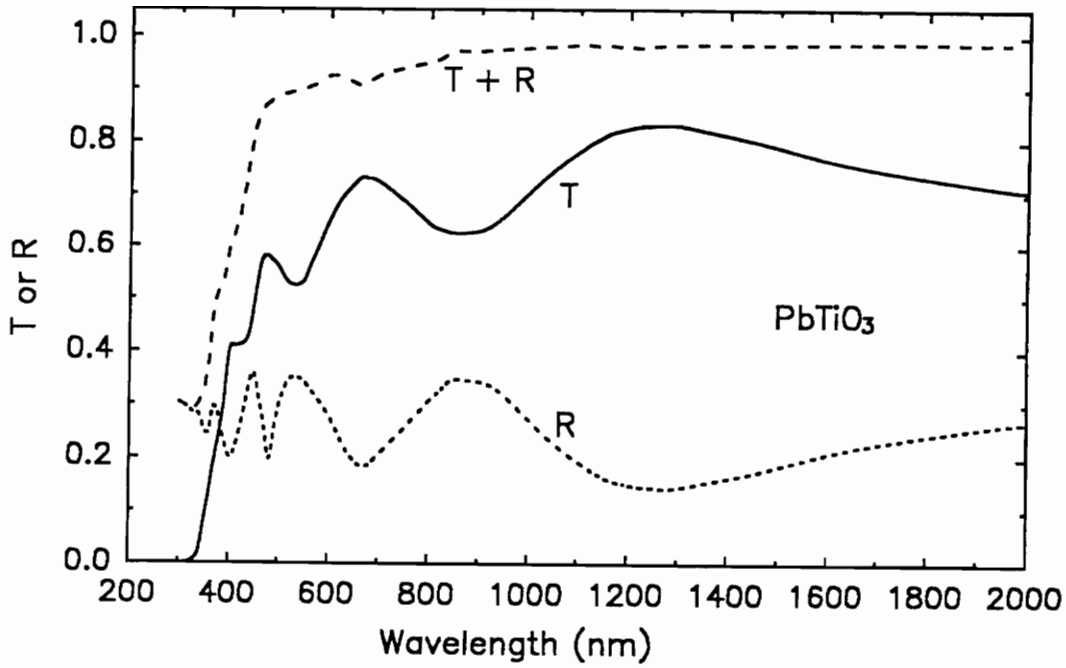

Figure B.1 The reflectance and the transmittance and their sum of $PbTiO_3$ film on sapphire in the wavelength range of 300 nm to 2000 nm. The reflection spectrum was measured without the black paint on the back surface of the substrate.

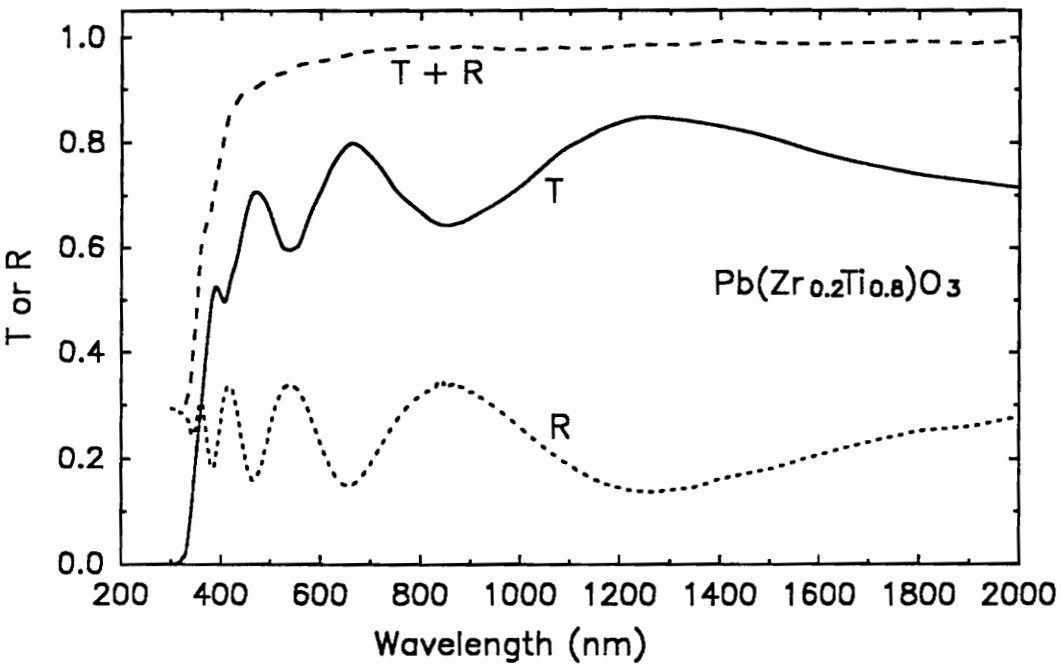

Figure B.2 The reflectance and the transmittance and their sum of $Pb(Zr_{0.2}Ti_{0.8})O_3$ film on sapphire in the wavelength range of 300 nm to 2000 nm. The reflection spectrum was measured without the black paint on the back surface of the substrate.

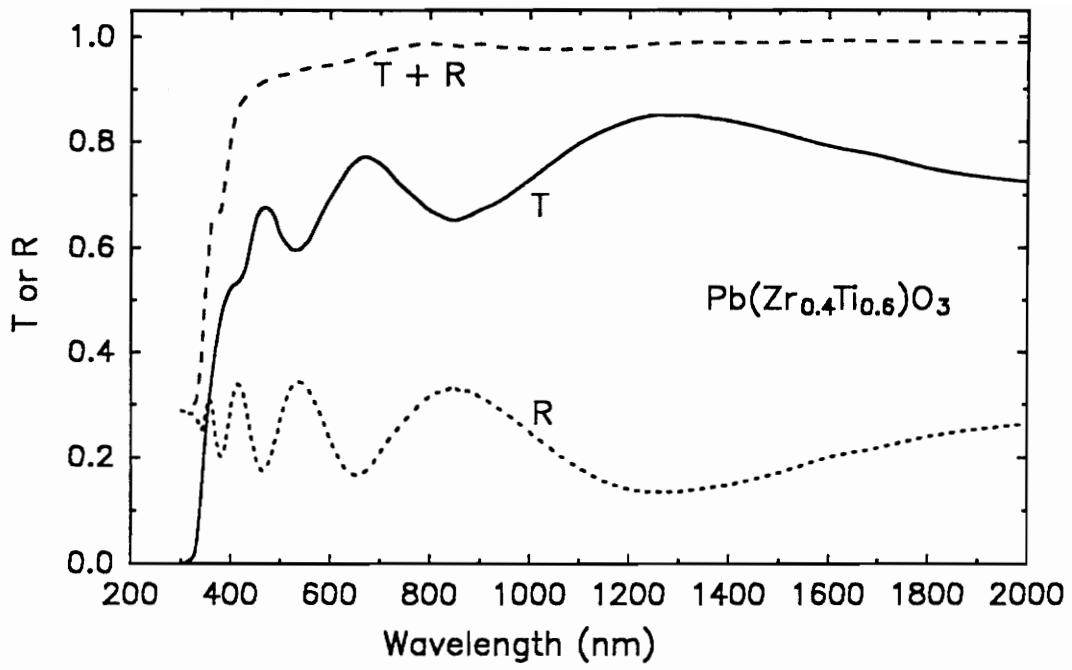

Figure B.3 The reflectance and the transmittance and their sum of $Pb(Zr_{0.4}Ti_{0.6})O_3$ film on sapphire in the wavelength range of 300 nm to 2000 nm. The reflection spectrum was measured without the black paint on the back surface of the substrate.

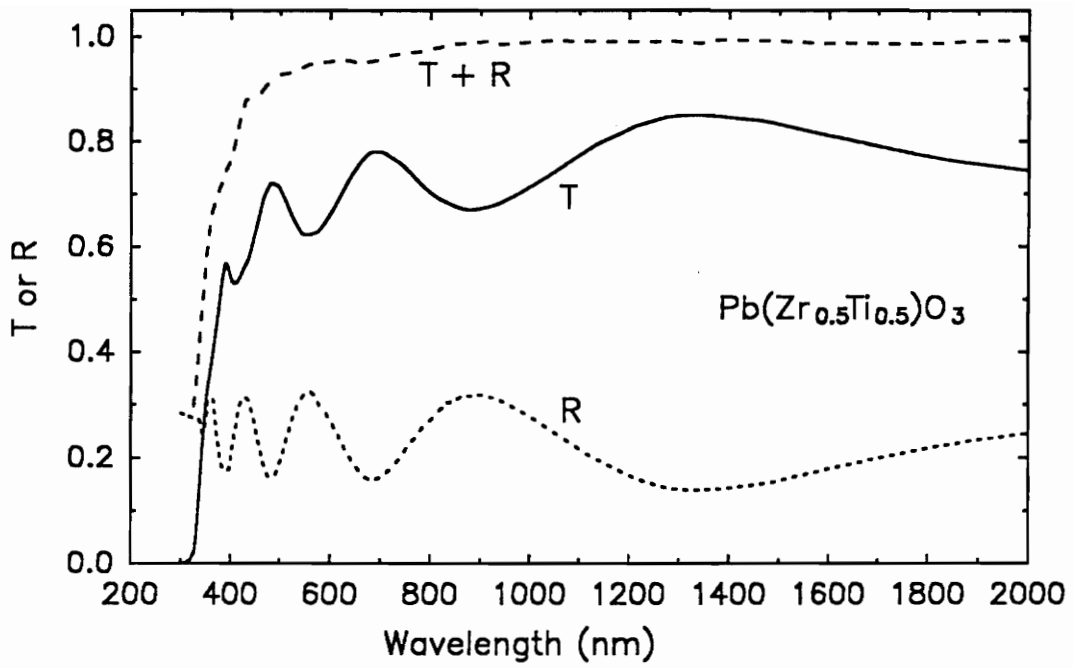

Figure B.4 The reflectance and the transmittance and their sum of $Pb(Zr_{0.5}Ti_{0.5})O_3$ film on sapphire in the wavelength range of 300 nm to 2000 nm. The reflection spectrum was measured without the black paint on the back surface of the substrate.

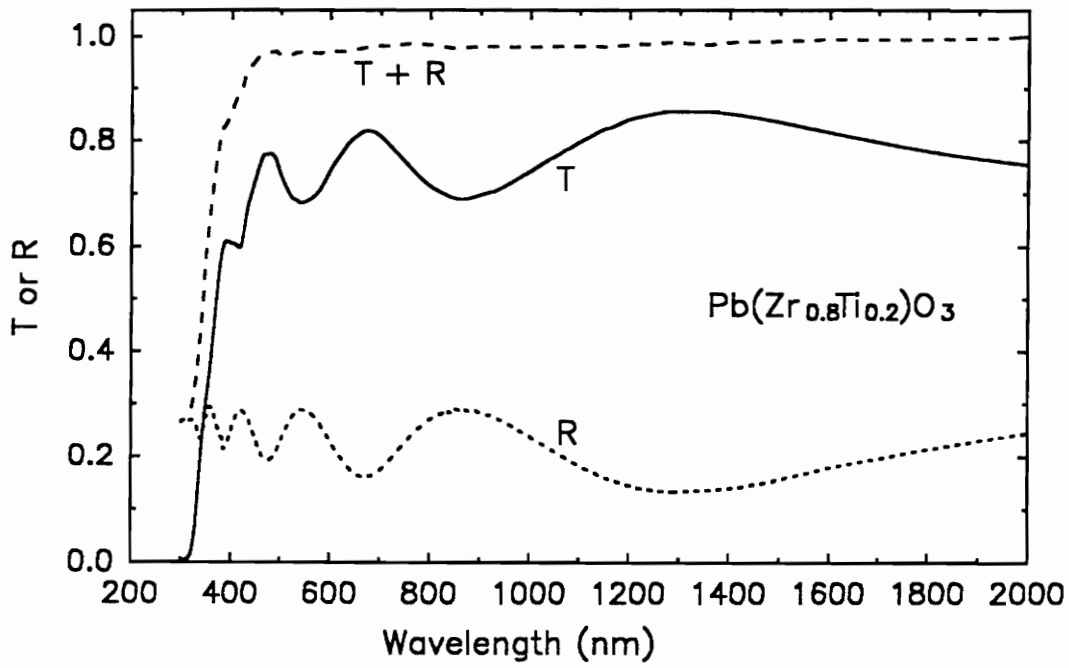

Figure B.5 The reflectance and the transmittance and their sum of $Pb(Zr_{0.8}Ti_{0.2})O_3$ film on sapphire in the wavelength range of 300 nm to 2000 nm. The reflection spectrum was measured without the black paint on the back surface of the substrate.

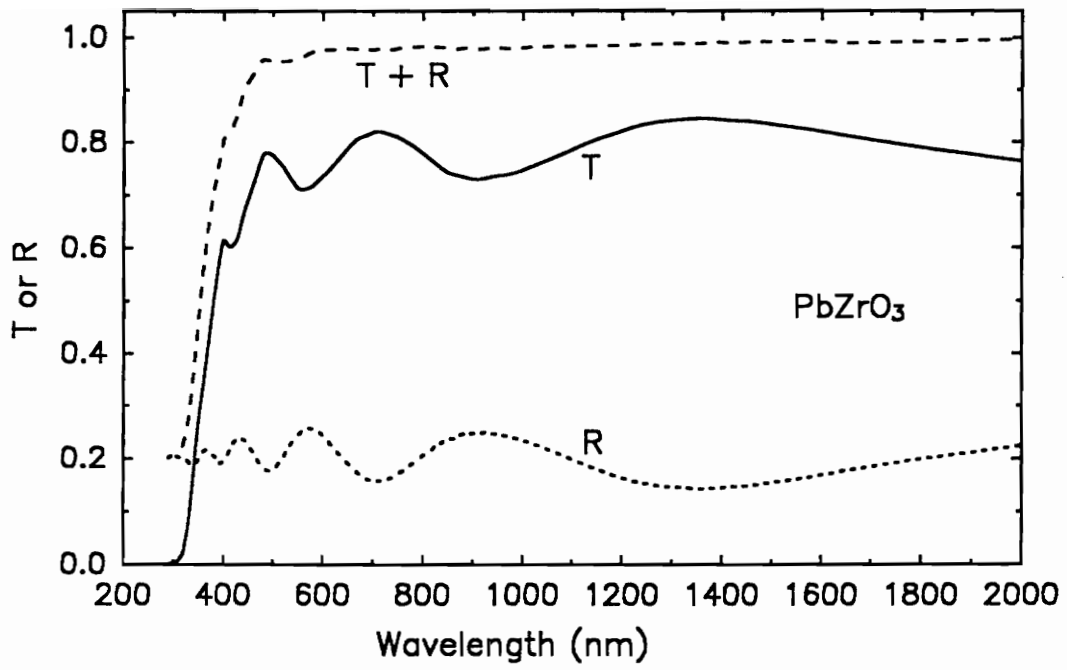

Figure B.6 The reflectance and the transmittance and their sum of $PbZrO_3$ film on sapphire in the wavelength range of 300 nm to 2000 nm. The reflection spectrum was measured without the black paint on the back surface of the substrate.

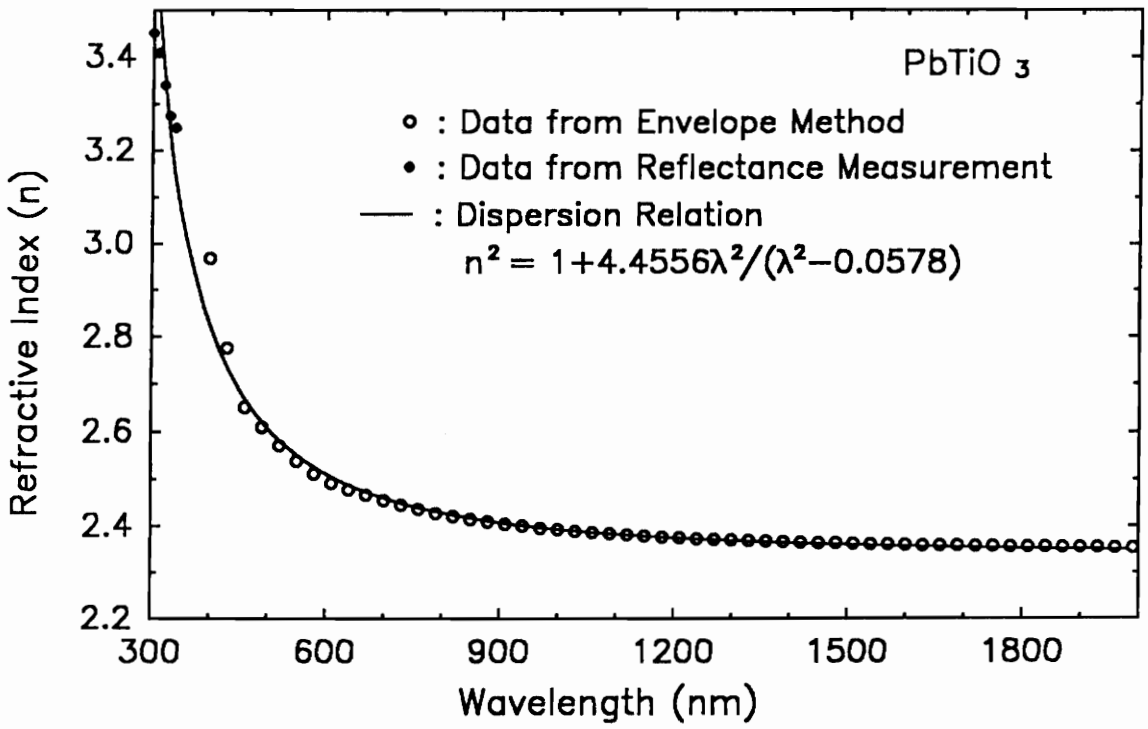

Figure B.7 The refractive index as a function of wavelength and the dispersion curve of $PbTiO_3$ film

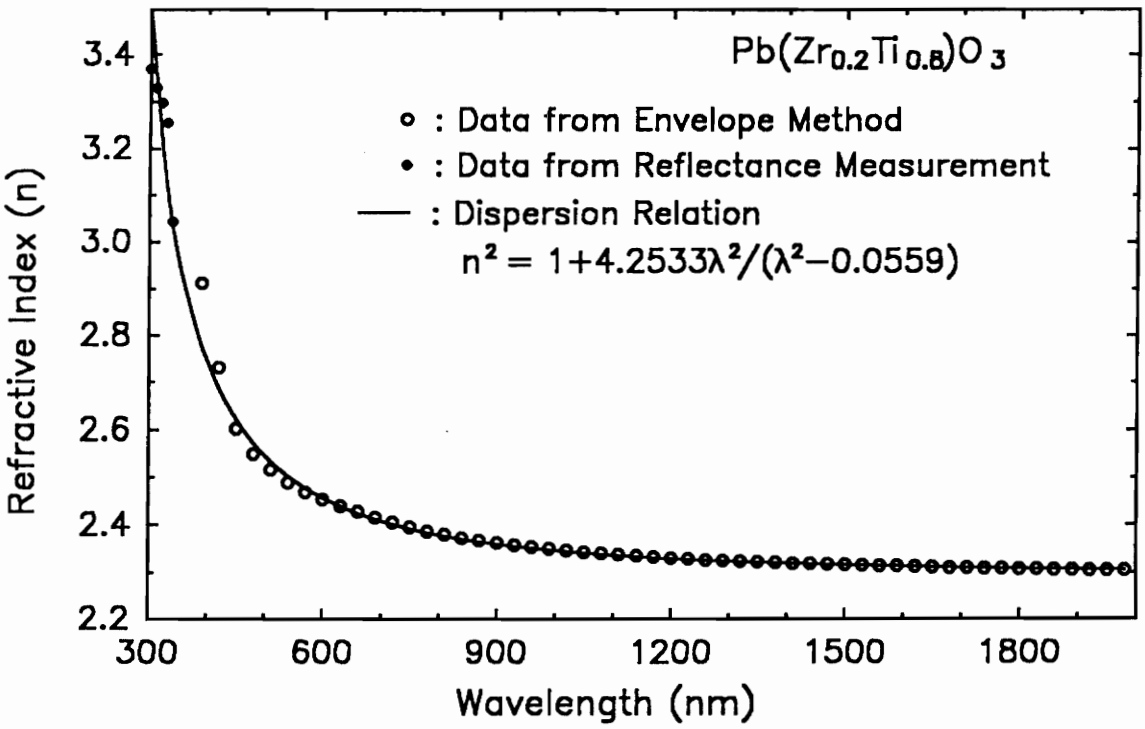

Figure B.8 The refractive index as a function of wavelength and the dispersion curve of $Pb(Zr_{0.2}Ti_{0.8})O_3$ film

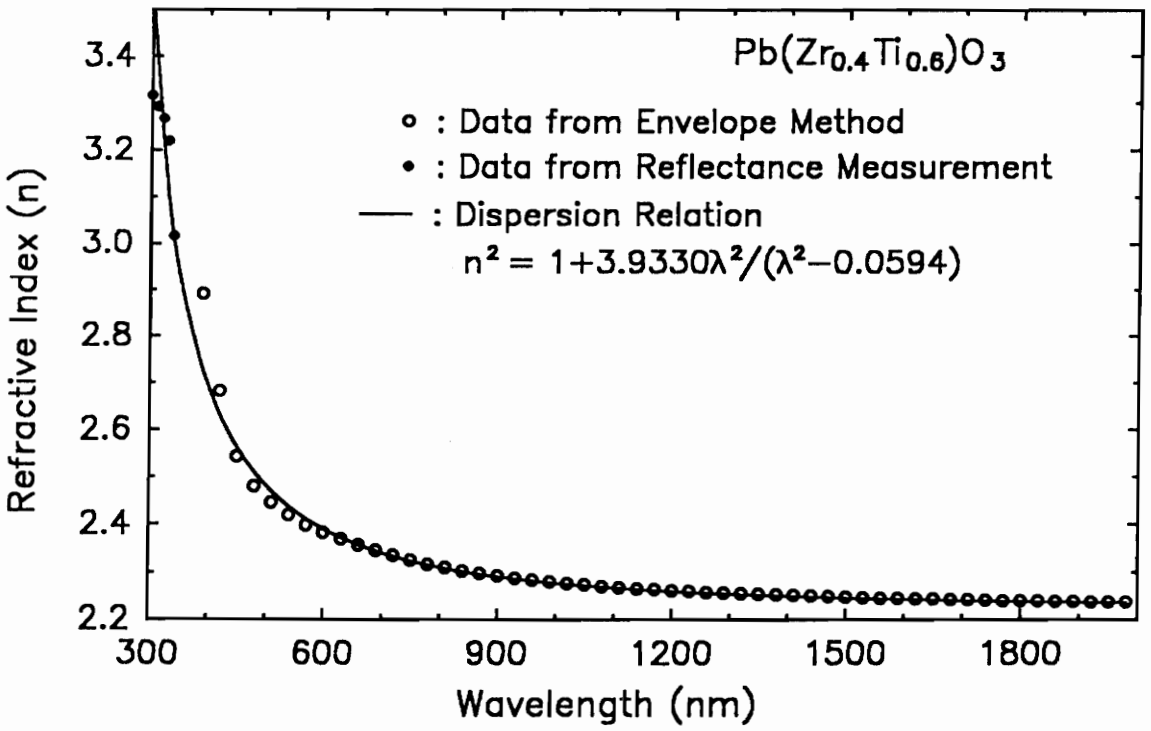

Figure B.9 The refractive index as a function of wavelength and the dispersion curve of $Pb(Zr_{0.4}Ti_{0.6})O_3$ film

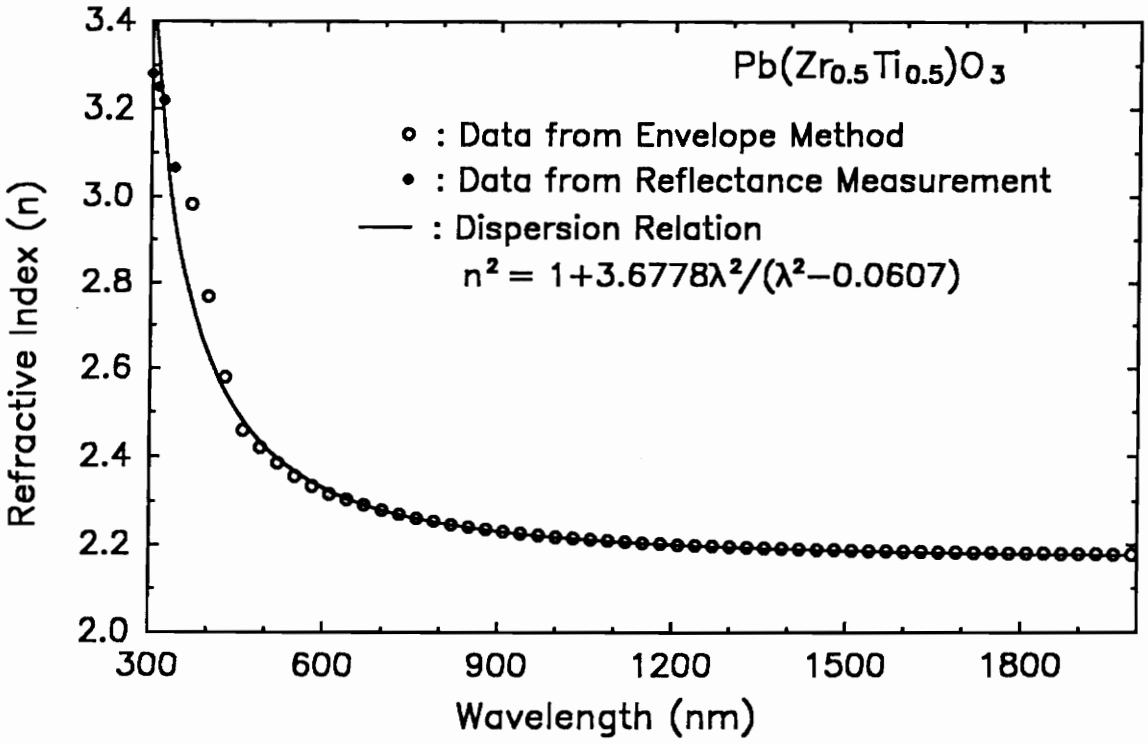

Figure B.10 The refractive index as a function of wavelength and the dispersion curve of $Pb(Zr_{0.5}Ti_{0.5})O_3$ film

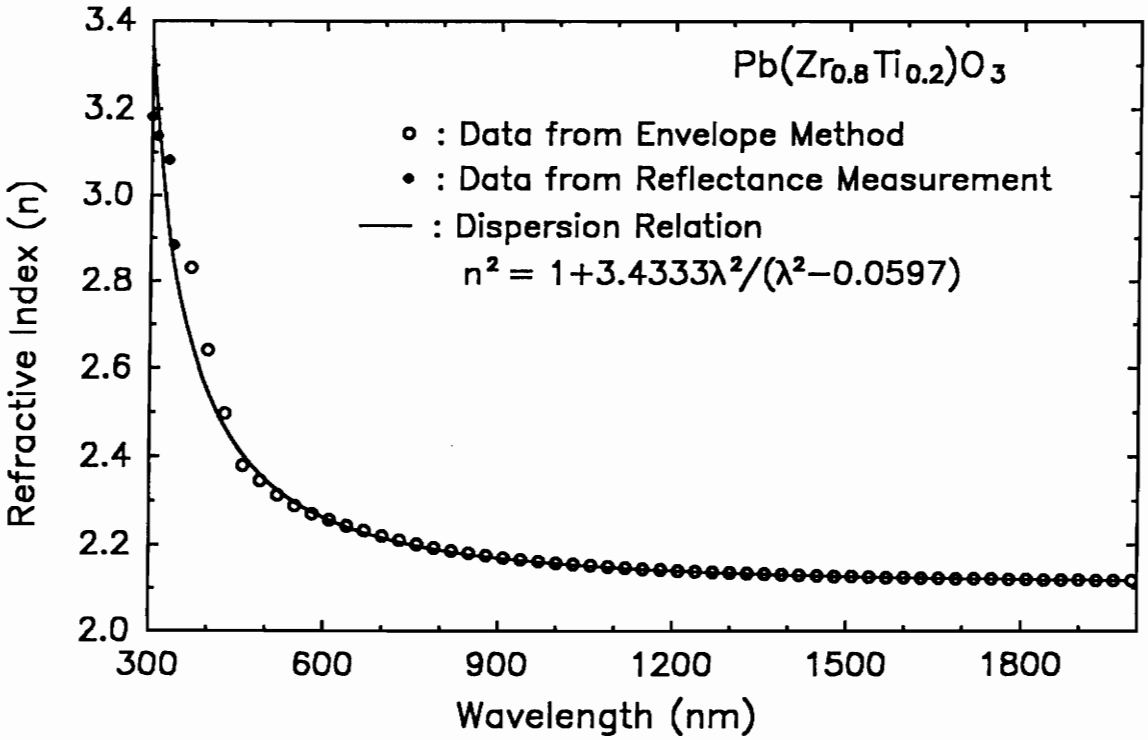

Figure B.11 The refractive index as a function of wavelength and the dispersion curve of $Pb(Zr_{0.8}Ti_{0.2})O_3$ film

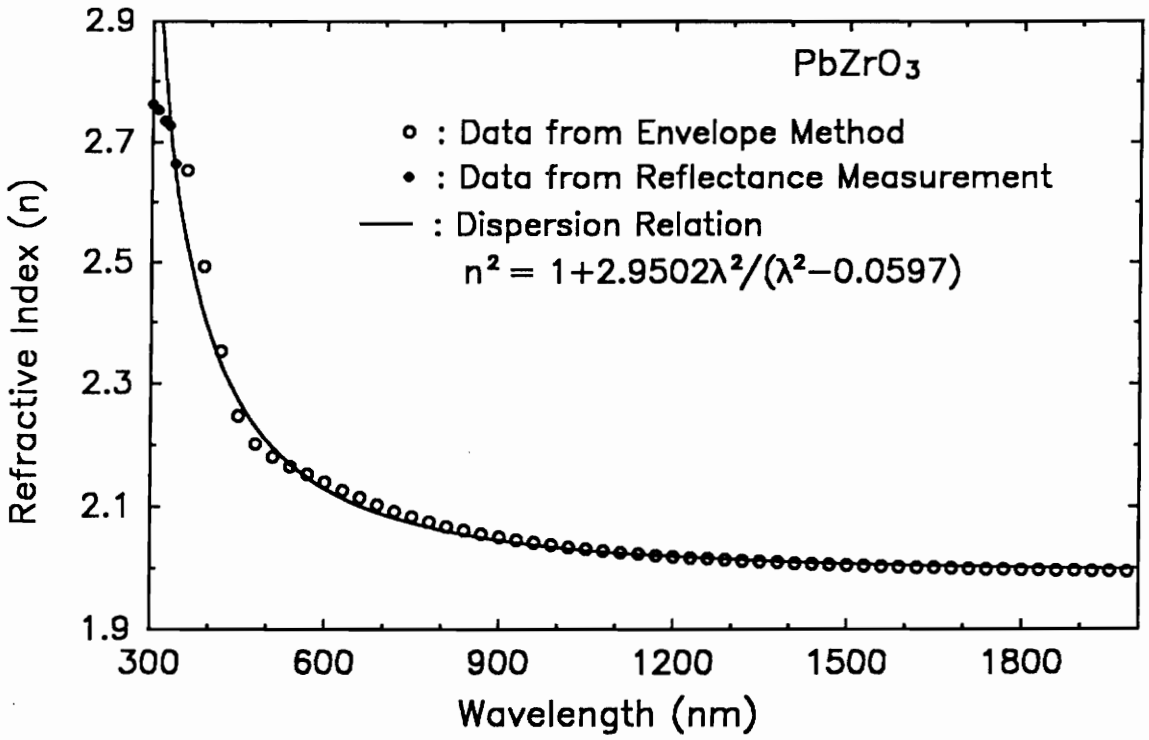

Figure B.12 The refractive index as a function of wavelength and the dispersion curve of $PbZrO_3$ film

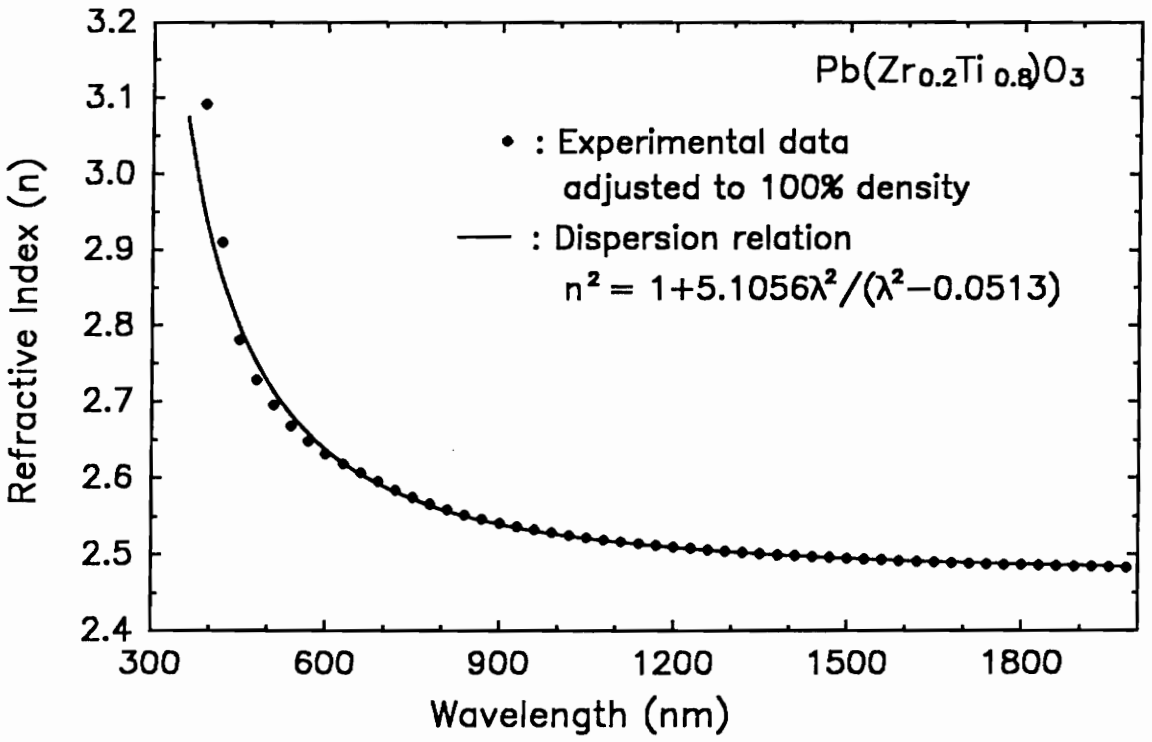

Figure B.13 Adjusted refractive index as a function of wavelength and the dispersion curve of $Pb(Zr_{0.2}Ti_{0.8})O_3$ film

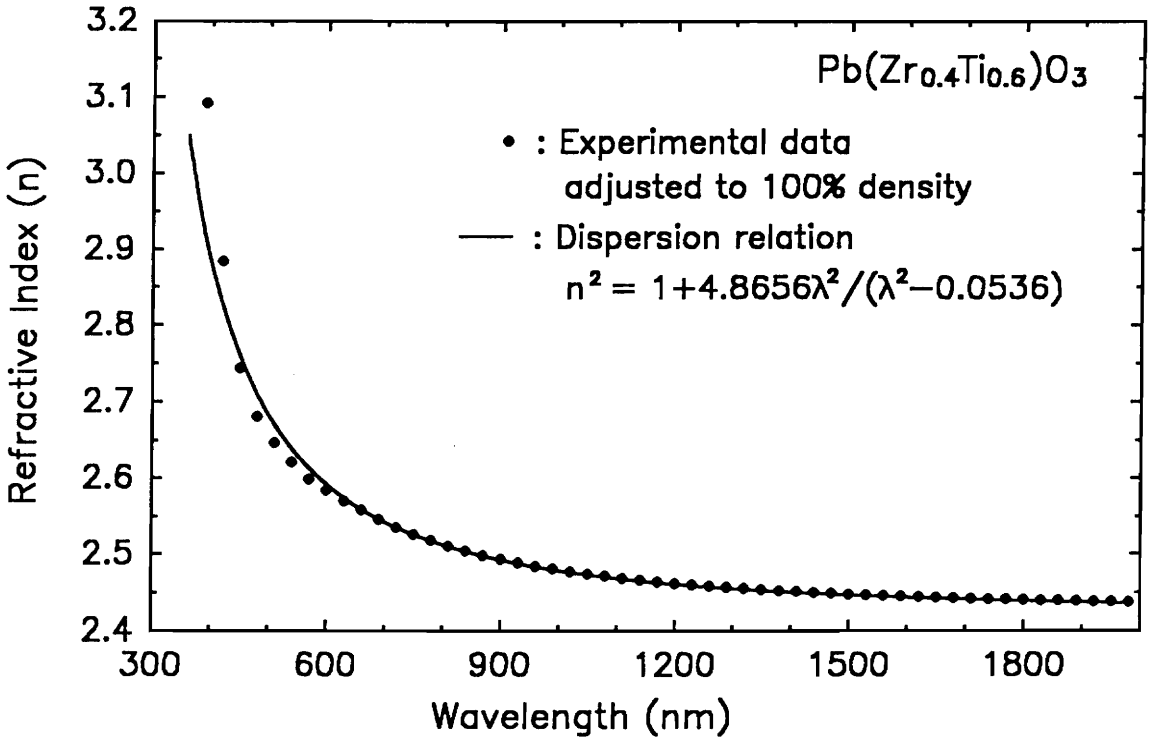

Figure B.14 Adjusted refractive index as a function of wavelength and the dispersion curve of $Pb(Zr_{0.4}Ti_{0.6})O_3$ film

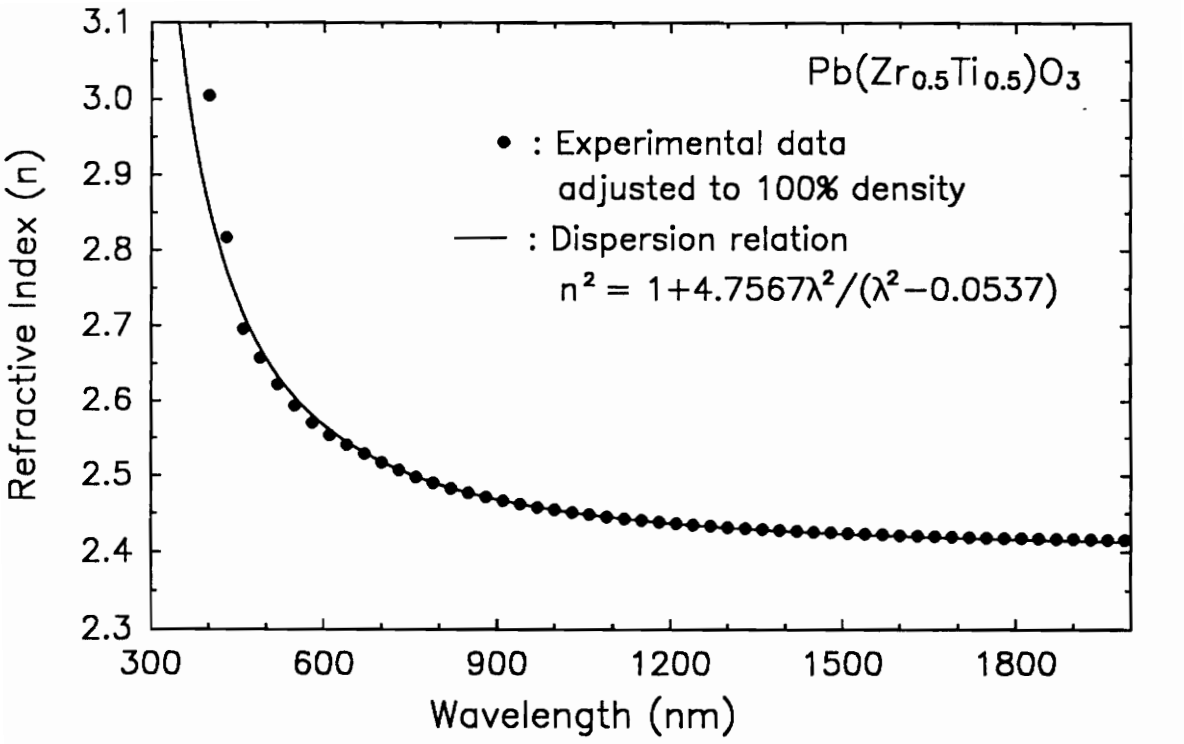

Figure B.15 Adjusted refractive index as a function of wavelength and the dispersion curve of $Pb(Zr_{0.5}Ti_{0.5})O_3$ film

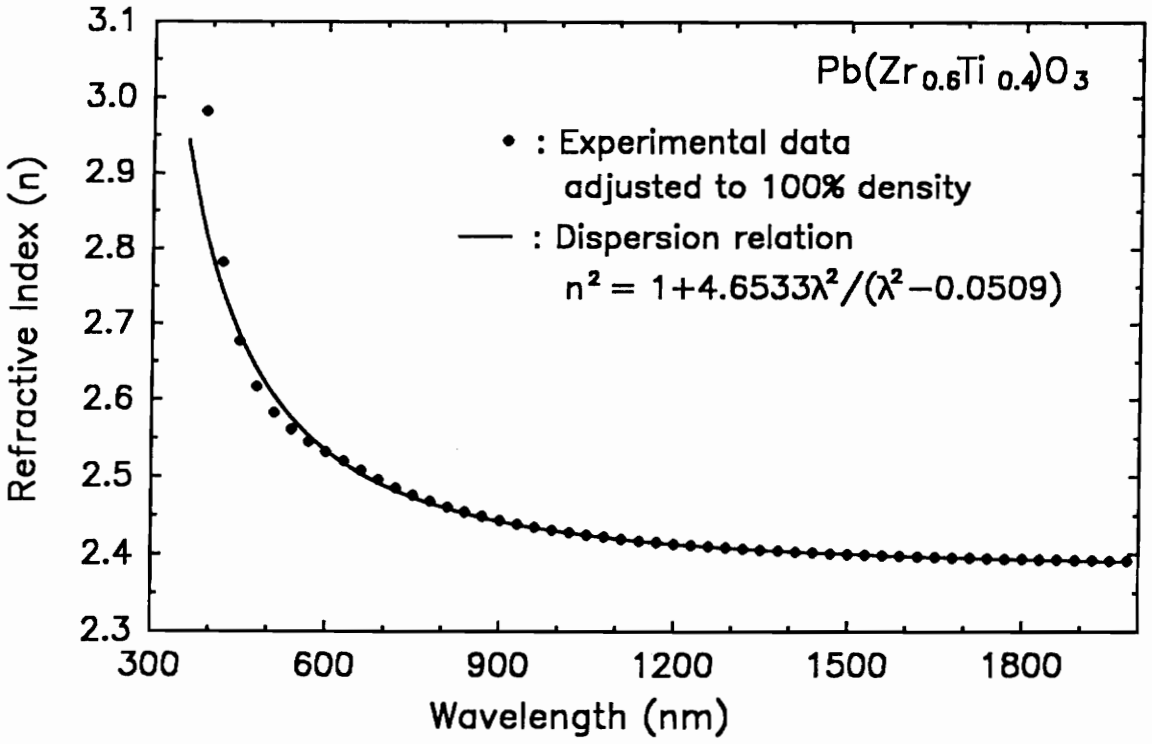

Figure B.16 Adjusted refractive index as a function of wavelength and the dispersion curve of $Pb(Zr_{0.6}Ti_{0.4})O_3$ film

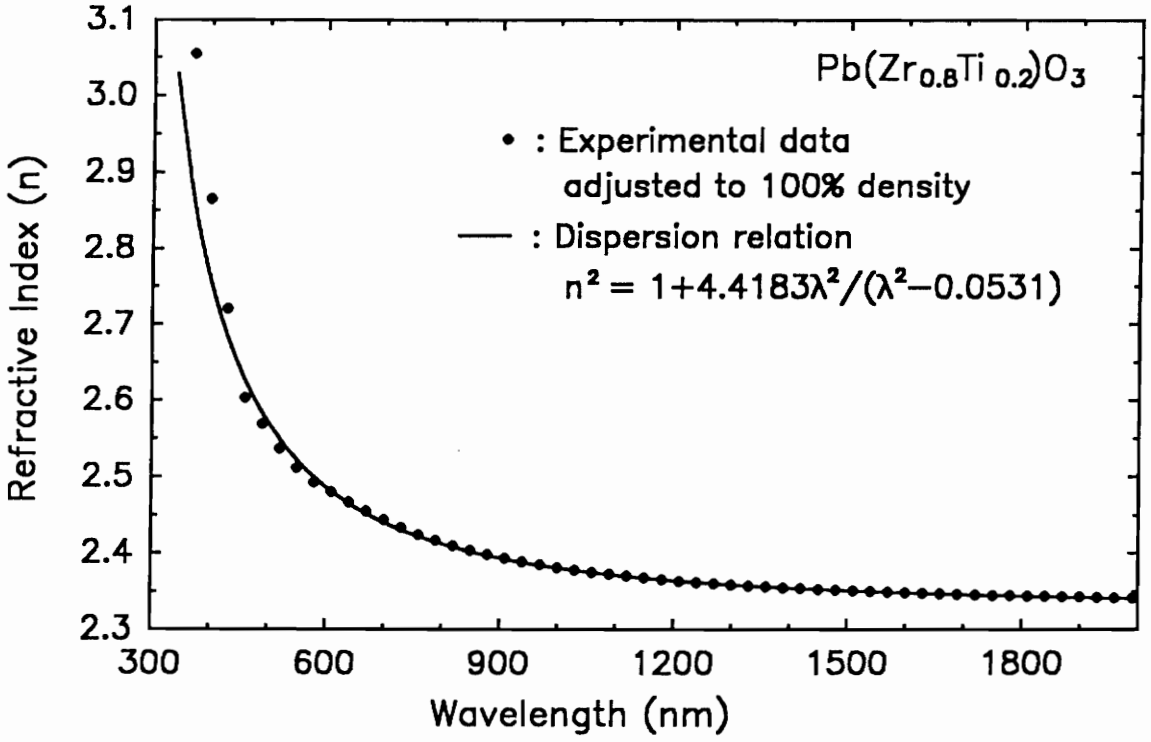

Figure B.17 Adjusted refractive index as a function of wavelength and the dispersion curve of $Pb(Zr_{0.8}Ti_{0.2})O_3$ film

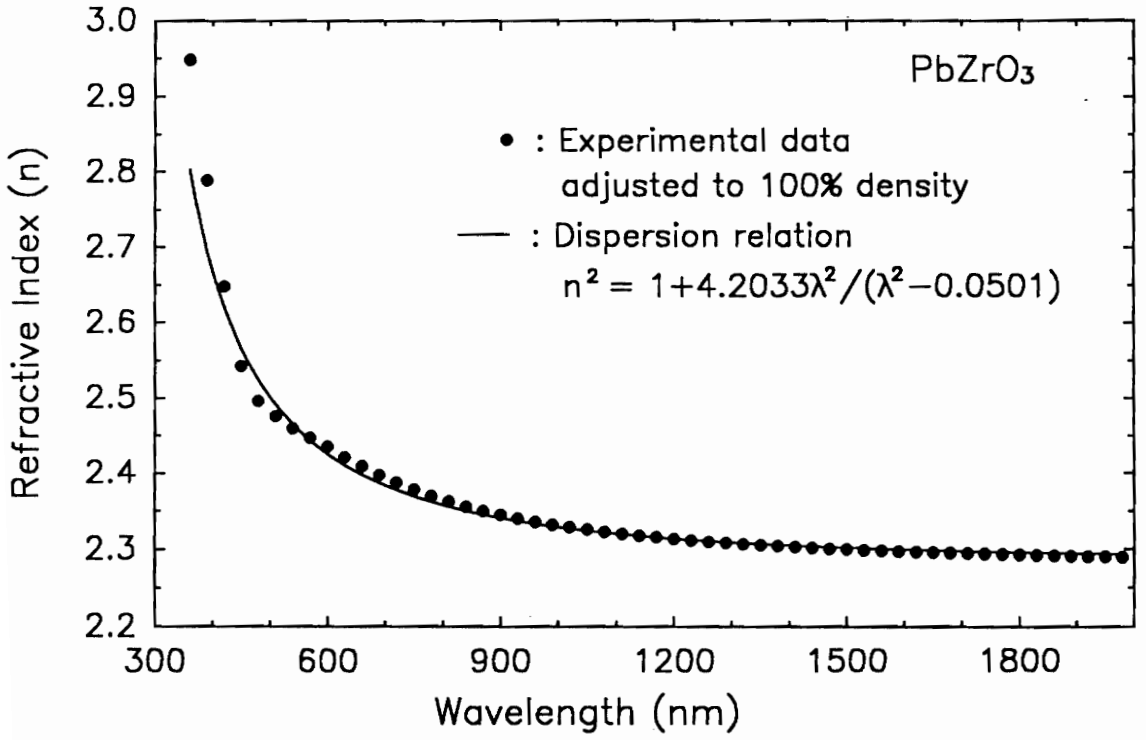

Figure B.18 Adjusted refractive index as a function of wavelength and the dispersion curve of $PbZrO_3$ film

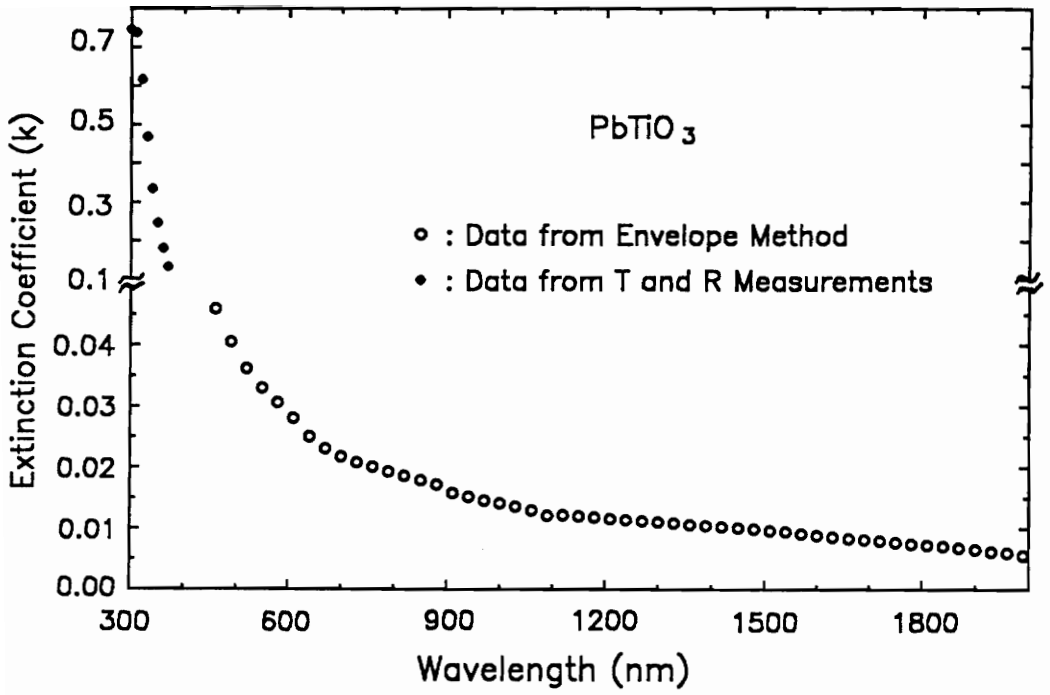

Figure B.19 The extinction coefficient as a function of wavelength of $PbTiO_3$ film

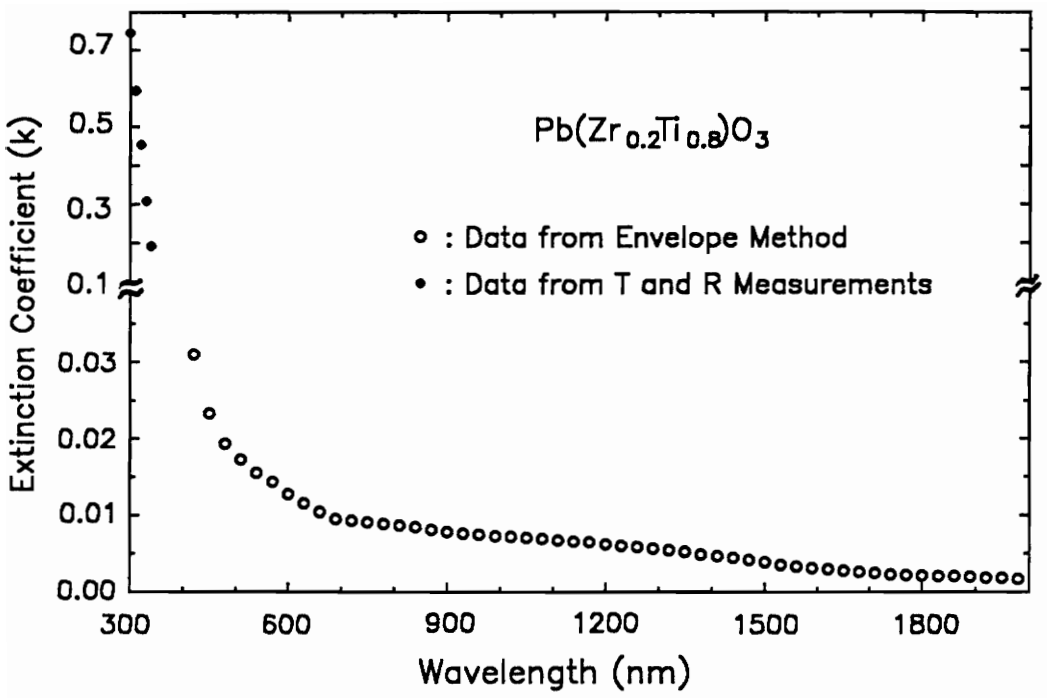

Figure B.20 The extinction coefficient as a function of wavelength of $Pb(Zr_{0.2}Ti_{0.8})O_3$ film

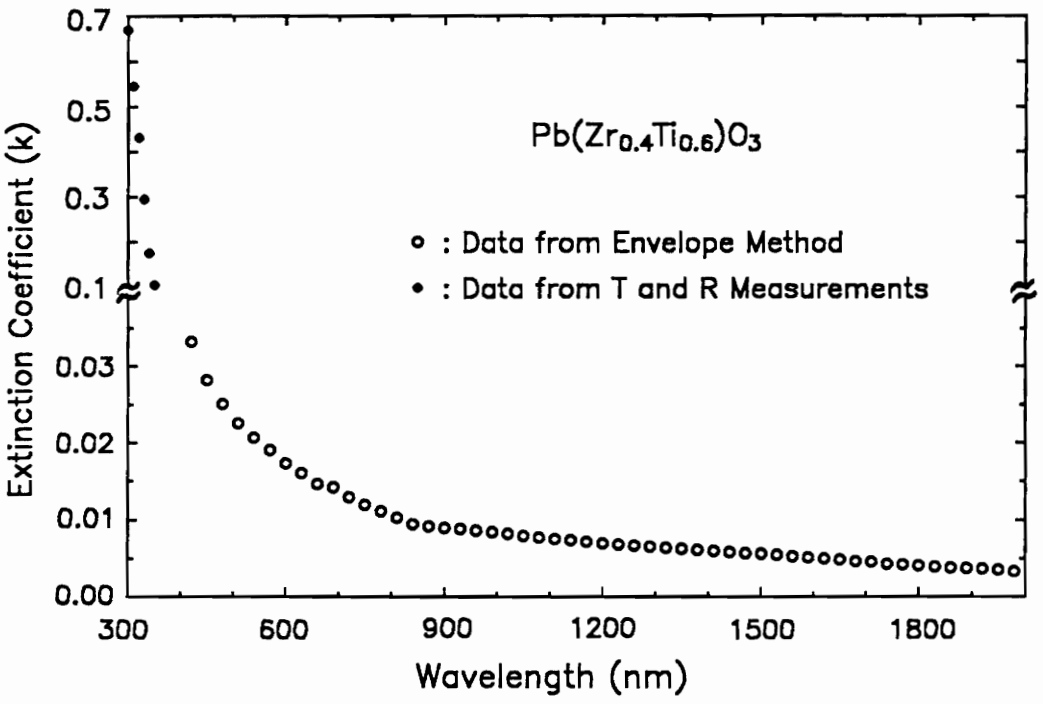

Figure B.21 The extinction coefficient as a function of wavelength of $Pb(Zr_{0.4}Ti_{0.6})O_3$ film

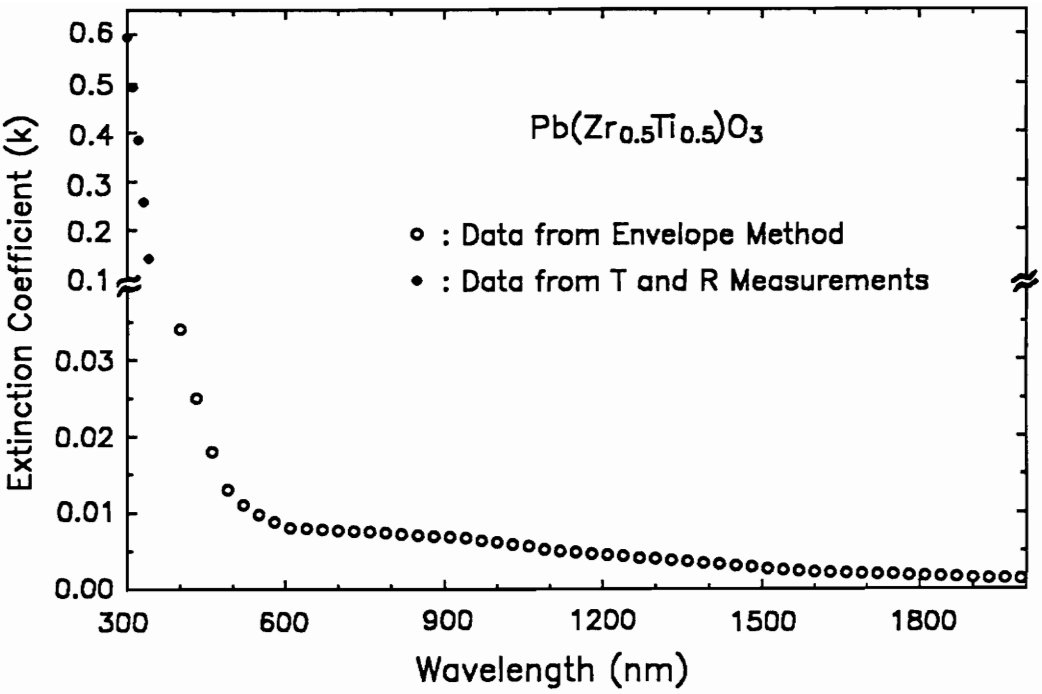

Figure B.22 The extinction coefficient as a function of wavelength of $Pb(Zr_{0.5}Ti_{0.5})O_3$ film

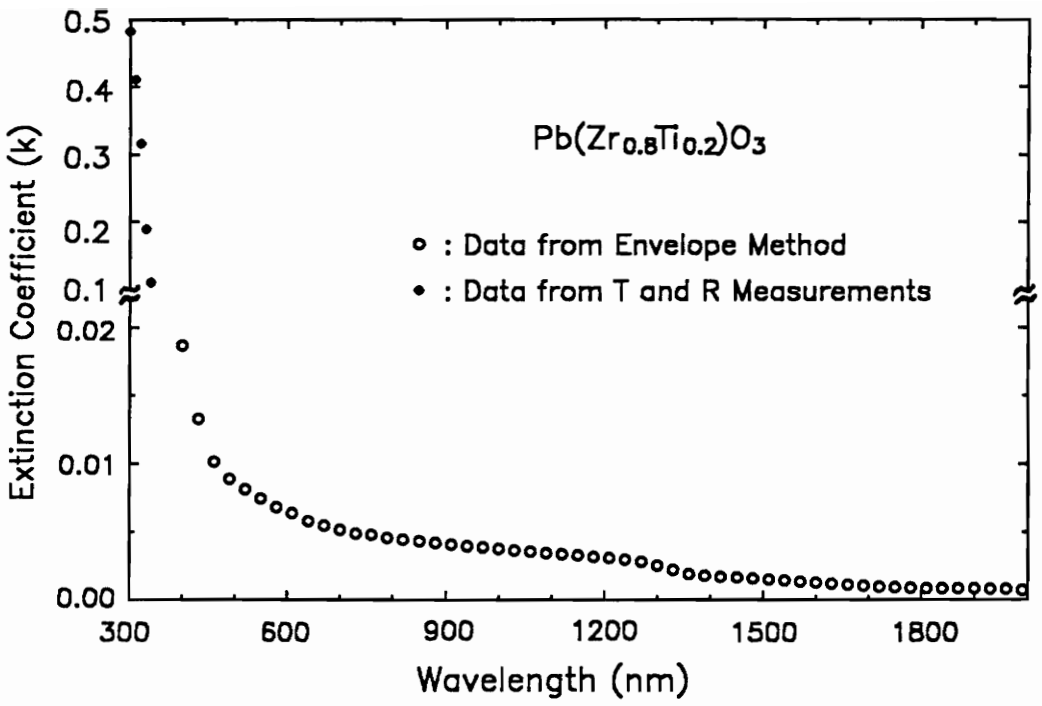

Figure B.23 The extinction coefficient as a function of wavelength of $Pb(Zr_{0.8}Ti_{0.2})O_3$ film

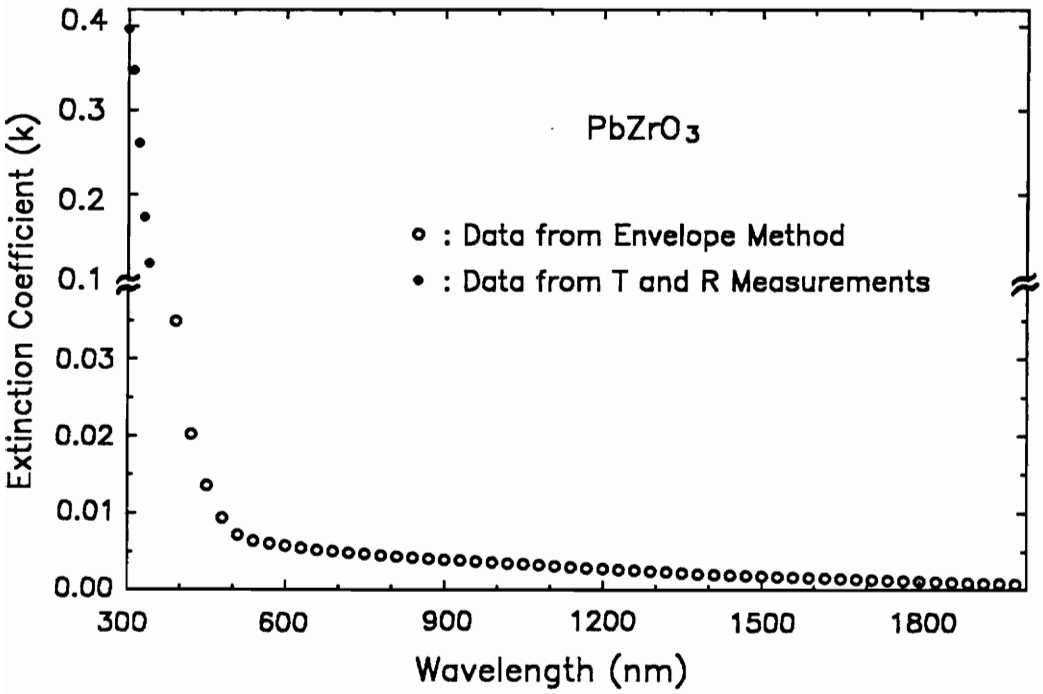

Figure B.24 The extinction coefficient as a function of wavelength of $PbZrO_3$ film

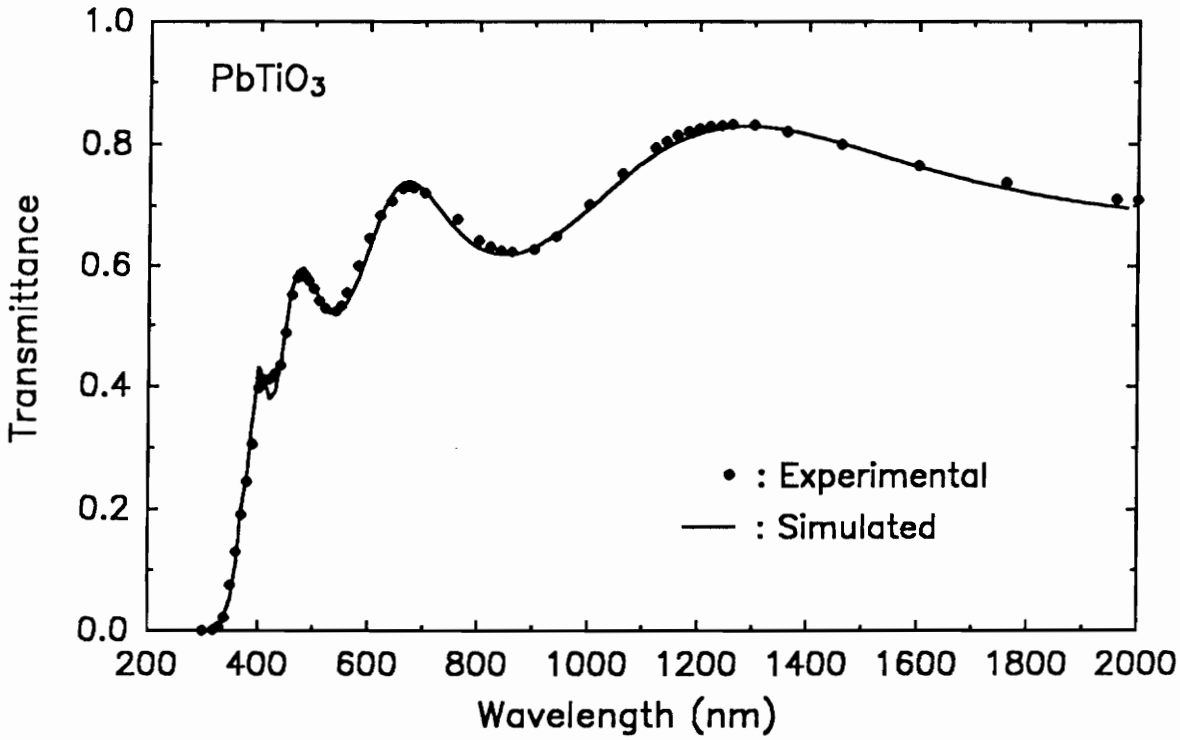

Figure B.25 The experimental and simulated transmission spectra of $PbTiO_3$ film

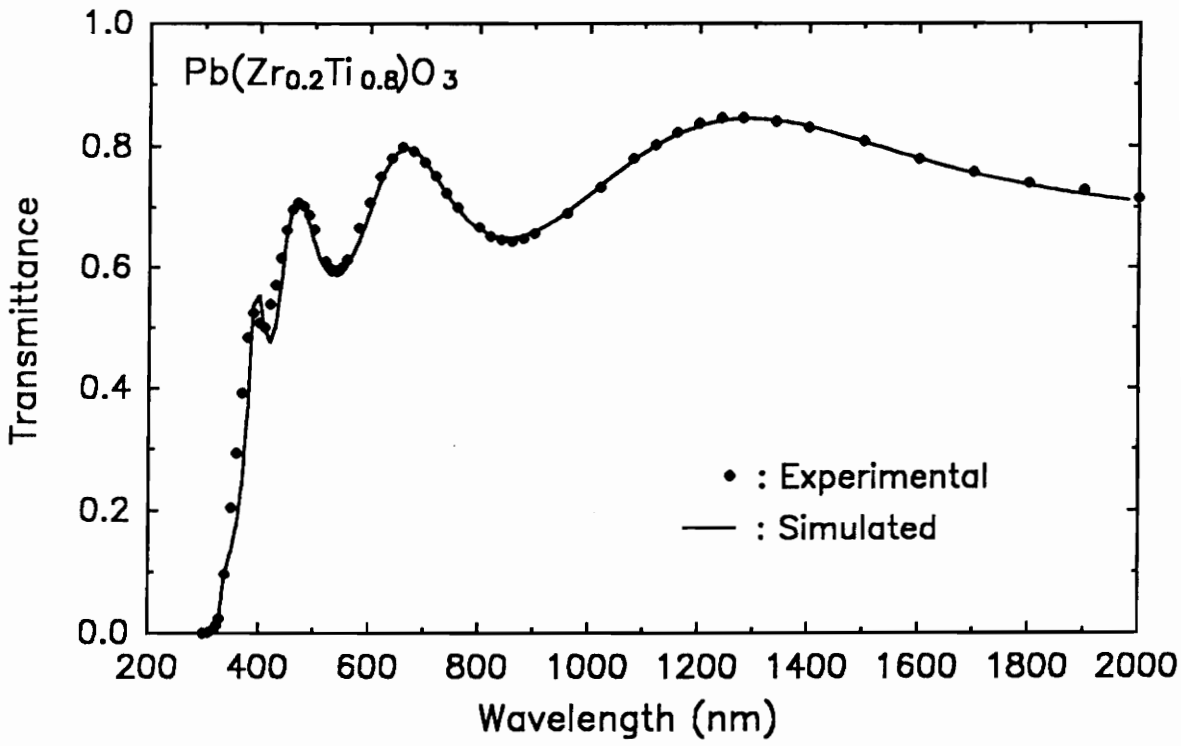

Figure B.26 The experimental and simulated transmission spectra of $Pb(Zr_{0.2}Ti_{0.8})O_3$ film

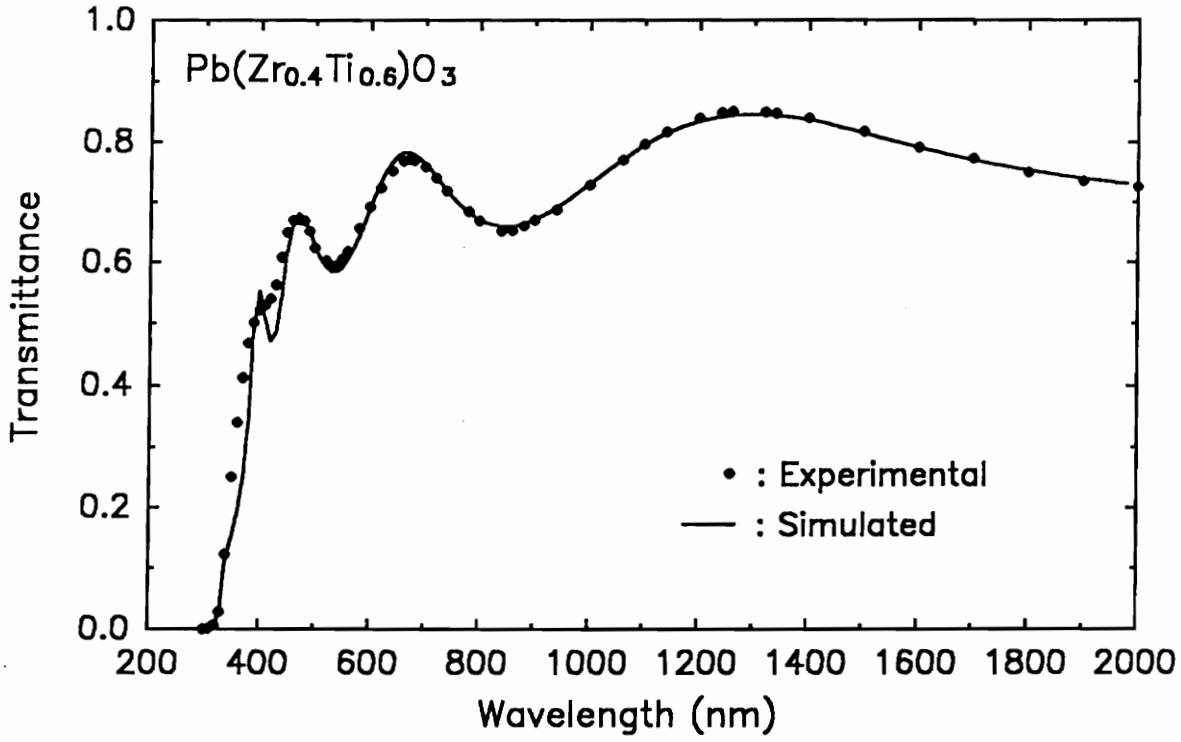

Figure B.27 The experimental and simulated transmission spectra of $Pb(Zr_{0.4}Ti_{0.6})O_3$ film

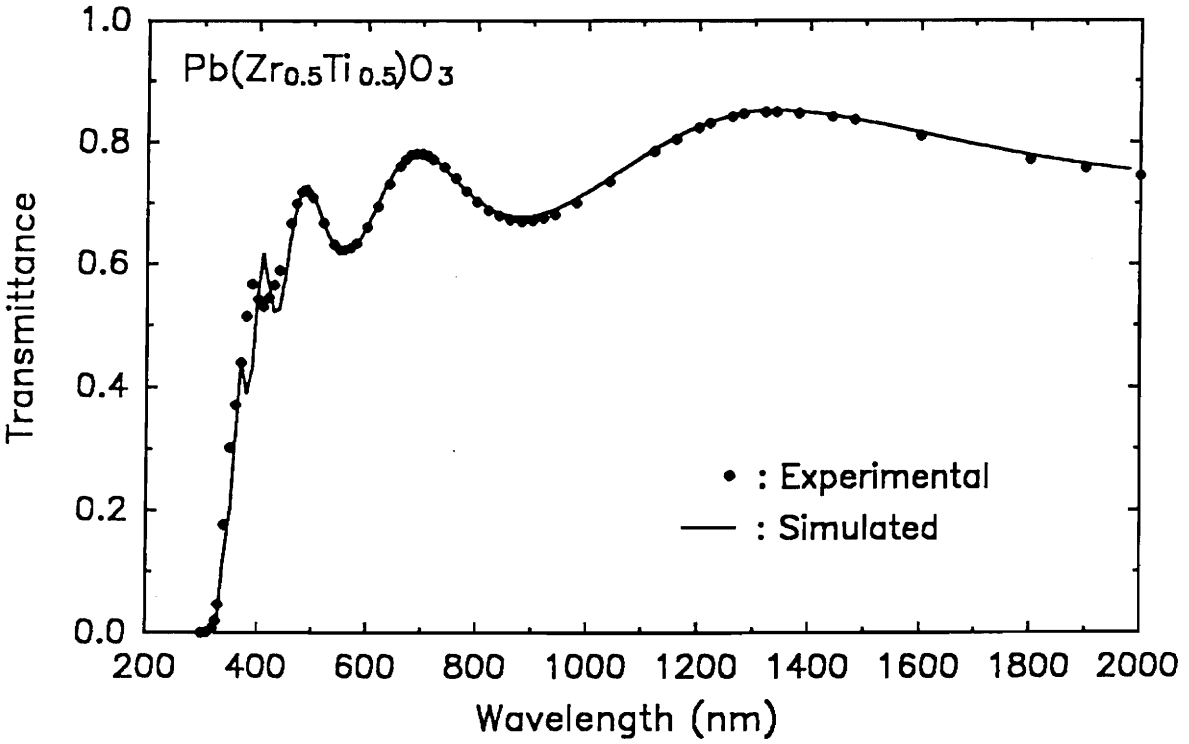

Figure B.28 The experimental and simulated transmission spectra of $Pb(Zr_{0.5}Ti_{0.5})O_3$ film

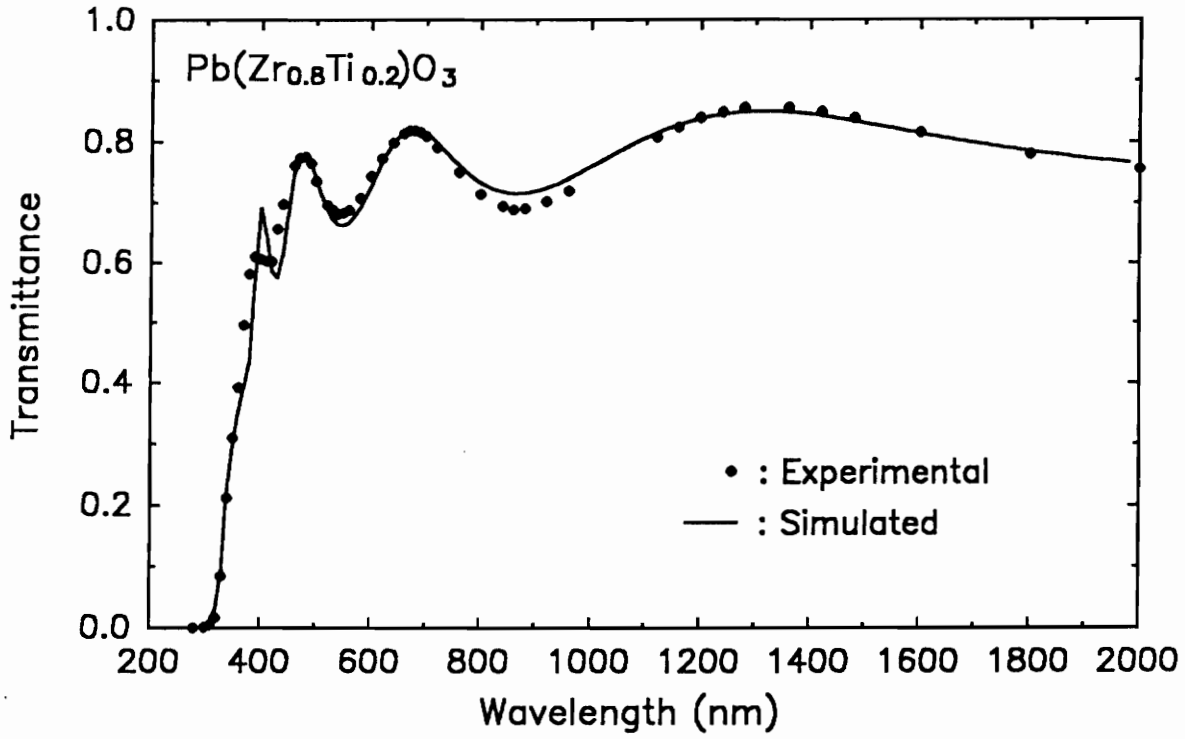

Figure B.29 The experimental and simulated transmission spectra of $Pb(Zr_{0.8}Ti_{0.2})O_3$ film

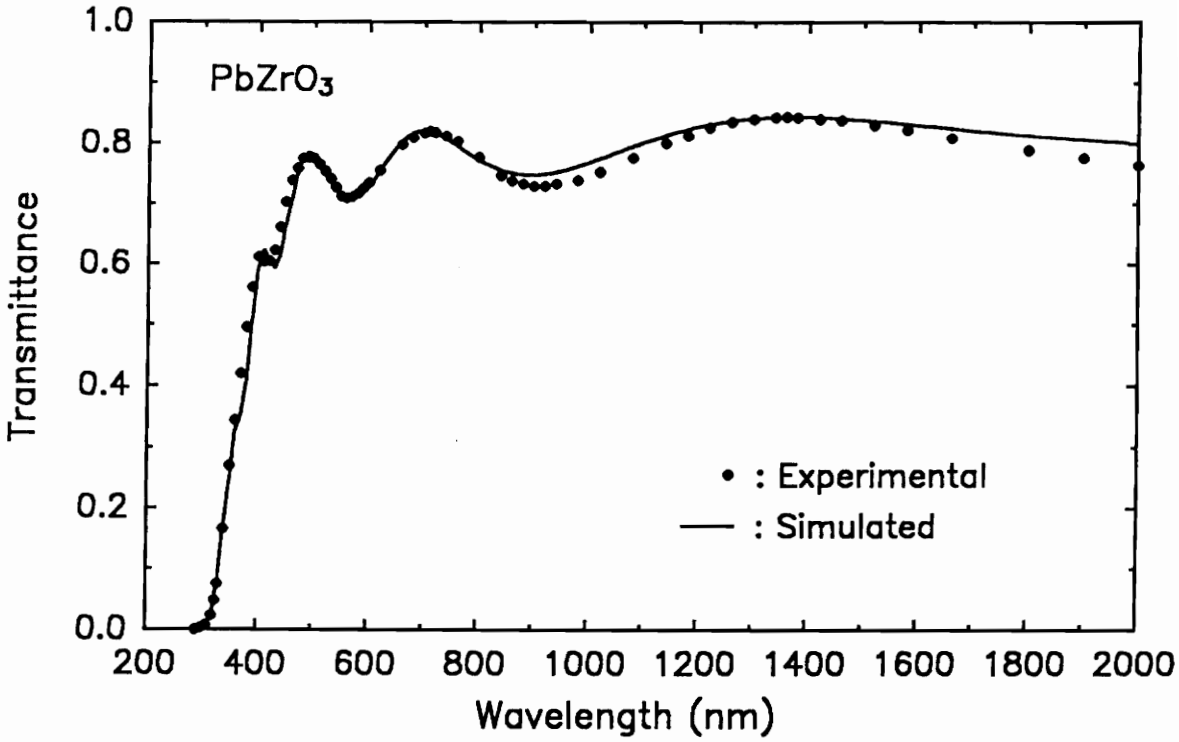

Figure B.30 The experimental and simulated transmission spectra of $PbZrO_3$ film

Appendix C

All the computer programs used in the optical properties study (Chapter 3) and structure development study (Chapter 4) are collected in this Appendix. These computer programs were written in BASIC:

ENV.BAS: Calculate optical constants using the Envelope Method.

THKENV.BAS: Calculate film thickness using the Envelope Method and the interference equation: $2nd = m\lambda$.

THKSIMU.BAS: Calculate film thickness by fitting the optical constants to the experimental transmission spectrum.

T&R.BAS: Calculate the transmittance and reflectance of a multi–layer thin film system.

DRFIT.BAS: Find the dispersion relation parameters by fitting the refractive index data to a Sellmeier type equation.

ALPHA.BAS: Calculate the absorption coefficient of a film on a transparent substrate at the strong absorption region.

VF.BAS: Calculate the volume fraction of a two phase mixture by Effective Medium Approximation.

```
10 REM ========================================================================
20 REM ENV.BAS calculates (lambda n k) and (E alpha alpha^2 alpha^.5) from
30 REM a transmission spectrum of a 'weakly absorbing thin film --
40 REM transperancy substrate' system. This is so-called "ENVELOPE METHOD".
50 REM
60 REM Input: (Lambda Tmax Tmin) -- Hand-made envelope curves
70 REM        The unit of lambda is nm. Wavelength should be tabulated from
80 REM        short to long. Tmax and Tmin are in fraction.
90 REM        Peaks and/or Valleys position (for thickness calculation)
100 REM       Substrate: Sapphire or Glass
110 REM
120 REM Output: (lambda n k) and/or (E alpha alpha^2 alpha^.5)
130 REM
140 REM The back surface of substrate has been taken into account.
150 REM
160 REM Reference: J. Phys. E: Sci. Instru. 9, 1002 (1976) for envelope
170 REM            method.
180 REM            J Opti. Soc. Am. 52, 1377 (1967) for the refractive
190 REM            index of sapphire.
200 REM ================== C. H. PENG   1/16/91 (6/18/92 revised) ========
210 DI1=3000:DI2=100:DI3=30
220 DIM LAMBDA(DI1),TMAX(DI1),TMIN(DI1),NS(DI1),N(DI1),K(DI1),ALPHA(DI1)
230 DIM LAMBDAS(DI2),LAMBDAF(DI2),TMAX1(DI2),TMIN1(DI2),NS1(DI2)
240 DIM LM(DI3),NM(DI3),DM(DI3),LM$(DI3)
250 A1=1.023798
260 A2=1.058264
270 A3=5.280792
280 L12=3.77588E-03
290 L22=.0122544
300 L32=321.3616
310 PI=3.1415926#
320 CLS
330 INPUT "Enter data filename of substrate ('S' for sapphire, 'G' for ";
        "glass): ",FILEN1$
340 IF FILEN1$="s" OR FILEN1$="S" THEN GOTO 450
350 IF FILEN1$="G" OR FILEN1$="g" THEN FILEN1$="AQUARTZ.DAT"
360 OPEN "I",#1,FILEN1$
370 INPUT #1,DESC$
380 I=0
390 WHILE NOT EOF(1)
400  I=I+1
410  INPUT #1,LAMBDAS(I),NS1(I)
420 WEND
430 NPS=I
440 CLOSE #1
450 INPUT "Enter data filename of (lambda, Tmax, Tmin): ",FILEN2$
460 OPEN "I",#1,FILEN2$
470 I=0
480 WHILE NOT EOF(1)
490  I=I+1
500  INPUT #1,LAMBDAF(I),TMAX1(I),TMIN1(I)
510  IF TMAX1(I)<TMIN1(I) THEN SWAP TMAX1(I), TMIN1(I)
520  IF TMAX1(I)>1 THEN TMAX1(I)=TMAX1(I)*.01
530  IF TMIN1(I)>1 THEN TMIN1(I)=TMIN1(I)*.01
540 WEND
550 NPF=I
560 CLOSE #1
570 INPUT"Enter wavelength min, max, and increment: ",LMIN,LMAX,LINC
580 IF LMIN<LAMBDAF(1) OR LMAX>LAMBDAF(NPF) THEN PRINT "Wavelength has to";
    " be within the range: ",LAMBDAF(1);" - ";LAMBDAF(NPF):GOTO 570
```

```
590 NP=INT((LMAX-LMIN)/LINC)+1
600 IF FILEN1$="s" OR FILEN1$="S" THEN GOSUB 1730:GOTO 710
610 JJ=1
620 FOR I=1 TO NP
630  LAMBDA(I)=LMIN+(I-1)*LINC
640  FOR J=JJ TO NPS
650   IF LAMBDA(I)=LAMBDAS(J) THEN NS(I)=NS1(J):JJ=J :GOTO 700
660   IF LAMBDA(I)<LAMBDAS(J) THEN JJ=J-1: GOTO 680
670  NEXT J
680  SLOPE=(NS1(J)-NS1(J-1))/(LAMBDAS(J)-LAMBDAS(J-1))
690  NS(I)=NS1(J-1)+(LAMBDA(I)-LAMBDAS(J-1))*SLOPE
700 NEXT I
710 JJ=1
720 FOR I=1 TO NP
730  LAMBDA(I)=LMIN+(I-1)*LINC
740  FOR J=JJ TO NPF
750   IF LAMBDA(I)=LAMBDAF(J) THEN TMAX(I)=TMAX1(J):TMIN(I)=TMIN1(J):JJ=J
        :GOTO 840
760   IF LAMBDA(I)<LAMBDAF(J) THEN JJ=J-1: GOTO 780
770  NEXT J
780  DE1=LAMBDAF(J)-LAMBDAF(J-1)
790  DE2=LAMBDA(I)-LAMBDAF(J-1)
800  SLOPE=(TMAX1(J)-TMAX1(J-1))/DE1
810  TMAX(I)=TMAX1(J-1)+DE2*SLOPE
820  SLOPE=(TMIN1(J)-TMIN1(J-1))/DE1
830  TMIN(I)=TMIN1(J-1)+DE2*SLOPE
840 NEXT I
850 REM Calculation refractive index of film
860 FLAG=0
870 FOR I=1 TO NP
880  IF FLAG=1 THEN 900
890  IF LAMBDA(I)>632.8 THEN L6=I-1:FLAG=1
900  DE=8*(NS(I)/(NS(I)+1))^2*(TMAX(I)-TMIN(I))/(TMAX(I)*TMIN(I))
910  NN=.5*(1+NS(I)*NS(I))+DE
920  N(I)=SQR(NN+SQR(NN*NN-NS(I)*NS(I)))
930 NEXT I
940 N6=N(L6)-(N(L6)-N(L6+1))*(632.8-LAMBDA(L6))/(LAMBDA(L6+1)-LAMBDA(L6))
950 PRINT"Refractive index of film at 632.8 nm is ";N6
960 PRINT
970 PRINT"    --==< Calculation of film thickness >==--"
980 PRINT"Enter wavelengths which correspond to extrema, 'P'=peaks, ";
       "'V'=valleys"
990 PRINT"--- Enter '0,0' to end entry."
1000 PRINT"For example,   361.3,P"
1010 PRINT"               413.2,V"
1020 PRINT"               573.3,P"
1030 PRINT"               883.8,V"
1040 PRINT"                   0,0"
1050 PRINT
1060 I=0
1070 I=I+1
1080 PRINT I;:INPUT " ",LM(I),LM$(I)
1090 IF LM(I)=0 THEN NLM=I-1 ELSE GOTO 1070
1100 FOR J=1 TO NLM
1110  FOR I=1 TO NP
1120   IF LM(J)=LAMBDA(I) THEN NM(J)=N(I): GOTO 1170
1130   IF LM(J)<LAMBDA(I) THEN GOTO 1150
1140  NEXT I
1150  SLOPE=(N(I)-N(I-1))/(LAMBDA(I)-LAMBDA(I-1))
1160  NM(J)=N(I-1)+(LM(J)-LAMBDA(I-1))*SLOPE
```

```
1170  PRINT J;" Lambda=";LM(J);"    ";"n=";NM(J)
1180 NEXT J
1190 NK=0:NV=0
1200 FOR I=1 TO NLM
1210  IF LM$(I)="p" OR LM$(I)="P" THEN NK=NK+1 ELSE NV=NV+1
1220 NEXT I
1230 D=0
1240 IF NK<2 THEN 1340
1250 L=1
1260 FOR I=1 TO NK-1
1270  F0=0:F3=0
1280  FOR J=L TO NLM
1290   IF (LM$(J)="p" OR LM$(J)="P") AND F0=1 THEN F3=J
1300   IF (LM$(J)="p" OR LM$(J)="P") AND F0=0 THEN F2=J:F0=1
1310   IF F3>F2 THEN L=F3:DES$="peaks":GOSUB 1790:GOTO 1330
1320  NEXT J
1330 NEXT I
1340 IF NK<2 AND NV<2 THEN PRINT"No sufficient peaks or valleys":RETURN
1350 IF NV<2 THEN 1450
1360 L=1
1370 FOR I=1 TO NV-1
1380  F0=1:F3=0
1390  FOR J=L TO NLM
1400   IF (LM$(J)="v" OR LM$(J)="V") AND F0=2 THEN F3=J
1410   IF (LM$(J)="v" OR LM$(J)="V") AND F0=1 THEN F2=J:F0=2
1420   IF F3>F2 THEN L=F3:DES$="valleys":GOSUB 1790:GOTO 1440
1430  NEXT J
1440 NEXT I
1450 D=D/(NK+NV-2)
1460 PRINT "Average thickness: ";D;"nm"
1470 INPUT"Enter thickness for extinction coefficient calculation:",D
1480 FOR I=1 TO NP
1490  C1=(N(I)+1)*(NS(I)+N(I))
1500  C2=(N(I)-1)*(NS(I)-N(I))
1510  A=(C1*(1-SQR(TMAX(I)/TMIN(I))))/(C2*(1+SQR(TMAX(I)/TMIN(I))))
1520  K(I)=(-LAMBDA(I)/(4*PI*D))*LOG(A)
1530  ALPHA(I)=1E+07*4*PI*K(I)/LAMBDA(I)
1540 NEXT I
1550 INPUT "Enter filename to save (lambda, n, and k): ",FILEN3$
1560 OPEN "O",#1,FILEN3$
1570 FOR I=1 TO NP
1580  PRINT #1,LAMBDA(I),N(I),K(I)
1590 NEXT I
1600 CLOSE #1
1610 PRINT "Enter filename to save (E, alpha, alpha^2, and sqr(alpha))"
1620 INPUT "Hit <RETURN> to skip: ",FILEN5$
1630 IF FILEN5$="" THEN 1690
1640 OPEN "O",#1,FILEN5$
1650 FOR I=1 TO NP
1660  PRINT #1,1239.85/LAMBDA(I),ALPHA(I),ALPHA(I)*ALPHA(I),SQR(ALPHA(I))
1670 NEXT I
1680 CLOSE #1
1690 INPUT "Another calculation? (Y/N) ",Z$
1700 IF Z$="Y" OR Z$="y" THEN GOTO 320
1710 CLS
1720 END
1730 FOR I=1 TO NP
1740  LAMBDA(I)=LMIN+(I-1)*LINC
1750  LS=LAMBDA(I)*LAMBDA(I)/1000000!
1760  NS(I)=SQR(1+A1*LS/(LS-L12)+A2*LS/(LS-L22)+A3*LS/(LS-L32))
```

```
1770 NEXT I
1780 RETURN
1790 REM
1800 DM(I)=ABS((LM(F2)*LM(F3))/(2*(NM(F2)*LM(F3)-NM(F3)*LM(F2))))
1810 D=D+DM(I)
1820 PRINT "t=";DM(I);"nm from ";DES$;" at";LM(F2);" and ";LM(F3)
1830 RETURN
```

```
10 REM ========================================================================
20 REM THKENV.BAS calculates the film thickness basing on the envelope
30 REM method along with the interference equation: 2nd=m*lambda.
40 REM Both lambda and thickness (d) are in nm.
50 REM
60 REM The algorithm is
70 REM  1. input the wavelengths of the interference peaks and/or valleys
80 REM     and the corresponding Tmax and Tmin.
90 REM  2. the refractive indices at these wavelengths are calculated based
100 REM     on the envelope method
110 REM  3. the thicknesses are calculated from pairs of peaks and/or valleys
120 REM  4. the order numbers m are then calculated from corresponding
130 REM     wavelength, refractive index, and film thickness.
140 REM  5. the order numbers m are rounded to the nearest integer or half-
150 REM     integer, then new thicknesses are calculated from these new m.
160 REM  6. the average thickness from step 5 is taken as the final answer.
170 REM
180 REM ===============  C. H. PENG   6/19/92  ==============================
190 CLS
200 DIM PL(20),PN(20),VL(20),VN(20),D1(20),D2(20)
210 DIM LM(20),N1(20),N2(20),M0(20),M(20)
220 DIM TMAXP(20),TMINP(20),TMAXV(20),TMINV(20)
230 A1=1.023798
240 A2=1.058264
250 A3=5.280792
260 L12=3.77588E-03
270 L22=.0122544
280 L32=321.3616
290 INPUT "Enter filename to save data: ",F$
300 OPEN "O",#1,F$
310 INPUT"Description: ",DS$
320 PRINT #1,DS$
330 INPUT"Enter Tmax and Tmin at 633 nm:",TMAX,TMIN
340 IF TMAX<1 THEN GOTO 360
350 TMAX=TMAX/18.71:TMIN=TMIN/18.71
360 IF TMAX<TMIN THEN SWAP TMAX,TMIN
370 LS=632.8*632.8/1000000!
380 NS=SQR(1+A1*LS/(LS-L12)+A2*LS/(LS-L22)+A3*LS/(LS-L32))
390 DE=8*(NS/(NS+1))^2*(TMAX-TMIN)/(TMAX*TMIN)
400 NN=.5*(1+NS^2)+DE
410 N633=SQR(NN+SQR(NN^2-NS^2))
420 PRINT #1,"   n(633)=";N633;"  Tmax=";TMAX;"  Tmin=";TMIN
430 PRINT"Enter lambda, Tmax, and Tmin for peaks:"
440 I=0:PL(0)=0
450 I=I+1
460 PRINT I;
470 INPUT "    lambda=",PL(I)
480 IF PL(I) > 200 THEN GOTO 500
490 PL(I)=CINT(PL(I)*1800/23+200)
500 IF PL(I)=200 THEN NP=I-1: GOTO 650
510 LS=PL(I)*PL(I)/1000000!
520 NS=SQR(1+A1*LS/(LS-L12)+A2*LS/(LS-L22)+A3*LS/(LS-L32))
530 INPUT "      Tmax=",TMAXP(I)
540 IF TMAXP(I)<1 THEN 560
550 TMAXP(I)=TMAXP(I)/18.71
560 INPUT "      Tmin=",TMINP(I)
570 IF TMINP(I)<1 THEN 590
580 TMINP(I)=TMINP(I)/18.71
590 IF TMAXP(I)<TMINP(I) THEN SWAP TMAXP(I),TMINP(I)
600 DE=8*(NS/(NS+1))^2*(TMAXP(I)-TMINP(I))/(TMAXP(I)*TMINP(I))
```

```
610 NN=.5*(1+NS^2)+DE
620 PN(I)=SQR(NN+SQR(NN^2-NS^2))
630 IF PL(I)<PL(I-1) THEN NP=I-1:VL(1)=PL(I):VN(1)=PN(I)
          :TMAXV(1)=TMAXP(I):TMINV(1)=TMINP(I):I=1:GOTO 670
640 GOTO 450
650 PRINT"Enter lambda(nm), Tmax, and Tmin (cm) for valleys:"
660 I=0
670 I=I+1
680 PRINT I;
690 INPUT "    lambda=",VL(I)
700 IF VL(I)>200 THEN 720
710 VL(I)=CINT(VL(I)*1800/23+200)
720 IF VL(I)=200 THEN NV=I-1: GOTO 860
730 LS=VL(I)*VL(I)/1000000!
740 NS=SQR(1+A1*LS/(LS-L12)+A2*LS/(LS-L22)+A3*LS/(LS-L32))
750 INPUT "      Tmax=",TMAXV(I)
760 IF TMAXV(I)<1 THEN 780
770 TMAXV(I)=TMAXV(I)/18.71
780 INPUT "      Tmin=",TMINV(I)
790 IF TMINV(I) <1 THEN 810
800 TMINV(I)=TMINV(I)/18.71
810 IF TMAXV(I)<TMINV(I) THEN SWAP TMAXV(I),TMINV(I)
820 DE=8*(NS/(NS+1))^2*(TMAXV(I)-TMINV(I))/(TMAXV(I)*TMINV(I))
830 NN=.5*(1+NS^2)+DE
840 VN(I)=SQR(NN+SQR(NN^2-NS^2))
850 GOTO 670
860 FOR I=1 TO NP
870  PRINT #1,USING "      ####";PL(I);
880 NEXT I
890 FOR I=1 TO NV
900  PRINT #1,USING "      ####";VL(I);
910 NEXT I
920 PRINT #1," "
930 FOR I=1 TO NP
940  PRINT #1,USING "     .####";TMAXP(I);
950 NEXT I
960 FOR I=1 TO NV
970  PRINT #1,USING "     .####";TMAXV(I);
980 NEXT I
990 PRINT #1," "
1000 FOR I=1 TO NP
1010  PRINT #1,USING "     .####";TMINP(I);
1020 NEXT I
1030 FOR I=1 TO NV
1040  PRINT #1,USING "     .####";TMINV(I);
1050 NEXT I
1060 PRINT #1," "
1070 FOR I=1 TO NP
1080  PRINT #1,USING "    #.####";PN(I);
1090 NEXT I
1100 FOR I=1 TO NV
1110  PRINT #1,USING "    #.####";VN(I);
1120 NEXT I
1130 PRINT #1," "
1140 FOR I=1 TO NP-1
1150  D1(I)=PL(I+1)*PL(I)/(2*(PL(I+1)*PN(I)-PL(I)*PN(I+1)))
1160  PRINT #1,USING "          ###.#";D1(I);
1170 NEXT I
1180 L=NP-1
1190 FOR I=1 TO NV-1
```

```
1200  L=L+1
1210  D1(L)=VL(I+1)*VL(I)/(2*(VL(I+1)*VN(I)-VL(I)*VN(I+1)))
1220  PRINT #1,USING "          ###.#";D1(L);
1230 NEXT I
1240 PRINT #1," "
1250 D1A=0
1260 FOR I=1 TO L
1270  D1A=D1A+D1(I)
1280 NEXT I
1290 D1A=D1A/L
1300 PRINT #1,"    Average thickness:";D1A
1310 FOR I=1 TO NP
1320  LM(I)=PL(I):N1(I)=PN(I)
1330 NEXT I
1340 LL=NP
1350 FOR I=1 TO NV
1360  LL=LL+1
1370  LM(LL)=VL(I):N1(LL)=VN(I)
1380 NEXT I
1390 NN=NP+NV
1400 D2A=0
1410 FOR I=1 TO NN
1420  M0(I)=2*N1(I)*D1A/LM(I)
1430  IF I>NP THEN M(I)=CINT(M0(I)+.5)-.5 ELSE M(I)=CINT(M0(I))
1440  D2(I)=LM(I)*M(I)/(2*N1(I))
1450  D2A=D2A+D2(I)
1460 NEXT I
1470 FOR I=1 TO NN
1480  PRINT #1,USING "     #.###";M0(I);
1490 NEXT I
1500 PRINT #1," "
1510 FOR I=1 TO NN
1520  PRINT #1,USING "       #.#";M(I);
1530 NEXT I
1540 PRINT #1," "
1550 FOR I=1 TO NN
1560  PRINT #1,USING "     ###.#";D2(I);
1570 NEXT I
1580 PRINT #1," "
1590 D2A=D2A/NN
1600 PRINT #1,"    Average thickness=";D2A
1610 FOR I=1 TO NN
1620  N2(I)=LM(I)*M(I)/(2*D2A)
1630  PRINT #1,USING "     #.###";N2(I);
1640 NEXT I
1650 PRINT #1," "
1660 PRINT #1," "
1670 INPUT"Another Calculation? (y/n) ",Z$
1680 IF Z$="N" OR Z$="n" THEN 1700
1690 GOTO 310
1700 CLOSE #1
1710 INPUT"Another Calculation and change new filename? (y/n) ",Z$
1720 IF Z$="N" OR Z$="n" THEN 1740
1730 GOTO 290
1740 CLS
1750 END
```

```
10 REM ========================================================================
20 REM  THKSIMU.BAS calculates the film thicknesses by fitting the
30 REM  calculated transmission spectrum to the experimental transmission
40 REM  spectrum.
50 REM
60 REM  Input: optical constants for substrate and each film
70 REM         initial thickness guess for each film
80 REM         thickness increment for each film
90 REM  Output: thickness for each film
100 REM          fitting error (chi square)
110 REM
120 REM The calculation of the transmission spectrum is based on the
130 REM program T&R.BAS with the consideration of the back surface of
140 REM the substrate.
150 REM The fitting process stops when the minimun fitting error is met.
160 REM The fitting error is defined as:
170 REM
180 REM   Error = {summation of [T(cal)^2-T(exp)^2]}/(# of data points)
190 REM
200 REM ============= C. H. PENG  5/16/92 ================================
210 CLS
220 D1=1000 :D2=5 :D3=1000
230 DIM X(D1),Y(D1),N(D2,D1),K(D2,D1),D(D2), X1(D3),Y1(2,D3)
240 DIM G(D2),H(D2),GAMMA(D2),ALPHA(D2),DI(D2)
250 DIM P(D2),Q(D2),R(D2),S(D2),T(D2),U(D2),V(D2),W(D2)
260 DIM P1(D2),Q1(D2),R1(D2),S1(D2),T1(D2),U1(D2),V1(D2),W1(D2)
270 INPUT "Spectral range (wavelength in nm, min, max): ",XMIN, XMAX
280 INPUT "Resolution (in nm): ",RSL
290 NP=INT((XMAX-XMIN)/RSL)+1
300 IF NP > 1000 THEN PRINT "Resolution too high!":BEEP:PRINT: GOTO 280
310 FOR I=1 TO NP
320  X(I)=XMIN+RSL*(I-1)
330  N(0,I)=1 :K(0,I)=0
340 NEXT I
350 PRINT
360 INPUT"How many layers (do not count the substrate)? ",NL
370 IF NL>5 THEN PRINT"Too many layers (max: 5)":GOTO 350
380 PRINT:PRINT"Input optical properties for each layer and substrate ..."
390 FOR I=1 TO NL
400  PRINT :PRINT"Layer # ";I
410  INPUT "Thickness and increment (in nm): ",D(I),DI(I)
420  INPUT "Filename for (n,k) -- ",RI$
430  GOSUB 1080
440 NEXT I
450 PRINT:PRINT"Substrate:"
460 PRINT "Refractive Index (n) (Enter 'S' for sapphire, 'G' for glass, a";
        " file name for other materials, or digits for constants):";
470 INPUT " ",RI$
480 IF RI$="S" OR RI$="s" THEN GOSUB 1800:GOTO 510
490 IF RI$="g" OR RI$="G" THEN GOSUB 1940:GOTO 510
500 IF ASC(RI$)>45 AND ASC(RI$)<58 THEN RI=VAL(RI$)
                                   ELSE GOSUB 1080: GOTO 510
510 INPUT"Enter experiment data filename for T -- ",FILEN$
520 OPEN "I",#1,FILEN$
530 J=0
540 WHILE NOT EOF(1)
550  J=J+1
560  INPUT #1,X1(J),Y1(1,J)
570 WEND
580 JJ=J
```

```
590 CLOSE #1
600 FOR J=1 TO NP
610  FOR J1=1 TO JJ
620   IF X(J)=X1(J1) THEN Y(J)=Y1(1,J1):GOTO 670
630   IF X(J)<X1(J1) THEN SLOPE=(X(J)-X1(J1-1))/(X1(J1)-X1(J1-1))
                      ELSE GOTO 660
640   Y(J)=(Y1(1,J1)-Y1(1,J1-1))*SLOPE+Y1(1,J1-1)
650   GOTO 670
660  NEXT J1
670 NEXT J
680 GOSUB 970
690 FLAG=0
700 GOSUB 1220
710 CHISQ=CHISQ1
720 D(1)=D(1)+DI(1)
730 GOSUB 1220
740 IF CHISQ1<CHISQ THEN FLAG=1:CHISQ=CHISQ1:GOTO 720
750 IF FLAG=1 AND CHISQ1>CHISQ THEN D(1)=D(1)-DI(1) : GOTO 810
760 D(1)=D(1)-DI(1)
770 D(1)=D(1)-DI(1)
780 GOSUB 1220
790 IF CHISQ1<CHISQ THEN CHISQ=CHISQ1:GOTO 770
800 D(1)=D(1)+DI(1)
810 PRINT "thickness=";D(1);"     chisq=";CHISQ
820 PRINT
830 INPUT "Another calculation? (Y/N) ",Y$
840 IF Y$="Y" OR Y$="y" THEN CLS: GOTO 270
850 END
860 REM ================================================================
870 REM   Get data (X,Y1,Y2)
880 REM ================================================================
890 OPEN "I",#1,FILEN$
900 J=0
910 WHILE NOT EOF(1)
920  J=J+1
930  INPUT #1,X1(J),Y1(1,J),Y1(2,J)
940 WEND
950 CLOSE #1
960 RETURN
970 REM ================================================================
980 REM   Display a wait message
990 REM ================================================================
1000 CLS
1010 FOR I=1 TO 8
1020 PRINT
1030 NEXT I
1040 PRINT CHR$(7)
1050 PRINT "              Please wait for calculations ..... "
1060 RETURN
1070 REM ================================================================
1080 REM Read n & k and convert them to (x,y) arrays.
1090 REM ================================================================
1100 FILEN$=RI$ : GOSUB 860
1110 JJ=J
1120 FOR J=1 TO NP
1130  FOR J1=1 TO JJ
1140   IF X(J)=X1(J1) THEN N(I,J)=Y1(1,J1):K(I,J)=Y1(2,J1) : GOTO 1200
1150   IF X(J)<X1(J1) THEN SLOPE=(X(J)-X1(J1-1))/(X1(J1)-X1(J1-1))
                      ELSE GOTO 1190
1160   N(I,J)=Y1(1,J1-1)+(Y1(1,J1)-Y1(1,J1-1))*SLOPE
```

```
1170   K(I,J)=Y1(2,J1-1)+(Y1(2,J1)-Y1(2,J1-1))*SLOPE
1180   GOTO 1200
1190  NEXT J1
1200 NEXT J
1210 RETURN
1220 REM ============================================================================
1230 REM  Multi-layer transmittance and reflectance calculation
1240 REM  See O. S. Heavens, "Optical Properties of Thin Solid Films"
1250 REM  (Academic, New York, 1955), pp.76-79
1260 REM ============================================================================
1270 CHISQ1=0
1280 FOR L=1 TO NP
1290  FOR I=1 TO NL+1
1300   NN=(N(I-1,L)+N(I,L))^2+(K(I-1,L)+K(I,L))^2
1310   G(I)=(N(I-1,L)^2+K(I-1,L)^2-N(I,L)^2-K(I,L)^2)/NN
1320   H(I)=(2*(N(I-1,L)*K(I,L)-N(I,L)*K(I-1,L)))/NN
1330  NEXT I
1340  P1(1)=1! :Q1(1)=0! :R1(1)=G(1) :S1(1)=H(1)
1350  T1(1)=G(1) :U1(1)=H(1):V1(1)=1! :W1(1)=0!
1360  FOR I=1 TO NL
1370   ALPHA(I)=6.2831853#*K(I,L)*D(I)/X(L)
1380   GAMMA(I)=6.2831853#*N(I,L)*D(I)/X(L)
1390  NEXT I
1400  FOR I=2 TO NL+1
1410   EA=EXP(ALPHA(I-1))
1420   CG=COS(GAMMA(I-1))
1430   SG=SIN(GAMMA(I-1))
1440   EMA=EXP(-ALPHA(I-1))
1450   P(I)=EA*CG
1460   Q(I)=EA*SG
1470   T(I)=EMA*(G(I)*CG+H(I)*SG)
1480   U(I)=EMA*(H(I)*CG-G(I)*SG)
1490   IF I=NL+1 THEN 1550
1500   R(I)=EA*(G(I)*CG-H(I)*SG)
1510   S(I)=EA*(H(I)*CG+G(I)*SG)
1520   V(I)=EMA*CG
1530   W(I)=-EMA*SG
1540  NEXT I
1550  FOR I=1 TO NL
1560   P1(I+1)=P1(I)*P(I+1)-Q1(I)*Q(I+1)+R1(I)*T(I+1)-S1(I)*U(I+1)
1570   Q1(I+1)=Q1(I)*P(I+1)+P1(I)*Q(I+1)+S1(I)*T(I+1)+R1(I)*U(I+1)
1580   T1(I+1)=T1(I)*P(I+1)-U1(I)*Q(I+1)+V1(I)*T(I+1)-W1(I)*U(I+1)
1590   U1(I+1)=U1(I)*P(I+1)+T1(I)*Q(I+1)+W1(I)*T(I+1)+V1(I)*U(I+1)
1600   IF I=NL THEN 1660
1610   R1(I+1)=P1(I)*R(I+1)-Q1(I)*S(I+1)+R1(I)*V(I+1)-S1(I)*W(I+1)
1620   S1(I+1)=Q1(I)*R(I+1)+P1(I)*S(I+1)+S1(I)*V(I+1)+R1(I)*W(I+1)
1630   V1(I+1)=T1(I)*R(I+1)-U1(I)*S(I+1)+V1(I)*V(I+1)-W1(I)*W(I+1)
1640   W1(I+1)=U1(I)*R(I+1)+T1(I)*S(I+1)+W1(I)*V(I+1)+V1(I)*W(I+1)
1650  NEXT I
1660  YRP=(T1(NL+1)^2+U1(NL+1)^2)/(P1(NL+1)^2+Q1(NL+1)^2)
1670  NUMER=1
1680  FOR I=1 TO NL+1
1690   NUMER=NUMER*((1+G(I))^2+H(I)^2)
1700  NEXT I
1710  DENOM=P1(NL+1)^2+Q1(NL+1)^2
1720  YTP=(N(NL+1,L)*NUMER)/(N(0,L)*DENOM)
1730  C1=((N(NL,L)-N(NL+1,L))/(N(NL,L)+N(NL+1,L)))^2
1740  C2=((1-N(NL+1,L))/(1+N(NL+1,L)))^2
1750  YT=YTP*(1-C2)/(1-C1*C2)
1760  CHISQ1=CHISQ1+(YT-Y(L))^2
```

```
1770 NEXT L
1780 CHISQ1=CHISQ1/NP
1790 RETURN
1800 REM ========================================================================
1810 REM Calculate n of sapphire or read n of fused quartz.
1820 REM ========================================================================
1830 A1=1.023798
1840 A2=1.058264
1850 A3=5.280792
1860 L12=3.77588E-03
1870 L22=.0122544
1880 L32=321.3616
1890 FOR J=1 TO NP
1900  LS=X(J)*X(J)*.000001
1910  N(NL+1,J)=SQR(1+A1*LS/(LS-L12)+A2*LS/(LS-L22)+A3*LS/(LS-L32))
1920 NEXT J
1930 GOTO 2120
1940 REM read n of fused quartz
1950 OPEN "I",#1,"AQUARTZ.DAT"
1960 J=0
1970 WHILE NOT EOF(1)
1980  J=J+1
1990  INPUT #1,X1(J),Y1(1,J)
2000 WEND
2010 CLOSE #1
2020 NPS=J
2030 JJ=1
2040 FOR I=1 TO NP
2050  FOR J=JJ TO NPS
2060   IF X(I)=X1(J) THEN N(NL+1,I)=Y1(1,J):JJ=J:GOTO 2110
2070   IF X(I)<X1(J) THEN JJ=J-1:GOTO 2090
2080  NEXT J
2090  SLOPE=(Y1(1,J)-Y1(1,J-1))/(X1(J)-X1(J-1))
2100  N(NL+1,I)=Y1(1,J-1)+(X(I)-X1(J-1))*SLOPE
2110 NEXT I
2120 REM Set k of substrate equal to 0.
2130 FOR K=1 TO NP
2140  K(NL+1,K)=0
2150 NEXT K
2160 RETURN
```

```
10 REM ========================================================================
20 REM  T&R.BAS calculates the transmittance and reflectance of a multi-
30 REM  layer thin films system.
40 REM
50 REM  Input: optical constants for substrate and each film
60 REM         thickness (nm) of each film
70 REM
80 REM  The refractive index (n) and extinction coefficient (k) can be non-
90 REM  dispersive or dispersive. The dispersive n and k have to be pre-
100 REM  saved in a data file which has the following format:
110 REM              1st line:  lambda(1)   n(1)   k(1)
120 REM              2nd line:  lambda(2)   n(2)   k(2)
130 REM                .                .
140 REM                .                .            etc.
150 REM where lambda(i) is in nm and is tabulated from short to long.
160 REM The result will be saved in a data file with the following format:
170 REM              1st line:  lambda(1)   T(1) or R(1)
180 REM              2nd line:  lambda(2)   T(2) or R(2)
190 REM                .                .
200 REM                .                .            etc.
210 REM The back surface of substrate has been taken into account during
220 REM calculation as follows:
230 REM          T = T' (1-r(m+2))/(1-r(m+1)r(m+2))
240 REM          R = R' + (T'-T) (R'+T')
250 REM where T = transmittance with the back surface of substrate
260 REM       R = reflectance with the back surface of substrate
270 REM       T' = transmittance without the back surface of substrate
280 REM       R' = reflectance without the back surface of substrate
290 REM       r(m+1) = reflectivity of the interface of film and substrate
300 REM       r(m+2) = reflactivity of the interface of substrate and air
310 REM Maximum # of layers: 5
320 REM Maximum # of data points: 1000
330 REM ============= C. H. PENG  7/16/91 ================================
340 CLS
350 D1=1000 :D2=5 :D3=1000
360 DIM X(D1),YT(D1),YR(D1),N(D2,D1),K(D2,D1),D(D2), X1(D3),Y1(2,D3)
370 DIM G(D2),H(D2),GAMMA(D2),ALPHA(D2)
380 DIM P(D2),Q(D2),R(D2),S(D2),T(D2),U(D2),V(D2),W(D2)
390 DIM P1(D2),Q1(D2),R1(D2),S1(D2),T1(D2),U1(D2),V1(D2),W1(D2)
400 INPUT "Spectral range (wavelength in nm, min, max): ",XMIN, XMAX
410 INPUT "Resolution (in nm): ",RSL
420 NP=INT((XMAX-XMIN)/RSL)+1
430 IF NP > 1000 THEN PRINT "Resolution too high!":BEEP:PRINT: GOTO 410
440 FOR I=1 TO NP
450  X(I)=XMIN+RSL*(I-1)
460  N(0,I)=1 :K(0,I)=0
470 NEXT I
480 PRINT
490 INPUT"How many layers (do not count the substrate)? ",NL
500 IF NL>5 THEN PRINT"Too many layers (max: 5)":GOTO 480
510 PRINT:PRINT"Input the thickness and optical properties for each layer";
520 PRINT" and substrate."
530 PRINT"For refractive index (n) and extinction coefficient (k), entering";
        "digits means constant value independent on wavelength or an ";
        "existed filename means (n,k) value dependent on wavelength."
540 FOR I=1 TO NL
550  PRINT :PRINT"Layer # ";I
560  INPUT "Thickness (in nm): ",D(I)
570  INPUT "Refractive Index (n): ",RI$
580  IF ASC(RI$)>45 AND ASC(RI$)<58 THEN RI=VAL(RI$)
```

```
                                        ELSE GOSUB 1300:GOTO 660
590  FOR J=1 TO NP
600   N(I,J)=RI
610  NEXT J
620  INPUT "Extinction coefficient (k): ",EC
630  FOR J=1 TO NP
640   K(I,J)=EC
650  NEXT J
660 NEXT I
670 PRINT:PRINT"Substrate:"
680 PRINT "Refractive Index (n) (Enter 'S' for sapphire, 'G' for glass, a";
        " file name for other materials, or digits for constants):";
690 INPUT " ",RI$
700 IF RI$="S" OR RI$="s" THEN GOSUB 2010:GOTO 800
710 IF RI$="g" OR RI$="G" THEN GOSUB 2150:GOTO 800
720 IF ASC(RI$)>45 AND ASC(RI$)<58 THEN RI=VAL(RI$)
                                    ELSE GOSUB 1300: GOTO 800
730 FOR J=1 TO NP
740  N(NL+1,J)=RI
750 NEXT J
760 INPUT "Extinction coefficient (k): ",EC
770 FOR J=1 TO NP
780  K(NL+1,J)=EC
790 NEXT J
800 GOSUB 1190
810 GOSUB 1440
820 GOSUB 870
830 PRINT
840 INPUT "Another calculation? (Y/N) ",Y$
850 IF Y$="Y" OR Y$="y" THEN CLS: GOTO 400
860 END
870 REM ================================================================
880 REM   Save data (X,Y)
890 REM   The data are saved in (x,y) array.
900 REM ================================================================
910 INPUT "Save T? (Y/N) ",YY$
920 IF YY$="N" OR YY$="n" THEN 990
930 INPUT "Enter data file name to save T:",FILEN$
940 OPEN "O", #1, FILEN$
950 FOR I=1 TO NP
960  PRINT #1,X(I),YT(I)
970 NEXT I
980 CLOSE #1
990 INPUT "Save R? (Y/N) ",YY$
1000 IF YY$="N" OR YY$="n" THEN 1070
1010 INPUT "Enter data file name to save R: ",FILEN$
1020 OPEN "O",#1,FILEN$
1030 FOR I=1 TO NP
1040  PRINT #1 ,X(I),YR(I)
1050 NEXT I
1060 CLOSE #1
1070 RETURN
1080 REM ================================================================
1090 REM   Get data (X,Y1,Y2)
1100 REM ================================================================
1110 OPEN "I",#1,FILEN$
1120 J=0
1130 WHILE NOT EOF(1)
1140  J=J+1
1150  INPUT #1,X1(J),Y1(1,J),Y1(2,J)
```

```
1160 WEND
1170 CLOSE #1
1180 RETURN
1190 REM ========================================================================
1200 REM   Display a wait message
1210 REM ========================================================================
1220 CLS
1230 FOR I=1 TO 8
1240 PRINT
1250 NEXT I
1260 PRINT CHR$(7)
1270 PRINT "               Please wait for calculation ..... (";NP;"pts )"
1280 RETURN
1290 REM ========================================================================
1300 REM Read n & k and convert them to (x,y) arrays.
1310 REM ========================================================================
1320 FILEN$=RI$ : GOSUB 1080
1330 JJ=J
1340 FOR J=1 TO NP
1350  FOR J1=1 TO JJ
1360   IF X(J)=X1(J1) THEN N(I,J)=Y1(1,J1):K(I,J)=Y1(2,J1) : GOTO 1420
1370   IF X(J)<X1(J1) THEN SLOPE=(X(J)-X1(J1-1))/(X1(J1)-X1(J1-1))
                      ELSE GOTO 1410
1380   N(I,J)=Y1(1,J1-1)+(Y1(1,J1)-Y1(1,J1-1))*SLOPE
1390   K(I,J)=Y1(2,J1-1)+(Y1(2,J1)-Y1(2,J1-1))*SLOPE
1400   GOTO 1420
1410  NEXT J1
1420 NEXT J
1430 RETURN
1440 REM ========================================================================
1450 REM  Multi-layer transmittance and reflectance calculation
1460 REM  See O. S. Heavens, "Optical Properties of Thin Solid Films"
1470 REM  (Academic, New York, 1955), pp.76-79
1480 REM ========================================================================
1490 FOR L=1 TO NP
1500  FOR I=1 TO NL+1
1510   NN=(N(I-1,L)+N(I,L))^2+(K(I-1,L)+K(I,L))^2
1520   G(I)=(N(I-1,L)^2+K(I-1,L)^2-N(I,L)^2-K(I,L)^2)/NN
1530   H(I)=(2*(N(I-1,L)*K(I,L)-N(I,L)*K(I-1,L)))/NN
1540  NEXT I
1550  P1(1)=1! :Q1(1)=0! :R1(1)=G(1) :S1(1)=H(1)
1560  T1(1)=G(1) :U1(1)=H(1):V1(1)=1! :W1(1)=0!
1570  FOR I=1 TO NL
1580   ALPHA(I)=6.2831853#*K(I,L)*D(I)/X(L)
1590   GAMMA(I)=6.2831853#*N(I,L)*D(I)/X(L)
1600  NEXT I
1610  FOR I=2 TO NL+1
1620   EA=EXP(ALPHA(I-1))
1630   CG=COS(GAMMA(I-1))
1640   SG=SIN(GAMMA(I-1))
1650   EMA=EXP(-ALPHA(I-1))
1660   P(I)=EA*CG
1670   Q(I)=EA*SG
1680   T(I)=EMA*(G(I)*CG+H(I)*SG)
1690   U(I)=EMA*(H(I)*CG-G(I)*SG)
1700   IF I=NL+1 THEN 1760
1710   R(I)=EA*(G(I)*CG-H(I)*SG)
1720   S(I)=EA*(H(I)*CG+G(I)*SG)
1730   V(I)=EMA*CG
1740   W(I)=-EMA*SG
```

```
1750  NEXT I
1760  FOR I=1 TO NL
1770   P1(I+1)=P1(I)*P(I+1)-Q1(I)*Q(I+1)+R1(I)*T(I+1)-S1(I)*U(I+1)
1780   Q1(I+1)=Q1(I)*P(I+1)+P1(I)*Q(I+1)+S1(I)*T(I+1)+R1(I)*U(I+1)
1790   T1(I+1)=T1(I)*P(I+1)-U1(I)*Q(I+1)+V1(I)*T(I+1)-W1(I)*U(I+1)
1800   U1(I+1)=U1(I)*P(I+1)+T1(I)*Q(I+1)+W1(I)*T(I+1)+V1(I)*U(I+1)
1810   IF I=NL THEN 1870
1820   R1(I+1)=P1(I)*R(I+1)-Q1(I)*S(I+1)+R1(I)*V(I+1)-S1(I)*W(I+1)
1830   S1(I+1)=Q1(I)*R(I+1)+P1(I)*S(I+1)+S1(I)*V(I+1)+R1(I)*W(I+1)
1840   V1(I+1)=T1(I)*R(I+1)-U1(I)*S(I+1)+V1(I)*V(I+1)-W1(I)*W(I+1)
1850   W1(I+1)=U1(I)*R(I+1)+T1(I)*S(I+1)+W1(I)*V(I+1)+V1(I)*W(I+1)
1860  NEXT I
1870  YRP=(T1(NL+1)^2+U1(NL+1)^2)/(P1(NL+1)^2+Q1(NL+1)^2)
1880  NUMER=1
1890  FOR I=1 TO NL+1
1900   NUMER=NUMER*((1+G(I))^2+H(I)^2)
1910  NEXT I
1920  DENOM=P1(NL+1)^2+Q1(NL+1)^2
1930  YTP=(N(NL+1,L)*NUMER)/(N(0,L)*DENOM)
1940  C1=((N(NL,L)-N(NL+1,L))/(N(NL,L)+N(NL+1,L)))^2
1950  C2=((1-N(NL+1,L))/(1+N(NL+1,L)))^2
1960  YT(L)=YTP*(1-C2)/(1-C1*C2)
1970  YR(L)=YRP+(YTP-YT(L))*(YRP+YTP)
1980  LOCATE 15,35 :PRINT L
1990 NEXT L
2000 RETURN
2010 REM ========================================================================
2020 REM Calculate n of sapphire or read n of fused quartz.
2030 REM ========================================================================
2040 A1=1.023798
2050 A2=1.058264
2060 A3=5.280792
2070 L12=3.77588E-03
2080 L22=.0122544
2090 L32=321.3616
2100 FOR J=1 TO NP
2110  LS=X(J)*X(J)*.000001
2120  N(NL+1,J)=SQR(1+A1*LS/(LS-L12)+A2*LS/(LS-L22)+A3*LS/(LS-L32))
2130 NEXT J
2140 GOTO 2330
2150 REM read n of fused quartz
2160 OPEN "I",#1,"AQUARTZ.DAT"
2170 J=0
2180 WHILE NOT EOF(1)
2190  J=J+1
2200  INPUT #1,X1(J),Y1(1,J)
2210 WEND
2220 CLOSE #1
2230 NPS=J
2240 JJ=1
2250 FOR I=1 TO NP
2260  FOR J=JJ TO NPS
2270   IF X(I)=X1(J) THEN N(NL+1,I)=Y1(1,J):JJ=J:GOTO 2320
2280   IF X(I)<X1(J) THEN JJ=J-1:GOTO 2300
2290  NEXT J
2300  SLOPE=(Y1(1,J)-Y1(1,J-1))/(X1(J)-X1(J-1))
2310  N(NL+1,I)=Y1(1,J-1)+(X(I)-X1(J-1))*SLOPE
2320 NEXT I
2330 FOR K=1 TO NP :K(NL+1,K)=0 :NEXT K:REM Set ks=0
2340 RETURN
```

```
10 REM ========================================================================
20 REM DRFIT.BAS finds the dispersion relation parameters by fitting the
30 REM refractive index data to a Sellmeier type equation:
40 REM      n^2 = 1 + (A*lambda^2)/(lambda^2-B)
50 REM where A and B are the parameters to be determined and lambda is in um.
60 REM
70 REM input: refractive index data file (lambda in nm)
80 REM        lower and upper bounds for A and B
90 REM output: fitting error and parameter A and B
100 REM
110 REM ================  C. H. PENG   7/15/92  ============================
120 DIM X(100),N(100)
130 CLS
140 INPUT "Enter data filename: ",F$
150 INPUT "Enter adjusted value for n: ",ADJ
160 OPEN "I",#1,F$
170 REM Skip the first few "bad" data point
180 INPUT "Enter number of data to be skipped: ",SK
190 I=0:L=0
200 WHILE NOT EOF(1)
210  I=I+1
220  INPUT #1,X1,X2,X3
230  IF I<(SK+1) THEN 250
240  L=L+1:N(L)=X2+ADJ:X(L)=X1
250 WEND
260 NP=L
270 CLOSE #1
280 INPUT "Enter lower and upper limit for A (0,0 to quit): ",AL,AU
290 IF AL=0 AND AU=0 THEN 510
300 AI=(AU-AL)/9
310 INPUT "Enter lower and upper limit for B: ",BL,BU
320 BI=(BU-BL)/9
330 CHISQ=1
340 FOR K=1 TO 10
350 A=AL+AI*(K-1)
360 FOR J=1 TO 10
370 B=BL+BI*(J-1)
380 CHISQ1=0
390 FOR I=1 TO NP
400  C=(X(I)/1000)^2
410  Y=N(I)
420  F=SQR(1+A*C/(C-B))
430  CHISQ1=CHISQ1+(Y-F)^2
440 NEXT I
450 CHISQ1=CHISQ1/NP
460 IF CHISQ1<CHISQ THEN CHISQ=CHISQ1:AA=A:BB=B
470 NEXT J
480 NEXT K
490 PRINT CHISQ,AA,BB
500 GOTO 280
510 INPUT"Another calculation? (Y/N) ",Z$
520 IF Z$="Y" OR Z$="y" THEN 130
530 CLS
540 END
```

```
10 REM ========================================================================
20 REM ALPHA.BAS calculates absorption coefficients of a single film on a
30 REM transparent substrate (sapphire) by using the formula:
40 REM      T = (1-R1)(1-R2)(1-R3)exp(-at)
50 REM where R1, R2, and R3 are reflectivity of air-film, film-substrate,
60 REM and substrate-air interface, respectively.
65 REM T is transmittance and t is the film thickness.
70 REM     R1 = R = reflectance at the sample surface
80 REM     R2 = 1 - (n-ns)^2/(n+ns)^2
90 REM     R3 = 1 - (ns-1)^2/(ns+1)^2
100 REM     n = (1+R^0.5)/(1-R^0.5)
110 REM     ns = refractive index of the substrate
120 REM ========================================================================
130 DI1=1000:DI2=100
140 DIM LAMBDA(DI1),T(DI1),R(DI1)
150 DIM LAMBDAS(DI2),NS1(DI2),NS(DI1),TEMP1(DI1),TEMP2(DI1)
160 A1=1.023798
170 A2=1.058264
180 A3=5.280792
190 L12=3.77588E-03
200 L22=.0122544
210 L32=321.3616
220 PI=3.1415926#
230 CLS
240 INPUT "Enter the file name of transmittance (lambda,T): ",FT$
250 INPUT "Enter the file name of reflectance (lambda,R): ",FR$
260 INPUT "Enter the thickness of film (nm): ",D
270 INPUT "Enter the wavelength range (nm, min, max): ",LMIN,LMAX
280 OPEN "I",#1,FT$
290 INPUT #1,X1,Y1
300 INPUT #1,X2,Y2
310 CLOSE #1
320 IF X1 > X2 THEN GOSUB 1130:GOTO 420
330 OPEN "I",#1,FT$
340 I=0
350 WHILE NOT EOF(1)
360  INPUT #1,X1,Y1
370  IF X1>=LMIN AND Y1>0 THEN I=I+1:LAMBDA(I)=X1:T(I)=Y1
380  IF X1>=LMAX THEN 400
390 WEND
400 NP=I
410 CLOSE #1
420 OPEN "I",#1,FR$
430 INPUT #1,X1,Y1
440 INPUT #1,X2,Y2
450 CLOSE #1
460 IF X1 > X2 THEN GOSUB 1290:GOTO 550
470 OPEN "I",#1,FR$
480 I=0
490 WHILE NOT EOF(1)
500  INPUT #1,X1,Y1
510  IF X1>=LAMBDA(1) THEN I=I+1:R(I)=Y1
520  IF X1>=LMAX THEN 540
530 WEND
540 CLOSE #1
550 IF R(NP)<1 THEN 590
560 FOR I=1 TO NP
570  R(I)=R(I)*.01
580 NEXT I
590 IF T(NP)<1 THEN 630
```

```
600 FOR I=1 TO NP
610  T(I)=T(I)*.01
620 NEXT I
630 PRINT
640 PRINT "Select Substrate:" :PRINT
650 PRINT "      1 ... Sapphire"
660 PRINT "      2 ... Fused Quartz":PRINT
670 INPUT "Enter your selection: ",S
680 IF S=1 THEN GOTO 800
690 IF S=2 THEN FILEN1$="AQUARTZ.DAT"
700 IF S>2 OR S<1 THEN GOTO 230
710 OPEN "I",#1,FILEN1$
720 INPUT #1,DESC$
730 I=0
740 WHILE NOT EOF(1)
750  I=I+1
760  INPUT #1,LAMBDAS(I),NS1(I)
770 WEND
780 NPS=I
790 CLOSE #1
800 IF S=1 THEN GOSUB 1080
810 IF S=2 THEN GOSUB 980
820 PRINT
830 INPUT "Enter file name to save (E(eV),A(cm-1),A^2,SQR(A)): ",FA$
840 OPEN "O",#1,FA$
850 FOR I=1 TO NP
860  NF=(1+SQR(R(I)))/(1-SQR(R(I)))
870  R2=(NF-NS(I))^2/(NF+NS(I))^2
880  R3=(1-NS(I))^2/(1+NS(I))^2
890  ALPHA=(1E+07/D)*LOG((1-R(I))*(1-R2)*(1-R3)/T(I))
900  IF ALPHA<0 THEN 930
910  PRINT #1,1239.85/LAMBDA(I),ALPHA,ALPHA^2,SQR(ALPHA)
920 NEXT I
930 CLOSE #1
940 PRINT:INPUT"Another calculation? (Y/N) ",Z$
950 IF Z$="Y" OR Z$="y" THEN GOTO 230
960 CLS
970 END
980 JJ=1
990 FOR I=1 TO NP
1000  FOR J=JJ TO NPS
1010   IF LAMBDA(I)=LAMBDAS(J) THEN NS(I)=NS1(J):JJ=J: GOTO 1060
1020   IF LAMBDA(I)<LAMBDAS(J) THEN JJ=J-1: GOTO 1040
1030  NEXT J
1040  SLOPE=(NS1(J)-NS1(J-1))/(LAMBDAS(J)-LAMBDAS(J-1))
1050  NS(I)=NS1(J-1)+(LAMBDA(I)-LAMBDAS(J-1))*SLOPE
1060 NEXT I
1070 RETURN
1080 FOR I=1 TO NP
1090  LS=LAMBDA(I)*LAMBDA(I)/1000000!
1100  NS(I)=SQR(1+A1*LS/(LS-L12)+A2*LS/(LS-L22)+A3*LS/(LS-L32))
1110 NEXT I
1120 RETURN
1130 REM
1140 OPEN "I",#1,FT$
1150 I=0
1160 WHILE NOT EOF(1)
1170  I=I+1
1180  INPUT #1,X1,Y1
1190  IF X1<=LMAX AND X1>=LMIN AND Y1>0 THEN TEMP1(I)=X1:TEMP2(I)=Y1
```

```
1200  IF X1<=LMIN THEN 1220
1210 WEND
1220 CLOSE #1
1230 NP=I+1
1240 FOR I=NP TO 1 STEP -1
1250  LAMBDA(NP-I+1)=TEMP1(I)
1260  T(NP-I+1)=TEMP2(I)
1270 NEXT I
1280 RETURN
1290 REM
1300 OPEN "I",#1,FR$
1310 I=0
1320 WHILE NOT EOF(1)
1330  I=I+1
1340  INPUT #1,X1,Y1
1350  IF X1<=LMAX AND X1>=LAMBDA(1) THEN TEMP1(I)=X1:TEMP2(I)=Y1
1360  IF X1<=LAMBDA(1) THEN 1380
1370 WEND
1380 CLOSE #1
1390 FOR I=NP TO 1 STEP -1
1400  LAMBDA(NP-I+1)=TEMP1(I)
1410  R(NP-I+1)=TEMP2(I)
1420 NEXT I
1430 RETURN
```

```
10 REM ========================================================================
20 REM VF.BAS calculates (1) the pyrochlore volume fraction of amorphous-
30 REM pyrochlore mixture PZT film and (2) the perovskite volume fraction
40 REM of pyrochlore-perovskite mixture PZT film by using effective medium
50 REM approximation.
60 REM         n(PT,bulk)=2.668     n(PZ,bulk)=2.42
70 REM Ref: Philip D. Thacher, Applied Optics, 16(12), 3210-3213 (1977)
80 REM
90 REM  Step 1: Calculation packing density
100 REM Step 2: Calculation bulk n of pyrochlore
110 REM Step 3: Calculation bulk n of amorphous
120 REM Step 4: Calculation volume fraction of pyrochlore of amorphous-
130 REM         pyrochlore mixture
140 REM Step 5: Calculation volume fraction of perovskite of pyrochlore-
150 REM         perovskite mixture
160 REM ==============  C. H. PENG  1/20/92  ==============================
170 CLS
180 DIM TP(2,20),NP(20),V(2,20)
190 PRINT
200 PRINT"Step 1: Calculation packing density"
210 INPUT"  Enter Zr content=",X
220 INPUT"  Dopant? (Description) ",X$
230 INPUT"  Enter measured n of perovskite phase:",NPEM
240 IF X>1 THEN X=X*.01
250 NPE=2.668-.248*X
260 A=(NPE^2-NPEM^2)/(NPE^2+2*NPEM^2)
270 B=(1-NPEM^2)/(1+2*NPEM^2)
280 PD=B/(B-A)
290 PRINT"  Packing density=";PD
300 PRINT"Step 2: Calculation bulk n of pyrochlore"
310 INPUT"  Enter measured n of pyrochlore phase:",NPYM
320 A=(1-PD)*(NPYM^2-1)/(PD*(1+2*NPYM^2))
330 NPY=SQR((2*A+1)/(1-A))*NPYM
340 PRINT"  bulk n of pyrochlore:";NPY
350 PRINT"Step 3: Calculation bulk n of amorphous (Hit <RETURN> to";
      " skip this step)"
360 INPUT"  Enter measured n of amorphous phase:",NAM
370 A=(1-PD)*(NAM^2-1)/(PD*(1+2*NAM^2))
380 NA=SQR((2*A+1)/(1-A))*NAM
390 PRINT"  bulk n of amorphous:";NA
400 PRINT"Step 4: Calculation volume fraction of pyrochlore of amorphous-"
410 PRINT"        pyrochlore mixture (Hit <RETURN> to skip this step)"
420 INPUT"  Enter initiation temperature of pyrochlore (in Celsius):",TIPY
430 IF TIPY=0 THEN 620
440 INPUT"  Enter completion temperature of pyrochlore (in Celsius):",TCPY
450 PRINT"  Enter T(C) and measured n between";TIPY;"and";TCPY;"C"
460 PRINT"  Enter (0,0) to end entry"
470 I=0
480 I=I+1
490 PRINT"  ";I;
500 INPUT" ",TP(1,I),NP(I)
510 IF TP(1,I)=0 THEN 530
520 GOTO 480
530 NY=I-1
540 PRINT"T(C)" TAB(10) "1/T(K)" TAB(22) "vol frc of py (alpha)" TAB(46)
      "normalized alpha" TAB(65) "Ln(alpha)"
550 FOR I=1 TO NY
560  N2=NP(I)^2:NA2=NA^2:NPY2=NPY^2
570  A=(1-PD)*(N2-1)/(1+2*N2)+PD*(N2-NA2)/(NA2+2*N2)
580  B=(NPY2-N2)/(NPY2+2*N2)-(NA2-N2)/(NA2+2*N2)
```

```
590  V(1,I)=A/B
600  PRINT TP(1,I) TAB(7) 1/(TP(1,I)+273) TAB(25) V(1,I) TAB(47)
          V(1,I)/PD TAB(65) LOG(V(1,I)/PD)
610 NEXT I
620 PRINT"Step 5: Calculation volume fraction of perovskite of pyrochlore-"
630 PRINT"        perovskite mixture (Hit <RETURN> to skip this step)"
640 INPUT"  Enter initiation temperature of perovskite (in Celsius):",TIPE
650 IF TIPE=0 THEN 840
660 INPUT"  Enter completion temperature of perovskite (in Celsius):",TCPE
670 PRINT"  Enter T(C) and measured n between";TIPE;"and";TCPE;"C"
680 PRINT"  Enter (0,0) to end entry"
690 I=0
700 I=I+1
710 PRINT"  ";I;
720 INPUT" ",TP(2,I),NP(I)
730 IF TP(2,I)=0 THEN 750
740 GOTO 700
750 NE=I-1
760 PRINT"T(C)" TAB(10) "1/T(K)" TAB(22) "vol fra of pero (alpha)" TAB(46)
      "normalized alpha" TAB(65) "Ln(alpha)"
770 FOR I=1 TO NE
780  N2=NP(I)^2:NPE2=NPE^2:NPY2=NPY^2
790  A=(1-PD)*(N2-1)/(1+2*N2)+PD*(N2-NPY2)/(NPY2+2*N2)
800  B=(NPE2-N2)/(NPE2+2*N2)-(NPY2-N2)/(NPY2+2*N2)
810  V(2,I)=A/B
820  PRINT TP(2,I) TAB(7) 1/(TP(2,I)+273) TAB(25) V(2,I) TAB(47)
          V(2,I)/PD TAB(65) LOG(V(2,I)/PD)
830 NEXT I
840 PRINT
850 INPUT"Save all results into a file? (Y/N) ",Z$
860 IF Z$="n" OR Z$="N" THEN 1090
870 INPUT"Enter file name to save results:",F$
880 OPEN "O",#1,F$
890 PRINT #1,"Zr content = ";X;"    Dopant = ";X$
900 PRINT #1,"  Measured n of perovskite = ";NPEM
910 PRINT #1,"  Measured n of pyrochlore = ";NPYM
920 PRINT #1,"  Measured n of amorphous = ";NAM
930 PRINT #1,"  Packing density = ";PD
940 PRINT #1,"  Calculated bulk n of pyrochlore = ";NPY
950 PRINT #1,"  Calculated bulk n of amorphous = ";NA
960 PRINT #1,"  Initiation temperature of pyrochlore = ";TIPY
970 PRINT #1,"  Completion temperature of pyrochlore = ";TCPY
980 PRINT #1,"  Initiation temperature of perovskite = ";TIPE
990 PRINT #1,"  Completion temperature of perovskite = ";TCPE
1000 PRINT #1,"T(C)" TAB(10) "1/T(K)" TAB(22) "vol fra of py (alpha)"
          TAB(46) "normalized alpha" TAB(65) "Ln(alpha)"
1010 FOR I=1 TO NY
1020  PRINT #1,TP(1,I) TAB(7) 1/(TP(1,I)+273) TAB(25) V(1,I) TAB(47)
          V(1,I)/PD TAB(65) LOG(V(1,I)/PD)
1030 NEXT I
1040 PRINT #1,"T(C)" TAB(10) "1/T(K)" TAB(22) "vol fra of pero (alpha)"
          TAB(46) "normalized alpha" TAB(65) "Ln(alpha)"
1050 FOR I=1 TO NE
1060  PRINT #1,TP(2,I) TAB(7) 1/(TP(2,I)+273) TAB(25) V(2,I) TAB(47)
          V(2,I)/PD TAB(65) LOG(V(2,I)/PD)
1070 NEXT I
1080 CLOSE #1
1090 INPUT "Another calculation? (Y/N) ",Z$
1100 IF Z$="y" OR Z$="Y" THEN 190
1110 CLS:END
```

Bibliography

1. J. Stankowski, "Molecular Dynamics of the Ferroelectric Crystals of the Triglycine Sulphate Family," Phys. Rep., 77(1), 1 (1981).
2 C. Araujo, J. F. Scott, R. B. Godfrey, and L. McMillan, "Analysis of Switching Transients in KNO_3 Ferroelectric Memories," Appl. Phys. Lett. 48(21), 1439 (1986).
3. T. Mitsui and E. Nakamura (Editors), *Landolt–Bornstein Series, Vol. 28 Ferroelectrics and Related Substances*, (Springer–Verlag, Berlin, 1990).
4. R. S. Weis and T. K. Gaylord, "Lithium Niobate: Summary of Physical Properties and Crystal Structure," Appl. Phys., A37, 191 (1985).
5. G. Arlt, D. Hennings, and G. de With, "Dielectric Properties of Fine–Grained Barium Titanate Ceramics," J. Appl. Phys., 58(4), 1619 (1985).
6. C. E. Land and P. D. Thacher, "Ferroelectric Ceramic Electrooptic Materials and Devices," Proc. IEEE, 57(5), 751 (1969).
7. B. Jaffe, W. Cook, and H. Jaffe, *Ferroelectric Ceramics*, (Academic Press, London, 1971), p.136.
8. J. Scott and C. Paz de Araujo, "Ferroelectric Memories," Science, 246, 1400 (1989).
9. Ramtron Corporation, Colorado Springs, CO 80918.
10. R. W. Whatmore, P. C. Osbond, and N. M. Shorrocks, "Ferroelectric Materials for Thermal IR Detectors," Ferroelectrics, 76, 351 (1987).
11. A. J. Moulson and J. M. Herbert, *Electroceramics*, (Chapman and Hall, London, 1990), Chapter 7.
12. J. J. Gagnepain, T. R. Meeker, T. Nakamura, and L. A. Shuvalov (Editors), *Special Issue on Piezoelectricity, In Commemoration of the Centenary of the Discovery of Piezoelectricity by Jacques and Pierre Curie*, Ferroelectrics, 40(3/4), 41(1/2/3/4), 42(1/2/3/4), 43(1/2), (1982).
13. P. Gunter, "Electro–optical Effects in Ferroelectrics," Ferroelectrics, 74, 305 (1987).

14. G. Busch, R. Blinc, T. Matsubara, V. H. Schmidt, and L. A. Shuvalov (Editors), *Special Issue on KH_2PO_4–Type Ferro– and Antiferroelectrics*, Ferroelectrics, 71(1/2/3/4), 72(1/2/3/4), (1987).
15. G. H. Haertling, "PLZT Electrooptic Materials and Applications – A Review," Ferroelectrics, 75, 25 (1987).
16. M. Okada and K. Tominaga, "Preparation and Properties of (Pb,La)(Zr,Ti)O_3 Thin Films by Metalorganic Chemical Vapor Deposition," J. Appl. Phys., 71(4), 1955 (1992).
17. M. Ishida, H. Matsunami, and T. Tanaka, "Preparation and Properties of Ferroelectric PLZT Thin Films by rf Sputtering," J. Appl. Phys., 48(3), 951 (1977).
18. G. H. Haertling, "Ferroelectric Thin Films for Electronic Applications," J. Vac. Sci. Technol., A9(3), 414 (1991).
19. M. Oikawa and K. Toda, "Preparation of Pb(Zr,Ti)O_3 Thin Films by an Electron Beam Evaporation Technique," Appl. Phys. Lett, 29(8), 491 (1976).
20. A. Okada, "Some Electrical and Optical Properties of Ferroelectric Lead–Zirconate–Lead–Titanate Thin Films," J. Appl. Phys., 48(7), 2905 (1977).
21. S. Krupanidhi, N. Maffei, M. Sayer, and K. El–Assal, "rf Planar Magnetron Sputtering and Characterization of Ferroelectric Pb(Zr,Ti)O_3 Films," J. Appl. Phys., 54(11), 6601 (1983).
22. R. Takayama and Y. Tomita, "Preparation of Epitaxial Pb(Zr_xTi_{1-x})O_3 Thin Films and their Crystallographic, Pyroelectric, and Ferroelectric Properties," J. Appl. Phys., 65(4), 1666 (1989).
23. M. Adachi, T. Matsuzaki, T. Yamada, T. Shiosaki, and A. Kawabata, "Sputter–Deposition of [111]–Axis Oriented Rhombohedral PZT Films and their Dielectric, Ferroelectric, and Pyroelectric Properties," Jpn. J. Appl. Phys., 26(4), 550 (1987).
24. K. Sreenivas, M. Sayer, D. J. Baar, and M. Nishioka, "Surface Acoustic Wave Propagation on Lead Zirconate Titanate Thin Films," Appl. Phys. Lett., 52(9), 709 (1988).
25. R. N. Castellano and L. G. Feinstein, "Ion–beam Deposition of Thin Films of Ferroelectric Lead Zirconate Titanate (PZT)," J. Appl. Phys., 50(6), 4406 (1979).

26. K. Saenger, R. Rpy, K. Etzold, and J. Cuomo, "Lead Zirconate Titanate Films Produced by Pulse Laser Deposition," Mat. Res. Soc. Symp. Proc., 200, 115 (1991).
27. K. Ramkumar, J. Lee, A. Safari, and S. Danforth, "Ferroelectric Thin Films Deposited by Laser Ablation," Mat. Res. Soc. Symp. Proc., 200, 121 (1991).
28. C. Chiang, C. Cook, P. Schenck, P. Brody, and J. Benedetto, "Lead Zirconate Titanate Thin Films Prepared by the Laser Ablation Technique," Mat. Res. Soc. Symp. Proc., 200, 133 (1991).
29. R. Ramesh, A. Inam, W. K. Chan, F. Tillerot, B. Wilkens, C. C. Chang, T. Sands, J. M. Tarascon, and V. G. Keramidas, "Ferroelectric $PbZr_{0.2}Ti_{0.8}O_3$ Thin Films on Epitaxial Y–Ba–Cu–O," Appl. Phys. Lett., 59(27), 3542 (1991).
30. J. Fukushima, K. Kodaira, and T. Marsushita, "Preparation of Ferroelectric PZT Films by Thermal Decomposition of Organometallic Compounds," J. Mater. Sci., 19, 595 (1984).
31. K. D. Budd, S. K. Dey, and D. A. Payne, "Sol–Gel Processing of $PbTiO_3$, $PbZrO_3$, PZT, and PLZT Thin Films," Proc. Brit. Cer. Soc., 36, 107 (1985).
32. G. Yi, Z. Wu, and M. Sayer, "Preparation of $Pb(Zr,Ti)O_3$ Thin Films by Sol–Gel Processing: Electrical, Optical, and Electro–optic Properties," J. Appl. Phys., 64(5), 2717 (1988).
33. M. Okada, K. Tominaga, T. Araki, S. Katayama, and Y. Sakashita, "Metalorganic Chemical Vapor Deposition of c–Axis Oriented PZT Thin Films," Jpn. J. Appl. Phys. 29(4), 718 (1990).
34. Y. Sakashita, T. Ono, H. Segawa, K. Tominaga, and M. Okada, "Preparation and Electrical Propertiws of MOCVD–deposited PZT Thin Films," J. Appl. Phys. 69(12), 8352 (1991).
35. H. Funakubo, K. Imashita, N. Kieda, and N. Mizutani, "Formation of Epitaxial $Pb(Zr,Ti)O_3$ Film by CVD," J. Ceram. Soc. Jpn. 99, 241 (1991).
36. K. Kashihara, H. Itoh, K. Tsukamoto, and Y. Akasaka, "Formation of PZT Films by MOCVD," Extended Abstracts of the 1991 International Conference on Solid State Devices and Materials (Yokohama, Japan), pp. 192–194 (1991).
37. G. J. M. Dormans, M. de Keijser, and P. J. van Veldhoven, "Ferroelectric $PbZr_xTi_{1-x}O_3$ Thin Films Grown by Organometallic Chemical Vapor Deposition," Mat. Res. Soc. Symp. Proc., 243, (1992), in press.
38. C. H. Peng and S. B. Desu, "Low–Temperature Metalorganic Chemical Vapor

Deposition of Perovskite $Pb(Zr_xTi_{1-x})O_3$ Thin Films," Appl. Phys. Lett., 61(1), 16 (1992).

39. J. –F. Chang, "Preparation and Characterization of Doped Lead Zirconate Titanate Films," M.S. Thesis, Virginia Polytechnic Institute and State University, August 1992.
40. H. E. Bennet and J. M. Bennet, in *Physics of Thin Films Vol.4*, edited by G. Hass and R. E. Thun (Acdemic Press, New York, 1967), pp. 1–96.
41. C. H. Peng, J. –F. Chang, and S. B. Desu, "Optical Properties of PZT, PLZT, and PNZT Thin Films," Mat. Res. Soc. Symp. Proc., 243, (1992), in press.
42. J. C. Manifacier, J. Gasiot, and J. P. Fillard, "A Simple Method for the Determination of the Optical Constants n, k and the Thickness of a Weakly Absorbing Thin Film," J. Phys. E: Sci. Instrum., 9, 1002 (1976).
43. R. Swanepoel, "Determination of the Thickness and Optical Constants of Amorphous Silicon," J. Phys. E: Sci. Instrum., 16, 1214 (1983).
44. H. H. Li, "Refractive Index of ZnS, ZnSe, and ZnTe and Its Wavelength and Temperature Derivatives," J. Phys. Chem. Ref. Data, 13(1), 103 (1984).
45. O. S. Heavens, *Optical Properties of Thin Solid Films*, (Dover, New York, 1955), Chapter 4.
46. R. M. A. Azzam and N. M. Bashara, *Ellipsometry and Polarized Light*, (North–Holland, Amsterdam, 1977), Chapter 4.
47. R. Swanepoel, "Determination of Surface Roughness and Optical Constants of Inhomogeneous Amorphous Silicon Films," J. Phys. E: Sci. Instrum., 17, 896 (1984).
48. D. E. Aspnes, "Optical Properties of Thin Films," Thin Solid Films, 89, 249 (1982).
49. A. G. Bruggeman, Ann. Phys. (Leipzig), 24, 636 (1935).
50. G. Feng, "Optical Studies of Ion–Bombarded Gallium Arsenide," PhD Thesis, Virginia Polytechnic Institute and State University, May 1989.
51. R. Tsu, W. E. Howard, and L. Esaki, " ," Phys. Rev., 172, 779 (1968).
52. I. H. Malitson, "Refraction and Dispersion of Synthetic Sapphire," J. Opt. Soc. Am., 52(12), 1377 (1967).
53. M. McClain, A. Feldman, D. Kahaner, and X. Ying, "An Algorithm and Computer Program for the Calculation of Envelope Curves," Computers in Physics, Jan/Feb 1991, p.45.

54. P. D. Thacher, "Refractive Index and Surface Layers of Ceramic (Pb,La)(Zr,Ti)O_3 Compounds," Appl. Opt., 16(12), 3210 (1977).
55. S. B. Desu (unpublished).
56. S. Singh, J. P. Remeika, and J. R. Potopowicz, "Nonlinear Optical Properties of Ferroelectric Lead Titanate," Appl. Phys. Lett., 20(3), 135 (1972).
57. V. I. Zametin, "Absorption Edge Anomalies in Polar Semiconductors and Dielectrics at Phase Transitions," Phys. Stat. Sol. (b), 124, 625 (1984).
58. C. K. Kwok, "Processing–Structure–Property Interrelationships of Ferroelectric Thin Films with Emphasis on Formation Finetics," PhD Thesis, Virginia Polytechnic Institute and State University, July 1992.
59. S. B. Desu, C. H. Peng, L. Kammerdiner, and P. J. Schuele, "Size Effects in Sputtered PZT Thin Films," Mat. Res. Soc. Symp. Proc., 200, 319 (1991).
60. G. Shirane and A. Takeda, "Phase Transitions in Solid Solution of Lead Zirconate and Lead Titanate," J. Phys. Soc. Japan, 7(1), 5 (1952).
61. Y. Matsuo and H. Sasaki, "Formation of Lead Zirconate – Lead Titanate Solid Solutions," J. Am. Ceram. Soc., 48(6), 289 (1965).
62. S. Chandratreya, R. Fulrath, and J. Pask, "Reaction Mechanisms in the Formation of PZT Solid Solutions," J. Am. Ceram. Soc., 71(10), 879 (1981).
63. E. Jaren and P. Duran, "Mechanism of the Solid State Formation of Lead Zirconate Titanate," J. de Phys. Colloque C1, 47(2), 537 (1986).
64. A. Okada, "Electrical Properties of Lead–Zirconate–Titanate Ferroelectric Thin Film and Their Composition Analysis by Auger Electron Spectroscopy," J. Appl. Phys., 49(8), 4495 (1978).
65. C. Kwok and S. B. Desu, "Pyrochlore–Perovskite Phase Transformation of Lead Zirconate Titanate (PZT) Thin Films," Ceramic Transactions: Ferroelectric Films, 25, A. Bhalla, ed., ACS, Westerville, OH, 73 (1992).
66. K. F. Jensen and W. Kern, in *Thin Film Processes Vol.2*, edited by J. L. Vossen and W. Kern (Academic Press, New York, 1991), p. 283.
67. T. Nakagawa, J. Yamaguchi, M. Okuyama, and Y. Hamakawa, "Preparation of $PbTiO_3$ Ferroelectric Thin Film by Chemical Vapor Deposition," Jpn. J. Appl. Phys. 21(10), L655 (1982).
68. G. K. Schweitzer, B. P. Pullen, and Y. H. Fang, "The Volatilities of Some Lead β–diketonates," Analyt. Chim. Acta, 43, 332 (1968).
69. D. C. Bradley, R. C. Mehrotra, P. D. Gaur, *Metal Alkoxides*, (Academic Press,

New York, 1978).

70. M. Nyman, "Synthesis and Characterization of Precursors for Chemical Vapor Deposition of Metal Oxide Thin Films," M.S. Thesis, Virginia Polytechnic Institute and State University, July 1992.
71. F. W. Ainger, C. J. Brierley, M. D. Hudson, C. Trundle, and R. W. Whatmore, "Ferroelectric Thin Films by Metalorganic Chemical Vapour Deposition," Mat. Res. Soc. Symp. Proc., 200, 37 (1991).
72. C. J. Brierley, C. Trundle, L. Considine, R. W. Whatmore, and F. W. Ainger, "The Growth of Ferroelectric Oxides by MOCVD," Ferroelectrics, 91, 181 (1989).
73. B. S. Kwak, E. P. Boyd, and A. Erbil, "Metalorganic Chemical Vapor Deposition of $PbTiO_3$ Thin Films," Appl. Phys. Lett. 53(18), 1702 (1989).
74. S. L. Swartz, D. A. Seifert, G. T. Noel, and T. R. Shrout, "Characterization of MOCVD $PbTiO_3$ Thin Films," Ferroelectrics 93, 37 (1989).
75. S. Tain, C. H. Peng, and S. B. Desu, (unpublished).
76. S. B. Desu, S. Tain, and C. Kwok, "Structure, Composition, and Properties of MOCVD ZrO_2 Thin Films," Mat. Res. Soc. Symp. Proc., 168, 349 (1990).
77. J. Si, C. H. Peng, and S. B. Desu, "Deposition abd Characterization of MOCVD ZrO_2 Thin Films Using $Zr(thd)_4$," Mat. Res. Soc. Symp. Proc., 243, (1992), in press.
78. Powder Diffraction File, Card No. 6–0547, Joint Committee on Powder Diffraction Standards (JCPDS), Swarthmore, PA.

VITA

Chien–Hsiung Peng was born on June 19, 1958 in Tainan, Taiwan. He received his undergraduate training at National Tsing Hua University, Hsinchu, Taiwan, where he earned a Bachelor of Science degree in Physics in 1980. He then completed his Master of Science degree in Materials Science and Engineering at National Tsing Hua University in 1982. He enrolled in the Materials Engineering Science Program at Virginia Tech to pursue his PhD in 1985. From Fall 1985 to Summer 1989, he worked with Profs. R. Zallen and D. Hoffman in the Physics Department. Later he worked with Prof. S. B. Desu in Materials Science Engineering Department. After receiving his PhD from Virginia Tech in August 1992, he will work for Ceram Incorporated in the field of electronic and optical thin films.